Transactions of the ASME®

Journal of Engineering for Gas Turbines and Power

Published Quarterly by The American Society of Mechanical Engineers
VOLUME 110 • NUMBER 4 • OCTOBER 1988

Technical Editor
ARTHUR J. WENNERSTROM
Senior Associate Technical Editor
G. K. SEROVY
Associate Technical Editors
Advanced Energy Systems
M. J. MORAN
Environmental Control
H. E. HESKETH
Fuels and Combustion Technologies
R. E. BARRETT
Gas Turbine
T. H. OKIISHI
Internal Combustion Engine
J. A. CATON
Nuclear Engineering
S. M. CHO
Power
R. W. PORTER

BOARD ON COMMUNICATIONS
Chairman and Vice-President
R. NICKELL

Members-at-Large
J. LLOYD
R. REDER
F. SCHMIDT
M. FRANKE
M. KUTZ
T. MIN
F. LANDIS
R. ROCKE
W. WINER
R. GENTILE
R. MATES
R. VOGLER

President, **E. L. DAMAN**
Executive Director,
D. L. BELDEN
Treasurer, **ROBERT A. BENNETT**

PUBLISHING STAFF
Mng. Dir., Publ., **JOS. SANSONE**
Managing Editor,
CORNELIA MONAHAN
Sr. Production Editor,
VALERIE WINTERS
Editorial Prod. Asst.
MARISOL ANDINO

Transactions of the ASME, Journal of Engineering for Gas Turbines and Power (ISSN 0022-0825) is published quarterly (Jan., Apr., July, Oct.) for $120 per year by The American Society of Mechanical Engineers, 345 East 47th Street, New York, NY 10017. Second class postage paid at New York, NY and additional mailing offices. POSTMASTER: Send address change to The Journal of Engineering for Gas Turbines and Power, c/o The AMERICAN SOCIETY OF MECHANICAL ENGINEERS, 22 Law Drive, Box 2300, Fairfield, NJ 07007-2300.
CHANGES OF ADDRESS must be received at Society headquarters seven weeks before they are to be effective. Please send old label and new address.
PRICES: To members, $29.00, annually; to nonmembers, $120.00.
Add $12.00 for postage to countries outside the United States and Canada.

STATEMENT from By-Laws. The Society shall not be responsible for statements or opinions advanced in papers or ... printed in its publications (B 7.1, para. 3).
COPYRIGHT © **1988** by the American Society of Mechanical Engineers. Reprints from this publication may be made on condition that full credit be given the TRANSACTIONS OF THE ASME—JOURNAL OF ENGINEERING FOR GAS TURBINES AND POWER, and the author, and date of publication be stated.

INDEXED by Applied Mechanics Reviews and Engineering Information, Inc.

TECHNICAL PAPERS

(Contents continued on p. 571)

Downloaded 03 Jun 2010 to 171.66.16.159. Redistribution subject to ASME license or copyright; see http://www.asme.org/terms/Terms_Use.cfm

(Contents Continued)

TECHNICAL BRIEFS

ANNOUNCEMENTS

P. Schwibinger

R. Nordmann

University of Kaiserslautern,
Kaiserslautern, Federal Republic of Germany

The Influence of Torsional-Lateral Coupling on the Stability Behavior of Geared Rotor Systems

In high-performance turbomachinery trouble often arises due to unstable asynchronous lateral vibrations. The instabilities are mostly caused by oil film bearings, clearance excitation, internal damping, annular pressure seals in pumps, or labyrinth seals in turbocompressors. In recent times as an additional influence the coupling between torsional and lateral vibrations is considered, which is of practical importance in geared rotor systems. In the literature [*1, 2*]*, some field problems are described, where in geared drive trains unstable lateral vibrations occurred together with torsional oscillations. This presentation studies the influence of torsional-lateral coupling on the stability behavior of a simple geared system supported by oil film bearings. The coupling effect is investigated by parameter studies and a sensitivity analysis for the uncoupled and the coupled system.*

Introduction

The dynamic behavior of many rotating machines, e.g., turbines, compressors, and pumps, is influenced by the stiffness and damping characteristics of nonconservative effects like oil film forces, forces in seals, clearing excitation forces, etc. In addition to the forced imbalance vibrations, unstable nonsynchronous vibrations may also occur, caused by the abovementioned self-exciting mechanisms. Usually the stability analysis for this turbomachinery is limited to a lateral rotor dynamic analysis, which is carried out independently from the torsional vibration analysis. However, for geared rotor systems, e.g., compressor or turbogenerator sets (Fig. 1), the torsional and lateral vibrations are coupled, due to the offset centerlines of the geared rotors. Until now, not much has been known about how this coupling affects the stability behavior of the machine.

In the literature we find several publications concerning torsional-lateral coupling in high-performance turbomachinery with gears. Wachel and Szenasi describe in [1] a field problem, where in a geared system unstable lateral vibrations occurred together with torsional oscillations. The authors don't describe the coupling mechanisms, but they point out the importance of gears for the exchange of energy between torsional and lateral vibrations. Similar instability phenomena were observed on several different units. Yamada and Mitsui deal in [2] with a two-stage ship gear supported by oil film bearings. During operation with partial load the pinion runs unstable. A coupled torsional-lateral analysis limited to the gear stage shows that the oil film bearings are the source of instability, but the stability threshold is decisively influenced by the torsional stiffness of the rotor system. Iannuzzelli and Elward point out in [3] that certain measured eigenfrequencies of a compressor train can be verified only by an analytical model considering the torsional-lateral coupling in a gear stage. Simmons and Smalley found by experimental and analytical investigations at a gas turbine/compressor train that torsional modes (or, more exactly, coupled torsional-lateral modes) with a superposed bending component at the gear wheel can be damped significantly by the oil film bearings [4].

In this paper the influence of the torsional-lateral coupling in the gear on the stability behavior of a simple geared system (Fig. 2) is investigated. The coupling effect is analyzed by means of parameter studies and a sensitivity analysis for the uncoupled and the coupled system.

Natural Vibrations of a Geared Rotor System

Mechanical Model. Figure 1 shows a typical turbomachine consisting of two elastic shafts connected by a reduction gear. The rotors are running in oil film bearings. Usually the lateral vibration analysis—including a stability analysis—is carried out for both shafts separately and independently from the torsional rotor dynamics analysis. But in fact torsional and lateral vibrations of both rotors are coupled by the gear. To

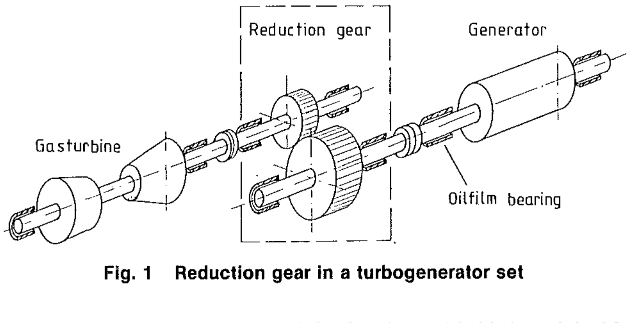

Fig. 1 Reduction gear in a turbogenerator set

Contributed by the International Gas Turbine Institute for publication in the JOURNAL OF ENGINEERING FOR GAS TURBINES AND POWER. Manuscript received by the International Gas Turbine Division September 1987.

study whether this coupling may really be ignored in a stability analysis, we consider in a first step a simpler geared rotor system. Figures 2 and 3 show the model with two elastic shafts connected by a gear. The axes of the shafts are offset by the angle of mesh so that the tooth force acts in the vertical plane on the gear wheels. Both shafts are elastic for torsion and bending. Shaft 1 is running in two identical oil film bearings, which are the only source of instability in the system. The second shaft is supported rigidly. It should be noted that not all the effects of the real machine can be investigated with the simple model. But we will concentrate on the coupling effect in the gear stage and its interaction with the self-excited vibrations of the system.

In a gear a strong torsional-lateral coupling exists naturally due to the mechanism of power transmission. The torsional moment fed into the gear is transmitted by tooth forces. For that reason transverse forces and bending moments result from the torsional moment. Also the torsional and lateral displacements of the gear wheels are coupled kinematically (Fig. 4), provided that both wheels maintain contact during operation. Without the lateral displacement of the gear wheels the kinematic relationship in a gear stage is

$$r_1 q_1 = r_2 q_2 \tag{1}$$

This is the model that is commonly used in rotor dynamics analysis. If we allow lateral movement of the gear wheels the geometric equation

$$r_1 q_1 + q_3 = r_2 q_2 + q_4 \tag{2}$$

implies a coupling of the torsional and lateral degrees of freedom.

From the theoretical considerations it is known that for small vibrations of the journal bearings around a static equilibrium position, a linear force motion relationship for the oil film holds true (Fig. 5):

$$\begin{bmatrix} \Delta f_1 \\ \Delta f_2 \end{bmatrix} = - \begin{bmatrix} c_{11} & c_{12} \\ c_{21} & c_{22} \end{bmatrix} \cdot \begin{bmatrix} \dot{q}_1 \\ \dot{q}_2 \end{bmatrix} - \begin{bmatrix} k_{11} & k_{12} \\ k_{21} & k_{22} \end{bmatrix} \cdot \begin{bmatrix} q_1 \\ q_2 \end{bmatrix} \tag{3}$$

where k_{ik} = stiffness coefficients of the bearings; c_{ik} = damping coefficients of the bearings.

The stiffness and damping coefficients depend on the rotational speed and the static load on the bearing. The resulting static equilibrium position of the shaft in the journal bearing is characterized by the dimensionless Sommerfeld number. In addition the bearing coefficients depend on the load direction, which must be taken into consideration for geared rotors, where the gear transmission forces often make up an appreciable part of the bearing load. Available data for these coefficients assume a specific load direction (gravity load direction), but in a geared rotor system the load direction may be different because it is governed by the gear mesh forces. Hence, if the bearing geometry is such that the coefficients are sensitive to load direction, they must be calculated from the lubrication equation or by using an approximate formula [5, 6]. As the coefficients normally are obtained in a bearing coordinate system that does not coincide with the chosen system for the geared rotor system, a transformation must be performed. Besides anisotropy, the stiffness cross-coupling terms are unequal in general. This asymmetry is the reason for self-excited vibrations of the shaft.

For the statically indeterminate supported shaft in journal bearings the calculation of the static load in the bearings leads to a nonlinear problem, which has to be solved numerically. The reason is the nonlinear force-motion relationship in the journals. In our study the static bearing loads due to the transmitted power and rotor weight are estimated with the rigidly supported shaft system.

An energy flow diagram demonstrates how self-excited bending vibrations in a geared system may exchange energy with torsional oscillations by means of the gear mechanism (Fig. 6). The main energy flows from the motor to the generator to transmit the required power for the unit. Due to shear forces in the oil film of the journal bearing, energy branches off from the main flow to the bearing, where it dissipates due to the oil film friction or excites bending vibrations of the shaft and the gear. Because torsional and bending displacements are coupled in the gear stage, torsional oscillations of the geared rotor train are also excited. It is clear from this consideration that the stability behavior is affected by this energy exchange between the torsional and the lateral system.

Equations of Motion. To obtain the equations of motion for the simple shaft system (Fig. 2) with N degrees of freedom,

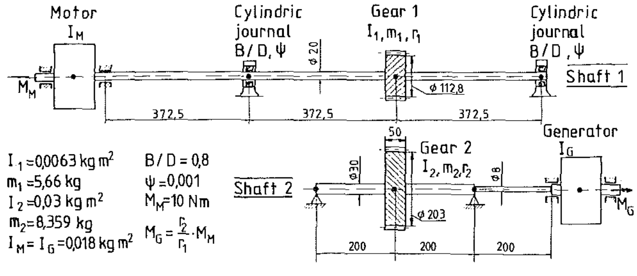

Fig. 3 Data for the geared rotor system

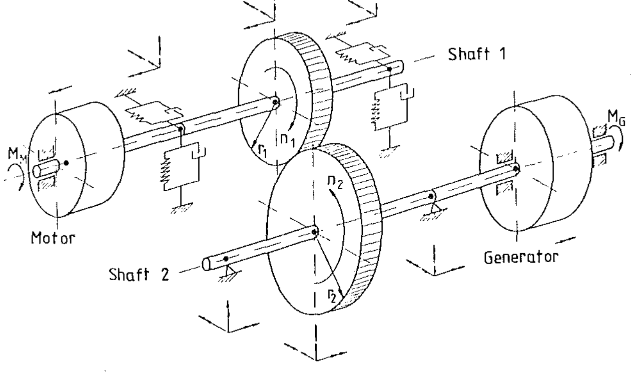

Fig. 2 Model of a geared rotor system

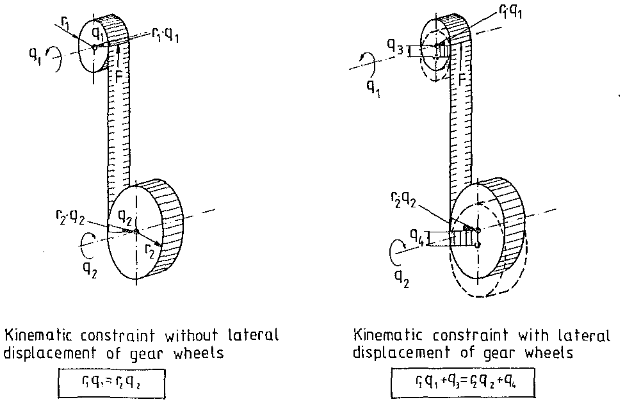

Fig. 4 Kinematic constraints in a gear stage

we apply the principle of virtual work. Using static deflection functions for the approximation of the displacements, we can discretisize the model with continuous mass and stiffness distribution into disk, beam, and bearing elements connected at their nodes. The resulting energy equation expresses that the sum of the virtual work done by the inertia, damping, stiffness, and external forces is equal to zero.

$$\delta\mathbf{q}^T\{\mathbf{M}\ddot{\mathbf{q}}+\mathbf{D}\dot{\mathbf{q}}+\mathbf{K}\mathbf{q}-\mathbf{f}(t)\}=0 \tag{4}$$

Here $\mathbf{M}(N\times N)$ = mass matrix; $\mathbf{D}(N\times N)$ = damping matrix; $\mathbf{K}(N\times N)$ = stiffness matrix; $\mathbf{q}(N\times 1)$ = vector of displacement; $\mathbf{f}(N\times 1)$ = vector of external forces. To connect both shafts we introduce the kinematic relationship of equation (1) for the uncoupled and equation (2) for the torsional-lateral coupled system by the matrix equation

$$\mathbf{q}=\mathbf{T}\cdot\tilde{\mathbf{q}} \tag{5}$$

with

$$\mathbf{q}=\left[\begin{array}{c}\cdot\\ \cdot\\ q_1\\ q_2\\ q_3\\ q_4\\ \cdot\\ \cdot\end{array}\right]\begin{array}{l}1\\ \cdot\\ \cdot\\ \cdot\\ \cdot\\ \cdot\\ \cdot\\ N\end{array}\quad\text{and}\quad\tilde{\mathbf{q}}=\left[\begin{array}{c}\cdot\\ \cdot\\ q_1\\ q_3\\ q_4\\ \cdot\\ \cdot\\ \cdot\end{array}\right]\begin{array}{l}1\\ \cdot\\ \cdot\\ \cdot\\ \cdot\\ \cdot\\ \cdot\\ \tilde{N}\end{array}$$

$$\begin{array}{cc}
 & \begin{array}{ccc} & q_1 & \end{array}\\
\mathbf{T}= & \left|\begin{array}{cc|c}\mathbf{E} & \vdots & \mathbf{0}\\ & & \\ \cdots\cdots & \dfrac{r_1}{r_2} & \cdots\\ & & \\ \mathbf{0} & & \mathbf{E}\end{array}\right|\begin{array}{l}1\\ \cdot\\ q_2\\ \cdot\\ N\end{array}\\
 & 1\cdots\cdots\cdots\cdots\tilde{N}
\end{array}$$

Torsion Bending uncoupled

$$\begin{array}{cc}
 & \begin{array}{ccccc} & q_1 & q_3 & q_4 & \end{array}\\
\mathbf{T}= & \left|\begin{array}{cc|cccc}\mathbf{E} & \vdots & \vdots & \mathbf{0} & \vdots & \\ \cdots & \dfrac{r_1}{r_2} & \dfrac{1}{r_2} & & -\dfrac{1}{r_2} & \cdots\\ \mathbf{0} & & & & & \mathbf{E}\end{array}\right|\begin{array}{l}1\\ \cdot\\ \cdot\\ q_2\\ \cdot\\ \cdot\\ N\end{array}\\
 & 1\cdots\cdots\cdots\cdots\cdots\cdots\tilde{N}
\end{array}$$

Torsion Bending coupled

$\tilde{N}=N-1$ = reduced number of degrees of freedom; $\tilde{\mathbf{q}}(\tilde{N}\times 1)$ = reduced vector of displacements; $\mathbf{T}(N\times\tilde{N})$ = coupling matrix; $\mathbf{E}$ = matrix of unity. The application of the constraint equation (5) to equation (4) eliminates the torsional degree of freedom at one gear wheel (Fig. 4) and yields the equation of motion for the coupled system

$$\mathbf{T}^T\mathbf{M}\mathbf{T}\ddot{\tilde{\mathbf{q}}}+\mathbf{T}^T\mathbf{D}\mathbf{T}\dot{\tilde{\mathbf{q}}}+\mathbf{T}^T\mathbf{K}\mathbf{T}\tilde{\mathbf{q}}=\mathbf{T}^T\mathbf{f}(t)$$

$$\tilde{\mathbf{M}}\ddot{\tilde{\mathbf{q}}}+\tilde{\mathbf{D}}\dot{\tilde{\mathbf{q}}}+\tilde{\mathbf{K}}\tilde{\mathbf{q}}=\tilde{\mathbf{f}}(t) \tag{6}$$

The matrices $\tilde{\mathbf{K}}$ and $\tilde{\mathbf{D}}$ contain stiffness and damping terms from the bearings. They are asymmetric and depend on the running speed of the rotor and the transmitted load. The external load may be caused by imbalance, or gear mesh errors. Because we will restrict our study to a stability analysis we look only on the homogeneous equations of motion ($\tilde{\mathbf{f}}=0$).

Lund introduced in [7] a similar modeling for a geared train of rotors and mentioned the influence torsional-lateral coupling may have on the critical speeds, stability, and imbalance response of the system. But in his paper he focused more on the solution algorithm, which is a modified transfer matrix method, than on the discussion of the stability behavior.

Natural Vibrations: Eigenvalues and Natural Modes. From the homogeneous equations of motion ($\tilde{\mathbf{f}}=0$) the natural vibrations can be calculated. Assuming a solution of the form

$$\tilde{\mathbf{q}}(t)=\mathbf{r}\cdot e^{\lambda t}$$

we obtain the quadratic eigenvalue problem

$$(\lambda^2\tilde{\mathbf{M}}+\lambda\tilde{\mathbf{D}}+\tilde{\mathbf{K}})\mathbf{r}=\mathbf{0} \tag{7}$$

with 2 $\tilde{N}$ eigenvalues λ_j and corresponding eigenvectors $\mathbf{r}_j$. Eigenvalues as well as eigenvectors in most cases occur in conjugate complex pairs.

$$\begin{array}{ll}\textit{Eigenvalues: } \lambda_j=\alpha_j+i\omega_j; & \bar{\lambda}_j=\alpha_j-i\omega_j\\ \textit{Eigenvectors: } \mathbf{r}_j=\mathbf{s}_j+i\mathbf{t}_j; & \bar{\mathbf{r}}_j=\mathbf{s}_j-i\mathbf{t}_j\end{array} \tag{8}$$

We consider only the part of the solution that belongs to a conjugate complex pair

$$\tilde{\mathbf{q}}_j(t)=B_je^{\alpha_jt}\{\mathbf{s}_j\sin(\omega_jt+\gamma_j)+\mathbf{t}_j\cos(\omega_jt+\gamma_j)\} \tag{9}$$

ω_j is the circular natural frequency of this part and α_j the damping constant. If the damping constant $\alpha_j>0$ the natural vibrations increase and make the system unstable; for $\alpha_j<0$ the natural vibrations decrease and the system runs stable.

For the torsional-lateral coupled system the eigenvalues are composed of torsional-lateral coupled damping constants and eigenfrequencies. The corresponding modes are set up by torsional and lateral components. We define the expression in parentheses { } of equation (9) as natural mode. As contrasted with conservative systems there is no constant modal shape; proportions and relative phasing in general vary from point to point at the shaft. The lateral components of one natural mode represent a time-dependent curve in space. The plane of motion of one point of the shaft is an elliptical orbit. The torsional components of one natural mode additionally twist the shaft along its axis.

The example indicated in Figs. 2 and 3 has eight nodes with a total of 8 torsional and 22 lateral degrees of freedom q_i. The eigenvalue problem is solved for this 30 DOF model.

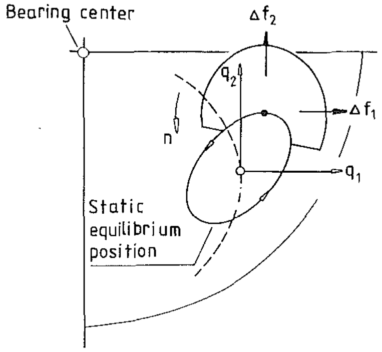

Fig. 5 Journal vibrations

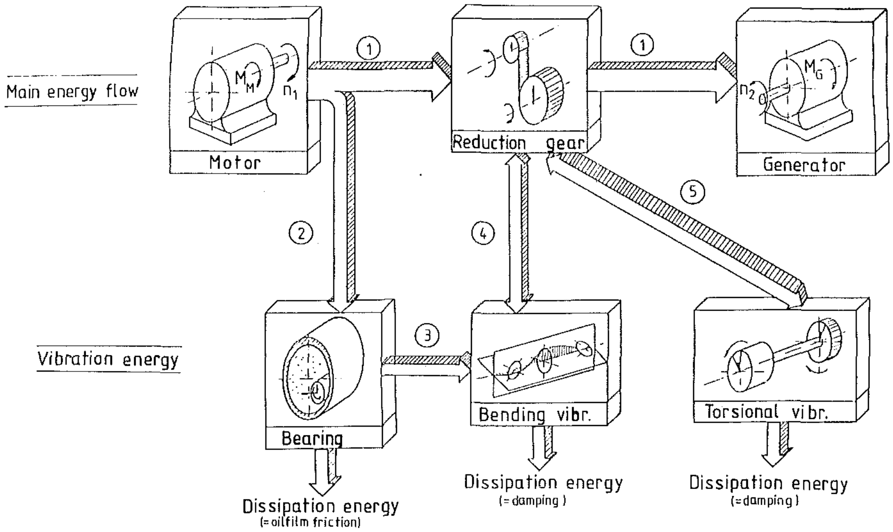

① Main energy flow from motor to generator.
② Energy flow branching off the main flow due to shear forces in the oilfilm.
③ Energy flowing from the oilfilm to the shaft bending vibrations.
④ Energy flowing from bending vibrations in the gear mechanism and back.
⑤ Energy flowing from the lateral excited gear wheels to the torsional motion and back, due to torsional-lateral coupling.

Fig. 6 Energy flow in a geared system with oil film excited torsional-lateral vibrations (schematic)

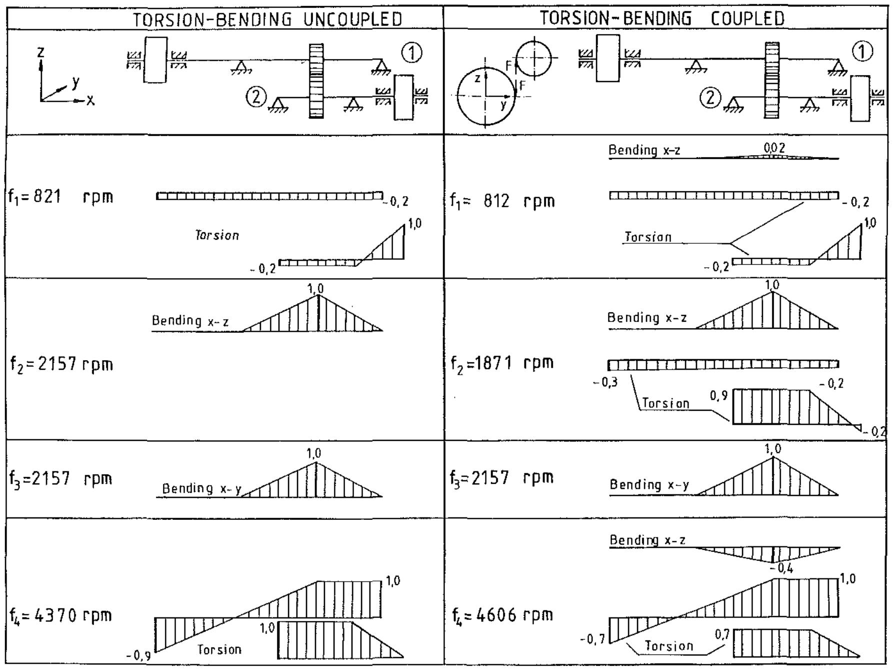

Fig. 7 Eigenfrequencies and eigenvectors of the rigidly supported gear system [8]

If we transpose the matrices $\tilde{\mathbf{M}}$, $\tilde{\mathbf{D}}$, and $\tilde{\mathbf{K}}$, we obtain the so-called left-hand eigenvalue problem

$$\{\lambda^2\tilde{\mathbf{M}}^T+\lambda\tilde{\mathbf{D}}^T+\tilde{\mathbf{K}}^T\}\mathbf{l}=\mathbf{0} \qquad (10)$$

which has the same eigenvalues λ but different eigenvectors $\mathbf{l}$. Both eigenvector sets are needed to decouple the system matrices for the sensitivity analysis of the eigenvalues.

First the eigenfrequencies and modes for the rigidly supported system are calculated in the abovedescribed manner. A similar system was studied from IIDA in [8]. Because of its geometry (Fig. 3), shaft 2 is very stiff for bending compared to shaft 1. Figure 7 shows the natural modes of vibration where the torsional displacement of shaft 1 is multiplied by the radius of gear wheel 1 and the twisting of shaft 2 by the radius of gear wheel 2 to match the dimension with the bending. With *this normalization the kinematic constraint equation (1) with* respect to equation (2) can be verified at once from the plot of the eigenvectors, because the sum of torsional and lateral displacement at shaft 1 and shaft 2 must be equal at the gear mesh.

In the first mode the torsional displacement is rather predominant, while it is comparable to the flexural one in the second and fourth modes. In these two modes the eigenfrequencies of the torsional-lateral coupled system differ by

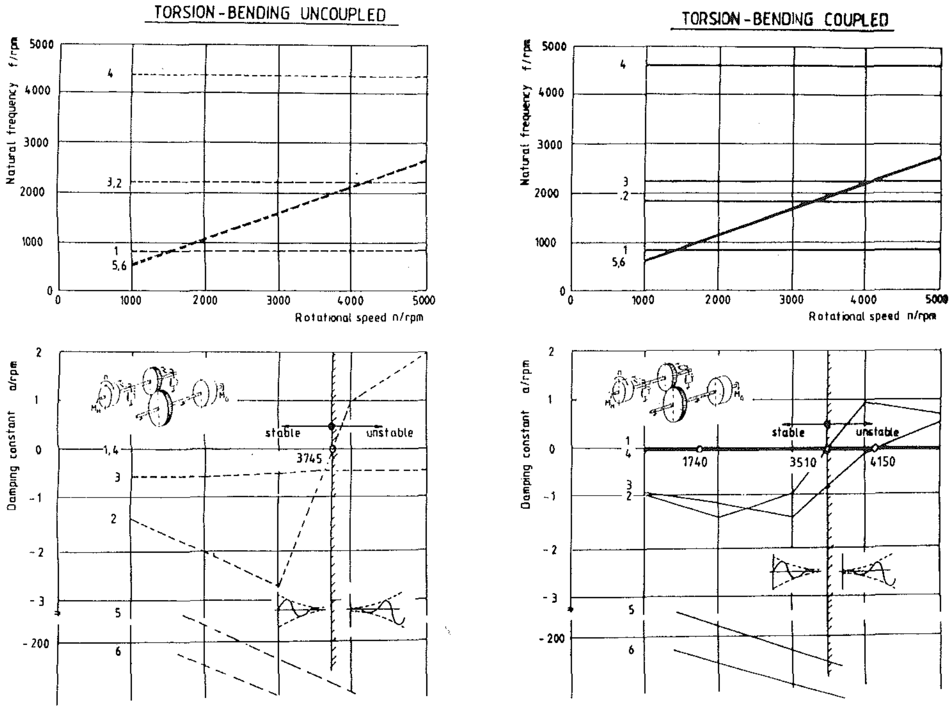

Fig. 8 Eigenfrequencies and damping for the uncoupled and torsional-lateral coupled systems

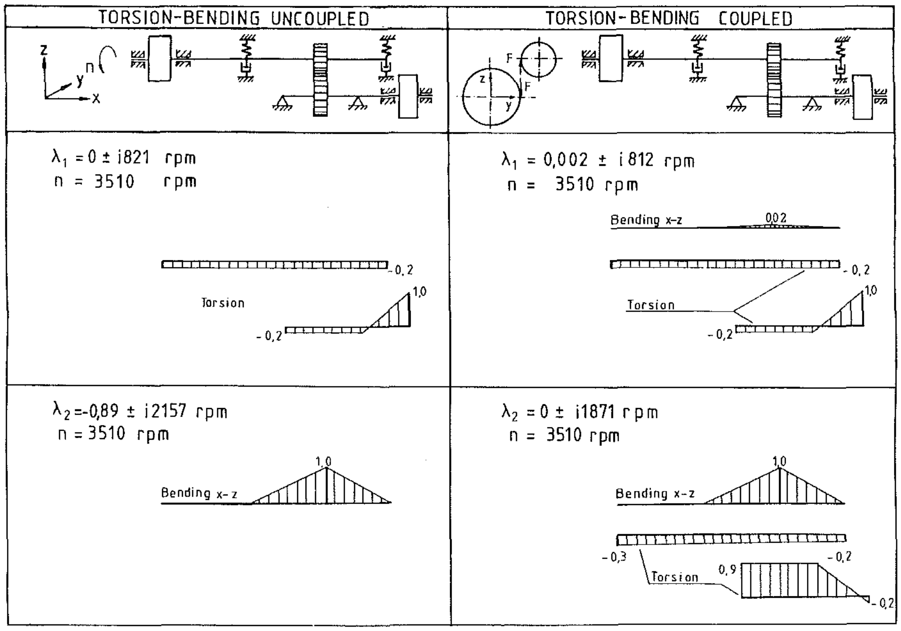

Fig. 9 First and second eigenvectors of the uncoupled and torsional-lateral coupled systems at the stability threshold (in the moment of maximum lateral displacement)

about 15 percent and 5 percent, respectively, from the solutions of the uncoupled system. The third eigenvector lies in the x-y plane, which is perpendicular to the direction of the tooth force. For that reason it is for the rigidly supported system a completely decoupled bending mode.

When the coupling effect has such a strong influence on the eigenfrequencies, how does it affect the damping constants of the eigenvalues for the oil film supported system in Fig. 2? To answer this question we calculate the eigenvalues for the uncoupled and the coupled system. Because the bearing coefficients depend on the rotational speed and the static load on the journal, the eigenvalues change with the running speed and the transmitted load.

In Fig. 8 for the six lowest eigenvalues, the eigenfrequencies ($f = 60\omega/2\pi$ rpm) and damping coefficients ($a = 60\alpha/2\pi$ rpm) are plotted as a function of the rotational speed of shaft 1 for the uncoupled (-----) and the torsional-lateral coupled (———) system. The static load on the bearings remains constant in this diagram during the alteration of shaft speed and it is determined by the weight of the shaft M_M and the transmitted moment M_G (Fig. 3).

It is obvious that most of the eigenfrequencies change only a little and that they almost coincide with the solutions for the rididly supported system. The reason is that the oil film bearings in the investigated speed range are relatively stiff compared to the elasticity of the shaft. An exception are the two whirling frequencies, which grow linear with the rotor speed. Their frequency is about half the speed of shaft 1. They belong to highly damped modes where the movement of the oil film supported shaft represents a conical whirl in one of the two bearings.

In some modes the frequencies for the uncoupled and torsional-lateral coupled systems differ essentially, e.g., the second frequency of the coupled system is about 15 percent lower than for the uncoupled one. Figure 9 shows the strong torsional-lateral coupling in the corresponding eigenmode in contrast to the first eigenvector, which remains an almost pure torsional mode even in the coupled model.

The coupling affects not only the eigenfrequencies and modes but also the damping constants (Fig. 8). The zero passage of one damping coefficient indicates the stability threshold of the system.

In the uncoupled system all the damping constants for the bending modes are negative up to a threshold speed of 3745 rpm, where the first bending mode ($f_2 = 2157$ rpm) becomes unstable. It proves true that the dangerous positive damping constants occur at the lower bending eigenvalues. Because we have not introduced additional torsional damping, the damping constants for the torsional modes ($f_1 = 821$ rpm, $f_4 = 4370$ rpm) are equal to zero.

In the torsional-lateral coupled system the lateral motion of the shaft in the journals may contribute additional damping to the torsional modes (Fig. 6). An additional negative damping is in general desirable, but a positive damping is also possible, which may destabilize the torsional modes. Figure 8 indeed shows that the first weakly coupled torsional eigenvalue ($f_1 = 812$ rpm) becomes slightly unstable at 1740 rpm. Obviously the instability whirl tends to lock in at the lowest system frequency, which in the coupled case may be a bending or a torsional mode. Because of the negative torsional damping, which is always present in real machines (material damping, damping of the surrounding media) the slight torsional instability of our coupled model wouldn't occur in practice. The next eigenvalue, which becomes clearly unstable at 3510 rpm, belongs to the second strongly torsional-lateral coupled mode ($f_2 = 1871$ rpm). Its threshold speed is 7 percent lower than in the uncoupled case. In addition the third eigenvalue, which remains stable in the uncoupled case, becomes unstable at a rotational speed of 4150 rpm in the torsional-lateral coupled model. The corresponding eigenfrequency and eigenvector (an almost pure bending mode lying in the x-y plane, which is perpendicular to the plane of tooth force action) nearly coincide with the solutions of the uncoupled system (Fig. 7). Therefore we conclude that although we can't recognize a strong torsional-lateral coupling in the frequencies and modes, the coupling may still affect the stability behavior. This is due to the energy exchange between the torsional and the bending vibrations at the gear mesh (Fig. 6).

It is important to note that the instability onset speed of the uncoupled and the torsional-lateral coupled system are not equal. The coupling mechanism in gears may essentially lower the threshold speed. The classical uncoupled stability analysis shows that the system becomes unstable at the lowest lateral threshold speed of the individual rotors. In a coupled analysis the acutal stability threshold may occur in a torsional or a strongly torsional-lateral coupled mode of the complete system.

Discussion of Stability Behavior

In a classical vibration analysis, which ignores the coupling between torsional and lateral vibrations in gears, the torsional critical speeds are only sensitive to "torsional system parameters," while the lateral eigenvalues of an individual rotor depend only on its "bending parameters." We use the expression torsional parameter in this context for, e.g., rotatory inertia or torsional stiffness, and bending parameters for quantities like mass or flexural stiffness. If we consider torsional and bending vibrations as coupled in the gear, an eigenvalue is generally sensitive to torsional and bending parameters of all shafts. The effect of the coupling on the stability behavior of the complete rotor system can therefore be studied by answering the questions:

- How do modifications of torsional and bending system parameters change the stability threshold? (Parameter study)
- How do changes of torsional and bending system parameters affect the damping constant of the eigenvalues? (Sensitivity analysis)

Parameter Studies. For the parameter study two torsional parameters and two bending parameters of the simple shaft system are selected (Fig. 10). Figures 11 and 12 show how the stability threshold speed due to the zero passage of the second eigenvalue (real part) changes when the chosen system parameters are varied. As a reference model we take the torsional-lateral coupled model with the data of Fig. 3. Its second eigenvalue becomes unstable at a speed of 3510 rpm. The question is now: How do torsional and bending parameters affect this instability onset speed?

Figure 11 shows the influence of the torsional stiffness $\widehat{k_2}$ and rotary inertia I_2 of shaft 2. Of course the torsional parameters do not change the stability threshold in the uncoupled model. In the coupled case the increase in the torsional stiffness $\widehat{k_2}$ stabilizes while a higher rotary inertia I_2 destabilizes the second eigenvalue. In Fig. 11 at first sight it looks like a torsionally stiffer shaft 2 would make the system more stable. But at the same time, when the second eigenvalue becomes more stable, the first eigenvalue is destabilized, and therefore the stability threshold of the coupled system is lowered by an increased torsional stiffness. Similar things hap-

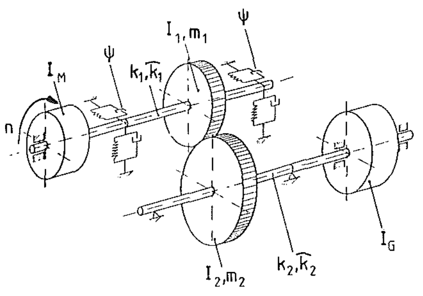

	Bending	Torsion
m_1	●	
m_2	○	
I_M		○
I_1		○
I_2		●
I_G		○
ψ	○	
k_1	●	
k_2	○	
$\bar{k}_1$		○
$\bar{k}_2$		●

●Varied parameters

Fig. 10 Variation of parameters

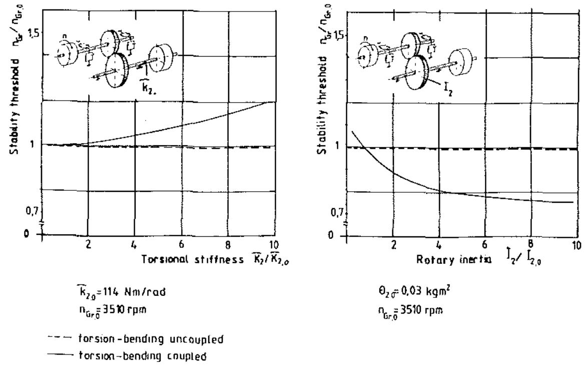

Fig. 11 Influence of torsional parameters on the stability threshold

pen when the rotary inertia I_2 decreases. This effect is ignored in Fig. 11 because only the real part of the second eigenvalue is considered.

Figure 12 discusses the bending parameters. Their influence on the threshold speed for the second eigenvalue is much stronger than the influence of the torsional parameters. It is again interesting to note that the instability onset speed essentially depends on whether an uncoupled or a torsional-lateral coupled model is used. In our case a stiffer shaft 1 (k_1) and a smaller mass m_1 make the system more stable. In both cases the stability threshold for the coupled model is lower than for the uncoupled one.

We conclude from this study that the stability threshold speed is substantially influenced: (1) by the used model: coupled or uncoupled; and (2) in the coupled case by the torsional *and* the bending system parameters. This fact indicates that a strong torsional-lateral coupling affects the stability behavior.

Sensitivity Analysis. As a second tool, besides the parameter study, to investigate the influence of the torsional-lateral coupling, we use a "Sensitivity Analysis" of the eigenvalues. This method yields so-called "Influence Coefficients," which describe the change of an eigenvalue λ_n caused by a small modification of a system parameter p_k. The influence coefficients for the real parts of the eigenvalues express how sensitive the stability of the system is to parameter changes. The stability threshold of an uncoupled model is only affected by the bending parameters of the individual rotors. In comparison to that for the torsional-lateral coupled system an eigenvalue is generally influenced by torsional *and* bending parameters of all shafts. Therefore, with the aid of the sensitivities of the real eigenvalue parts for the uncoupled and the coupled system, the influence of the torsional-lateral coupling on the stability behavior can be discussed.

This sensitivity analysis is based on an expansion of the eigenvalues in terms of the generalized system parameters p_k, where the p_k may be mass, damping, stiffness, or even physical parameters, e.g., bearing clearance [10]

$$\lambda_n = \lambda_{n,0} + \frac{\partial \lambda_n}{\partial p_{1/0}} \cdot \Delta p_1 + \frac{\partial \lambda_n}{\partial p_{2/0}} \cdot \Delta p_2 + \ldots \frac{\partial \lambda_n}{\partial p_{k/0}} \cdot \Delta p_k \tag{11}$$

Truncation of Taylor's expansion after the first derivatives leads to a linear approximate formula. It is shown in [10] that the eigenvalue derivatives can be expressed by the eigenvalues and the left and right-hand eigenvectors of the original system (subscript "0") and by derivatives of the system matrices $\tilde{\mathbf{M}}$, $\tilde{\mathbf{D}}$, and $\tilde{\mathbf{K}}$ to the parameters p_k (subscript "k").

$$\frac{\partial \lambda_n}{\partial p_{k/0}} = -\mathbf{l}_n^T (\lambda_n^2 \cdot \tilde{\mathbf{M}},_k + \lambda_n \tilde{\mathbf{D}},_k + \tilde{\mathbf{K}},_k) \mathbf{r}_{n/0} = g_{n,k} \tag{12}$$

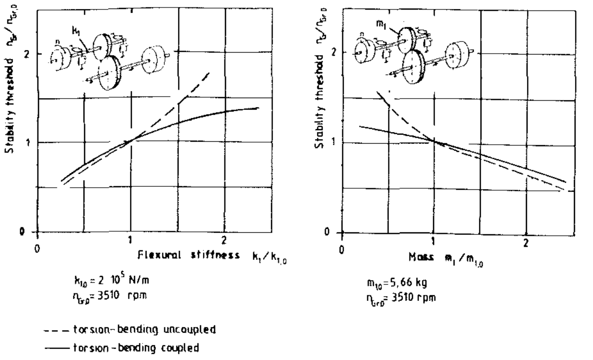

Fig. 12 Influence of bending parameters on the stability threshold

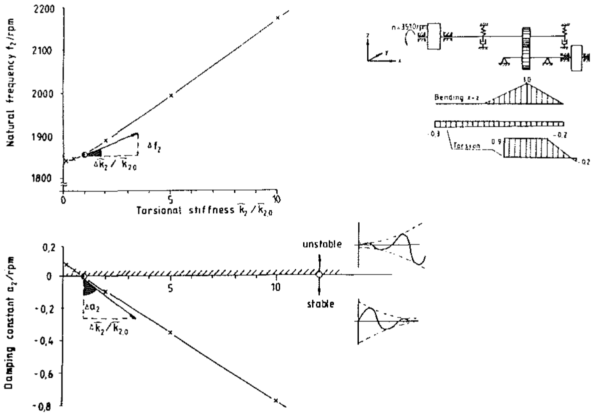

Fig. 13 Effect of change in torsional stiffness $\tilde{k}_2$ on the second eigenvalue for the torsional-lateral coupled system

Element	Force-Motion-Relation	Influence-Coefficient g_{nk}
Disk 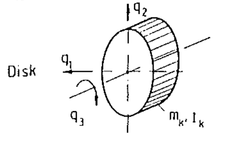	Bending: $\begin{bmatrix} F_1 \\ F_2 \end{bmatrix} = \begin{bmatrix} m_k & 0 \\ 0 & m_k \end{bmatrix} \begin{bmatrix} q_1 \\ q_2 \end{bmatrix}$ Torsion: $F_3 = I_k \ddot{q}_3$	Bending: $g_{n,k} = \frac{\partial \lambda_n}{\partial m_k} = -\lambda_n^2 (l_1 r_1 + l_2 r_2)_n$ Torsion: $g_{nk} = \frac{\partial \lambda_n}{\partial I_k} = -\lambda_n^2 (l_3 r_3)_n$
Journal Bearing 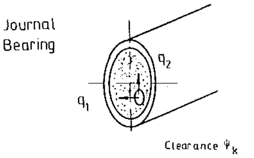	$\begin{bmatrix} F_1 \\ F_2 \end{bmatrix} = \begin{bmatrix} c_{11} & c_{12} \\ c_{21} & c_{22} \end{bmatrix} \begin{bmatrix} q_1 \\ \dot{q}_2 \end{bmatrix} + \begin{bmatrix} k_{11} & k_{12} \\ k_{21} & k_{22} \end{bmatrix} \begin{bmatrix} q_1 \\ q_2 \end{bmatrix}$	Bending: $g_{n\psi} = \frac{\partial \lambda_n}{\partial \psi_k} = \sum_{i=1}^{2} \sum_{j=1}^{2} \frac{\partial \lambda_n}{\partial c_{ij}} \frac{\partial c_{ij}}{\partial \psi_k} + \frac{\partial \lambda_n}{\partial k_{ij}} \frac{\partial k_{ij}}{\partial \psi_k}$ $= \sum_{i=1}^{2} \sum_{j=1}^{2} -\lambda_n (l_i r_j)_n \frac{\partial c_{ij}}{\partial \psi_k} - (l_i r_j)_n \frac{\partial k_{ij}}{\partial \psi_k}$
Beam 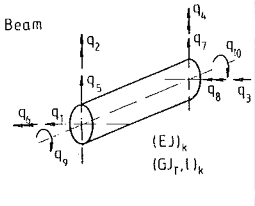	Bending: $\begin{bmatrix} F_1 \\ \vdots \\ F_8 \end{bmatrix} = EJ \begin{bmatrix} K_{11} & \cdots & K_{18} \\ \vdots & \ddots & \vdots \\ K_{81} & \cdots & K_{88} \end{bmatrix}_k \begin{bmatrix} q_1 \\ \vdots \\ q_8 \end{bmatrix}$ Torsion: $\begin{bmatrix} F_9 \\ F_{10} \end{bmatrix} = \frac{GJ_T}{l} \begin{bmatrix} 1 & -1 \\ -1 & 1 \end{bmatrix}_k \begin{bmatrix} q_9 \\ q_{10} \end{bmatrix}$	Bending: $g_{n,k} = \frac{\partial \lambda_n}{\partial (EJ)_k} = -[l_1 \cdots l_8]_n \begin{bmatrix} K_{11} & \cdots & K_{18} \\ \vdots & \ddots & \vdots \\ K_{81} & \cdots & K_{88} \end{bmatrix}_k \begin{bmatrix} r_1 \\ \vdots \\ r_8 \end{bmatrix}_n$ Torsion: $g_{n,k} = \frac{\partial \lambda_n}{\partial \left(\frac{GJ_T}{l}\right)_k} = -[l_9, l_{10}]_n \begin{bmatrix} 1 & -1 \\ -1 & 1 \end{bmatrix}_k \begin{bmatrix} r_9 \\ r_{10} \end{bmatrix}_n$

Fig. 14 Influence coefficients for the disk, journal bearing, and beam elements

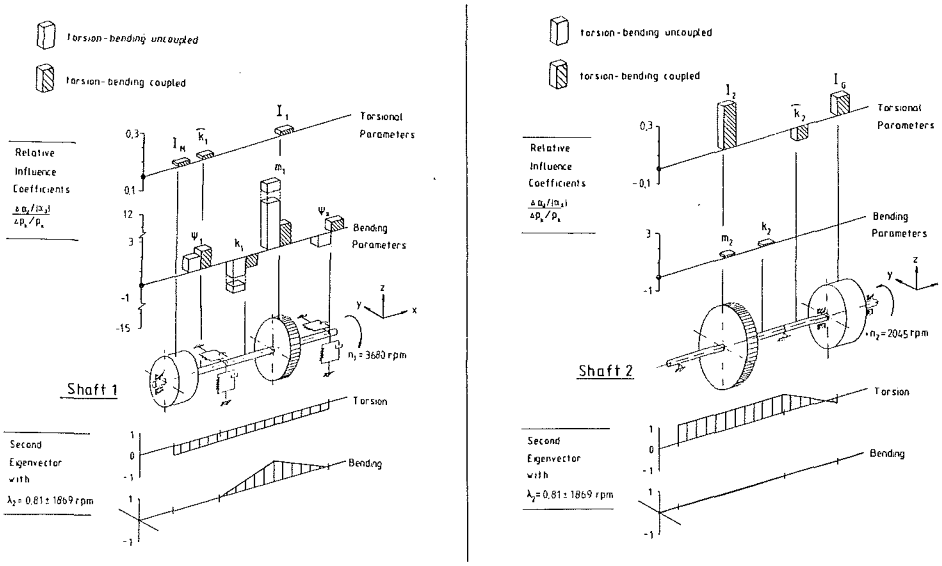

Fig. 15 Sensitivities of the second eigenvalue

The eigenvectors must be normalized in a special way [10]. The derivates are also called "influence coefficients."

For the simple gear model we start from a point near the stability threshold speed and investigate how particular parameters affect the stability behavior. Figure 13 shows the influence of the torsional stiffness $\widetilde{k_2}$ on the real and imaginary parts of the second eigenvalue. It can be seen that an increase of the torsional stiffness has a stabilizing effect on the second eigenvalue. The corresponding influence coefficient calculated with the given linear formula is indicated by the tangent at the graph.

Figure 14 contains influence coefficients for the elements used in our gear model like disks, journal bearings, and beams. The given influence coefficients in equation (12) represent an absolute measure for the changes of the complex eigenvalues $\lambda_n = \alpha_n + i\omega_n$ caused by parameter modifications. By means of these coefficients a relative measure, the nondimensional sensitivity, can be defined

$$\frac{\Delta\alpha_n/|\alpha_n|}{\Delta p_k/p_k} = S^{\alpha}_{n,k} = \mathrm{Re}(g_{n,k}) \cdot \frac{p_k}{\alpha_n}$$
$$\frac{\Delta\omega_n/\omega_n}{\Delta p_k/p_k} = S^{\omega}_{n,k} = \mathrm{Im}(g_{n,k})\ \frac{p_k}{\omega_n} \tag{13}$$

$S^{\alpha}_{n,k}$ is the nondimensional sensitivity of the damping coefficient $S^{\omega}_{n,k}$ of the natural frequency. This presentation has the great advantage that the influence of several parameters on different modes can be compared immediately.

To show the influence of torsional and bending system parameters to the stability behavior of our rotor system, relative sensitivities for the real part of the second eigenvalue are calculated near the threshold speed of the uncoupled and the coupled model ($n_1 = 3680$ rpm) and plotted in Fig. 15.

It is important to note that the values of the relative sensitivities for the uncoupled and the coupled model are different.

Of course in the *uncoupled model* the torsional parameters do not affect the real part of the second eigenvalue, which belongs to a pure bending mode. The corresponding sensitivities are therefore equal to zero.

Nevertheless in the uncoupled model changes of the bending parameters of shaft 1 have a strong influence to the real part of the second eigenvalue. Because the oil film bearings are relatively stiff compared with the bending stiffness of shaft 1 the changes of the shaft parameters (e.g., bending stiffness, mass of the pinion) have a much stronger effect on the damping constant than the bearing parameters (e.g., clearance ψ). The bending of the rigidly supported shaft 2 is in the uncoupled case not connected to the oil film supported shaft 1, which becomes unstable. Therefore the bending parameters of shaft 2 have no influence on the stability behavior.

In the *coupled model* it is obvious that changes of the torsional parameters can have a strong influence on the real part of the second eigenvalue. A comparison of the different torsional parameters points out that the main influence is coming from the torsional parameters of shaft 2. Their relative sensitivities are much greater than those of the torsional parameters of shaft 1. A look on the torsional components of the corresponding second mode makes the reasons clear: Shaft 2 shows a maximum displacement due to torsion at the gear wheel and is much more twisted than shaft 1.

The sensitivity of the torsional stiffness has a negative sign. An increasing stiffness stabilizes the rotor system as we have already seen in the parameter study (Figs. 11 and 13). The rotatory inertia of the second gear wheel and the generator have a positive sensitivity. Increasing the values of this parameter has a destabilizing effect (Fig. 11).

Changes of the bending parameters have a stronger effect on the real part of the second eigenvalue than the torsional parameters. Because the bending of shaft 2 is in the coupled model connected to the oil film supported shaft 1 by the coupling equation (2), its parameters also influence the stability behavior of our model. But as shaft 2 is almost rigid for bending in the second mode, the influence coefficients of its parameters (e.g., mass of the wheel, lateral stiffness) are relatively small.

Obviously the dimensionless sensitivities of the bending parameters of shaft 1 differ essentially from the values of the uncoupled model. For example the influence coefficient of the clearance for the right bearing is of about the same magnitude as in the uncoupled case but has the opposite sign. The sensitivities of the bending stiffness and the mass of the pinion are essentially smaller than in the uncoupled model.

The results show that the stability behavior of our model is particularly influenced by the bending parameters of shaft 1 *and* the torsional parameters of shaft 2. The differences in the solutions for the sensitivities in the uncoupled and the coupled model indicate that the torsional-lateral coupling must not be neglected in discussing the stability behavior of geared rotors.

Conclusions

In this paper a study of the stability behavior is given for a simple geared shaft system. It is shown that the classical eigenvalue analysis, which ignores the coupling of torsional and lateral vibrations in gears, may lead to serious errors in the prediction of the stability onset speed, the critical speeds and the natural modes. Also it does not account for the damping of the torsional modes, which is contributed from the lateral motion in the journals.

The strong torsional-lateral coupling in connection with the stability behavior is proven by parameter studies and a sensitivity analysis, which show the influence of torsional *and* bending system parameters on the stability threshold and the damping constants.

Next the analytical results for the simple geared model should be verified by experimental investigations and extended to more complex rotor systems.

Acknowledgments

This research was supported by Deutsche Forschungsgemeinschaft, Federal Republic of Germany.

References

1 Wachel, J. C., and Szenasi, F. R., "Field Verification of Lateral-Torsional Coupling Effects on Rotor Instabilities in Centrifugal Compressors," NASA Conference Publication No. 2147, 1980.

2 Yamada, T., and Mitsui, J., "A Study on the Unstable Vibration Phenomena of a Reduction Gear System, Including the Lightly Loaded Journal Bearings for a Marine Steam Turbine," *Bull. JSME*, Vol. 22, No. 163, 1979.

3 Iannuzzelli, R. J., and Elward, R. M., "Torsional-Lateral Coupling in Geared Rotors," ASME Paper No. 84-GT-71, 1984.

4 Simmons, H. R., and Smalley, A. J., "Lateral Gear Shaft Dynamics Control Torsional Stresses in Turbine-Driven Compressor Train," ASME JOURNAL OF ENGINEERING FOR GAS TURBINES AND POWER, Vol. 106, 1984, pp. 946-951.

5 Dubois, G. B., and Ocvirk, F. W., "Analytical Derivation and Experimental Evaluation of Short-Bearing Approximation for Full Journal Bearings," NACA Report 1157, 1953.

6 Ott, H. H., "Zylindrisches Gleitlager bei instationärer Belastung," Dissertation ETH Zürich, 1948.

7 Lund, J. W., "Critical Speeds, Stability and Response of a Geared Train of Rotors," ASME Paper No. 77-DET-30, 1977.

8 Iida, H., Tamura, A., Kikuch, K., and Agata, H., "Coupled Torsional-Flexural Vibration of a Shaft in a Geared System of Rotors," *Bull. JSME*, Vol. 23, No. 1986, Dec. 1980.

9 Glienicke, J., "Feder- und Dampfungskonstanten von Gleitlagern und deren Einfluβ auf das Schwingungsverhalten eines einfachen Rotors," Thesis TH Karlsruhe, 1966.

10 Fritzen, C. P., and Nordmann, R., "Influence of Parameter Changes to the Stability Behavior of Rotors," NASA Conference Publication No. 2250, 1982.

A New Concept of High-Performance Marine Reversing Reduction Gears

D. J. Folenta
President,
Transmission Technology Co., Inc.,
Fairfield, NJ 07006

This paper presents a brief description and several illustrations of a new concept of marine reversing gears that utilize high-performance differentially driven epicyclic gear arrangements. This new marine power transmission has the potential to offer high reliability, simplicity, light weight, high mechanical efficiency, compactness, and technological compatibility with aircraft derivative marine gas turbine engines. Further, this new reversing gear minimizes the danger of driving the free turbine in reverse as might be the case with conventional parallel shaft reversing gear arrangements. To illustrate the weight reduction potential, a modern naval ship propulsion system utilizing an aircraft derivative gas turbine engine as the prime mover in conjunction with a conventional parallel shaft reversing gear can be compared to the subject reversing gear differential. A typical 18,642 kW (25,000 hp) marine gas turbine engine might weigh approximately 5000 kg (11,000 lb) and a conventional marine technology parallel shaft reversing gear might weigh on the order of 90,000 to 136,000 kg (200,000 to 300,000 lb). Using gear technology derived from the aircraft industry, a functionally similar differentially driven marine reversing gear might weigh approximately 13,600 kg (30,000 lb).

Introduction

To achieve propeller thrust reversal in a marine propulsion system, the design engineer has several options from which to choose. Some of the more popular arrangements include reversing the direction of rotation of the prime movers, reversing gearboxes, and controllable-reversible pitch propellers. This paper, aside from making some generalized observations about various propeller thrust reversing systems, is limited to the discussion of reversing gears and more specifically to the introduction of a new concept of a marine reversing transmission. A brief description of this new reversing gear, along with a technical discussion and operational characteristics, are also illustrated in this paper.

Traditionally, marine reversing gears employ various arrangements of gears, bearings, shafts, and energy-absorbing clutches and couplings to reverse the direction of rotation of the propeller shaft while the prime mover continues to operate in a unidirectional mode. These reversals, and particularly the crash astern maneuvers, subject the propulsion system to high loads and convert a significant amount of energy into heat. In propulsion arrangements where low-inertia gas turbine engines are coupled to conventional parallel shaft reversing gears having high mass moments of inertia, there is a potential danger that the free turbine might be damaged by being driven backward during the reversing sequence.

The reversing gear concept presented herein utilizes a low-inertia, lightweight, two-stage epicyclic gear module, which in addition to providing the necessary speed reduction and power transmission capability, contains an arrangement of differentially driven reversing gears. In this new arrangement, since the mass inertia of the reduction gear is more in line with the inertia of the engine, the danger of damaging the free turbine during the reversing process is minimized while the gear system allows for quick reversals, is compact and quiet, and has a built-in potential for high reliability.

The subject gear also offers versatility in propulsion system arrangements and can be used with multiple engine inputs, can be driven in either the CW or CCW direction, can have contrarotating concentric output shafts, and the propeller speed can be modulated from 0 rpm to the rated rpm. The gear elements can transmit full power either in the forward or reverse modes of operation. During prolonged low-speed and low-power operation when the brakes are operating at high slipping speeds, the power transmission is limited only by the capacity and heat dissipation of the brakes.

Technical Discussion

In examining some of the characteristics of the reversing systems that are in service today, it can be noted, for example, that some prime movers can reverse the direction of rotation more readily than others without excessive complication and without loss of performance. To illustrate, steam turbines can achieve output shaft reversal by diverting the steam flow from the forward turbine to the aft turbine. This method of reversing propeller thrust has been found to be viable, not only from

---

Contributed by the International Gas Turbine Institute and presented at the 33rd International Gas Turbine and Aeroengine Congress and Exhibition, Amsterdam, The Netherlands, June 5-9, 1988. Manuscript received by the International Gas Turbine Institute November 30, 1987. Paper No. 88-GT-274.

technical and performance points of view, but also from an economic point of view.

Reversing the direction of rotation of other prime movers, such as diesel engines and gas turbine engines, has been found to be more complicated. In the case of gas turbine engines, the reversing techniques evolved to date appear to be complex and degrade the performance of the propulsion system as noted by Yates (1976). Thus, there is a clear need for a marine propeller thrust reversing device. These reversing systems need to be reliable, efficient, compatible with the overall propulsion system, and cost effective.

A review of the design and operational characteristics of contemporary marine reversing devices shows that the design of reversing gears is a straightforward process. The resultant power transmissions contain various gear, clutch, and coupling arrangements, which when properly actuated facilitate reversing the direction of rotation of the output shaft. To accomplish the reversal, and particularly the crash forward and crash astern maneuvers, the clutches and the couplings within the reversing reduction gear are called upon to convert a significant amount of shaft power into heat. Thus, the design of the energy conversion components must be carefully analyzed and tested to insure adequate capacity and satisfactory performance.

Another variant of a reversing gear employs fluid couplings. However, it was noted by Fortunato and Clements (1979) that the efficiency of operation of this scheme is lower than that normally achieved with friction clutches. In high-power installations, the added heat might further complicate the propulsion system by requiring installation of large heat exchangers into the engine room.

Another option available to the designer to reverse the direction of thrust is to employ a reversible pitch propeller (CRP). Selection of this mode of reversing requires introduction and incorporation of a significant amount of complex mechanisms, high-pressure hydraulics, and intricate propeller structural attachments that are not found in other marine propulsion systems. The increased diameter of the CRP hub decreases propeller efficiency, while the increased propeller weight requires more structure outside of the hull, which in turn could result in higher ship resistance. Further, inspection and maintenance problems are increased when CRPs are used.

Each of the reversing systems identified above has certain characteristics, advantages, and disadvantages. Much has been written and can be found in the literature (see references cited) about this subject and the detailed characteristics of various types of reversing systems. No clear consensus can be gleaned from the literature reviewed as to which system of reversing is "best."

If one could realistically quantify the various technical and performance variables normally associated with engineering tradeoff studies and compare them to the ideal system, the selection of the optimum reversing system would be self-evident. This quantification, however, is difficult and subject to many interpretations, past experiences, imposed limitations, and other constraints not necessarily related to the engineering variables under consideration. Thus, due to these difficulties and due to the subjective nature of this problem, the marine industry is replete with a variety of propulsion reversing systems.

As ship propulsion requirements change in response to a need for higher performance, higher powers, modular form, lighter weight, increased reliability, ease of inspection and maintenance, etc., the design engineer needs to respond with new ideas that will satisfy the system's functional requirements while offering significant improvements over existing systems. The introduction of high-performance aircraft derivative gas turbine engines into marine propulsion systems is an excellent example of change and progress.

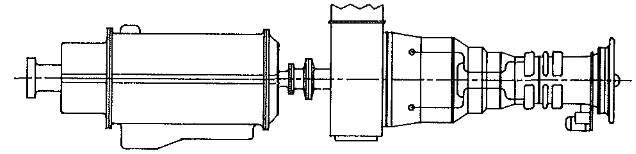

Fig. 1 Propulsion system outline

Many modern Navy ships that are propelled by high-performance gas turbine engines or intermediate speed diesel engines achieve astern propulsion by using controllable-reversible pitch propellers (CRP) or reversing gears. By and large, the design concept used for reversing gears appears to be a modification of traditional parallel shaft marine reduction gears as originally designed and developed for steam turbine propulsion. From a technological point of view, these reversing gears do not appear to be compatible with or complementary to the gas turbine technology. For example, the containership *Admiral Callaghan* has in its propulsion system two LM2500 gas turbine engines that weigh approximately 5000 kg (11,000 lb) per engine while the parallel shaft reversing reduction gears weigh about 136,000 kg (300,000 lb) per gear as noted by Bryant (1985).

What appears to be needed is a reversing system that is compatible with and complementary to the gas turbine engine and that would satisfy the performance requirements without incurring additional complexities, performance degradations, weight penalties, or reliability reductions. Thus, the purpose of this paper is to present a new concept of a marine reversing gear that is compatible with modern gas turbine engines while offering the potential for significant reductions in weight, volume, complexity, and life cycle costs. Further, it offers increased reliability, improved propulsive efficiency, and minimizes the danger of driving the free turbine backward.

System Description. The reversing gear module described in this paper consists of two stages of epicyclic gears, a differential gear drive, and forward and reverse brakes. The first stage, or the high-speed stage, in addition to providing a specific amount of speed reduction, contains an arrangement of gears and brakes, which when actuated in a given mode converts the first-stage planetary gear from a fixed-ratio speed reducer to a differentially driven variable-speed transmission. This variable-speed ratio transmission is capable of reversing the direction of rotation of the output shaft. The second gear stage, or the low-speed planetary, is a conventional fixed-ratio speed reducer and operates as such in all modes of operation.

Figure 1 presents a typical outline of this gear module. Both gear stages, differential drive, thrust bearing, and brakes are contained in a common gear housing. To make the illustration of the physical compatibility of this gear arrangement meaningful, a high-performance marine gas turbine engine rated at 18,624 kW (25,000 hp) and having a free turbine output speed of 3600 rpm was selected. In this figure, the output speed of the reduction gear has been arbitrarily set at 200 rpm; thus, the gear unit in the forward mode of operation operates as a fixed ratio speed reducer with a reduction ratio of 18:1.

Figure 2 presents a schematic arrangement of this reversing gear. As can be noted, there are two stages of epicyclic gears, a forward brake, an astern brake, and a differential gear drive. A conventional thrust bearing can be incorporated to complete the gear module.

Modes of Operation. The gear module as configured here has three fixed modes of operation and two transitional modes. The fixed modes are neutral, forward, and reverse. Transitional operation, during which the brakes are being engaged or disengaged, permits the operator to modulate propeller speed and to set the desired mode of operation. Full engine power can be delivered to the propeller in either the for-

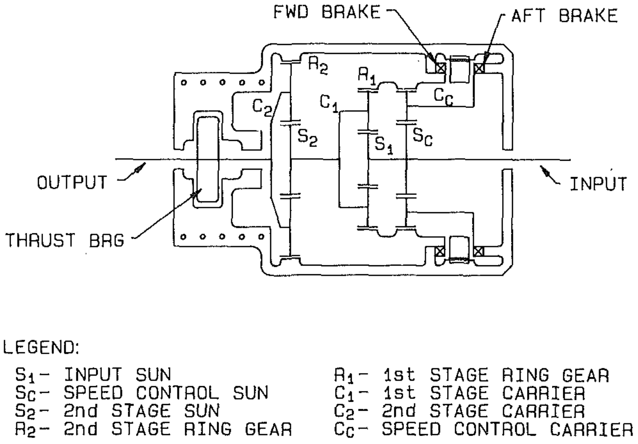

Fig. 2 Gear schematic

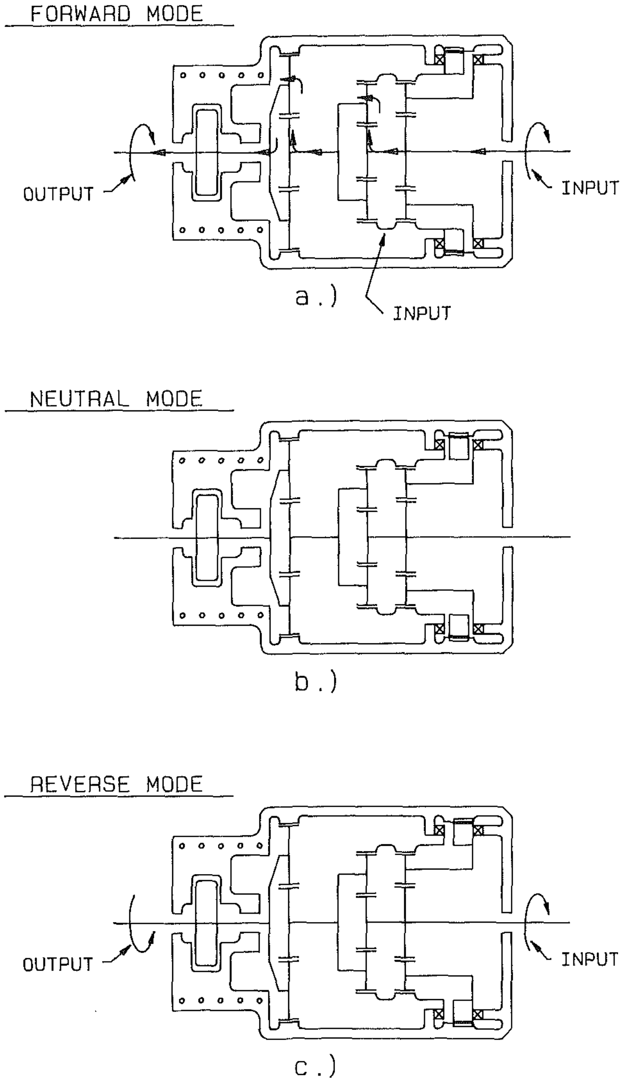

Fig. 3 Modes of operation

ward or the astern mode of operation. In the steady state forward mode, the first-stage ring gear (R_1) is locked to ground, via the forward brake, and the differential drive is free to rotate (windmill); thus, the power flows from the input shaft through the sun gear (S_1) to the carrier (C_1) and into the second-stage sun gear (S_2) and through the second-stage carrier (C_2) into the output shaft.

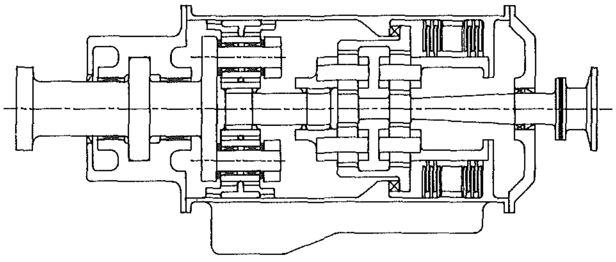

Fig. 4 Transmission cross-sectional view

Figure 3(*a*) is a schematic arrangement that illustrates the gear arrangements during the forward mode of operation.

In the neutral mode, Fig. 3(*b*), both brakes are disengaged. Selection of this mode of operation allows the input shaft to rotate at any desired speed while the output shaft stands still or turns in either the CW or the CCW direction. Since there is no mechanical connection between the input shaft and the output shaft, transmission of power is not possible while the gear is in the neutral mode.

In the reverse mode of operation, the reverse brake is locked to ground and the power flows from the input shaft through the differential to the second-stage carrier (C_2) and into the output shaft; see Fig. 3(*c*).

To proceed from the forward mode of operation to either the neutral or reverse mode, the operator needs only to move the lever to the desired position. The control system automatically energizes the necessary microprocessors to control engine operation and brake actuation. The control and the dynamic response of any given propulsion system are interrelated and interdependent and are functions of many parameters, such as ship size, ship speed, engine power rating, engine response, system inertias, various design rates of change, etc.

Since the primary purpose of this paper is to introduce a new high-performance reversing gear concept, the discussion of ship dynamics will be held to a minimum. In order to facilitate component sizing (gears, brakes, bearings, etc.) and to conduct system comparisons, some assumptions concerning the levels of power transmission and heat generation/dissipation, including the crash forward and crash astern maneuvers, need to be made. Assuming the engine rating of 18,625 kW (25,000 hp), turbine speed of 3600 rpm, and a propeller speed of 200 rpm in the forward mode and 150 rpm in the reverse mode, the corresponding design torques at various points in the transmission can be calculated. For this analysis and component sizing, it was assumed that the maximum overtorque conditions would be two times the normal design torque; thus, all shafts, gears, bearings, etc. were sized to have a 20-year life at the 18,625 kW (25,000 hp) level and a limited life capacity at two times the rated torque level. The factor of two is considered to be a conservative value and includes some margin of safety.

Using the above assumptions and the resultant torque values, the sizes of the respective gear elements and brake diameters were calculated. The results of this sizing effort are illustrated in Figs. 1 and 4. As can be noted, the gear unit is cylindrical in shape, has a diameter of approximately 1.5 m (60 in.) and is about 2.8 m (110 in.) long, excluding the thrust bearing. This module can now be compared to the gas turbine, which has a diameter of approximately 1.5 m (60 in.) and is about 6.6 m (260 in.) long. As a further comparison, the size of this gear module can be compared to the *Callaghan's* reversing gear, which is 4.1 m (162 in.) high, 5.7 m (225 in.) athwartship, and 4.3 m (168 in.) fore and aft as noted by Zeien (1969).

Description of Reversing Differential Gear. The use of differential gears for power transmission, motion control,

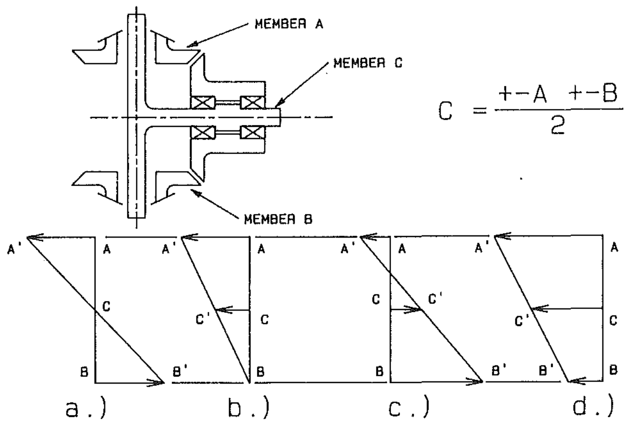

Fig. 5 Bevel differential kinematics

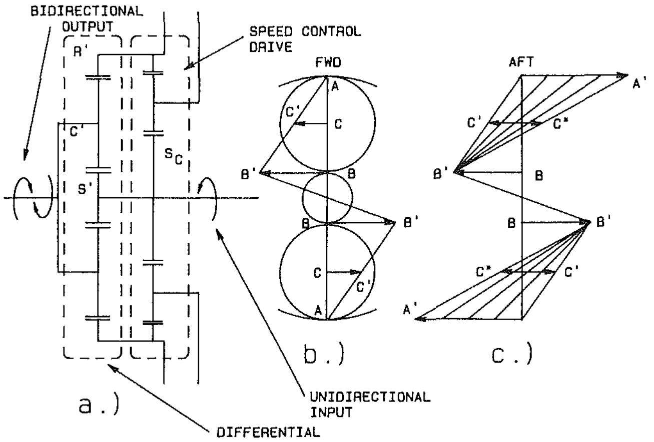

Fig. 6 Epicyclic differential kinematics

power distribution, and various analog speed summation and subtraction devices can be found all around us. An automobile's differential is one example of the wide use of this mechanism. In addition, the computer manufacturing industry, the process industry, and the instrumentation trade are replete with differential gear drives. Power differential devices, for the most part, can be grouped into the epicyclic gear family. They have two degrees of freedom; thus, for one input, two outputs can be obtained or for two inputs, one output can be realized.

In its simplest form, the differential can be thought of as a three-legged motion and power transmitting device whereby a change in speed and power absorption in one leg will produce a predictable change in the other two legs or two different inputs will produce a predictable output. Recognition of this fact permits the designer, for example, to maintain a constant speed on one leg, vary the speed of the second leg, and predict the speed of the third leg. To date, many arrangements of differential drives have been evolved and can be found in service and in the literature. Yates (1976), Dudley (1962), and Baumeister (1967), are but a few authors who present a variety of differential gear arrangements. Some of the most common of these devices are bevel gear differentials, external spur or helical gear differentials, and internal gear differentials.

To illustrate the concept of speed change and gear reversing, a simple bevel differential is presented in Fig. 5.

In examining Fig. 5(*a*) it can be readily noted that if the carrier C is fixed to ground and member A moved to A′ position, member B would move an equal amount to B′ position but in the opposite direction. Figure 5(*b*) illustrates the results if member B were held to ground and member A were rotated to A′; the carrier or member C would move to C′. By inspection, it can be seen that CC′ = 1/2 AA′.

Figure 5(*c*) illustrates a very interesting speed relationship among the three members. Namely, if member B were driven in the opposite direction to member A and at a higher speed than member A, the carrier would turn in the same direction as B and opposite to A.

Figure 5(*d*) illustrates the resultant speed relationship if both members A and B were driven in the same direction.

The above illustrations depict some of the rotational relationships of a bevel gear differential and, for example, show that member A can be driven at some constant speed in the CW direction while the control member B, in this instance, is driven in a CCW direction. By increasing the rate of rotation of the control member B, the speed of member C is changed. At a given speed of A and B, the output member C has zero rotational speed as can be seen by Fig. 5(*a*). By increasing the speed of the control member B further and by maintaining constant speed in member A, the direction of rotation of member C reverses (see Fig. 5*c*). It can be observed from the bevel gear differential illustrated above that the carrier C moves one half the algebraic sum of the other two members.

These illustrations showed and discussed a 1:1 bevel gear differential. The same general rules apply to other types of differential. When spur or helical epicyclic gear differentials are considered, the designer needs to account for the built-in gear ratio, recirculating power, and corresponding torque changes.

Figure 6(*a*) presents a schematic illustration of the reversing, differentially driven epicyclic gear arrangement presented in this paper. The operation of the high-speed first stage (sun gear S_1, carrier C_1, and ring gear R_1) as a differential will now be discussed. Here, the ring gear has been selected as the speed control member and is driven in this illustration by the sun gear S_c. It should be noted that the ring gear can be driven by any power source and that the power required to drive the ring gear can be extracted from any convenient shaft or rotating member.

In the forward mode of operation, the ring gear R_1 is held fixed to ground and the output carrier rotates in the same direction as the input shaft but at a reduced speed (Fig. 6*b*). Here, the speed reduction is a function of the ring gear diameter and the sun gear diameter.

To reverse the direction of rotation of the output shaft, ring gear R_1 is released from the ground connection. This action causes the ring gear to be driven in the opposite direction of rotation to the sun gear. The initial energy required to drive the ring gear is extracted from the energy, which is within the system at that point in time. As the speed of the ring gear increases, the carrier, which is mechanically connected to the output shaft, slows down. To slow the output shaft to 0 speed and to drive it in the opposite direction, additional power must be supplied to the ring gear. This additional power can be conveniently provided by the main engine via an input shaft control drive mechanism.

Figure 6(*b*) illustrates the directional velocity vector relationship of members S' and C' while the gear unit is in the forward mode of operation. Similarly, Fig. 6(*c*) illustrates the directional relationship of the differential while the system is in the transitional mode of operation going from the CW direction of rotation to zero to the CCW direction of rotation.

The power flow during the steady-state forward mode of operation and the astern mode of operation is further illustrated in Fig. 7.

As shown in Fig. 7(*a*), the power flow in this mode of operation is representative of a conventional two-stage planetary gear module. The power flow shown in Fig. 7(*b*) illustrates that in the reverse mode of operation, split torque is feeding the C' carrier. The ratio of this torque split is a function of the gear geometry selected for the differential drive. Care must be exercised during the configuration selection and sizing of these

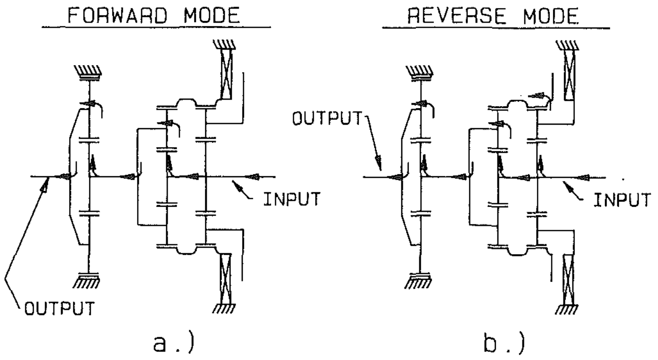

Fig. 7 Power flow schematics

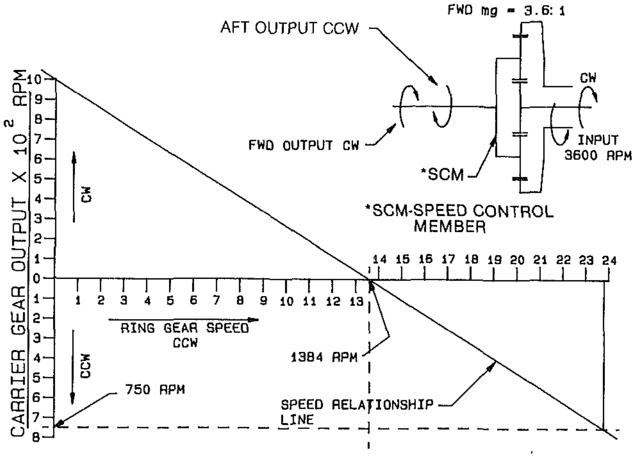

Fig. 8(*a*) Shaft speed relationship

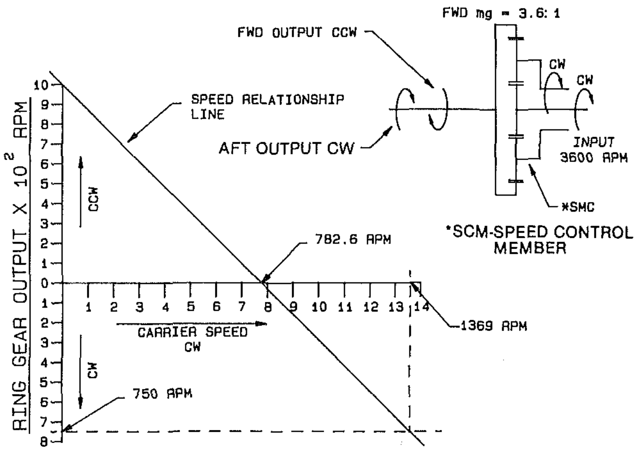

Fig. 8(*b*) Shaft speed relationship

components since a significant amount of recirculating power could be present within a differential.

Figures 8(*a*) and 8(*b*) further illustrate the speed relationship of an epicyclic gear differential. Figure 8(*a*) utilizes the carrier as the output member and the ring gear as the speed control member. Thus, for example, with the sun gear input speed maintained at 3600 rpm CW and the ring gear being driven at 800 rpm CCW, the carrier would turn at 422 rpm CW. If the speed of the ring gear were increased to 2423 rpm CCW, the output carrier would then change the direction of rotation and would turn at 750 rpm CCW. Similarly, Fig. 8(*b*) illustrates a differential where the carrier is the speed control member. Thus, with an input speed of 3600 rpm and driving the carrier CW, the output ring gear would change its speed and direction of rotation from 1000 rpm CCW to 750 rpm CW while the carrier is driven from 0 to 1369 rpm CW.

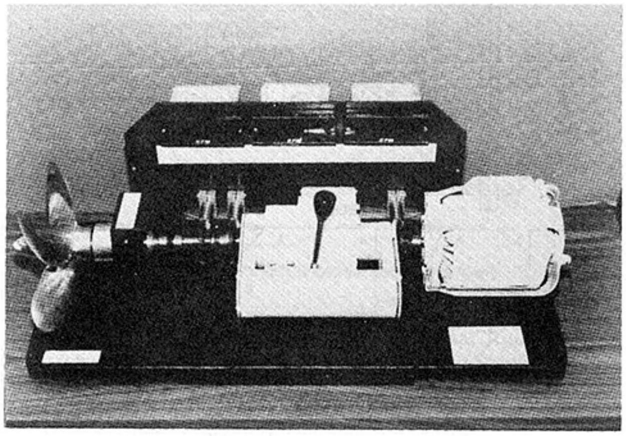

Fig. 9 Differentially driven reversing gear model

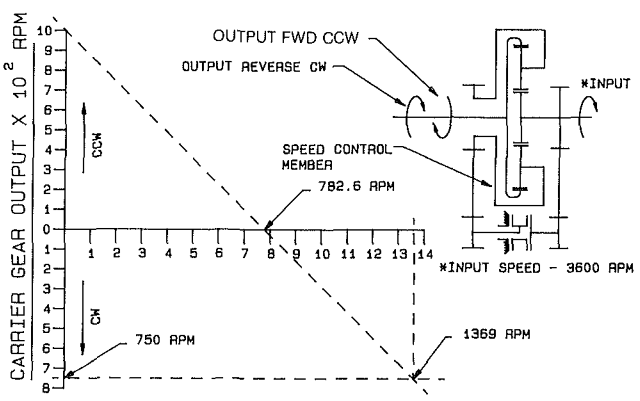

Fig. 10 Shaft speed relationship

Figure 9 is a photograph of a model of a differentially driven reversing gear arrangement schematically illustrated in Fig. 10. The differential gear configuration utilized in this figure is similar to the arrangement shown in Fig. 8(*b*) except that the speed control module is external to the gear module. The hardware shown in Fig. 9 has been used for demonstration purposes, and the gear unit can be reversed from full speed ahead to full speed astern in less than 1 second. It should be noted that the model is running essentially unloaded and that the gear and propeller inertias are very small. The significant item to note here is that during these quick reversals in the laboratory, the motor input speed remained basically unchanged.

Gear Sizing. Using a design power rating of 18,624 kW (25,000 hp) and 20-year gear life at a gear tooth strength reliability level of 99.99 percent, the gear elements were sized for both compressive and bending strength. All external gears were assumed to be AGMA class 11 accuracy hardened and ground. The internal gears were assumed to be through hardened to R_c 35 minimum. The low-speed epicyclic gear output stage has an internal ring gear with a pitch diameter of 1.22 m (48 in.) and utilizes five planets, a flexible ring gear, and a floating sun gear. Likewise, the first stage utilizes hardened and ground external gears. The pitch diameter of the ring gear of the first stage is approximately 0.71 m (28 in.). The two gear stages are housed in a 1.5 m (60 in.) diameter gear case.

Brake Sizing. Preliminary brake sizing was based on utilizing friction brakes and designed to hold twice the normal forward steady-state torque. A maximum operating clutch pressure of 140 N/m^2 (200 psi) was assumed. All brakes are internal to the gearbox and can be cooled by radiation or conduction.

To accomplish the crash astern mode of operation, it was assumed that the reverse brake must decelerate the inertia of the reversing gear including the clutch disks and must accelerate the inertia of the differential drive while opposing the torque of the water milling propeller. By keeping the engagement torque at approximately the design level and assuming some representative values of system inertia, brake engagement times were calculated and were found to be in line with reversing cycle times as reported by Phinney (1971).

Brake Actuations. A simple hydraulically or pneumatically operated shuttle, as illustrated in Figs. 3 and 4, can be employed to actuate the respective brakes for the forward or astern modes of operation or to keep the system in the neutral position. By applying pressure to either the forward side or the astern side of the shuttle, the shuttle slides axially along the fixed spline loading the respective disk pack and transmitting torque to the desired member. Since the mass and the corresponding inertia of the rotating components of this new reversing gear are low when compared to the large bull gears found in parallel shaft marine gears, it is reasonable to anticipate that for a given value of shaft torque, the reversing cycle for this new gear arrangement can be made comparable to or shorter than reversing cycles as reported by Phinney (1971). Further, since the initial rotation of the reversing gear components is achieved with energy extracted from the propeller, the total energy to be absorbed by the clutches is reduced.

Summary

A new concept of a reversing marine reduction gear was presented and briefly illustrated. This concept utilizes a differentially driven epicyclic gear to reverse the direction of rotation of the output shaft while, if desired, maintaining a constant speed on the input shaft. The resultant gear unit is technologically compatible with and complementary to the high-performance gas turbine engines currently used in many naval ship applications.

In addition to offering a significant reduction in weight, volume, and complexity when compared to parallel shaft reversing gears or CRPs, this new gear unit minimizes the danger of driving the free turbine backward, offers a potential for high reliability, increased propulsive efficiency, low noise, and ease of installation, alignment, and maintenance. Since the gear inertias in this arrangement are small, the reversing cycle, if desired, can be made shorter.

The simplicity of the design, effective use of materials, high efficiency, propulsion system compatibility, and differentially driven reversing module offers an exciting new concept for future marine propulsion systems.

References

Anon., 1964, "Built to Precision Tolerances," *Design News*, Jan. p. 107.

Anon., 1986, "Epicyclic Gear Units From Renk Drive Fast Navy Vessels," *Diesel and Gas Turbine Worldwide*, Sept. pp. 18–19.

Anon., 1987, "Reversing Gear Displaces Variable – Pitch Screw," *Machine Design*, July, p. 16.

Baumeister, T., and Marks, L., eds., 1967, "Automobiles," *Standard Handbook for Mechanical Engineers*, 7th ed., McGraw-Hill, New York.

Bryant, R., 1985, "The Development of the DDG-51 High Power Density Gear," SNAME Paper No. 3.

Dudley, D. W., ed., 1962, *Gear Handbook, the Design, Manufacture, and Application of Gears*, 1st ed., McGraw-Hill, New York.

Folenta, D. J., 1976, "Design and Development of High Horsepower Marine Planetary Gears," ASME Paper No. 76-GT-28.

Fortunato, E., and Clements, H. A., 1979, "Marine Reversing Gear Incorporating Single Reversing Hydraulic Coupling and Direct-Drive Clutch for Each Turbine," ASME Paper No. 79-GT-61.

Gugliuzza, T. A., 1969, "Gear Design and Laboratory Test Experience – Marine Gas Turbine Propulsion," ASME Paper No. 69-GT-3.

Hicks, R. J., 1981, "Epicyclic Gearboxes for High Speed Craft," The Institute of Marine Engineers, Paper No. 2.

McKenna, M. N., and Rogers, D., 1982, "HMS Invincible Propulsion Machinery From Concept to Fulfillment," The Institute of Marine Engineers, Paper No. 27.

Phinney, J. M., 1971, "Reverse Reduction Marine Drives for High Powered Gas Turbines," ASME Paper No. 71-GT-82.

Richardson, W. S., 1969, "The Friction Clutch Reverse-Reduction Gears for the GTS," ASME Paper No. 69-GT-5.

Rubis, J., 1986, "Governing Ship Propulsion Gas Turbine Engines," Nov. SNAME Paper No. 11.

Yates, D. E., 1976, "Epicyclic Gearing for Gas Turbine Main Propulsion," ASME Paper No. 76-GT-24.

Zeien, C. 1969, "The Gas Turbine Ship *Callaghan's* First Two Years of Operation," SNAME Paper No. 10.

Application of an Advanced Hybrid Rotordynamics Model to the Complete Structure of a Marine Gas Turbine Engine

B. D. Thompson
Mechanical Engineer,
Naval Sea Systems Command,
Washington, DC
Assoc. Mem. ASME

R. H. Badgley
President, Expert Systems, Inc.,
Reston, VA
Mem. ASME

Extensive fleet experience with the LM2500 marine gas turbine engine has identified it as an engine that exhibits wear-accelerating vibration effects. The critical speeds and associated mode shapes were not well understood by U.S. Navy engineers. To help deal with vibration-related problems, an analytical model was developed to calculate engine rotordynamic and structural response. The procedure is a multilevel, multirotor hybrid extension of the classical Myklestad–Prohl method. Presented herein are some of the model's predictions, and correlations with actual engine vibration measurements. The model predicted in excess of 20 different critical speeds in the engine's operating range. Because of the engine's structural flexibility, most of the critical speeds were engine casing and structural support resonances, driven by imbalance or misalignment in one or both of the engine rotors. Rotor-bending critical speeds were found to be strongly influenced by engine casing and support structure stiffness and mass. Using the model's predicted mode shapes, new mounting locations for accelerometers could be selected to determine vibration severity at various frequencies better. This has given the U. S. Navy new insights into fleet vibration problems, and provides a useful tool for achieving reduced engine removals.

Introduction

Comprehensive analytical transfer matrix models, capable of representing the structural dynamic characteristics of jet or gas turbine engines, have been presented by Hibner (1975), Sevcik (1963), Myklestad (1944), Prohl (1945), Koenig (1961), Lund and Orcutt (1967), and other authors. Finite element approaches to the rotor dynamics problem have also been presented by Ruhl and Booker (1972) and Nelson and McVaugh (1976). It appears that previous efforts (Sevcik, 1963) were used to model jet engines in the preliminary design phase in order to ensure that no critical speed "surprises" were encountered when the development engine was run. The dynamic model of the development engine was then adjusted to reflect the actual behavior of the development engine during testing.

The approach presented here has resulted in a model oriented toward engines that have extensive service. This effort was undertaken to understand better some of the vibration related problems encountered by some of the U.S. Navy's gas turbine engines. The LM2500 gas turbine engine (Fig. 1), which provides main propulsion power in U.S. Navy frigates, destroyers, and cruisers, is considered a reliable and rugged work horse of the fleet. Although considered reliable, the LM2500 does exhibit some of the undesirable wear-accelerating effects of vibration. This effort was undertaken in order to understand the causes and possible effects of this engine-derived vibration on the gas turbine structure, the attached accessories, and ultimately on the gas turbine's reliability.

Modeling Approach

The computational and element definition procedure used in this analysis is a multilevel, multirotor, hybrid extension of the classical Myklestad–Prohl method, perhaps more commonly known as the transfer matrix approach. The computational approach is based on the work of Hibner (1975) and includes allowances for many levels of structure (sump supports, inner and outer liners, and outer casings) with interconnecting stiffnesses. Additionally there are allowances for several rotors, each of which could be rotating at a different speed. The element definition procedure is based on traditional transfer matrix beam elements (see Pilkey, 1969, and Pestel and Leckie, 1963), hybrid transfer matrix elements (elements not based on beam theory), spring or bearing stiffness elements, and transitional elements.

It was recognized that many parts of a gas turbine cannot be modeled accurately as constant-cross-sectional beam elements. In order to model such components (or sections of them) correctly, it was necessary to use finite element techniques. The finite element model was then used to define coefficients Nv, Nm, Wv, and Wm, which are defined as follows:

Contributed by the International Gas Turbine Institute and presented at the 33rd International Gas Turbine and Aeroengine Congress and Exhibition, Amsterdam, The Netherlands, June 5–9, 1988. Manuscript received at ASME Headquarters February 23, 1988. Paper No. 88-GT-123.

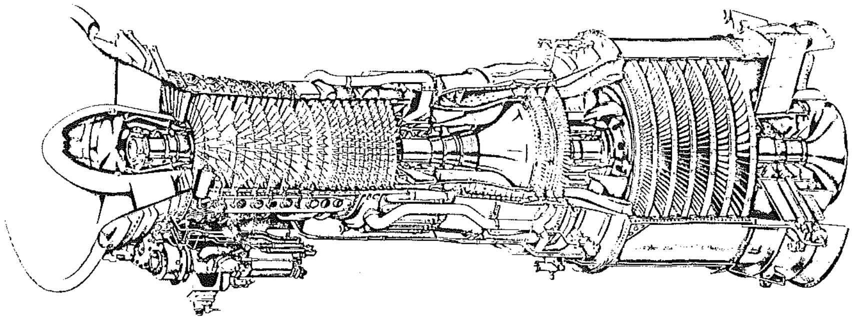

Fig. 1 LM2500 engine

Nv = Deflection due to a unit shearing force along the element length
Nm = Deflection due to a unit bending moment along the element length
Wv = Rotation due to a unit shearing force along the element length
Wm = Rotation due to a unit bending moment along the element length

The development of the appropriate expressions to enable these coefficients to be introduced into the transfer matrix form is contained in the appendix. The matrix multiplication process proceeds normally across the hybrid elements.

Transitional elements occur at joints between different levels of the structure, and at points where an overhanging structural element joins with the main supporting structure (such as cantilevered sections on compressor and turbine rotors). For each transitional element, compatibility equations are written defining the transfer of shear, bending moment, slope, and deflection across the element or from one structural level to another. Hibner (1975) and Sevcik (1963) contain more information on some of the compatibility equations used. Compatibility equations for joining overhanging structures with their main supporting structure are contained in the appendix.

Polar moments of inertia cause different effects in the various rotors rotating at different speeds. These are allowed for by specifying which rotor is the synchronous rotor and then by defining the other rotor speeds as functions of the synchronous rotor's speed. Alternatively, the speed relationship between the synchronous and nonsynchronous rotors may be defined as constant. The stiffnesses of flexible couplings, journal bearings, and squeeze film damper bearings can be defined in a similar way. In the case of journal bearings or squeeze film damper bearings, off-line calculations can be made to develop the functional relationships between rotor speed and bearing load on bearing properties. These relationships can then be used directly in the computer program through lookup tables or functional equations.

NAVROTOR is the generic name of a series of computer programs and associated subroutines that make up this application of the hybrid transfer matrix method. To define a model the structure is broken into a series of connected elements called LINEs. Generally the starting point is the gas turbine core or, in the case of the LM2500, the gas generator rotor, which is LINE A in Fig. 2. The supporting structure and other rotors are then defined as other LINEs (LINEs B through M in Fig. 2). Interconnections representing bearings, bearing supports, struts, mounts, and shock mounts are defined as radial and moment springs, structurally coupling two LINEs together. In the forced response analysis, the springs can have viscous and structural damping properties.

The next step in preparing the model is to define the order in which the matrix multiplication will take place. This includes the order in which each of the joints or interconnections will be crossed in moving from the front to the rear of the structure or from left to right. Upon completion of the matrix multiplication process, the displacement, slope, moment, and shear at the end (right) of the structure will be defined in terms of the displacement, slope, moment, and shear at the beginning (left) of the structure. The boundary conditions are then applied for rotors or structural members with free ends; moment and shear are zero at the free ends. The result is a square matrix, the determinant of which is equal to zero for the eigenvalues, or in this case the critical speeds or natural frequencies. From the eigenvalues, through back substitution, the eigenvectors (normalized mode shapes) are calculated.

A computer model defining the vertical and horizontal (lateral) directions with the level of detail shown in Fig. 2 can be programmed on a Digital Equipment Corporation VAX 11/750 or on an IBM, PC-AT microcomputer or compatible with a math coprocessor. This gives the engineer the capability to run a sophisticated vibration analysis with relatively modest computing facilities. A typical critical speed analysis on the LM2500 engine might consist of 100 points through the speed range of interest. It could locate six eigenvalues and calculate the associated eigenvectors, and would require 30 to 45 min on the VAX 11/750 or 75 to 100 min on a PC-AT.

Validation of the Analytical Model

Validation of the engine dynamic model's correctness is a very important first step after the model has been completed. This involves comparing the model's predictions with vibration data obtained in field vibration surveys. Generally there are a few well-known engine critical speeds. Comparison of these speeds with the model's predicted critical speeds will give a rough guide to the correctness of the model. For more detailed verification of the model one can use the model's predicted mode shapes as a guide to the placement of vibration monitoring sensors.

Another area of model validation is the analysis of some of the important interconnecting stiffnesses used between the structural levels in the model. Initially, finite element techniques are used to calculate the radial and moment stiffnesses of these elements. The dimensions of the part can usually be obtained from the part production drawings. Physical inspection of the part and its attachment mechanism may also be necessary, however, to verify that the boundary conditions specified in the finite element model are correct. This is particularly true of somewhat steep conical sections such as sump and bearing supports. Calculating the stiffnesses of engine and accessory mount links must also be done with particular care. The mount links may have inserts, or may become susceptible to localized deformation where a pin attaches it to an engine frame. Additionally, the vertical and horizontal stiffnesses of the mount links may be somewhat different. This is due to the orientation of the links.

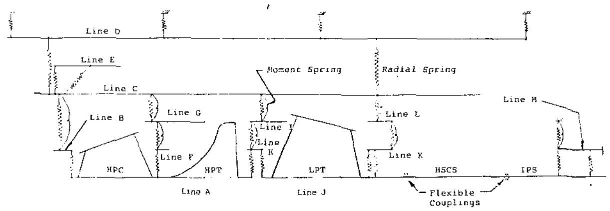

LINE	IDENTIFICATION	LINE	IDENTIFICATION
A	Gas Generator Rotor	G	Combustor Inner Liner
B	A-Sump	H	C-Sump
C	Gas Turbine Outer Case	I	Turb Mid Fr Inner Liner
D	Module	J	Pwr Turb/HSCS/Inp Pinion
E	Accessory Gearbox	K	D-Sump
F	B-Sump	L	Turb Rr Fr Inner Liner
		M	Red Gear Outer Case

Fig. 2 Dynamic analysis model of LM2500 marine gas turbine

Application of the Model

It was known, from extensive vibration surveys of operational LM2500 engines, that two gas generator rotor and two power turbine rotor critical speed modes existed in the gas turbine operating range. One of these modes had been identified as a compressor imbalance driven critical speed that was mainly seen at the compressor rear frame (CRF) location (which is the standard vibration monitoring position). This critical is seen between 8100 and 8500 rpm in the high-speed range. The existence of a high-pressure turbine imbalance driven mode at between 5000 and 7000 rpm in the high-speed range was also known. This mode is also seen predominantly at the CRF location. In the low-speed range the existance of two criticals both driven by low-pressure turbine imbalance had been previously identified. One of these criticals is located at between 1500 and 1700 rpm and is seen primarily at the CRF location. The other low-speed critical is seen between 3200 and 3500 rpm and is seem primarily on the compressor front frame. This was the state of the U.S. Navy's knowledge on the LM2500 vibration characteristics prior to the existence of the model.

The initial application of the LM2500 computer model, shown in Fig. 2, was to calculate all the critical speeds and associated mode shapes in the gas turbine operating range. This included both the low-speed and the high-speed ranges in both lateral directions, vertical and horizontal. These calculations resulted in the prediction of surprising 20+ critical speeds in the LM2500's operating range (Table 1). The four known criticals were predicted by the model; the model's mode shapes at these critical speed correlated well with vibration survey measurements. The mode shapes of three of these critical speeds are shown in Fig. 3. Additionally, the model's mode shapes gave insights into defining the important structural elements of these four modes. The mode shapes also confirmed the most sensitive locations on the outer engine case (the best accessible places to measure the response to these modes). It also identified other areas on the engine structure where the response to these modes could be measured.

An investigation into each of the calculated critical speeds and associated modes shapes was carried out. A number of these critical speeds are duplicative, being complementary pairs of modes in the vertical and horizontal directions. Identification of complementary pairs can be done quickly by comparison of the horizontal and vertical mode shapes. A number of these critical speeds, however, did not have a complementary critical speed with a similar mode shape in the other direction. The primary reason for this is the different effective engine mount stiffnesses between the vertical and horizontal directions. Some of the engine criticals depend more on engine mount stiffnesses than other criticals; in the cases where engine mount stiffness differences are important, the critical speed and mode shape differences between the two lateral directions are great.

Table 1 Calculated LM2500 engine critical speeds

CRIT SPEED (ROT FREQ)	SPEED (RPM)	DIRECTION	MODE DESCRIPTION
1 (LPT)	331	Vertical	Module Rocking
2 (LPT)	346	Vertical	Module Rocking
3 (LPT)	835	Vert/Horiz	1ST Stage HPT Nozzle Rattle
4 (LPT)	1090	Horizontal	Accessory Gearbox In-Phase
5 (LPT)	1400	Vertical	Accessory Gearbox In-Phase
6 (LPT)	1632	Horizontal	Gas Turbine Bending Acc. Gearbox Out-of-Phase
7 (LPT)	1916	Vertical	Gas Turbine Bending Acc. Gearbox Out-of-Phase
8 (LPT)	2565	Horizontal	LPT Rotor
9 (LPT)	3520	Vert/Horiz	LPT Rotor, HSCS, GT Case
10 (GG)	4400	Vert/Horiz	LPT Rotor, HSCS and Diffuser
11 (GG)	5400-9000	Vert/Horiz	HPT Rotor, GT Case
12 (GG)	5227	Vertical	LPT Rotor, HSCS and CRF Inner Liner
13 (GG)	5615	Horizontal	HSCS, Input Shaft CRF Inner Liner
14 (GG)	5997	Vertical	LPT Rotor and HSCS CRF Inner Liner
15 (GG)	6226	Horizontal	HSCS, Input Shaft CRF Inner Liner
16 (GG)	6558	Horizontal	HSCS, LPT Case GG Rotor Bending
17 (GG)	7000	Vertical	LPT Case, HSCS GG Rotor Bending CRF Inner Liner
18 (GG)	7500	Vertical	HSCS LPT Case GG Rotor Bending CRF Inner Liner
19 (GG)	8400-8600	Vert/Horiz	CRF Inner Liner HPC Rotor Bending
20 (GG)	9500-9750	Vert/Horiz	CRF Resonance HPC Bending

A careful analysis was also performed on the previously unknown engine critical speeds and mode shapes. It was found that a series of modes involving the back end of the engine (turbine rear frame, power turbine case, diffuser, and the high-speed coupling shaft) could be important. It was believed that these modes (two of which are shown in Fig. 4) could be part of the reason for some of the wearout modes seen on U.S. Navy operational LM2500s. In order to determine whether this was true, a review of old vibration survey data was performed. The review did show that there was a sudden increase in turbine rear frame response at speeds where the model predicted these modes. To increase the size of the data base on this newly discovered mode, vibration survey teams were instructed to look for increases in turbine rear frame response in the suspect speed range. As further confirmation, a detailed analysis was performed on data obtained from a specially instrumented vibration survey on an engine later found to have a severe case of one of the wearout modes. This special survey made extensive use of power turbine case measurements, which gave excellent correlation with the model predictions. The model also predicted that the primary exciting force behind this newly discovered engine vibration mode was gas generator rotor imbalance. As a result of an in-place trim balance on the HPC, further verification of the model's predictions were obtained. The initial response of this LM2500 to HPC imbalance was 6.0 mils peak to peak (p-p) at 8250 rpm at the CRF location and 4.5 mil p-p at 7000 to 7500 rpm at the TRF location. This engine was estimated to have several hundred gram inches of imbalance in the HPC. After the trim balance, the peak TRF response was reduced to 2.2 mil p-p at 7000 to 7500 rpm and the peak CRF response was reduced to

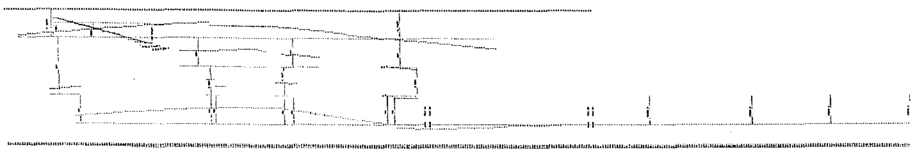

Fig. 3(*a*) Accessory gearbox (26 Hz) mode

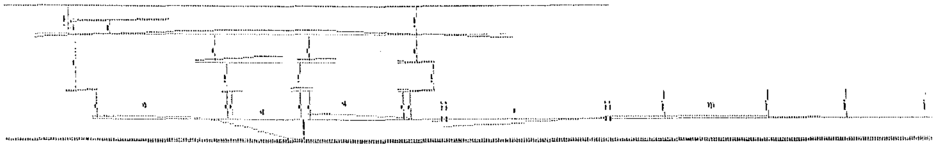

Fig. 3(*b*) High-pressure turbine mode, damper stiffness = 280,000 lb/in

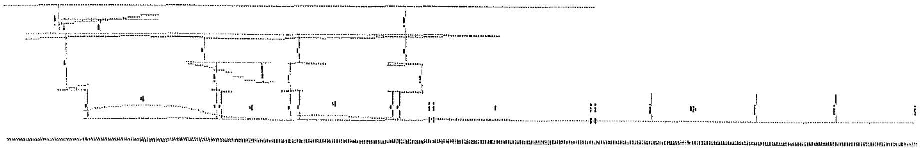

Fig. 3(*c*) Compressor bending mode

Fig. 3 Mode shapes for previously known critical speeds

Fig. 4(*a*) Gas generator system mode (vertical)

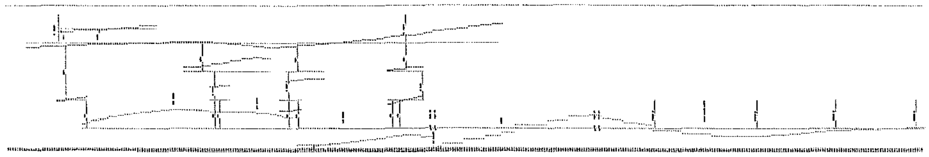

Fig. 4(*b*) Gas generator system mode (horizontal)

Fig. 4 Mode shapes for newly identified critical speeds

2.7 mil p-p at 8100 rpm. Before the trim balance, the peak turbine midframe (TMF) response was 3.0 mils p-p at 7250 rpm. After the trim balance the peak TMF response was 1.4 mils p-p at 7250 rpm. This demonstrated that the model provides a better understanding of presently known vibration modes, and can also be used to gain insight into the causes of vibration related wear out and failure modes. It can also be used to identify previously unknown vibration modes.

A further advantage in having a vibration model of the LM2500 that includes both the rotors and the multiple levels of the engine structure is that it allows a comparison to be made between case motion and the motions of interior structural components. It had been reported by repair engineers at the LM2500 depot that one internal component was particularly prone to cracks. It was also reported that several engines had broken combustor retaining pins. It was suspected that these failure modes were due to vibration, since these symptoms showed up primarily on engines that were removed for vibration. The LM2500 model showed that in most of the high-speed modes the affected component was dynamically very active. In one case, the compressor imbalance driven mode between 8100 and 8500 rpm showed a cantilevered combustor component as the primary recipient of the kinetic energy generated by compressor bending.

Several new modes have been identified in the LM2500's low-speed range (power turbine frequency), and increased definition has been given to the modes that had been previously identified. In seven out of ten identified low-speed modes, the accessory gearbox is the most active part of the gas turbine. The four modes between 1000 rpm and 2000 rpm are of particular concern. In the first two, the accessory gearbox is in phase with the engine casing (at 1090 and 1400 rpm); in the last two the accessory gearbox is out of phase with the engine casing (at 1627 and 1916 rpm). The 1000 to 2000 rpm range is one of the primary operating ranges for the low-speed rotor during normal operational use. These model predictions confirm and add clarity to what has been observed during fleet use: Accessory gearbox mount links wear, become loose, and allow the gearbox to move relative to the engine through degrees of freedom it was never designed to have. The gearbox supports the main fuel pump, the lubricating oil pump, the main fuel control, the starter, the air oil separator, and the transfer gearbox. The main fuel control (MFC) is the component that is cantilevered farthest from the center of the gearbox mounts, and, therefore, experiences the highest amplitudes of all the components on the gearbox. The effects of these vibration levels on the MFC are presently under study.

Two of the newly identified low-speed modes involve translation and rocking motions of the engine enclosure module. These two very low-speed modes were predicted to occur at 331 rpm and 346 rpm, and appear to be directly related to the module mount stiffnesses. At present these modes seem to be unimportant since they are predicted to occur at speeds below the normal power turbine operating line. A modification in the ship's operating profile to lower propeller shaft operating speeds, however, would also push power turbine speeds lower. This could make these modes important and could cause dynamic interactions.

Engine Response as a System

During LM2500 engine fleet vibration surveys, it had been noted that the response of the high-speed modes (those in the gas generator running range) was to a certain extent dependent on the power turbine speed. This was seen during pier side operation (power turbine unloaded), as well as during single and two-engine operation. In each of these cases, the functional relationship between the power turbine speed and the gas generator speed is different. This high-speed mode dependency went unexplained until this analysis, because it was not understood how the power turbine could affect gas generator vibration.

The structural dynamic behavior of a gas turbine, such as the LM2500, is a system problem, rather than just a problem of a single rotor. Most of the modes, in the normal operating range of the engine, involve the gas turbine structure as a whole. It has been found that a complete model of the response of such an engine cannot ignore the rotational stiffening effects of other (nonsynchronous) rotors. The LM2500 gas turbine has two main rotors: the high-speed gas generator rotor and low-speed power turbine rotor. In evaluating the response of the gas turbine at gas generator frequencies, it has been found that power turbine speed can change both the frequency and mode shape of the gas generator rotor critical speeds. The ratio of the power turbine speed to the gas generator speed will, of course, introduce important inertial effects. Additionally, the particular power turbine speed also defines the stiffnesses of the flexible diaphragms in the high-speed coupling shaft (HSCS), through which engine power is transmitted to the reduction gears. Identified earlier in this paper were high-speed modes involving response at the turbine rear frame due to the compressor imbalance. The speed range over which these modes appear depends on the particular speed of the power turbine, which controls the stiffnesses of the flexible diaphragms in the HSCS.

Included in the LM2500 model, shown in Fig. 2, are the four input pinion shaft bearings found in the reduction gear. These bearings are plain journal bearings whose stiffness and damping properties depend heavily on the speed and load these bearings carry. Because of the flexible diaphragms in the HSCS, the effect of the input pinion shaft on the high-speed modes is minimal. On the other hand, the effect of the journal bearings on the gas turbine low-speed modes can be pronounced. The HSCS shaft tends to isolate the power turbine rotor from excessive forces and motions deriving from the drive train (input pinion shaft, etc.). But a condition where the first or the second input pinion shaft bearings become unloaded (thereby reducing their effective stiffness and damping) could cause some damaging vibration modes, particularly to the HSCS.

Summary

A comprehensive analytical transfer matrix model has been developed that will model the complete structure of a gas turbine or jet engine. The program has been configured to allow the modeling of elements that don't behave as constant cross-sectional beams, as well as multilevels of structure, many rotors, overhanging structure and the insertion of the effects of flexible couplings, journal bearings, and squeeze film damper bearings. The computational scheme allows this sophisticated analysis to run on fairly modest computing facilities.

This analytical procedure has been used to model an entire LM2500 gas turbine engine. The model predictions are an important tool in understanding the structural behavior of the LM2500. Not only did the model give added insight into the behavior of the engine at known critical speeds or natural frequencies, but it identified critical speeds that previously had not been identified. The identification of these previously unknown critical speeds or natural frequencies gave added insight into some of the common failure modes encountered during operational use of the LM2500 gas turbine.

Conclusion

The analytical model presented and discussed in this paper has proven to be a useful tool in understanding and analyzing the dynamic response of the LM2500 gas turbine.

References

Hibner, D. H., 1975, "Dynamic Response of Viscous Damped Multi-Shaft Jet Engines," *Journal of Aircraft*, Vol. 12, No. 4.

Koenig, E. C., 1961, "Analysis for Calculating Lateral Vibration Characteristics of Rotating Systems With Any Number of Flexible Supports; Part I—Method of Analysis," ASME *Journal of Applied Mechanics*, Vol. 28, pp. 585–590.

Lund, J. W., and Orcutt, F. K., 1967, "Calculations and Experiments on the Unbalance Response of a Flexible Rotor," ASME *Journal of Engineering for Industry*, Vol. 89, pp. 785–791.

Myklestad, N. O., 1944, "A New Method of Calculating Natural Modes of Uncoupled Bending Vibration of Airplane Wings and Other Types of Beams," *Journal of Aeronautical Sciences*, Vol. 12, pp. 153–162.

Nelson, H. D., and McVaugh, J. M., 1976, "The Dynamics of Rotor Bearing Systems Using Finite Elements," ASME *Journal of Engineering for Industry*, Vol. 98, pp. 593–600.

Pestel, E. C., and Leckie, F. A., 1963, *Matrix Methods in Elasto Mechanics*, McGraw-Hill, New York.

Pilkey, W. D., 1969, "Manual for the Response of Structural Members," Vols. I, II, III, Engineering Mechanics Division, IIT Research Institute, Chicago, IL.

Prohl, M. A., 1945, "A General Method for Calculating the Critical Speeds of Flexible Rotors," ASME *Journal of Applied Mechanics*, Vol. 12, pp. 142–148.

Ruhl, R., and Booker, J. F., 1972, "A Finite Element Model for Distributed Parameter Turborotor Systems," ASME *Journal of Engineering for Industry*, pp. 126–132.

Sevcik, J. K., 1963, "System Vibration and Static Analysis," ASME Paper No. 63-AHGT-57.

APPENDIX

Development of Recurrence Formulas

Continuous Beam. Referring to Fig. A1, one can develop the standard transfer matrix relations defining the displacement (W), slope (θ), moment (M), and shear (V) at location $i+1$ in terms of W, θ, M, and V at location i for a massless elastic beam of constant properties.

This relation can be shown to be (see Pilkey, 1969, and Pestel and Leckey, 1963, for derivations):

$$
\begin{aligned}
W_{i+1} &= W_i - \Delta L\theta_i - (\Delta L^2/2EJ)M_i \\
&\quad - (\Delta L^3(6EJ - \alpha\Delta L/GA)V_i \\
\theta_{i+1} &= \theta_i + (\Delta L/EJ)M_i + (\Delta L^2/EJ)V_i \\
M_{i+1} &= M_i + \Delta L V_i \\
V_{i+1} &= V_i
\end{aligned}
\tag{1}
$$

Included in this formulation is the term for shear deformation. A gas turbine rotor may be considered as a series of cylindrical elements, which are short relative to their diameters. This greatly increases the importance of shear deformation on the bending stiffness of the element. To obtain an accurate formulation for the transfer across a lengthless (point) disk, one should include the influence of both gyroscopic effects and rotary inertia. A formulation for a point disk transfer matrix can be defined as follows (Pilkey, 1969, Pestel and Leckey, 1963):

$$
\begin{aligned}
W_{i+1} &= W_i \qquad M_{i+1} = (\beta I_p - I_t)\omega^2\theta_i + M_i \\
\theta_{i+1} &= \theta_i \qquad V_{i+1} = -M\omega^2 W_i + V_i
\end{aligned}
\tag{2}
$$

where β is the ratio (for rotating shafts only):

Rotor rotational frequency/Vibration frequency

Note that the latter ratio is 1 for a synchronous rotor. The β term allows the accurate modeling of the inertial effects in engines with several rotors all rotating at different speeds. The two transfer matrices (massless-elastic shear beam and the point disk) can be premultiplied to give the form

$$
\begin{aligned}
W_{i+1} &= B_{11}W_i + B_{12}\theta_i + B_{13}M_i + B_{14}V_i \\
\theta_{\theta+1} &= B_{21}W_i + B_{22}\theta_i + B_{23}M_i + B_{24}V_i \\
M_{i+1} &= B_{31}W_i + B_{32}\theta_i + B_{33}M_i + B_{34}V_i \\
V_{i+1} &= B_{41}W_i + B_{42}\theta_i + B_{43}M_i + B_{44}V_i
\end{aligned}
\tag{3}
$$

where

$B_{11} = 1,\quad B_{12} = -\Delta L,\quad B_{13} = -(\Delta L^2/2EJ),$

$B_{14} = -(\Delta L^2/6EJ - \alpha\Delta L/GA)$

$B_{21} = 0,\quad B_{22} = 1,\quad B_{23} = (\Delta L/EJ),$

$B_{24} = (\Delta L^2/2EJ)$

$B_{31} = 0,\quad B_{32} = (\beta I_p - I_t)\omega^2$

$B_{33} = 1 + (\beta I_p - I_t)\omega^2(\Delta L/EJ)$

$B_{34} = \Delta L + (\beta I_p - I_t)\omega^2(\Delta L^2/2EJ)$

$B_{41} = -M\omega^2,\quad B_{42} = M\omega^2\Delta L$

$B_{43} = M\omega^2(\Delta L^2/2EJ)$

$B_{44} = 1 + M\omega^2(\Delta L^3/6EJ - \alpha\Delta L/GA)$

The method outlined above allows other methods to be used to define the flexibility parameters in the transfer matrix (B_{13}, B_{14}, B_{23}, and B_{24}).

Hybrid Transfer Matrix. In the rotor and structure of a gas turbine engine, the flexibility of an element can be defined with increased accuracy by deflection coefficients, instead of deflection formulas of a continuous beam. This is particularly true of casings and other structures that do not behave like continuous beams in bending.

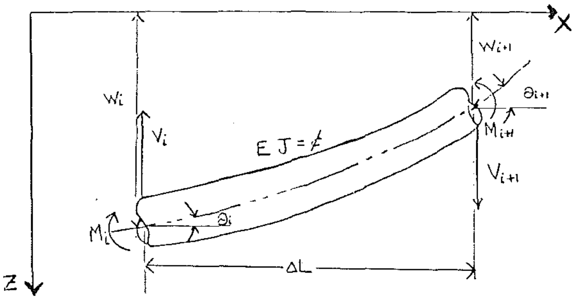

Fig. 1A Continuous beam model freebody diagram

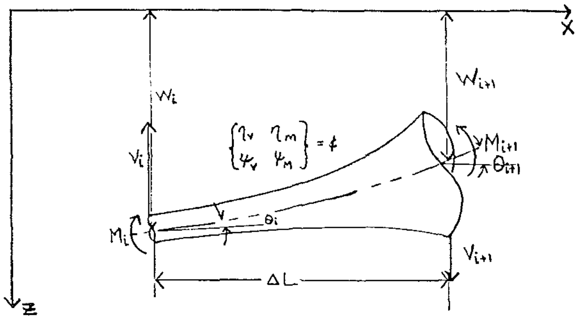

Fig. A2 Hybrid model freebody diagram

Referring to Fig. A2, a relationship between the state variables at stations i and $i+1$ can be written, assuming that the deflection coefficients η_v, η_m, ψ_v, and ψ_m are constant between the stations. Beginning with relations defining the end deflection and slope of a cantilever beam subject to moment M and shear V, we have

$$
W = -\eta_m M + \eta_v V \quad \theta = \psi_m M + \psi_v V \tag{4}
$$

Applying these relationships to Fig. A2, we obtain the equations

$$
\begin{aligned}
W_{i+1} &= W_i - \theta_i\Delta L - \eta_m M_{i+1} + \eta_v V_{i+1} \\
\theta_{i+1} &= \theta_i + \psi_m M_{i+1} - \psi_v V_{i+1}
\end{aligned}
\tag{5}
$$

From equilibrium we have

$$
V_{i+1} = V_i \quad \text{and}\, M_{i+1} = M_i + V_i\Delta L
$$

We then obtain the desired relationships for W_{i+1} and θ_{i+1} in terms of W_i and θ_i

$$
\begin{aligned}
W_{i+1} &= W_i - \theta_i\Delta L - \eta_m M_i + (\eta_v - \eta_m\Delta L)V_i \\
\theta_{i+1} &= \theta_i + \psi_m M_i + (\psi_m\Delta L - \psi v)V_i
\end{aligned}
\tag{6a}
$$

Adding the additional two relationships between V_{i+1}, M_{i+1} and V_i, M_i we have

$$
\begin{aligned}
M_{i+1} &= M_i + \Delta L V_i \\
V_{i+1} &= V_i
\end{aligned}
\tag{6b}
$$

This defines a transfer matrix where deflection coefficients replace formulas for a continuous beam. The hybrid "deflection coefficient" transfer matrix can be premultiplied with the point matrix for a lengthless disk (2). The following relationships are obtained, referring to equation (3), where:

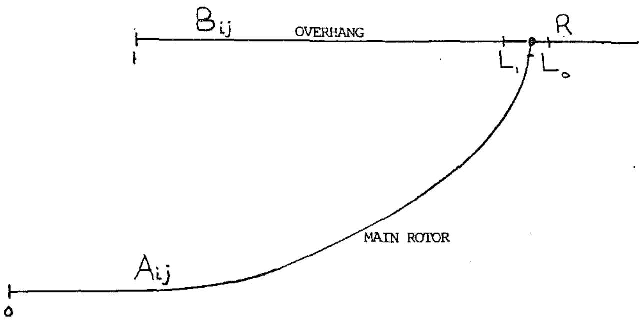

Fig. A3 Overhang (branch) analysis model

$B_{11}=1,\quad B_{12}=-\Delta L,\quad B_{13}=-\eta_m,$

$B_{14}=(\eta_v-\eta_m\Delta L)$

$B_{21}=0,\quad B_{22}=1,\quad B_{23}=\psi_m,$

$B_{24}=(\psi_m\Delta L-\psi_v)$

$B_{31}=0,\quad B_{32}=(\beta I_p-I_t)\omega^2$

$B_{33}=1+(\beta I_p-I_t)\omega^2\psi_m$

$B_{34}=\Delta L+(\beta I_p-I_t)\omega^2(\psi_m\Delta L-\psi_v)$

$B_{41}=-M\omega^2,\quad B_{42}=M\omega^2\Delta L$

$B_{43}=M\omega^2\eta_m$

$B_{44}=1+M\omega^2(\eta_m\Delta L-\eta_v)$

A General Method for Transferring Over a Forward Extending Overhang. In many aircraft derivative gas turbines additional stages of compression or expansion are obtained by cantilevering them from the basic rotor. This has the advantage that the length of the rotor is not increased. These overhangs, though, present a challenge to the line solution transfer matrix method. This section discusses a method that includes the effects of an overhung stage or stages, and which uses the transfer matrix approach. Referring to Fig. A3, if locations L_1 and L_0 are considered to be infinitely close to the joint, a point transfer matrix may be written to transit from L_0 to R, and to include the effects (elastic and mass) of the overhang B_{ij}. The stage variables at L_1 and L_0 can be defined in terms of the respective free ends by matrix multiplication in the standard transfer matrix approach.

$$\begin{bmatrix} A_{11} & A_{12} & A_{13} & A_{14} \\ A_{21} & A_{22} & A_{23} & A_{24} \\ A_{31} & A_{32} & A_{33} & A_{34} \\ A_{41} & A_{42} & A_{43} & A_{44} \end{bmatrix} \times \begin{bmatrix} W_0 \\ \theta_0 \\ M_0 \\ V_0 \end{bmatrix} = \begin{bmatrix} W_{L0} \\ \theta_{L0} \\ M_{L0} \\ V_{L0} \end{bmatrix} \qquad (7a)$$

$$\begin{bmatrix} B_{11} & B_{12} & B_{13} & B_{14} \\ B_{21} & B_{22} & B_{23} & B_{24} \\ B_{31} & B_{32} & B_{33} & B_{34} \\ B_{41} & B_{42} & B_{43} & B_{44} \end{bmatrix} \times \begin{bmatrix} W_1 \\ \theta_1 \\ M_1 \\ V_1 \end{bmatrix} = \begin{bmatrix} W_{L1} \\ \theta_{L1} \\ M_{L1} \\ V_{L1} \end{bmatrix} \qquad (7b)$$

The standard boundary conditions at both free ends are

$$V_1=M_1=\mathrm{V}_0=M_0=0$$

Using these, equations (7*a*) and (7*b*) reduce to:

$$\begin{aligned} B_{11}W_1+B_{12}\theta_1 &= W_{L0}=W_{L1} \\ B_{21}W_1+B_{22}\theta_1 &= \theta_{L0}=\theta_{L1} \\ B_{31}W_1+B_{32}\theta_1 &= M_{L1} \\ B_{41}W_1+B_{42}\theta_1 &= V_{L1} \end{aligned} \qquad (8)$$

Since positions L_1, L_0, and R are infinitely close together, $W_{L0}=W_{L1}=W_R$ and $\theta_{L0}=\theta_{L1}=\theta_R$. At position R

$$\begin{aligned} M_R &= M_{L0}+M_{L1} \\ V_R &= V_{L0}+V_{L1} \end{aligned} \qquad (9)$$

From equations (8), expressions relating V_{L1} and M_{L1} in terms of B_{ij}, W_{L0}, and θ_{L0} can be written:

$$\begin{aligned} B1\,W_{L0}+B2\theta_{L0} &= M_{L1} \\ B3\,W_{L0}+B4\theta_{L0} &= V_{L1} \end{aligned} \qquad (10)$$

where

$B1=(B_{31}B_{22}-B_{32}B_{21})/(B_{22}B_{11}-B_{21}B_{12})$

$B2=(B_{32}B_{11}-B_{31}B_{12})/(B_{22}B_{11}-B_{21}B_{12})$

$B3=(B_{41}B_{22}-B_{42}B_{21})/(B_{22}B_{11}-B_{21}B_{12})$

$B4=(B_{42}B_{11}-B_{41}B_{12})/(B_{22}B_{11}-B_{21}B_{12})$

The expressions for M_{L1} and V_{L1} can be substituted into equations (8), which results in the following point matrix to transfer from position L_0 to R:

$$\begin{bmatrix} W \\ \theta \\ M \\ V \end{bmatrix}^{R} = \begin{bmatrix} 1 & 0 & 0 & 0 \\ 0 & 1 & 0 & 0 \\ B1 & B2 & 1 & 0 \\ B3 & B4 & 0 & 1 \end{bmatrix} \begin{bmatrix} W \\ \theta \\ M \\ V \end{bmatrix}^{L_0} \times \qquad (11)$$

The Effect of Anisotropic Support on Rotor Instability Due to Fluid Leakage

Jhy-Horng Wang

Ming-Te Tsai

Department of Power Mechanical Engineering,
National Tsing-Hua University,
Hsinchu, Taiwan 30043

The instability caused by fluid leakage leads to limited performance in turbomachines. This instability may be improved by using flexible bearing supports with anisotropic stiffness. With a simplified model this effect is investigated, including the influence of many parameters. The results show that the optimum range of anistropy is strongly dependent on the parameters of the rotor-bearing system. In this paper an explanation from an energy point of view is presented to clarify the different stability behaviors with anisotropic bearing support.

Introduction

Oil whip and steam whirl are the two most important instabilities found in turbomachines. Steam whirl is caused by fluid leakage in blade shrouds and in the shaft labyrinth seal. Normally the exciting force caused by the fluid leakage is proportional to the power generated by turbomachines (Alford, 1965). As a consequence, the leakage exciting force becomes the most important barrier in the design of high-output turbomachines. Since 1965 this problem has been discussed either theoretically or experimentally in many papers (Krämer, 1968; Pollman et al., 1978; Thompson, 1978; Vance et al., 1984). With the present technique one can reduce the leakage exciting force, but it cannot be eliminated completely. Therefore, many methods have been suggested to improve the instability. One of the methods is to use an external anisotropic support. The study of Gunter et al. (1969) concluded that the instability caused by internal damping can be improved by an undamped support with anisotropic stiffness. The effect of external anisotropic support on the threshold performance of a rotor system subjected to fluid leakage was investigated by Ebner (1983, 1985) using a simplified model. He concluded that the threshold performance can be improved by the anisotropy of bearing support stiffness in some cases. The instability behavior of a 900 MW turbine-generator system with anisotropic support was studied by Wang (1987). Wang's results showed also that the stability of some systems can be improved by anisotropic support, but some cases can not. The validity of the original concept, namely that the work done by the leakage exciting force becomes smaller by using an anisotropic bearing support, needs further investigation.

In this paper a simplified lumped-mass model is used to study the threshold performance of the rotor-bearing system supported by damped flexible bearing supports. The concept that the net work done by the nonconservative forces will be zero at the threshold state, as indicated by Adams (1981) and Iwatsubo (1981), is used to get a comprehensive understanding of the effect of the anisotropic bearing support.

Analysis

A simplified rotor-bearing model is shown in Fig. 1. The model consists of a Laval rotor mounted on two fluid film bearings supported with a damped flexible bearing support. It is assumed that the mass of the shaft is concentrated at the central points of journals. The rotor contains the mass m_d and rotary inertia I_p, while the bearings are treated as point masses.

The fluid leakage effect is characterized by the change in boundary losses at the circumference of blades resulting from rotor displacement, which is caused by any disturbance. The variation of blade force at circumference causes a resultant

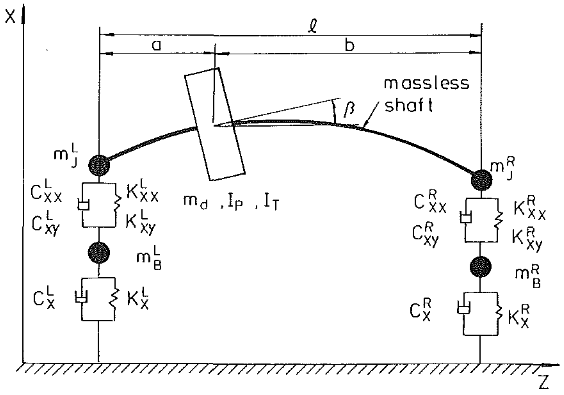

Fig. 1 Simplified rotor-bearing model. Only the projection in the x-z plane is shown.

Contributed by the International Gas Turbine Institute and presented at the 33rd International Gas Turbine and Aeroengine Congress and Exhibition, Amsterdam, The Netherlands, June 5–9, 1988. Manuscript received by the International Gas Turbine Institute December 5, 1987. Paper No. 88-GT-253.

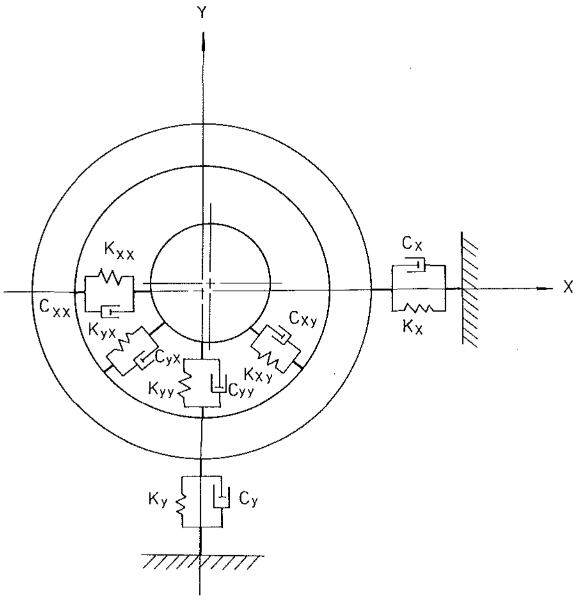

Fig. 2 Model of bearing and flexible bearing support

force, which acts on rotor in a direction perpendicular to rotor displacement

$$\begin{Bmatrix} F_{xq} \\ F_{yq} \end{Bmatrix} = -\begin{bmatrix} 0 & q \\ -q & 0 \end{bmatrix} \begin{Bmatrix} u_q \\ v_q \end{Bmatrix} \tag{1}$$

where u_q and v_q are displacements of the rotor in the x and y directions, and q is the leakage excitation factor or aerodynamic coupling stiffness, which can be evaluated for different machines theoretically and experimentally (Wright, 1977; Pollman, 1978; Vance, 1984). The magnitude of the factor q is approximately proportional to the output of the turbomachine.

The nonlinear characteristics of the journal bearing can be linearized at the static equilibrium position under the assumption of small vibration. The dynamic characteristics of journal bearing are represented by eight stiffness and damping coefficients, which are functions of the Sommerfeld number (Glienicke, 1980; Lund, 1987). The model of bearing supported by the flexible bearing support is shown in Fig. 2. The forces acting on the journal and bearing can be expressed as:

$$\begin{aligned}
\begin{Bmatrix} F_{xJ} \\ F_{yJ} \end{Bmatrix} &= -\begin{bmatrix} c_{xx} & c_{xy} \\ c_{yx} & c_{yy} \end{bmatrix} \begin{Bmatrix} \dot{u}_J - \dot{u}_b \\ \dot{v}_J - \dot{v}_b \end{Bmatrix} \\
&\quad - \begin{bmatrix} k_{xx} & k_{xy} \\ k_{yx} & k_{yy} \end{bmatrix} \begin{Bmatrix} u_J - u_b \\ v_J - v_b \end{Bmatrix} \\
\begin{Bmatrix} F_{xb} \\ F_{yb} \end{Bmatrix} &= -\begin{bmatrix} c_{xx} & c_{xy} \\ c_{yx} & c_{yy} \end{bmatrix} \begin{Bmatrix} \dot{u}_b - \dot{u}_J \\ \dot{v}_b - \dot{v}_J \end{Bmatrix} \\
&\quad - \begin{bmatrix} k_{xx} & k_{xy} \\ k_{yx} & k_{yy} \end{bmatrix} \begin{Bmatrix} u_b - u_J \\ v_b - v_J \end{Bmatrix} \\
&\quad - \begin{bmatrix} c_x & 0 \\ 0 & c_y \end{bmatrix} \begin{Bmatrix} \dot{u}_b \\ \dot{v}_b \end{Bmatrix} \\
&\quad - \begin{bmatrix} k_x & 0 \\ 0 & k_y \end{bmatrix} \begin{Bmatrix} u_b \\ v_b \end{Bmatrix}
\end{aligned} \tag{2}$$

The complete equations of motion can be written in matrix form

$$[M]\{\ddot{p}\} + ([C] - \Omega[G])\{\dot{p}\} + [K]\{p\} = \{F\} \tag{3}$$

where $[M]$, $[C]$, $[G]$, $[K]$ are the mass, damping, gyroscopic, and stiffness matrices of order 12 × 12. The details of the matrices can be found in the work of Wang (1987).

Using the state variable, the system equation (3) can be written in state form as

$$[M^*]\{\dot{z}\} + [K^*]\{z\} = \{R\} \tag{4}$$

where the matrices $[M^*]$, $[K^*]$ and vectors $\{z\}$, $\{R\}$ are defined as

$$[M^*] = \begin{bmatrix} [0] & [M] \\ [M] & [C] - \Omega[G] \end{bmatrix}$$

Nomenclature

A_q = orbit area of rotor on which leakage exciting force acts
$c_{xx}, c_{xy}, c_{yx}, c_{yy}$ = damping coefficient of bearing
c_x, c_y = damping coefficient of bearing support
$[C]$ = damping matrix
E = modulus of elasticity
E_1, E_2, E_3, E_4, E_5 = work done by nonconservative force
$\{F\}$ = force vector
$\{F_0\}$ = impulsive force vector
$[G]$ = gyroscopic matrix
I_T = diametral moment of inertia
I_p = polar moment of inertia
k_s = stiffness of shaft
$k_{xx}, k_{xy}, k_{yx}, k_{yy}$ = stiffness coefficient of bearing
k_x, k_y = stiffness coefficient of bearing support
$[K]$ = stiffness matrix
$[K^*]$ = system state variable matrix
l = length of shaft or rotor element
m_b, m_d, m_J = mass of bearing, disk, journal
$[M]$ = mass matrix
$[M^*]$ = system state variable matrix
N_b, N_e = number of bearing and rotor elements
N_q = number of points on which leakage exciting force acts
N_r = the rth component of force vector in normal coordinates
P = anisotropy of bearing support
$\{p\}$ = displacement vector in physical coordinates
$\{p_r\}$ = rth vibration mode
$p_{r,J}$ = jth component in $\{p_r\}$
Q = stiffness ratio, support/shaft
q = leakage excitation factor
$q_{\max}$ = threshold performance
R_a = nondimensional moment of inertia
R_B = mass ratio, bearing/rotor
R_J = mass ratio, journal/rotor
$\{R\}$ = force vector in state variable form
S = nondimensional leakage excitation factor
$S_{\max}$ = nondimensional threshold performance $= q_{\max}/k_s$

$$[K^*] = \begin{bmatrix} -[M] & [0] \\ [0] & [K] \end{bmatrix}$$

$$\{z\} = \begin{Bmatrix} \dot{p} \\ p \end{Bmatrix} \quad \{R\} = \begin{Bmatrix} 0 \\ F \end{Bmatrix} \tag{5}$$

Assume the homogeneous solution of equation (5) to be in the form

$$\{z\} = \{\Phi\} e^{\lambda t} \tag{6}$$

Equation (4) becomes a generalized eigenvalue problem

$$(\lambda[M^*] + [K^*])\{\Phi\} = \{0\} \tag{7}$$

with $2N$ eigenvalues λ_i, $i = 1, \ldots, 2N$. Corresponding to each eigenvalue λ_i, a right eigenvector $\{\Phi_i\}$ and a left eigenvector $\{\Psi_i\}$ are defined by

$$(\lambda_i[M^*] + [K^*])\{\Phi_i\} = \{0\} \tag{8}$$

$$\{\Psi_i\}^T(\lambda_i[M^*] + [K^*]) = \{0\}^T \tag{9}$$

The eigenvalues are generally in complex form

$$\lambda_i = \sigma_i + j\omega_i \tag{10}$$

It is well known that the system becomes unstable if there are any positive σ_i. The instability threshold is defined as a state that has at least one of the eigenvalues with zero real part while the others have negative real parts. If the system parameters are kept constant, the eigenvalues are functions of leakage excitation factor q. The threshold performance $q_{\max}$ is defined as the maximum leakage excitation factor q that the system can stand without becoming unstable. This maximum q can be found by the bisection method. The best anisotropy of support stiffness, which results in the largest threshold performance, is found by a line search technique, called the Golden Section Algorithm (Vanderplattes, 1984).

Energy Conservation of Rotor-Bearing System

In order to develop the relation between threshold performance and system energy, an impulsive force is applied to the rotor-bearing system. Since the spectrum of the impulsive force is constant for all frequencies, the response of all natural frequencies can be excited. Assume that the rotor is well balanced, then the force term in equation (4) becomes

$$\{R\} = \{R_0\}\delta(t) \tag{11}$$

where

$$\{R_0\} = \begin{Bmatrix} 0 \\ F_0 \end{Bmatrix}$$

and $\delta(t)$ is the Dirac delta function.

The eigenvectors can be normalized to satisfy the following biorthogonality relations:

$$[\Psi]^T[M^*][\Phi] = [I] \tag{12}$$

$$[\Psi]^T[K^*][\Phi] = -\lceil \lambda \rfloor \tag{13}$$

According to the expansion theorem, a state variable in physical coordinates can be expressed as a linear combination of eigenvectors

$$\{z\} = [\Phi]\{\eta\} \tag{14}$$

We substitute equation (14) into equation (4), premultiply with $[\Psi]^T$, and with the help of biorthogonality relation, $2N$ sets of uncoupled differential equations can be achieved

$$\dot{\eta}_i - \lambda_r \eta_r = N_r \qquad r = 1, \ldots, 2N \tag{15}$$

where N_r is defined by

$$N_r = \{\Psi_r\}^T\{R\} \tag{16}$$

If zero initial conditions are assumed, the solution of equation (4) can be expressed as

$$\{z\} = \sum_{r=1}^{2N} \{\Phi_r\}\{\Psi_r\}^T\{R_0\} e^{\lambda_r t} \tag{17}$$

The response at the jth degree of freedom of the rth mode is

$$p_{r,j} = 2e^{\sigma_r t}\,(a_{rj}\cos\omega_r t + b_{rj}\sin\omega_r t) \tag{18}$$

where

$$a_{rj} = \mathrm{Re}(\Phi_{r,N+j}\{\Psi_r\}^T\{R_0\})$$
$$b_{rj} = -\mathrm{Im}(\Phi_{r,N+j}\{\Psi_r\}^T\{R_0\})$$

and $\Phi_{r,N+j}$ is the $N+j$ component of the rth right eigenvector. Although there are many eigenmodes, the system becomes unstable whenever one of the vibration modes becomes unstable. Therefore the study of the unstable mode is enough to know the characteristics of instability. The following energy analysis will be concentrated at the unstable mode. The real

Nomenclature (cont.)

So = Sommerfeld number
T = anisotropy of support damping
$u_{bc}, u_{bs}, v_{bc}, v_{bs}$ = sine and cosine components of bearing displacement in x, y direction
$u_{Jc}, u_{Js}, v_{Jc}, v_{Js}$ = sine and cosine components of journal displacement in x, y direction
$u_{qc}, u_{qs}, v_{qc}, v_{qs}$ = sine and cosine components of displacement at the point where leakage exciting force acts in x, y direction
W = ratio of running to critical speed
$\{z\}$ = state variable vector in physical coordinate
α, β = angular displacement
α_a, α_b = length ratio
$\{\eta\}$ = state variable vector in normal coordinate
η_r = the rth component of $\{\eta\}$
λ = eigenvalue
μ = relative shaft stiffness
σ = real part of eigenvalue
$[\Phi]$ = right modal matrix
$\{\Phi_r\}$ = the rth right eigenvector in state variable
$\Phi_{r,j}$ = the jth component of $\{\Phi_r\}$
$[\Psi]$ = left modal matrix
$\{\Psi_r\}$ = the rth left eigenvector in state variable
ω = whirl frequency
Ω = rotational frequency

Superscripts

L = left
R = right

Subscripts

B, b = bearing
c = cosine component
d = disk
i, j, r, s = indices
J, j = journal
s = sine component
x = horizontal direction
y = vertical direction

part of the eigenvalue of this unstable mode becomes zero when the system changes from a stable to an unstable state. Because the real part of eigenvalue is zero, from equation (18) the vibration of this unstable mode is a harmonic motion with constant amplitude and can be represented as

$$u = u_c \cos \omega t + u_s \sin \omega t \tag{19}$$

$$v = v_c \cos \omega t + v_s \sin \omega t \tag{20}$$

The law of energy conservation guarantees that

$$\oint \{\dot{p}\}^T [M] \{\ddot{p}\} dt + \oint \{\dot{p}\}^T ([C] - \Omega [G]) \{\dot{p}\} dt + \oint \{\dot{p}\}^T [K] \{p\} dt = 0 \tag{21}$$

in one cycle. At the state of instability threshold, the first term of equation (21) becomes zero on account of harmonic motion with constant amplitude. Since the net work done by conservative forces, like spring force, will be zero after a complete cycle, the summation of work done by all nonconservative force shall also be zero. The work done by each nonconservative force can be found by performing the integration.

1 The work done on the *i*th rotor by the leakage exciting force is

$$E_{1i} = 2q_i A_{qi} \tag{22}$$

where A_{qi} is the orbit area of the point on which the leakage exciting force acts, and can be expressed as

$$A_{qi} = \pi (u_{qc} v_{qs} - v_{qc} u_{qs})_i$$

u_{qc}, u_{qs}, v_{qc}, v_{qs} are the associated displacement components of rotor in equations (19) and (20).

2 The work done by cross-coupling stiffness force in the *j*th bearing is

$$E_{2j} = \pi (k_{xy} - k_{yx})_j [(u_{Jc} - u_{bc})(v_{Js} - v_{bs}) - (v_{Jc} - v_{bc})(u_{Js} - u_{bs})]_j \tag{23}$$

3 The work done by the direct damping force in the *j*th bearing is

$$E_{3j} = -\pi \omega \{ c_{xx} [(u_{Jc} - u_{bc})^2 + (u_{Js} - u_{bs})^2] + c_{yy} [(v_{Jc} - v_{bc})^2 + (v_{Js} - v_{bs})^2] \}_j \tag{24}$$

Table 1 Nondimensional parameters

dimensionless parameter	symbol	definition
relative shaft stiffness	μ	$g/\omega_k^2 \Delta R_{min}$
mass ratio bearing/rotor	R_B	m_B/m_d
mass ratio journal/rotor	R_J	m_J/m_d
dimensionless moment of inertia	R_a	$I_T/m_d l^2$
dimensionless polor moment of inertia	R_p	$I_p/m_d l^2$
length ratio	α_a	a/l
length ratio	α_b	b/l
ratio of running to critical speed	W	Ω/ω_k
stiffness ratio pedestal/shaft	Q	K_y/K_S
stiffness ratio pedestal/shaft	Q'	K_x/K_S
anisotropic degree of pedestal stiffness	P	K_x/K_y
anisotropic degree of pedestal stiffness	P'	K_y/K_x
damping ratio pedestal/bearing	U	C_y/C_{yy}
anisotropic degree of pedestal damping	T	C_x/C_y
leakage excitation factor	S	q/K_S

$\omega_k = \sqrt{K_S/m_d}$; K_S : shaft stiffness

ΔR_{min} : smallest radial bering clearance

4 The work done by the cross-coupling damping force in the *j*th bearing is

$$E_{4j} = -\pi \omega (c_{xy} + c_{yx})_j [(u_{Jc} - u_{bc})(v_{Jc} - v_{bc}) + (u_{Js} - u_{bs})(v_{Js} - v_{bs})]_j \tag{25}$$

5 The work done by the external damping force in the *j*th bearing support is

$$E_{5j} = -\pi \omega [c_x (u_{bc}^2 + u_{bs}^2) + c_y (v_{bs}^2 + v_{bs}^2)]_j \tag{26}$$

E_3 and E_5 are the dissipative energy of damping, while E_1 is positive work fed into system. Whether E_2 and E_4 are cumulative or dissipative depends on the sign of the damping and stiffness coefficients, and the phase angle between u_b, u_J and v_b, v_J.

On the state of threshold equation (21) becomes

$$\sum_{i=1}^{N_q} E_{1i} = -\sum_{j=1}^{N_b} (E_{2j} + E_{3j} + E_{4j} + E_{5j}) \tag{27}$$

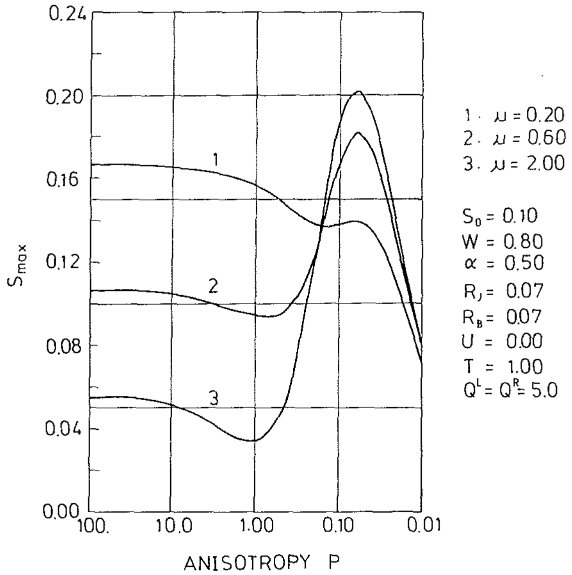

Fig. 3 The variation of threshold performance as a function of anisotropy at low speed ratio (five-pad tilting-pad bearing, *B/D* = 0.5)

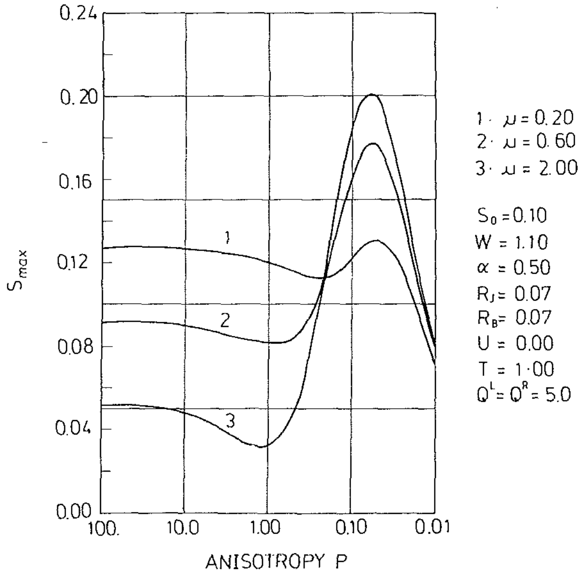

Fig. 4 The variation of threshold performance as a function of anisotropy at high speed ratio (five-pad tilting-pad bearing, *B/D* = 0.5)

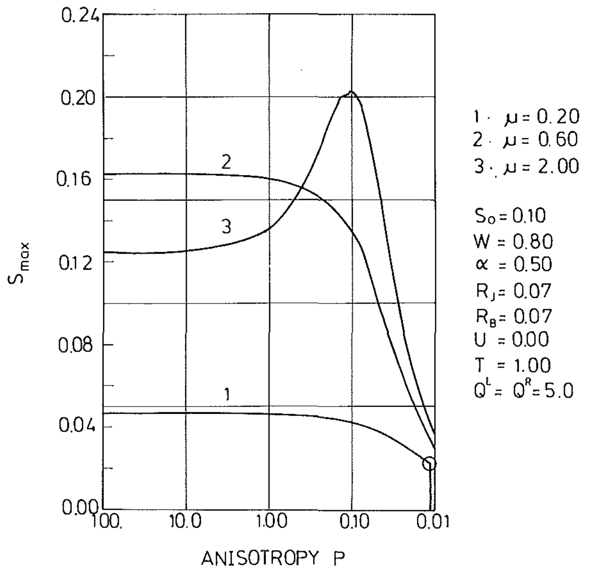

Fig. 5 The variation of threshold performance as a function of anisotropy at low speed ratio (two-lobed bearing, *B/D* = 0.5); circle indicates the occurrence of oil whip

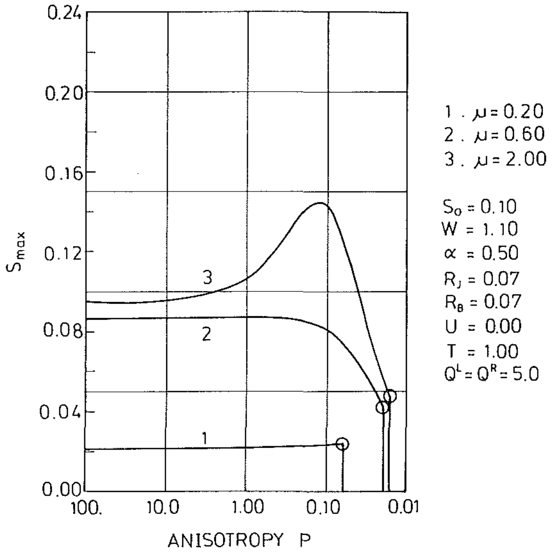

Fig. 6 The variation of threshold performance as a function of anisotropy at high speed ratio (two-lobed bearing, *B/D* = 0.5); circle indicates the occurrence of oil whip

where N_b is the number of bearings and N_q is the number of points on which the leakage exciting force acts. If the leakage exciting force is approximated as a concentrated force acting on one point of the rotor, on the state of threshold the threshold performance $q_{\max}$ becomes

$$q_{\max} = \frac{E_1}{2A_q}$$

$$= \frac{-1}{2A_q} \sum_{j=1}^{N_b} (E_{2j} + E_{3j} + E_{4j} + E_{5j}) \qquad (28)$$

Results of Stability Analysis

The simplified model of Fig. 1 is used to investigate the stability under the effect of many system parameters variations. All nondimensional parameters used here are listed in Table 1. Figures 3 to 7 show that the nondimensional threshold performance $S_{\max}$ of a rotor-bearing system varies with anisotropy of bearing support stiffness. The threshold performance $S_{\max}$ is the ratio of the leakage excitation factor to the shaft stiffness. The results of a system mounted on a five-pad tilting-pad bearing are shown in Figs. 3 and 4, while Figs. 5 and 6 are the results of a system with two-lobed bearing.

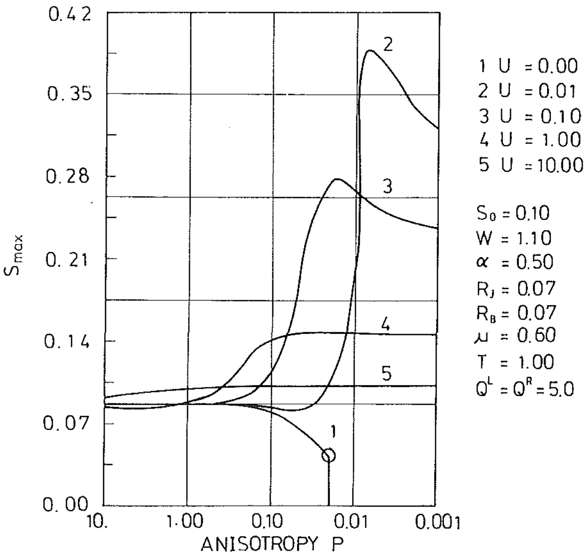

Fig. 7 The variation of threshold performance as a function of anisotropy with external damping (two-lobed bearing, *B/D* = 0.5)

It can be seen from Figs. 3 and 4 that in most cases the threshold performance has been improved by anisotropic support even without external damping. But in the case of low speed ratio and high relative shaft stiffness ($W = 0.8$, $\mu = 0.2$) the stability becomes worse with anisotropic support. The change of threshold performance in the range of $P = 100.0$ to 1.0 is not significant because the support condition can be regarded as rigid. But an obvious change can be observed if the horizontal stiffness keeps decreasing. The stability of a system with a more flexible shaft (larger μ) can be improved more effectively than the system with a stiffer shaft (smaller μ) by anisotropic support. The threshold performance of systems with high speed ratio ($W = 1.1$) is lower than those with low speed ratio ($W = 0.8$) owing to lower damping of the bearing at high speed.

Figures 5 and 6 are the results of the same systems as in Figs. 3 and 4, but with two-lobed bearing. Some different behavior can be observed. Comparing these plots, an interesting result, which is in conflict with the usual experience associated with oil whip, can be noted. At low speed ratio, with two-lobed bearing, the system with more flexible shaft (larger μ) has higher performance than the system with five-pad bearing. That means, if the instability due to leakage exciting force is concerned, the tilting-pad bearing is not unconditionally better than the two-lobed bearing. One should assess the influence of instability sources (bearing force or leakage exciting force) to select correctly the best bearing. Another interesting phenomenon is that the system loses the ability to sustain any leakage excitation suddenly at some support conditions (marked with a circle in Figs. 5 and 6). This is due to the fact that the increase of anisotropy of bearing support stiffness may induce the instability of oil whip.

The stability behavior of the system mounted on two-lobed bearing with external damping is shown in Fig. 7. The results show that an adequate selection of external damping incorporated with anisotropic bearing support stiffness can greatly improve threshold performance, as indicated by drastic change between curves 1 and 2 in Fig. 7. But the results also in-

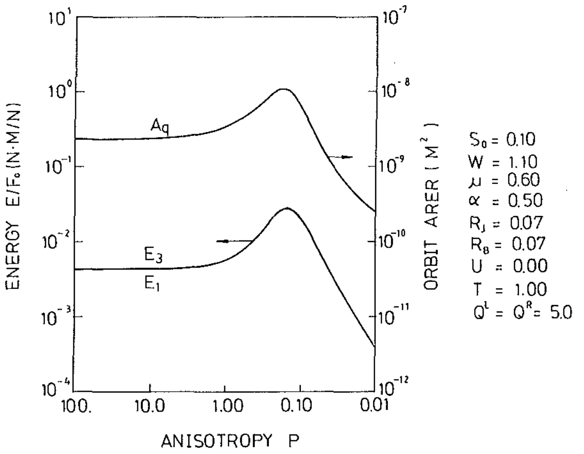

Fig. 8 Variation of rotor orbit area and energy with anisotropy (five-pad tilting-pad bearing)

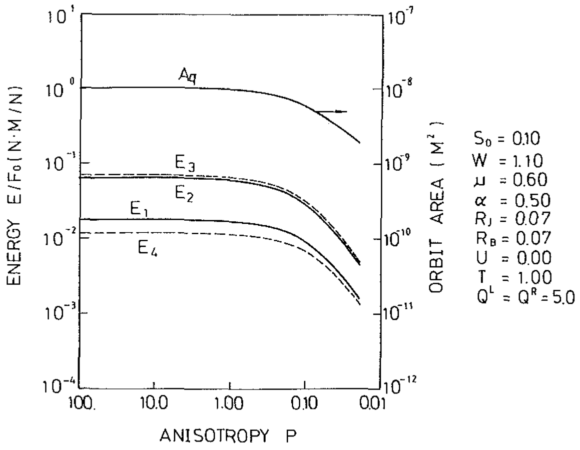

Fig. 9 Variation of rotor orbit area and energy with anisotropy (two-lobed bearing)

dicate that the larger external damping is not the better for high anisotropy. The reason will be explained later.

From the results discussed above, one can find that the threshold performance of some systems can be improved by anisotropic support, and for some systems it cannot. The same results were also found by Ebner (1983, 1985), but the reason was not discussed. Here the reason will be explained from an energy point of view. It should be noted that the effect of anisotropic support is to change both mode shape and energy imparted to the system. Equation (28) can be rewritten with a nondimensional parameter

$$S_{\max}=\frac{E_1}{2A_q k_s}$$

$$=\frac{-1}{2A_q k_s}\sum_{j=1}^{N_b}(E_{2j}+E_{3j}+E_{4j}+E_{5j}) \tag{29}$$

The term E_1 can be regarded as the energy that the system should dissipate to keep stable. The work done by the leakage exciting force is proportional to the orbit area of the rotor on which the exciting force acts. Clearly, the threshold performance will increase if the orbit area decreases or the energy dissipation increases.

We differentiate $S_{\max}$ with respect to anisotropy of support stiffness P

$$\frac{\partial S_{\max}}{\partial P}=\frac{-E_1}{2A_q^2 k_s}\left[A_q\,\frac{\partial E_1}{\partial P}-E_1\,\frac{\partial A_q}{\partial P}\right] \tag{30}$$

It is obvious that the stability will be improved by the anisotropy of bearing support stiffness when

$$\frac{\partial A_q}{\partial P}-\frac{A_q}{E_1}\,\frac{\partial E_1}{\partial P}>0 \tag{31}$$

for the region of $P<1.0$. The first and second terms of equation (31) are regarded as the effectiveness of anisotropic support to change orbit area (or energy input) and energy dissipation, respectively.

Figures 8 to 10 show some typical plots of orbit area of rotor and work done by nonconservative forces varying with anisotropy of bearing support stiffness. The solid line indicates positive work while the dashed line indicates negative work.

Figure 8 is a case of a system mounted on a five-pad bearing (corresponding to curve 2 in Fig. 4). It is noted that E_2 and E_4 become zero because of no cross-coupling force in this kind of bearing. The overlapping of E_1 and E_3 can prove the validity of equation (27). The support condition, which results in maximum energy dissipation (P = 0.178), does not coincide with the support condition, which results in maximum threshold performance (P = 0.0586). This means the effort to reduce orbit area and to increase energy dissipation may conflict. The threshold performance can be improved only when the reduction of rotor orbit area is greater than the reduction of energy dissipation, or the effect in increase of energy dissipation is higher than the increase of orbit area. The original concept of using anisotropic support to increase stability, namely, that the energy transferred to the rotor system by leakage excitation will be decreased by using anisotropic support and system will become more stable, is not always valid. The result of Fig. 8 indicates clearly that the improvement of threshold performance is due to more energy dissipation caused by bearing damping in the range of P = 1.0–0.178, not due to less energy transferred to rotor by leakage excitation. Figure 9 is another plot (corresponding to curve 2 in Fig. 6), which represents the result of a system mounted on a two-lobed bearing. The result of Fig. 9 is used to explain why the stability of the system cannot be improved by anisotropic support. As expected, with anisotropic support the orbit area of rotor becomes smaller, but the capability of the system to dissipate energy decreases faster. So the anisotropic support cannot improve the stability in this case. Figure 10 shows the case of high external damping. The mode shape, orbit area, and energy show almost no change with the variation of the anisotropy. So there is little improvement in threshold performance in curve 5 of Fig. 7.

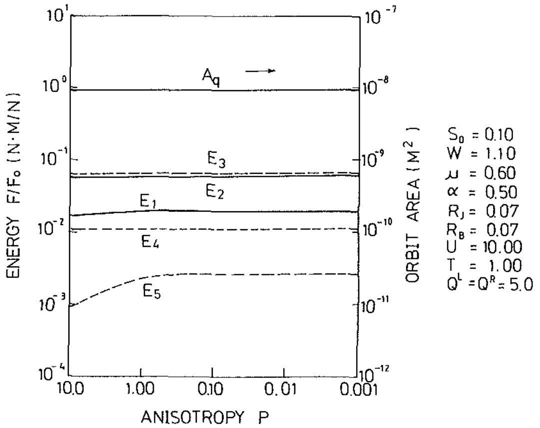

Fig. 10 Variation of rotor orbit area and energy with anisotropy (two-lobed bearing)

Conclusion

The instability due to fluid leakage of the rotor system supported with different anisotropic supports is investigated. An energy point of view is introduced here to explain the drastically different stability behaviors of the rotor systems supported with anisotropic supports. Strictly speaking, the concept that the orbit area of the rotor (or work done by leakage excitation) will become smaller with anisotropic bearing support is not valid. The threshold performance can be improved only when the effect due to the reduction of rotor orbit area is greater than the reduction of energy dissipation, or when the increase of energy dissipation is higher than the effect due to the increase of orbit area.

References

Adams, M. L., and Padovan, J., 1981, "Insights Into Linearized Rotordynamics," *Journal of Sound and Vibration*, Vol. 76, No. 1, pp. 129–142.

Alford, J. S., 1965, "Protecting Turbomachinery From Self-Excited Rotor Whirl," ASME JOURNAL OF ENGINEERING FOR POWER, pp. 333–343.

Ebner, F. L., 1983, "Schwingungs- und Stabilitätsverhalten von Turborotoren mit Spalterregung bei äusserer Anisotropie," VDI-Berichte 536, pp. 155–170.

Ebner, F. L., 1985, "Stability Behaviour of Clearance-Excited Turborotors With External Anisotropy," ASME Paper No. 85-DET-149.

Glienicke, J., Han, D. C., and Leonhark, M., 1980, "Practical Determination and Use of Bearing Dynamic Coefficients," *Tribology International*, pp. 297–309.

Gunter, E. J., and Trumpler, P. R., 1969, "The Influence of Internal Friction of the Stability on High Speed Rotors With Anisotropic Supports," ASME *Journal of Engineering for Industry*, Vol. 91, pp. 1105–1113.

Iwatsubo, T., Kawai, T., and Ikkai, H., 1981, "Stability Analysis of Multi Span Rotor System and Its Application," *Bulletin of the JSME*, Vol. 24, No. 196, pp. 1853–1858.

Krämer, E., 1968, "Selbsterregte Schwingungen von Wellen infolge von Querkräften," *Brennst.-Wärne-Kraft*, Vol. 20, No. 7, pp. 307–312.

Lund, J. W., 1987, "Review of Concept of Dynamic Coefficients for Fluid Film Journal Bearing," ASME *Journal of Tribology*, Vol. 109, pp. 37–41.

Pollman, E., Schwerdtfeger, H., and Termuehlen, H., 1978, "Flow Excited Vibration in High Pressure Turbines (Steam Whirl)," ASME JOURNAL OF ENGINEERING FOR POWER, Vol. 100, pp. 219–228.

Thompson, W. E., 1978, "Fluid Dynamic Excitation of Centrifugal Compressor Rotor Vibrations," ASME *Journal of Fluids Engineering*, Vol. 100, pp. 73–78.

Vance, J. M., and Laudadio, E. J., 1984, "Experimental Measurement of Alford's Force in Axial Flow Turbomachinery," ASME JOURNAL OF ENGINEERING FOR GAS TURBINES AND POWER, Vol. 106, pp. 585–590.

Vanderplaats, G. N., 1984, *Numerical Optimization Techniques for Engineering Design With Application*, McGraw-Hill, New York, Chap. 2, pp. 24–70.

Wang, J. H., and Tsai, M. T., 1987, "Increase the Rotor Stability by Anisotropic Suspension," *The Seventh World Congress on the Theory of Machines and Mechanisms*, Sevilla, Spain, pp. 1777–1783.

Wright, D. V., 1977, "Air Model Tests of Labyrinth Seal Forces on a Whirling Rotor," ASME *Winter Annual Meeting*, Atlanta, GA, Nov. 27–Dec. 2, pp. 61–73.

Minimum Weight Design of a Rotor Bearing System With Multiple Frequency Constraints

Ting Nung Shiau

Jon Li Hwang

National Cheng Kung University,
Institute of Aeronautics and Astronautics,
Tainan, Taiwan

The objective of the present study is to develop an efficient design algorithm for minimum weight design of a rotor bearing system under the requirements of operational speed range, i.e., multiple frequency constraints, to increase the performance of an existent rotor system. The system is modeled as an assemblage of rigid disks, shaft elements with distributed mass and stiffness, and discrete bearings. The system design variables are the inner radius of shaft elements and the stiffnesses of bearings. The optimization techniques employed to compare the results are method of exterior penalty function, method of feasible directions, and method of modified feasible directions. The parameter sensitivity analysis of the system is also presented. Three examples are used to demonstrate the merits of the design algorithm. The results indicate that the weight of the rotor bearing system can be significantly reduced at the optimum stage.

Introduction

A good design of rotors of high-speed rotating machinery, such as aircraft engines and generators, usually requires a number of sophisticated modifications of system parameters to achieve the design objectives.

Many authors (Lund and Sternlicht, 1962; Lund, 1963; Gunter, 1970; Dworski, 1964; Nelson, 1980; Childs and Graviss, 1982) have shown that the parameters, including the geometry of system, coefficients of bearings, inertia properties of rigid disk, and the distribution of the mass and stiffness of rotating assemblies, can significantly influence the dynamic characteristics of a rotor-bearing system.

The system sensitivity analysis has been studied (Lund, 1979) for a rotor system using a state vector-transfer matrix approach (Fritzen and Nordman, 1982) for a general vibrating system with application to simple rotor models, and (Rajan et al., 1985) for complex nonconservative rotors using finite element discretization. The optimal placement of critical speeds in rotor-bearing is investigated (Rajan et al., 1987) using a method of gradient projections.

Recently, structural designers have searched for efficient algorithms for optimum design of structures (Venkayya, 1971; Venkayya et al., 1973; Schmit and Farshi, 1974; Haug et al., 1972). Moreover, the increase of computational efficiency and compact modern computers has led to the possibility of an automated design process of a large structural system.

The minimization of response amplitudes within the operating range of the rotor system may be the most primary design objective. The problem of weight minimization usually arises from the revision of an existing rotor bearing system to increase the system performance. In this paper, we focus on weight minimization of the rotor system, which is of the design satisfying the stress requirements, with restrictions on critical speeds. Since it is often difficult to measure accurately the damping in the system, it is practical to restrict our attention to compute the undamped critical speeds. Due to the nature of problem, the initial design of the rotor system is infeasible. Hence the optimization techniques employed have to overcome this inconvenience.

Optimum Design Problem Statement

A rotor bearing system subject to restrictions on critical speeds is considered for a minimum weight design. This is equivalent to the design problem of weight minimization under multiple frequency constraints. Figure 1 shows the typical rotor configuration and coodinates.

The system design variables are the inner radius of shaft elements and the stiffnesses of bearings. The violations of constraints are checked through the structural dynamic characteristic analysis. The weight objective function W is a nonlinear explicit function in the inner radius of shaft element but implicit in the bearing stiffnesses.

The design problem posed in this paper may be stated as: Find the set of d_i, $i=1, n$, such that the weight of the rotor system, $W(\mathbf{d})$, is a minimum and the behavior constraints g_j are satisfied in the meantime. Mathematically, this can be rewritten as (Vanderplaats, 1982): Find the set of d_i, such that

$$\text{minimize} \qquad W(\mathbf{d}) = \sum_{i=1}^{n_e} \pi \, \rho_i (r_{oi}^2 - r_{Ii}^2) l_i \tag{1}$$

$$\text{subject to} \qquad g_j(\mathbf{d};\, t) \le 0, \; j=1, J \tag{2}$$

$$d_i^l \le d_i \le d_i^u, \; i=1, n \tag{3}$$

where ρ_i and l_i are the material density and the length of shaft

---

Contributed by the International Gas Turbine Institute and presented at the 33rd International Gas Turbine and Aeroengine Congress and Exhibition, Amsterdam, The Netherlands, June 5–9, 1988. Manuscript received by the International Gas Turbine Institute December 21, 1987. Paper No. 88-GT-254.

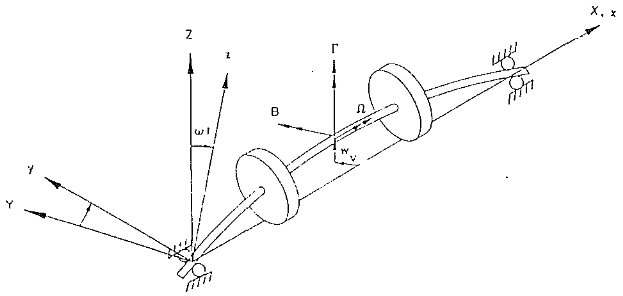

Fig. 1 Typical rotor configuration and coordinates

elements, respectively. Vector **d** represents the set of design variables d_i, $i=1, n$. The number of total design variables n is equal to the sum of the number of shaft elements (n_e) and the number of bearings (n_b). The nonlinear constraint functions g_j, $j=1, J$ are only the limitations on the critical speeds of the rotor system. It has to be pointed out that the stress constraints may be primary. However, in this paper, the design of an existing rotor bearing system with satisfactory stress requirements is revised and the weight of the revised system is kept as low as possible to increase the system performance. Since the design variables are the inner radii of shaft, the effect of changes of design variables on the system stress is negligible.

Rotor Model and Critical Speeds

Figure 1 shows a rotor composed of the shaft, which carries disks and is mounted on bearings. Two reference frames are utilized to describe the system motion. One is a fixed reference $X-Y-Z$ and the other is a rotating reference $x-y-z$. The X and x axes are collinear and coincident with the undeformed bearing centerline. The two reference frames have a single rotation ωt difference about X with ω denoting a precession speed.

All deflections and forces are assumed to be parallel to the Y, Z plane, and the rotor has four degrees of freedom at each finite-element station. The equations of motion shown by the authors Nelson and McVaugh (1976) and Nelson (1980) have been rederived and Kane's theory (Kane and Levinson, 1985) is employed to ensure the accuracy of equations. Because the finite element analysis procedure has been well documented, the equations are presented in the whirl reference frame neglecting the details.

The discs are considered as point masses of four-degree-of-freedom rigid body with the generalized coordinate defined as two translations (v, w) of mass center in the (y, z) directions and two rotations (β, γ) of the plane of the disk about (y, z) axes. It is necessary to locate the rigid disk at a finite element station. Let Ω be the rotational speed of system and $\bar{p}=(v, w, \beta, \gamma)$ be the deflections in rotating frame R. The equation of motion for the disks is given by

$$([M^d]+[N^d])\ddot{\bar{p}}^d+\omega(2[\hat{M}^d]+2[\hat{N}^d]-\lambda[G^d]\dot{\bar{p}}^d \\ -\omega^2([M^d]+[N^d]-\lambda[\hat{G}^d])=\bar{F}^d_{4\times 1} \tag{4}$$

where the matrices $[M^d]$, $[N^d]$, $[\hat{M}^d]$, $[\hat{N}^d]$, $[G^d]$, $[\hat{G}^d]$ have been shown by Nelson and Mcvaugh (1976) and Nelson (1980) and λ is the ratio of the shaft rotational speed Ω to the precession speed ω. The vector $\bar{p}^d$ denotes displacement of disk at located station and $\bar{F}^d$ is the corresponding external force vector.

The flexible shaft is discretized into finite shaft elements. By specifying spatial shape functions and treating the rotor element as an integration of an infinite set of differential disks, one can develop the equation of motion for shaft element as follows:

$$([M^e]-[N^e])\ddot{\bar{p}}^e+\omega(2[\hat{M}^e]+(1-\lambda)[G^e])\dot{\bar{p}}^e \\ +([K^e]-\omega^2([M^e]+(1-2\lambda)[N^e]))\bar{p}^e=\bar{F}^e \tag{5}$$

where $\bar{p}^e$ is the (8×1) displacement vector and $\bar{F}^e$ is the external force vector.

The translational bearings are assumed to be linear and isotropic and modeled by the equation

$$k\begin{bmatrix}1 & 0\\ 0 & 1\end{bmatrix}\begin{Bmatrix}v\\ w\end{Bmatrix}=\bar{F}^b \tag{6}$$

where k denotes the stiffness coefficient of bearing and $\bar{F}^b$ is the bearing external force vector.

System equations, which describe the behavior of the entire rotor system, are formulated by taking into account the contributions from all the finite elements in the model. The assembled equations of motion with n elements in the whirl frame coordinates are of the form

$$([M]+[N])\ddot{\bar{p}}+\omega(2[\hat{M}]+2[\hat{N}]-\lambda[G])\dot{\bar{p}} \\ +([K]-\omega([M]+[N]-\lambda[\hat{G}]))\bar{p}=\bar{F}_{4n_e\times 1} \tag{7}$$

where the global displacement vector is defined by

$$\bar{p}=[v_1 w_1 \beta_1 \gamma_1 \ \ldots \ v_{n_e} w_{n_e} \beta_{n_e} \gamma_{n_e}]^T \tag{8}$$

The natural circular precession speeds and mode shapes can be determined from the homogeneous form of equation (7), i.e., $\bar{F}$ vanishes. Since we seek the modes in the circular whirl frame with $\bar{p}$ equal to a constant, i.e., $\ddot{\bar{p}}=\dot{\bar{p}}=0$, the solution is assumed $\bar{p}=\bar{p}_o=$constant. Moreover, only one of two planes

Nomenclature

d_i = design variables
$\bar{F}^b$, $\bar{F}^d$, $\bar{F}^e$ = external force vector of bearing, disk, and shaft element, respectively
$[G]$, $[\hat{G}]$ = gyroscopic matrix and transformed gyroscopic matrix
g_j = constraint functions
J = number of constraint functions
$[K]$, $[\hat{K}]$ = stiffness matrix and transformed stiffness matrix
l_i = length of ith shaft element
$[M]$, $[\hat{M}]$ = translational mass matrix and transformed mass matrix
$[N]$, $[\hat{N}]$ = rotational mass matrix and transformed rotational mass matrix
n_e, n_b = number of shaft element and bearings
$\bar{p}$ = displacement vector relative to rotating reference $x-y-z$
r_o, r_I = outer radius and inner radius of shaft element
v, w = translations in y, z axes
$W(\mathbf{d})$, $W^*(\mathbf{d})$ = objective function and pseudo-objective function
β, γ = angle rotations about y, z axes
ζ = radius ratio $=r_{oi}/r_{Ii}$
κ' = shear factor
λ = whirl ratio $=\Omega/\omega$
μ = Poisson ratio
ν = eigenvalue of system $=\omega^2$
ρ = mass density
Ω = rotational speed
ω = precession speed

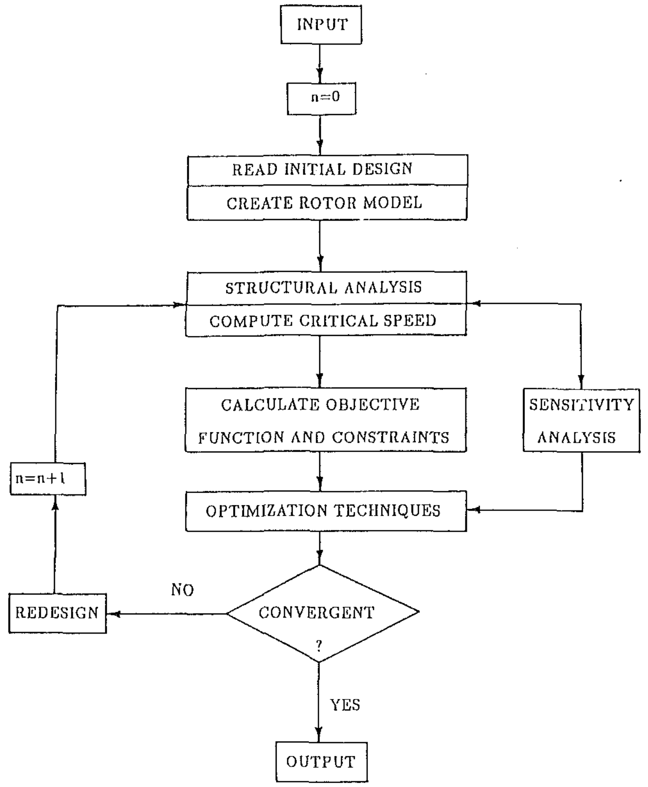

Fig. 2 Flow chart of optimum design algorithm

of motion is treated due to harmonic circular property. The equation is reduced to the following form:

$$([K]-\omega^2([M]+[N]-\lambda[\hat{G}]))\bar{p}_o=0 \tag{9}$$

There are $2n$ real and positive eigenvalues, ω_i, which can be calculated from equation (9). The critical speeds and associated mode shapes can be determined by choosing a whirl ratio of $\lambda=1$. It should be noted that the values of parameter λ decide whether the motion is forward ($\lambda>0$) or backward ($\lambda<0$). Moreover, the whirl mode is called subsynchronous, synchronous, or supersynchronous whirl corresponding to the values of $\lambda>1$, $\lambda=1$, or $\lambda<1$, respectively.

Optimization Algorithm

The optimum design of a rotor bearing system is cast into a nonlinear mathematical programming problem as stated by equations (1)–(3). The examples included in this paper are all single-spool machines. The first two modes of the system may be regarded as rotor rigid-body modes while the third mode appears to be the first bending critical speed. Let ω_1^c and ω_2^c denote rigid-body critical speeds and ω_3^c represent the first bending critical speed. Since most rotor systems are designed to operate below the first bending critical speed, equation (2) can be rewritten as

$$g_1(\mathbf{d})=\omega_2^c-\frac{\Omega_{\text{low}}}{a_1}\leq 0 \tag{10a}$$

$$g_2(\mathbf{d})=a_2\bullet\Omega_{\text{high}}-\omega_3^c\leq 0 \tag{10b}$$

where Ω_{low} and Ω_{high} are the low end and high end of the operating range of the original system, respectively. The constants a_1 and a_2 are any positive numbers greater than one. Equation (10a) shows that the second critical speed has to be smaller than Ω_{low} by dividing by a factor a_1. However, equation (10b) shows that the first bending critical speed has to be larger than Ω_{high} by multiplying by a factor a_2. These give the inequality behavior constraints on critical speeds of system.

Because the initial design of the present optimal problem is an infeasible design, a method of Sequential Unconstrained Minimization Techniques (SUMT), namely the exterior penalty function method (EPFM), is first used as a strategy for solving this optimum design problem. Then two direct methods, called the method of feasible directions (MFD) and modified method of feasible directions (MMFD), are employed to compare the results of different optimization techniques.

The use of EPFM requires the creation of pseudo-objective function and the choices of penalty parameters. This method particularly approaches the optimum from an infeasible design region, which is the nature of the present design problem. To use both MFD and MMFD, one can add two more nonnegative design variables d_{n+1} and d_{n+2} to increase the feasibility. Hence, the new design problem becomes

$$\text{minimize}\qquad W^*(\mathbf{d})=\sum_{i=1}^{n_e}\pi\rho_i(r_{oi}^2-r_{Ii}^2)\bullet l_i$$

$$+a_3d_{n+1}+a_4d_{n+2} \tag{11}$$

$$\text{subject to}\qquad g_1^*(\mathbf{d})=\omega_2^c-\frac{\Omega_{\text{low}}}{a_1}-d_{n+1}\leq 0 \tag{12}$$

$$g_2^*(\mathbf{d})=a_2\bullet\Omega_{\text{high}}-\omega_3^c-d_{n+2}\leq 0 \tag{13}$$

where the parameters a_3 and a_4 are any positive real numbers. When the optimum is reached, the values of d_{n+1} and d_{n+2} tend to zero. A general flow chart of the optimum design algorithm is shown in Fig. 2.

Sensitivity Analysis

To perform an optimum design, three component analysis categories are required:

(*i*) Approximate analysis procedure for objective function and constraint evaluation.

(*ii*) Optimization algorithm.

(*iii*) Refined analysis procedures for optimum design validation.

The derivatives of the objective function and the constraint function have to be obtained to calculate each iterative design. These include the derivatives of eigenvalues and eigenvectors (Fox and Kapoor, 1968; Plaut and Huseyin, 1973). Other authors who studied the sensitivity analysis have been included in the introduction.

The derivatives of the objective function can be obtained by differentiating equation (1) with respect to d_i

$$\frac{\partial W(\mathbf{d})}{\partial d_i}=-2\pi\rho_il_ir_{Ii},\ \text{as } d_i=r_{Ii},\ i=1,\ n_e \tag{14a}$$

$$\frac{\partial W(\mathbf{d})}{\partial d_i}=0,\ \text{as } d_i=k_j,\ j=1,\ n_b \tag{14b}$$

Similarly by differentiating the equations (10a) and (10b) with respect to d_i, the derivatives of the constraint function can be obtained as

$$\frac{\partial g_1(\mathbf{d})}{\partial d_i}=\frac{\partial\omega_2^c}{\partial d_i} \tag{15a}$$

$$\frac{\partial g_2(\mathbf{d})}{\partial d_i}=-\frac{\partial\omega_3^c}{\partial d_i} \tag{15b}$$

The derivatives of critical speed shown on the right-hand side of equations (15a) and (15b) can be calculated by the following procedures. For convenience, one can rewrite equation (9) in the standard form of qth mode:

$$([A]-\nu_q[B])\bar{X}_q=0 \tag{16}$$

where

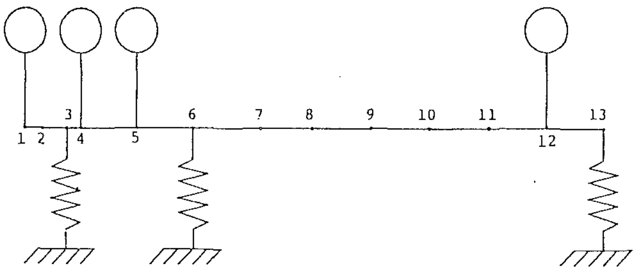

Fig. 3 Rotor schematic

$$[A] \equiv [K]$$
$$[B] \equiv [M]+[N]-[\hat{G}]$$
$$\nu_q = (\omega_q^2)^2 = q\text{th eigenvalue}$$
$$\bar{X}_q = (\bar{p}_o)_q = q\text{th eigenvector}$$

The orthogonality of normalized eigenvectors is given by

$$\bar{X}_j[B]\bar{X}_q = \delta_{jq} \tag{17}$$

where δ_{jq} is the Kronecker delta function. Differentiating equation (16) with respect to d_i and premultiplying by $\bar{X}_q^T$, one can obtain

$$\nu_{q,i} = \frac{\partial \nu_q}{\partial d_i} = \bar{X}_q^T\left(\frac{\partial [A]}{\partial d_i} - \nu_q \frac{\partial [B]}{\partial d_i}\right)\bar{X}_q \tag{18}$$

Substituting $\nu_q = (\omega_q^c)^2$ into the above equation gives the expression of derivatives of critical speed.

$$\frac{\partial \omega_q^c}{\partial d_i} = \frac{1}{2\omega_q^c} \bullet \nu_{q,i} \tag{19}$$

Similarly, for the $(q+1)$th critical speed, the expressions of the derivatives are given by

$$\nu_{q+1,i} = \frac{\partial \nu_{q+1}}{\partial d_i} = \bar{X}_{q+1}^T\left(\frac{\partial [A]}{\partial d_i} - \nu_{q+1} \frac{\partial [B]}{\partial d_i}\right)\bar{X}_{q+1} \tag{20}$$

$$\frac{\partial \omega_{q+1}^c}{\partial d_i} = \frac{1}{2\omega_{q+1}^c} \bullet \nu_{q+1,i} \tag{21}$$

The gradients, $\partial[A]/\partial d_i$ and $\partial[B]/\partial d_i$, shown in equations (18) and (20) can be computed by the following processes:

(*i*) When the bearing stiffness is the design variable, i.e., $d_i = k_i$, it is simple to notice that $\partial[B]/\partial d_i$ vanishes and $\partial[A]/\partial d_i$ is of the form

$$\frac{\partial [A]}{\partial d_i} = \text{block}(k_i)\begin{bmatrix} 1 & 0 \\ 0 & 1 \end{bmatrix}_{2\times 2} = \begin{bmatrix} \bigcirc & & \bigcirc \\ & \begin{bmatrix} 1 & 0 \\ 0 & 1 \end{bmatrix} & \\ \bigcirc & & \bigcirc \end{bmatrix}_{2n\times 2n} \tag{22}$$

(*ii*) For the case where the inner radius is the design variable, i.e., $d_i = r_{Ii}$, one can obtain

$$\frac{\partial [B]}{\partial d_i} = \text{block}(r_{Ii})[M,\, r_{Ii}]_{8\times 8} - \text{block}(r_{Ii}[N,\, r_{Ii}]_{8\times 8} \tag{23}$$

$$\frac{\partial [A]}{\partial d_i} = \text{block}(r_{Ii})[K,\, r_{Ii}]_{8\times 8} \tag{24}$$

where

$$[M,\, r_{Ii}] = \left(\frac{-2r_{Ii}}{r_{oi}^2 - r_{Ii}^2} - \frac{2}{(1+\Phi)}\frac{\partial \Phi}{\partial r_{Ii}}\right)\bullet$$
$$([M]_o + \Phi[M]_1 + \Phi^2[M]_2) + ([M]_1 + 2\Phi[M]_2)\bullet \frac{\partial \Phi}{\partial r_{Ii}} \tag{25}$$

Table 1 Fixed rigid disk data

Station No.	Mass (Kg)	Polar Inertia (Kg - cm^2 x 10^{-2})	Diametral Inertia (Kg - cm^2 x 10^{-2})
1	11.38	19.53	9.82
4	7.88	16.70	8.35
5	7.7	17.61	8.80
12	21.7	44.48	22.24

Table 2 Initial configuration data of rotor system

Station No.	Axial Distance to Station 1(cm)	Shaft Element No.	Inner Radius (cm)	
			Example 1	Example 2
1	0.			
2	4.29	1	r_{Ii} = 1.68 i = 1, 12	1.882
3	8.89	2		1.940
4	10.49	3		1.466
5	20.17	4		1.660
6	27.69	5		2.151
7	44.20	6		2.690
8	59.44	7		2.690
9	74.68	8		2.690
10	89.92	9		2.690
11	105.16	10		2.690
12	120.14	11		1.420
13	127.94	12		1.880

Shaft Elastic Modulus $E = 20.69 \times 10^6$ N/cm^2
Density $\rho = 8193.0$ Kg/m^3
Outer Radius $r_{Oi} = 2.95$ cm i = 1, 12

$$[N,\, r_{Ii}] = \left(\frac{-4r_{Ii}^3}{r_{oi}^4 - r_{Ii}^4} - \frac{2}{(1+\Phi)} \bullet \frac{\partial \Phi}{\partial r_{Ii}}\right)\bullet$$
$$([N]_o + \Phi[N]_1 + \Phi^2[N]_2) + ([N]_1 + 2\Phi[N]_2)\bullet \frac{\partial \Phi}{\partial r_{Ii}} \tag{26}$$

$$[K,\, r_{Ii}] = \left(\frac{-4r_{Ii}^3}{r_{oi}^4 - r_{Ii}^4} - \frac{1}{(1+\Phi)}\frac{\partial \Phi}{\partial r_{Ii}}\right)\bullet$$
$$([K]_o + \Phi[K]_1) + [K]_1 \bullet \frac{\partial \Phi}{\partial r_{Ii}} \tag{27}$$

$$\Phi = \frac{3E}{\kappa' G l_i^2}(r_{oi}^2 + r_{Ii}^2) \tag{28}$$

The shear factor κ' (Cowper, 1966) is of the form

$$\kappa' = \frac{6(1+\mu)(1+\zeta^2)^2}{(7+6\mu)(1+\zeta^2)^2 + (20+12\mu)\zeta^2} \tag{29}$$

where μ is the Poisson ratio and $\zeta = r_{Ii}/r_{oi}$.

Differentiation of equation (29) with respect to r_{Ii} yields

$$\frac{\partial \Phi}{\partial r_{Ii}} = \frac{3Er_{oi}}{\kappa' G l_i^2}\left[2\zeta - \frac{(1+\zeta^2)}{\kappa'}\frac{\partial \kappa'}{\partial \zeta}\right] \tag{30}$$

If $\mu = 0.25$, one can express $\partial\kappa'/\partial\zeta$ as

$$\frac{\partial \kappa'}{\partial \zeta} = \frac{345(\zeta^4 - 1)\zeta}{[8.5(1+\zeta^2)^2 + 23\zeta^2]^2} \tag{31}$$

Numerical Results and Discussion

Based on the theoretical study, three optimization algorithms for two flexible rotor systems are selected for

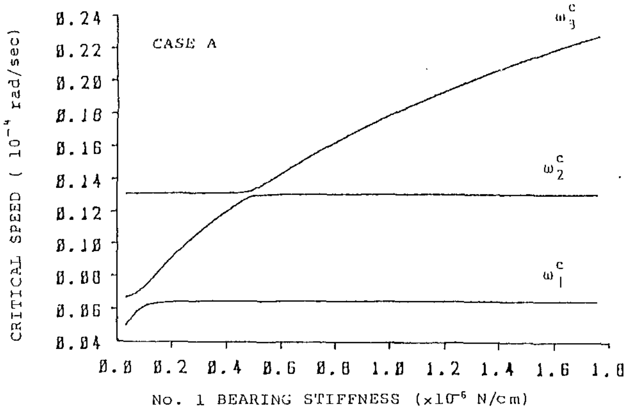

Fig. 4 The effect of No. 1 bearing stiffness on critical speed, $k_2 = k_3 = 1.75 \times 10^5$ N/cm

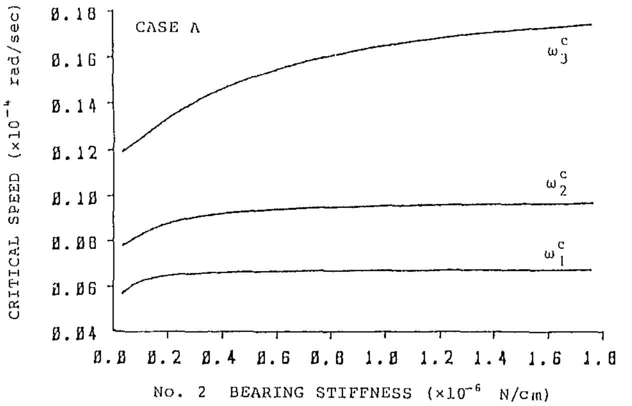

Fig. 5 The effect of No. 2 bearing stiffness on critical speed, $k_1 = k_3 = 1.75 \times 10^5$ N/cm

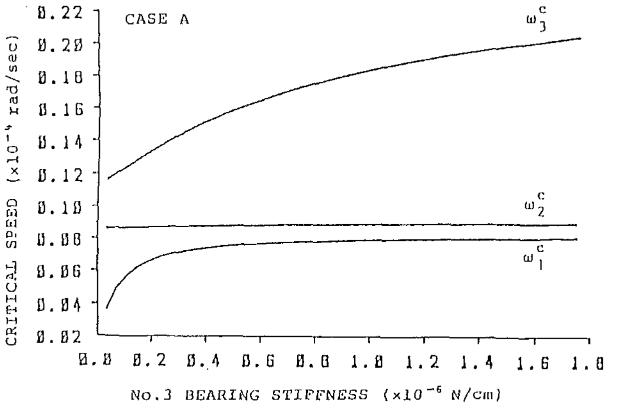

Fig. 6 The effect of No. 3 bearing stiffness on critical speed, $k_1 = k_2 = 1.75 \times 10^5$ N/cm

numerical investigation. Two algorithms, MFD and MMFD, are based on feasible direactions and a gradient projection method. The other algorithm is the SUMT based on the exterior penalty function method (EPFM). Figure 3 shows the rotor schematic of the system, which is composed of a single spool supported by bearings at stations 3, 6, and 13. The bearings are referred to as No. 1, No. 2, and No. 3, with corresponding stiffness k_1, k_2, and k_3. There are 12 elements, 13 stations, 26 degs of freedom for rotating reference shown in the model of Fig. 4. Four disks with fixed masses are located at stations 1, 4, 5, and 12. The details of rotor configuration

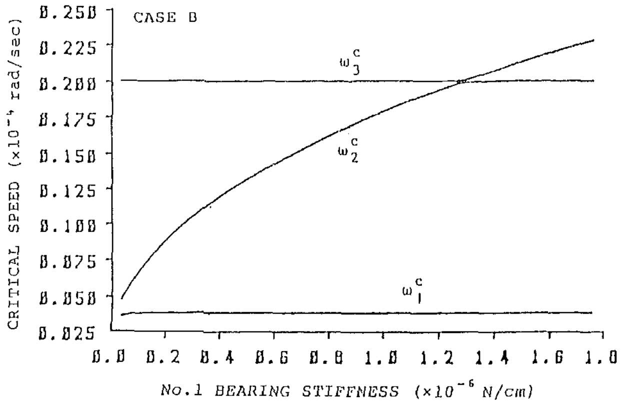

Fig. 7 The effect of No. 1 bearing stiffness on critical speed, $k_2 = 1.95 \times 10^5$ N/cm, $k_3 = 3.5 \times 10^4$ N/cm

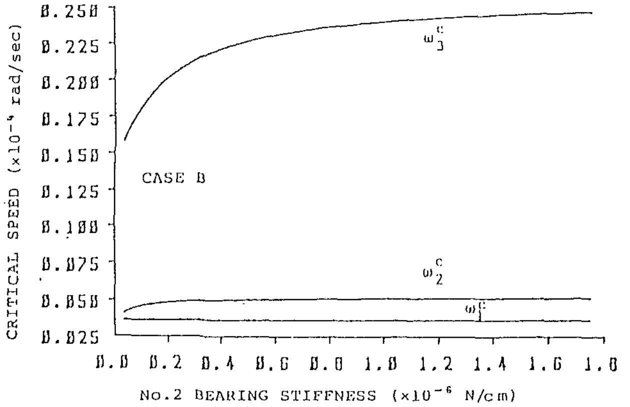

Fig. 8 The effect of No. 2 bearing stiffness on critical speed, $k_1 = k_3 = 3.5 \times 10^4$ N/cm

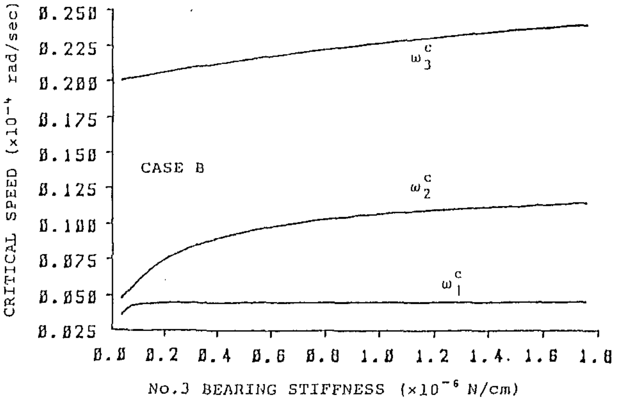

Fig. 9 The effect of No. 3 bearing stiffness on critical speed, $k_1 = 3.5 \times 10^4$ N/cm, $k_2 = 1.95 \times 10^5$ N/cm

data are listed in Tables 1 and 2. In addition, two sets of data, case A and case B, are indicated in Table 2.

Before doing the search of minimum weight of system, the choice of design variables has to be made. Obviously the system weight is very dependent on the radius of the shaft. Probably, the inner radius of shaft element is the most preferable parameter. But the effects of bearing coefficients on the critical speeds of system are pursued here and then chosen to be subset of the design variables. For case A, the effects of each bearing stiffness k_1, k_2, and k_3 on critical speeds, holding the stiffnesses of the rest bearings as constant, are shown in Figs. 4–6, respectively. Similarly, for case B, Figs.

Table 3 System data of final design of example 1: (3*a*) inner radius; (3*b*) bearing stiffness; (3*c*) other parameters

Shaft Element	Initial Inner Radius (cm)	Final Inner Radius (cm)	
		MFD	EPFM
1	$r_{Ii} = 1.68$ $i = 1, 12$	2.690	2.690
2		2.690	2.690
3		2.690	2.690
4		2.690	2.689
5		2.245	2.557
6		2.690	2.666
7		2.690	2.690
8		2.690	2.690
9		2.690	2.690
10		2.690	2.690
11		2.410	2.443
12		2.690	2.690

(3a)

Bearing No.	Initial (N/cm)	Final	
		MFD	EPF
1	1.75×10^5	3.50×10^4	3.53×10^4
2	1.75×10^5	1.36×10^6	1.75×10^6
3	1.75×10^5	3.50×10^4	1.26×10^5

(3b)

	Initial	Final	
		MFD	EPF
ω_2^c (rad/sec)	870.29	520.00	686.72
ω_3^c (rad/sec)	1316.54	2304.40	2301.90
Shaft Weight(Kg)	19.364	5.804	5.508
Computation Time VAX - 8600 CPU (Sec)		137.62	146.68

(3c)

Table 4 System data of final design of example 2: (4*a*) inner radius; (4*b*) bearing stiffness; (4*c*) other parameters

Shaft Element	Initial Inner Radius (cm)	Final Inner Radius (cm)	
		MMFD	EPFM
1	1.882	1.989	2.690
2	1.940	1.778	2.690
3	1.466	1.504	2.674
4	1.660	2.504	2.512
5	2.151	2.406	2.632
6	2.690	2.690	2.690
7	2.690	2.690	2.690
8	2.690	2.690	2.690
9	2.690	2.690	2.690
10	2.690	2.690	2.690
11	1.420	2.204	2.384
12	1.880	2.067	2.690

(4a)

Bearing No.	Initial Stiffness (N/cm)	Final Stiffness (N/cm)	
		MMFD	EPFM
1	3.50×10^4	3.50×10^4	3.54×10^4
2	9.45×10^5	9.45×10^5	1.06×10^6
3	3.50×10^4	3.61×10^4	1.28×10^5

(4b)

	Initial	Final	
		MMFD	EPFM
ω_2^c (rad/sec)	511.28	691.67	691.64
ω_3^c (rad/sec)	2390.99	2301.00	2300.81
Shaft Weight (Kg)	10.235	7.911	5.759
VAX - 8600 CPU (Sec)		32.08	120.16

(4c)

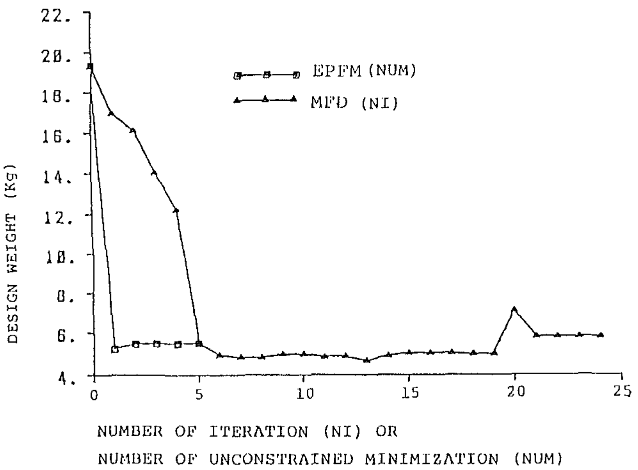

Fig. 10 The comparison of weight of the design history for example 1

7-9 show the effects of each bearing stiffness on the critical speeds. The results shown in Figs. 4-9 indicate that the critical speeds may greatly rely on the bearing stiffness. The changes of bearing stiffness may lead to considerably different optimum designs. This study gives the selection of shaft inner radius and bearing stiffnesses as the system design variables.

Three examples are used to illustrate the minimum weight design procedures of rotor systems. The outer radius is held at constant value $r_{oi} = 2.95$ cm, $i = 1, \ldots, 12$ and the low end and high end of operating range are given by

$$\Omega_{\text{low}} = 830.0 \text{ rad/s}, \; \Omega_{\text{high}} = 1770.0 \text{ rad/s}$$

The constants a_1 and a_2 shown in equatons (10*a*) and (10*b*) are chosen such that the second critical speed ω_2^c is at least lower than Ω_{low} by a factor of 1.2, while the first bending mode is at least 30 percent higher than the high end of rotational speed range, i.e., $a_1 = 1.2$, $a_2 = 1.3$. In this case, the behavior constraints of critical speeds can be written as

$$g_1(\mathbf{d}) = \omega_2^c - 691.67 \text{ rad/s} \leq 0 \qquad (32)$$

$$g_2(\mathbf{d}) = 2301.00 \text{ rad/s} - \omega_3^c \leq 0 \qquad (33)$$

The side constraints of the design variables are given by

$$1.42 \text{ cm} \leq r_{Ii} \leq 2.69 \text{ cm}, \; i = 1, 12 \qquad (34)$$

$$3.50 \times 10^4 \text{ N/cm} \leq k_i \leq 1.75 \times 10^6 \text{ N/cm}, \; i = 1, 3 \qquad (35)$$

The behavior constraints stated by equations (32) and (33) and the side constraints of equations (34) and (35) are considered as the system design constraints for all three examples in this paper. The computing system used in this study is VAX-8600.

Example 1. This example concerns a flexible rotor system with data listed in Table 2 for case A, i.e., the initial inner radii are all the same: $r_{Ii} = 1.68$ cm, $i = 1, \ldots, 12$ and the initial bearing stiffnesses are $k_i = 1.75 \times 10^5$ N/cm, $i = 1, 2, 3$. The optimization techniques of MFD and EPFM are employed to find the optimum design of the system. The designs at optimum stage using MFD and EPFM are listed in Table 3. The weight of this system is significantly reduced when the optimum is reached as indicated in Table 3. The comparison of weight of design history is shown in Fig. 10.

Example 2. The data listed in Table 2 for case B are considered in this example. The initial inner radius and bearing stiffness and their final design values using MMFD and EPFM are given in Table 4. The results show that the computing time using MMFD is much smaller than that using EPFM. However, the optimum weight obtained using MMFD is greater than that using EPFM. The weight design histories using both MMFD and EPFM are shown in Fig. 11. The weight is reduced as the optimum is reached.

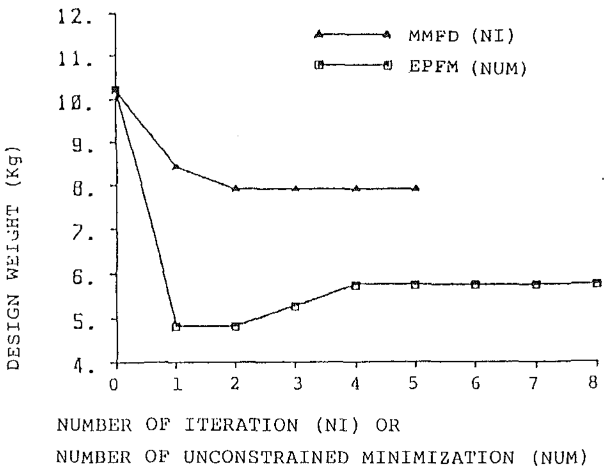

Fig. 11 The comparison of weight of the design history for example 2

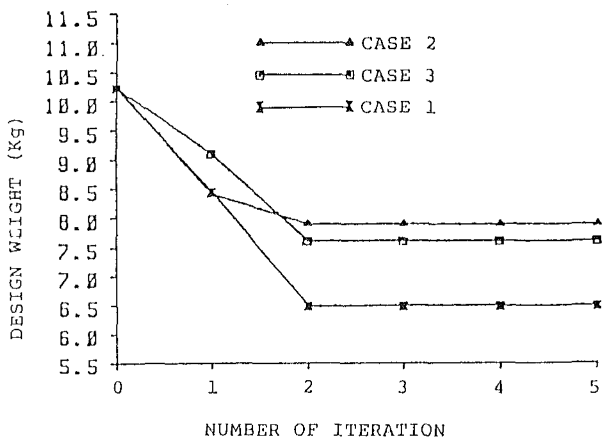

Fig. 12 The comparison of weight of the design history for example 3

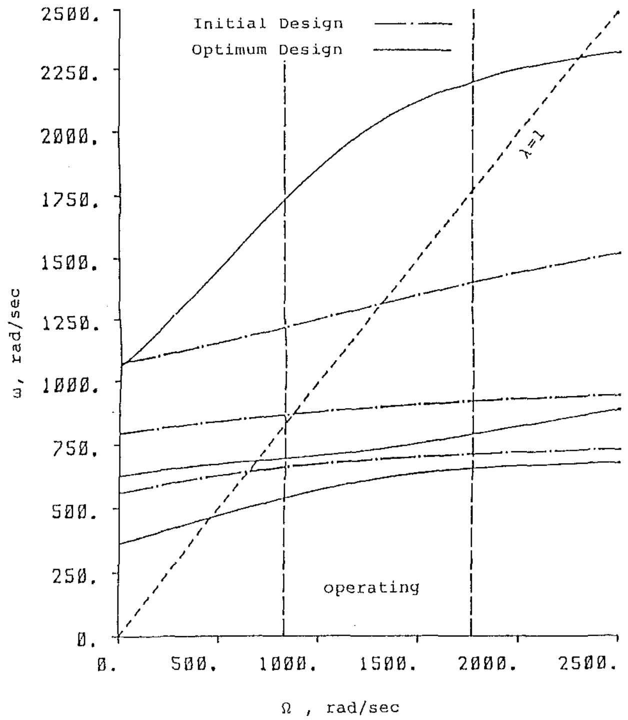

Fig. 13 Whirl speed maps of initial design and optimum design

Table 5 Initial data for example 3

	Case 1	Case 2	Case 3
k_1 (N/cm)	7.59×10^4	3.50×10^4	3.50×10^4
k_2 (N/cm)	1.15×10^6	9.45×10^5	1.27×10^6
k_3 (N/cm)	4.60×10^4	3.50×10^4	1.28×10^5
ω_2^c (rad/sec)	672.72	511.28	688.65
ω_3^c (rad/sec)	2429.52	2390.99	2448.14

Table 6 Final design data for example 3: (6*a*) inner radius; (6*b*) bearing stiffness; (6*c*) other parameters

Shaft Element	Final Inner Radius (cm), MMFD		
	Case 1	Case 2	Case 3
1	2.098	1.989	2.182
2	2.690	1.778	1.942
3	1.420	1.504	1.619
4	2.686	2.504	2.155
5	2.685	2.406	2.690
6	2.690	2.690	2.690
7	2.690	2.690	2.690
8	2.690	2.690	2.690
9	2.690	2.690	2.690
10	2.690	2.690	2.690
11	2.074	2.204	2.241
12	2.690	2.067	2.268

(6a)

	Final Bearing Stiffness (N/cm)		
k_1	7.79×10^4	3.50×10^4	3.50×10^4
k_2	1.15×10^6	9.45×10^5	1.27×10^6
k_3	1.08×10^5	3.61×10^4	1.27×10^5

(6b)

ω_2^c (rad/sec)	691.67	691.67	691.67
ω_3^c (rad/sec)	2301.00	2301.00	2301.00
Shaft Weight (Kg)	6.499	7.911	7.622
VAX-8600 CPU (sec)	29.02	32.08	19.48

(6c)

Example 3. Three cases are considered in this example for studying the effect of different initial bearing stiffnesses on the optimum design. The data given in case 2 are the same as those given in example 2. The initial bearing stiffnesses and critical speeds of original system are listed in Table 5. The final design data are indicated in Table 6.

Figure 12 shows the comparison of weight of design history for these three cases. The results indicate that the optimum weight depends on the chosen initial design. The local minimum designs may exist in these cases. It is required that all the constraints have to be satisfied at the optimum stage. The satisfactory requirement can be seen from the whirl speed maps of Fig. 13. It shows the precession speeds for the preliminary design and final design of system. The mode shapes of preliminary and final designs are also shown in Fig. 14 for case A.

Conclusions

The minimum weight design of an undamped, isotropic bearing supported rotor system with consideration of constraints on multiple natural frequency has been investigated. Optimization of the system is cast into a nonlinear mathematical programming problem. Three examples are studied and the results show that the weight of rotor system

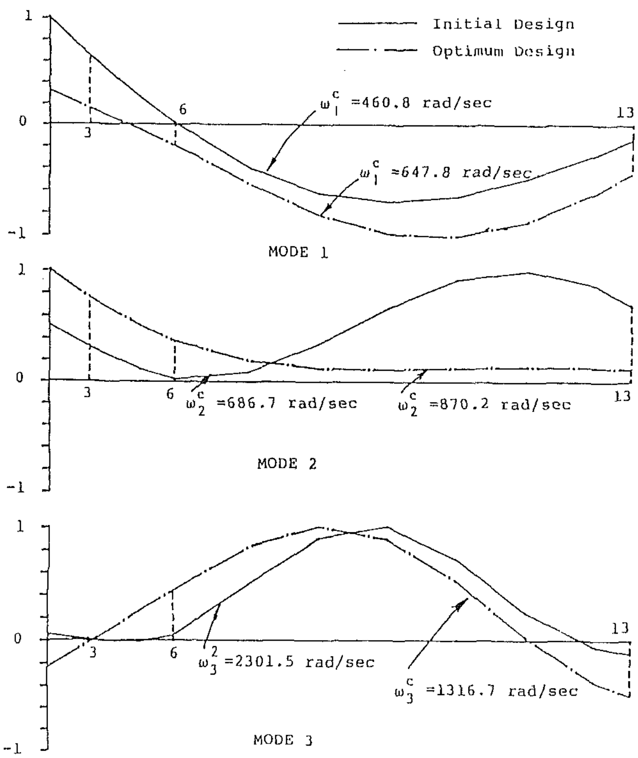

Fig. 14 Mode shapes of initial and optimum designs for Case A

can be significantly reduced when the optimum is reached. Because of the nonlinearity of constraint function, the algorithm of MMFD may be not a very appropriate one unless the computing time is a concern. When the MFD algorithm is employed, the method of the increase of design variables presented in this paper can be directly applied without taking care of infeasible initial designs. The careful choice of bearing stiffness and different initial design values may lead to a lot of weight saving.

References

Childs, D. W., and Graviss, K., 1982, "A Note on Critical Speed Solutions for Finite-Element-Based Rotor Models," ASME *Journal of Mechanical Design*, Vol. 104, pp. 412-416.

Cowper, G. R., 1966, "The Shear Coefficient in Timoshenko's Beam Theory," ASME *Journal of Applied Mechanics*, Vol. 33, pp. 335-341.

Dworski, J., 1964, "High-Speed Rotor Suspension Formed by Fully Floating Hydrodynamic Radial and Thrust Bearings," ASME JOURNAL OF ENGINEERING FOR POWER, Vol. 86, No. 2, pp. 149-160.

Fritzen, C. P., and Nordman, R., 1982, "Influence of Parameter Changes to Stability Behavior of Rotor," NASA Conference Publication 2250, *Rotor-Dynamic Instability Problems in High-Performance Turbomachinery*, Texas A & M University, College Station, TX, pp. 284-297.

Fox, R. L., and Kapoor, M. P., 1968, "Rates of Change of Eigenvalues and Eigenvectors," *AIAA Journal*, Vol. 6, No. 12, pp. 2426-2429.

Gunter, E. J., 1970, "Influence of Flexibility Mounted Rolling Element Bearings on Rotor Response, Part 1: Linear Analysis," ASME *Journal of Lubrication Technology*, Vol. 92, No. 1, pp. 59-75.

Haug, E. J., Pan, K. C., and Strecter, T. C., 1972, "A Computational Method for Optimal Structural Design. I. Piecewise Uniform Structures," *Int. J. Num. Meth. Engng.*, Vol. 5, pp. 171-184.

Kane, T. R., and Levinson, D. A., 1985, *Dynamics: Theory and Applications*, McGraw-Hill, New York.

Lund, J. W., and Sternlicht, B., 1962, "Rotor-Bearing Dynamics With Emphasis on Attenuation," ASME *Journal of Basic Engineering*, Vol. 84, No. 4, pp. 491-502.

Lund, J. W., 1963, "Attenuation of Bearing Transmitted Noise—Vol. 2, Part 1: Attenuation of Rotor Unbalance Forces by Flexible Bearing Supports," Report No. EC232, Bureau of Ships, Contract No. BS-86914.

Lund, J. W., 1979, "Sensitivity of the Critical Speeds of a Rotor to Changes in Design," ASME *Journal of Mechanical Design*, Vol. 102, pp. 115-121.

Nelson, H. D., and McVaugh, J. M., 1976, "The Dynamics of Rotor Bearing Systems Using Finite Elements," ASME *Journal of Engineering for Industry*, Vol. 93, No. 2, pp. 593-600.

Nelson, H. D., 1980, "A Finite Rotating Shaft Element Using Timoshenko Beam Theory," ASME *Journal of Mechanical Design*, Vol. 102, pp. 793-804.

Plaut, R. H., and Huseyin, K., 1973, "Derivatives of Eigenvalues and Eigenvectors in Non-Self-Adjoint Systems," *AIAA Journal*, Vol. 11, No. 2, pp. 250-251.

Rajan, M., Nelson, H. D., and Chen, W. J., 1986, "Parameter Sensitivity in Dynamics of Rotor-Bearing Systems," ASME *Journal of Vibration, Acoustics, Stress, and Reliability in Design*, Vol. 108, No. 2, pp. 197-206.

Rajan, M., Rajan, S. D., Nelson, H. D., and Chen, W. J., 1987, "Optimal Placement of Critical Speed in Rotor Bearing System," ASME *Journal of Vibration, Acoustics, Stress, and Reliability in Design*, Vol. 109, pp. 152-157.

Schmit, L. A., and Farshi, B., 1974, "Some Approximation Concepts for Structural Synthesis," *AIAA Journal*, Vol. 12, No. 5, pp. 692-699.

Vanderplaats, G. N., 1982, "Structural Optimization Past, Present, and Future," *AIAA Journal*, Vol. 20, No. 7, pp. 992-998.

Venkayya, V. B., 1971, "Design of Optimum Structures," *International Journal of Computers and Structures*, Vol. 1, pp. 265-309.

Venkayya, V. B., Khot, N. S., and Berke, L., 1973, "Application of Optimality Criteria Approaches to Automated Design of Large Practical Structures," presented at AGARD Second Symposium on Structural Optimization, Milan, Italy.

Impact Excitation Tests to Determine the Influence Coefficients for Balancing Lightly Damped Rotors

J. Tonnesen

J. W. Lund

Department of Machine Elements,
The Technical University of Denmark,
DK-2800 Lyngby, Denmark

Experiments have been conducted to evaluate a supplementary method for balancing lightly damped rotors. The rotor, while running, is excited by an impact generator, and the response is measured at the bearings by transducers for displacement, force, and acceleration. An FFT analyzer is employed to obtain the frequency-dependent transfer functions from which the corresponding influence coefficients can be calculated. The results are compared with the values obtained from the conventional trial weight method, and they are also used in a successful balancing of the rotor.

Introduction

In balancing a flexible rotor, a common procedure is to determine the correction weights from measured influence coefficients (Goodman, 1964; Lund and Tonnesen, 1972). The measurements are obtained by inserting trial weights, one at a time, in the respective balancing planes. As this may be time consuming, an alternative method is investigated where the influence coefficients are found from impacting the rotor.

The impact method has been used in previous investigations (Glienicke, 1966; Morton, 1974; Normann and Scholhorn, 1980), but primarily for the purpose of determining the dynamic characteristics of the bearings. In the present tests, a Fourier transform analysis of the impact force and the response signals is used to compute the transfer functions from which the influence coefficients for balancing are derived. They are compared with the results obtained by inserting trial weights and subsequently employed in a balance correction.

Description of Test Rig. The test rotor is shown schematically in Fig. 1. The rotor consists of a shaft with a basic diameter of 35 mm, an overall length of 1.085 m, and a bearing span of 0.785 m. The rotor configuration is symmetric with most of its mass concentrated in three disks mounted on the shaft between the bearings. The common diameter of the disks is 0.2 m, the thickness of the central disk is 70 mm, while the disks next to the bearings are 110 mm thick. A slight asymmetry is caused by the coupling end overhang being only 82.5 mm (outboard of bearing 1) while the free end overhang (outboard of bearing 2) is 217.5 mm. Each of the disks has circumferential grooves cut in the sides in which weights can be inserted for balancing purposes.

The rotor is supported in two identical standard deep groove ball bearings, which are axially preloaded and grease lubricated. The bearing housings are bolted to the bearing pedestal structure and the mechanical layout of the pedestals is such that the stiffness in the horizontal direction is much weaker than in the vertical direction. The pedestals are bolted to a 2000 kg steel plate, which rests on rubber pads on a concrete foundation.

The rotor is connected through a floating double-diaphragm type coupling to a d-c motor, which can be controlled to maintain a selected speed within 0.2 percent.

The rotor system mass is 65.3 kg and the reactions at the bearings rate 314 N at bearing No. 1 and 327 N at bearing No. 2. The maximum speed of the test rig is 200 Hz and the critical speeds of the rotor system have been measured to be:

1st	critical horizontally:	36.0 Hz
1st	critical vertically:	38.7 Hz
2nd	critical horizontally:	120.0 Hz
2nd	critical vertically:	133.5 Hz

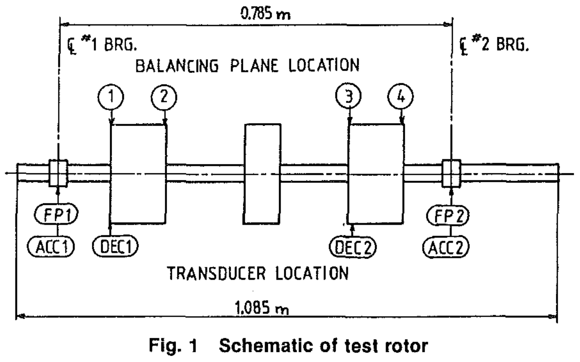

Fig. 1 Schematic of test rotor

Contributed by the International Gas Turbine Institute and presented at the 33rd International Gas Turbine and Aeroengine Congress and Exhibition, Amsterdam, The Netherlands, June 5–9, 1988. Manuscript received by the International Gas Turbine Institute September 1987. Paper No. 88-GT-75.

Instrumentation. The rotor is excited by an impact generator consisting of a spring-loaded piston in a pressurized air-bearing and a release mechanism. The piston impacts the rotor through a piezo-electric force transducer and a relatively soft and curved cap, the selected cap material being a compromise between the required frequency response span and the ability to withstand the sliding speeds of the rotor without being worn flat too quickly. The impact generator is calibrated by impacting a reference mass to which a calibrated accelerometer is attached.

The response of the rotor system is measured on and near the bearing pedestals. On the bearing pedestals are installed piezo-electric transducers measuring the transmitted force and acceleration. The rotor displacement is measured by eddy current type noncontacting displacement transducers placed at impact planes PL1 and PL3. All the transducers sense the response in the horizontal direction. An FFT analyzer is employed to obtain the frequency dependent transfer functions.

The rotational speed of the shaft is measured by a photoelectric tachometer probe, which is activated by markings painted on the shaft. The same markings provide also the reference phase information.

Analysis

A harmonic signal a with frequency ω can be expressed as

$$a = a_c \cos \omega t - a_s \sin \omega t = \mathrm{Re}\{ (a_c + ia_s) e^{i\omega t} \} \tag{1}$$

By adopting the conventional complex notation, equation (1) may be written formally as

$$a = a_c + ia_s \tag{2}$$

with exp $(i\omega t)$ and the real part operator implied.

The rotor is assumed to behave linearly such that if it is excited by harmonic forces f_x and f_y in orthogonal directions, the resulting response becomes

$$a = H_{ax} f_x + H_{ay} f_y \tag{3}$$

where the H are transfer functions. They are complex and depend on frequency.

In the rotor there is a fixed reference coordinate system with a 1-axis and a 2-axis, located by means of the markings painted on the rotor. Thus, any mass imbalance can be specified by its two components U_1 and U_2, and the corresponding mass imbalance forces at the rotational frequency Ω become

$$\begin{aligned} f_x &= \Omega^2 (U_1 \cos \Omega t - U_2 \sin \Omega t) \sim \Omega^2 U \\ f_y &= \Omega^2 (U_1 \sin \Omega t + U_2 \cos \Omega t) \sim - i\Omega^2 U \end{aligned} \tag{4}$$

where

$$U = U_1 + iU_2 \tag{5}$$

Upon substitution into equation (3) it is found that

$$a = H_{au} U \tag{6}$$

where

$$H_{au} = \Omega^2 (H_{ax} - iH_{ay}) \tag{7}$$

H_{au} is the transfer function (influence coefficient) to be used in balancing the rotor.

The transfer functions H_{ax} and H_{ay} are determined by impacting the rotor at the balancing planes and by performing a Fourier transform analysis of the response. If the Fourier transforms of a and f_x are A and F_x, respectively, then the analyzer obtains H_{ax} as

$$H_{ax} = \frac{S_{xa}}{S_{xx}} = \frac{S_{aa}}{S_{ax}} \tag{8}$$

where S_{xx} and S_{aa} are the auto-spectral densities, and S_{xa} and S_{ax} are the cross-spectral densities:

$$\begin{aligned} S_{aa} &= \lim_{T \to \infty} \left\{ \frac{2}{T} \bar{A} A \right\} \\ S_{ax} &= \lim_{T \to \infty} \left\{ \frac{2}{T} \bar{A} F_x \right\} \end{aligned} \tag{9}$$

and analogously for S_{xx} and S_{xa}. $\bar{A}$ is the complex conjugate of A, and T is the time length of the recorded signal.

The transfer functions depend on speed because of the influence from gyroscopic moments and changing bearing characteristics. Hence, in equation (7) H_{ax} and H_{ay} should be evaluated at the desired balancing speed and at synchronous frequency $(\omega = \Omega)$. At that frequency, however, the response has a strong component a_0, caused by the existing unbalance in the rotor, and that component must be subtracted out of the measured response a in order to get the net signal, due solely to the impact excitation:

$$a - a_0 = H_{ax} f_x \qquad (f_y = 0) \tag{10}$$

such that H_{ax} should be computed as

$$H_{ax} = \frac{S_{xa} - S_{xa0}}{S_{xx}} = (H_{ax})_{\mathrm{meas}} - (H_{ax})_0 \tag{11}$$

Here, S_{xa0} is the cross spectrum between f_x and a_0, and $(H_{ax})_0$ the corresponding transfer function where the f_x signal is obtained, not from impacting the rotor, of course, but some other surface that will produce an identical impulse signal.

At the same time it is necessary to synchronize the force with the reference system in the rotor. For this purpose the impact generator is provided with a release mechanism, which can be triggered by means of the markings on the rotor.

Subsequent tests demonstrated the workability of the idea, but it was not found possible to supply enough impact energy to the rotor to get the difference between the two measured H_{ax} values in equation (11) significantly above the measurement tolerances. The scheme was therefore abandoned and, although in principle this is not correct, H_{ax} and H_{ay} are instead measured at nonsynchronous frequencies as discussed later.

An additional concern is the potential error introduced by the friction between the impact head and the rotating shaft (and the "smearing-out" of the impact force). Thus, in the force reference x-y coordinate system with rotation positive from the x axis toward the y axis the actual force directions will be along axes in a ζ-η coordinate system, rotated an angle γ in the positive direction:

$$\begin{aligned} f_x &= f_\zeta \cos \gamma - f_\eta \sin \gamma \\ f_y &= f_\zeta \sin \gamma + f_\eta \cos \gamma \end{aligned} \tag{12}$$

where f_ζ and f_η are the measured forces. The measured signal can be expressed as

$$a = H_{a\zeta} f_\zeta + H_{a\eta} f_\eta \tag{13}$$

where $H_{a\zeta}$ and $H_{a\eta}$ become the meaured transfer functions. By substitution of equation (12) into equation (3), by comparison with equation (13), and by making use of equation (7) it is found that

$$H_{au} = \Omega^2 (H_{a\zeta} - iH_{a\eta}) e^{-i\gamma} \tag{14}$$

Hence, it is necessary to correct the measured phase angle:

$$\phi = \tan^{-1} [\mathrm{Im}\{ H_{a\zeta} - iH_{a\eta} \} / \mathrm{Re}\{ H_{a\zeta} - iH_{a\eta} \}] \tag{15}$$

by subtracting the friction angle γ. This correction, however, has not been carried out because the test results are inconclusive as to establishing a consistent value of γ.

Experimental Procedure. As the purpose of the test program is to evaluate the accuracy of the calculated influence coefficients found from the impact excitation, the procedure adopted for the tests consists of impact exciting the rotor at the same positions where the balance correction weights are installed. A comparison between the calculated influence coefficients and those found from the conventional method of placing trial weights gives a direct check on the accuracy of the method.

The impacting or balance weight planes are numbered PL1 to PL4 as shown in Fig. 1. The measurements for impacting are taken with the rotor at standstill and running at 13.5 Hz and 87 Hz, these speeds being well below an associated critical speed.

The response measurements are taken at frequencies as close as possible to the critical speed frequencies and several points are chosen, so if the rotor cannot be operated to the highest selected response frequency, the next lower is used and so on. For the first critical speeds are selected 30.5, 32.5, and 34.5 Hz and for the second critical speed are selected 111.5, 115, and 117 Hz. Figure 2 shows some typical response curves from which the data are obtained at the selected frequencies. Whereas the measurements with the force and displacement transducers are taken at all six response frequencies, the signals from the accelerometers are too weak at the three lowest response frequencies to be of any use.

The measurements for the trial weight runs are taken at the six response frequencies just mentioned. However, prior to the actual test program, the rotor is balanced as well as possible. This is done only to ensure a sufficiently low level of vibration to allow installation of a sufficiently large trial weight while still being able to pass the first critical speed. This reference rotor runs smoothly through the two horizontal critical speeds; however, pronounced resonant peaks are observed at the vertical speeds. The phenomenon is caused by the rotor being very lightly damped and some local foundation plate resonances coinciding with the rotor's vertical critical speeds. As such it has nothing to do with the method.

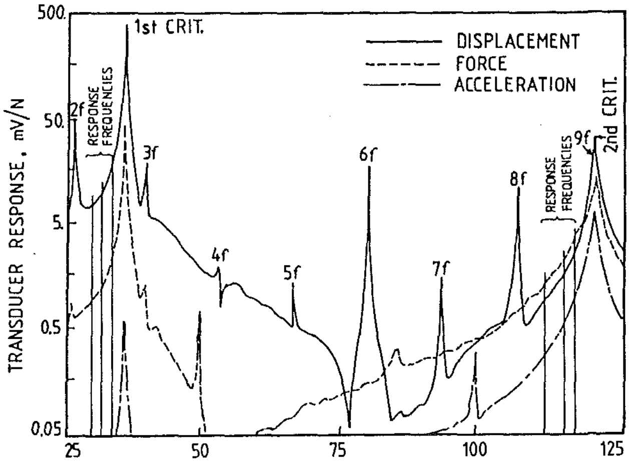

Fig. 2 Measured transfer functions

The same trial weight is used in all the tests. It weighs 1.53 g and is located on a 60 mm radius. In order to eliminate the nonlinear behavior normally originating from rolling element bearings the trial weight is positioned at four angular positions, 90 deg apart, and the four measurements are averaged.

Finally the rotor is balanced, using first the influence coefficients from the trial weights and afterward for comparison, the calculated impact influence coefficients, and in both cases the rotor's original unbalance condition is used. The rotor is first balanced at 32.5 Hz using balancing planes Nos. 2 and 3, and final balancing is done at 32.5 Hz and 115 Hz using balancing planes Nos. 1 and 4 and the calculated influence coefficients from both the cases where the rotor is run at 13.5 Hz and 87 Hz.

Experimental Results. The results for the calculated influence coefficients are summarized in tables Nos. 1 to 3, where they are compared directly to the influence coefficients obtained from the conventional trial weight method. In the calculations the influence coefficients are evaluated on the basis of two test series, where in the first series the impact excitation direction is in the horizontal and vertical planes, and in the second series where the direction is displaced 45 deg. It is the average of the two test series that is shown in the tables. The average deviation between the two series is approximately 6 percent on the amplitudes and 3 deg on the phase.

The results of some typical balancing tests are summarized in Table 4 and typical residual vibrations are shown in Fig. 3.

The table shows the reduction of the vibration amplitudes expressed as the ratio between the rms uncorrected vibration amplitudes and the rms residual amplitudes based on measurement taken at 32.5 Hz and 115 Hz and using balancing planes Nos. 1 and 4. Trial weight influence coefficients were used in all cases for balancing at 32.5 Hz. The final balancing at 115 Hz could be done in one run but on the average two runs were required before the rotor could pass the second critical speeds safely and operate up to 200 Hz.

Discussion of Results. It is seen from Tables 1 to 3 that the impact influence coefficients, generally speaking, are speed

Table 1

TRANSDUCER TYPE: ACCELEROMETER, PIEZO-ELECTRIC

		BEARING #1								BEARING #2							
		IMPACT INFLUENCE COEFFICIENTS						TRIAL WEIGHT INFLUENCE COEFFICIENTS		IMPACT INFLUENCE COEFFICIENTS						TRIAL WEIGHT INFLUENCE COEFFICIENTS	
ROTOR SPEED WHEN IMPACTING; Hz.		0		13.5		87				0		13.5		87			
RESPONSE FREQ.Hz.	IMPACT OR T.W. POSITION	AMPL. µV/N	PHASE DEG.	AMPL. µV/N	PHASE DEG.	AMPL. µV/N	PHASE DEG.	AMPL. µV/N	PHASE DEG.	AMPL. µV/N	PHASE DEG.	AMPL. µV/N	PHASE DEG.	AMPL. µV/N	PHASE DEG.	AMPL. µV/N	PHASE DEG.
111.5	PL1	163.	175.2	170.	-175.3	150.	-178.9	143.	178.6	184.	2.4	167.	2.2	161.	2.5	156.	-1.1
	PL2	143.	178.7	148.	183.5	119.	182.4	117.	179.4	211.	2.1	213.	3.5	188.	-0.6	181.	-0.8
	PL3	161.	1.9	136.	6.4	129.	-0.9	129.	-0.5	189.	176.2	181.	177.2	160.	179.1	151.	179.9
	PL4	145.	-2.7	123.	8.3	125.	-2.0	120.	0	233.	180.4	214.	-174.2	217.	-179.4	202.	179.2
115.	PL1	227.	183.3	230.	181.6	215.	180.3	214.	178.8	280.	-1.7	273.	0.7	241.	0.3	247.	-2.0
	PL2	206.	181.6	230.	178.9	184.	-177.0	186.	179.6	327.	-1.5	313.	4.9	267.	-0.8	278.	-1.2
	PL3	234.	-2.3	210.	2.6	196.	-1.7	195.	-0.3	302.	-179.5	282.	177.6	243.	178.6	241.	178.9
	PL4	203.	0.2	216.	6.4	184.	-5.5	188.	-0.5	353.	180.6	303.	-176.9	312	-177.7	304.	178.9
117.	PL1	326.	179.0	325	181.2	284.	179.8	320.	176.8	390.	-3.7	379.	7.9	336.	-5.5	394.	-5.3
	PL2	309.	177.9	319.	180.6	288.	179.9	291.	177.7	451.	-3.3	434.	0.6	415.	-1.3	425.	-3.1
	PL3	316.	-3.5	292.	1.1	271.	-4.1	287.	-3.3	427.	177.3	381.	-179.0	353.	170.3	380.	176.8
	PL4	306.	-0.4	259.	4.1	283.	-2.3	291.	-3.5	463.	177.1	417.	-177.8	448.	-178.6	455.	175.2

Table 2

TRANSDUCER TYPE: FORCE, PIEZO-ELECTRIC																	
		BEARING #1								BEARING #2							
		IMPACT INFLUENCE COEFFICIENTS						TRIAL WEIGHT		IMPACT INFLUENCE COEFFICIENTS						TRIAL WEIGHT	
ROTOR SPEED WHEN IMPACTING; Hz.		0		13.5		87		INFLUENCE COEFFICIENTS		0		13.5		87		INFLUENCE COEFFICIENTS	
RESPONSE	IMPACT OR T.W.	AMPL.	PHASE	AMPL.	PHASE	AMPL.	PHASE	AMPL.	PHASE	AMPL.	PHASE	AMPL.	PHASE	AMPL.	PHASE	AMPL.	PHASE
FREQ.Hz.	POSITION	µV/N	DEG.	µV/N	DEG.	µV/N	DEG.	µV/N	DEG.	µV/N	DEG.	µV/N	DEG.	µV/N	DEG.	µV/N	DEG:
30.5	PL1	384.	-2.7	306.	-3.7			247.	-0.8	419.	2.6	306.	-3.1			258.	7.2
	PL2	396.	-0.3	324.	3.3			280.	-0.4	656.	5.1	529.	1.9			449.	6.6
	PL3	278.	-2.5	204.	-4.4			196.	-2.9	924.	3.8	672.	2.1			693.	3.0
	PL4	186.	-9.9	127.	-12.2			107.	1.8	839.	5.5	587.	4.1			595.	4.1
32.5	PL1	474.	0.6	407.	6.8			359.	5.1	635.	4.7	560.	18.5			506.	9.5
	PL2	532.	3.0	465.	11.6			459.	6.5	988.	6.8	904.	12.2			839.	9.9
	PL3	405.	4.6	322.	17.8			367.	8.7	1372.	4.7	1090.	17.2			1093.	7.9
	PL4	274.	0.8	262.	28.9			231.	10.5	1241.	0.5	897.	16.4			875.	7.1
34.5	PL1	720.	-0.3	586.	12.3			609.	2.9	1248.	0.9	1038.	13.0			1051.	5.2
	PL2	967.	1.1	805.	11.3			879.	5.1	1959.	3.7	1676.	15.1			1768.	6.5
	PL3	870.	4.4	677.	9.3			777.	5.0	2285.	2.5	1817.	10.8			2035.	5.4
	PL4	553.	0.2	411.	10.9			498.	5.7	1767.	-3.0	1319.	13.0			1500.	5.4
111.5	PL1	400.	-4.6	402.	3.1	365.	1.5	341.	-0.9	745.	179.5	701.	-176.5	663.	-179.4	632.	179.8
	PL2	342.	-3.3	331.	0.3	292.	-0.2	276.	-0.4	841.	-179.0	858.	-176.9	758.	-177.2	739.	180.5
	PL3	362.	179.9	337.	-173.5	317.	-178.5	301.	179.8	783.	-0.3	706.	4.2	669.	3.1	626.	0.8
	PL4	327.	179.9	319.	-167.9	320.	-173.3	278.	179.8	978.	1.6	973.	5.1	867.	-1.7	846.	0.5
115.	PL1	522.	0.1	512.	3.6	489.	-0.6	471.	-1.0	1055.	-178.9	1059.	-174.9	908.	-179.4	934.	179.5
	PL2	486.	-2.7	504.	0.7	443.	1.7	414.	-0.5	1227.	180.0	1165.	-176.1	1105.	-177.9	1063.	180.2
	PL3	509.	177.4	484.	-175.9	433.	-176.5	429.	179.8	1182.	0.3	980.	8.0	976.	2.0	938.	0.4
	PL4	475.	-178.5	470.	-168.6	454.	-178.2	410.	179.5	1375.	0.3	1218.	7.7	1188.	1.9	1179.	0.2
117.	PL1	685.	-3.5	645.	5.7	637.	-3.1	671.	-3.0	1426.	178.3	1384.	-174.0	1198.	176.3	1420.	176.4
	PL2	660.	-1.1	625.	1.2	570.	0.5	617.	-1.9	1650.	178.7	1486.	-175.6	1438.	-178.3	1553.	178.5
	PL3	662.	178.7	668.	-174.2	595.	178.3	609.	177.5	1544.	-1.9	1560.	3.6	1274.	1.2	1383.	-2.2
	PL4	649.	178.9	628.	-173.4	616.	178.8	609.	176.5	1743.	-1.4	1641.	10.8	1731.	-3.9	1681.	-2.9

Table 3

TRANSDUCER TYPE: DISPLACEMENT, EDDY CURRENT																	
		BEARING #1								BEARING #2							
		IMPACT INFLUENCE COEFFICIENTS						TRIAL WEIGHT		IMPACT INFLUENCE COEFFICIENTS						TRIAL WEIGHT	
ROTOR SPEED WHEN IMPACTING; Hz.		0		13.5		87		INFLUENCE COEFFICIENTS		0		13.5		87		INFLUENCE COEFFICIENTS	
RESPONSE	IMPACT OR T.W.	AMPL.	PHASE	AMPL.	PHASE	AMPL.	PHASE	AMPL.	PHASE	AMPL.	PHASE	AMPL.	PHASE	AMPL.	PHASE	AMPL.	PHASE
FREQ.Hz.	POSITION	µV/N	DEG.	µV/N	DEG.	µV/N	DEG.	µV/N	DEG.	µV/N	DEG.	µV/N	DEG.	µV/N	DEG.	µV/N	DEG.
30.5	PL1	2839.	2.3	2318.	7.8			2095.	5.0	3874.	2.1	3299.	1.6			2732.	8.2
	PL2	4242.	2.5	3545.	10.5			3303.	8.3	6113.	2.2	5372.	6.4			4583.	7.2
	PL3	3955.	3.0	3052.	14.0			2961.	6.5	6541.	1.5	5281.	14.6			5089.	4.8
	PL4	2540.	1.9	1795.	14.5			1860.	11.2	4363.	2.0	2843.	8.3			3184.	8.3
32.5	PL1	4000.	4.0	3932.	14.1			3512.	7.0	5899.	3.6	5204.	13.5			5006.	6.3
	PL2	6029.	5.1	5482.	14.5			5451.	7.0	9068.	4.7	8473.	12.6			8020.	7.4
	PL3	5770.	4.4	5794.	19.0			5189.	7.4	9480.	4.3	8023.	16.5			8701.	7.3
	PL4	3845.	3.8	3179.	22.9			3355.	9.4	6316.	3.3	5038.	14.6			5714.	8.2
34.5	PL1	7345.	2.1	6141.	14.3			6350.	4.0	11020.	0.8	9292.	14.4			9513.	8.8
	PL2	11513.	3.7	9733.	15.4			10606.	5.1	17350.	3.6	14226.	14.7			16304.	5.4
	PL3	10839.	3.2	8923.	12.2			10210.	4.5	17702.	3.5	14539.	10.1			16560.	4.0
	PL4	7091.	1.4	5536.	13.4			6675.	5.3	11613.	2.0	9070.	14.8			10955.	5.9
111.5	PL1	927.	0.2	814.	8.7	790.	1.3	775.	-0.2	1147.	179.5	1002.	-173.0	1016.	-176.1	993.	179.7
	PL2	910.	1.8	791.	14.6	727.	3.3	715.	-0.6	1371.	179.6	1448.	-175.9	1168.	-175.5	1176.	-179.7
	PL3	1164.	179.9	1119.	-173.5	1016.	-178.2	978.	180.8	948.	-0.9	779.	14.4	695.	2.6	677.	0.1
	PL4	1041.	-179.8	986.	-177.4	897.	-178.2	897.	180.1	938.	-0.5	840.	9.5	755.	2.7	750.	0.3
115.	PL1	1296.	0.2	1295.	5.3	1182.	0.7	1147.	0.6	1512.	-178.3	1598.	-173.8	1429.	-179.3	1373.	179.4
	PL2	1369.	0.8	1296.	1.9	1111.	8.7	1088.	-0.5	1809.	-179.7	1835.	-178.2	1593.	-176.2	1555.	180.2
	PL3	1599.	179.6	1391.	-177.3	1348.	-179.7	1310.	180.2	1370.	-1.1	1323.	1.4	1129.	6.1	1074.	-0.1
	PL4	1447.	-179.0	1310.	-170.0	1247.	-177.6	1258.	179.7	1344.	1.0	1317.	6.6	1207.	3.5	1158.	-0.1
117.	PL1	1746.	-1.2	1760.	2.6	1696.	1.5	1695.	-3.6	2005.	178.1	1967.	-169.4	1842.	-176.6	1982.	177.0
	PL2	1843.	-1.5	1800.	3.1	1604.	4.6	1666.	-1.8	2335.	179.0	2222.	-177.6	2315.	-177.9	2164.	178.8
	PL3	2043.	178.3	1830.	-175.0	1880.	177.2	1846.	178.7	1872.	-1.8	1683.	7.5	1732.	0.0	1658.	1.4
	PL4	1843.	178.9	1699.	-171.0	1825.	179.9	1832.	177.1	1844.	-1.8	1738.	8.2	1617.	5.0	1804.	-2.8

dependent as far as the amplitudes are concerned, the trend being a lowering as the speed of the rotor increases. This effect is most likely due to two not easily separable causes: the rolling element bearings' variable stiffness and damping, and the influence of gyroscopic moments. However, if a comparison is made between those influence coefficients where the rotor speed is closest to the response frequency it is seen that the impact influence coefficients amplitudes are still greater than those determined from the trial weight method, the average deviation being about 15 percent at the lower frequencies and approximately 5 percent at the higher frequencies. Based on this it may be expected that balancing of the rotor close to the first critical speed will not be as good as balancing it close to the second critical speed. This is confirmed later at the balancing tests where normally the rotor could be balanced very close to the first critical speed using the trial weight influence coefficients in just one balancing run, whereas repeated use is required of the impact influence coefficients in order to obtain comparable results, but the procedure converges quickly.

In contrast, the phase deviation is small and in most cases within the measurement tolerances, which is typically 1 deg. It cannot be explained only by the fact that the rotor system is slightly damped because two other factors should theoretically have caused a larger phase discrepancy. The first one is the

Table 4

	$\frac{RMS_{UNCORRECTED}}{RMS_{RESIDUAL}}$	
Transducer type	TRIAL WEIGHT ONLY	IMPACT INFLUENCE COEF. METHOD
Accelerometer	5.31	2.79
Force, Piezo	3.64	5.06
Displacement	3.36	5.80

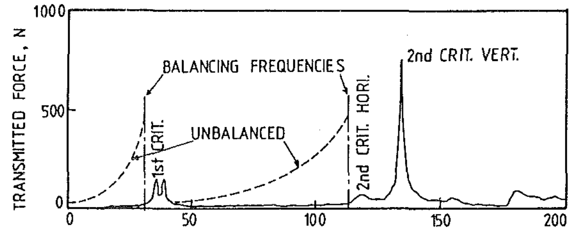

Fig. 3 Result of balancing

length of the impact pulse as compared to the rotational period. The impulse is typically 0.8 ms long, and at rotor speeds of 13.5 Hz and 87 Hz the rotational periods are 74.1 ms and 11.5 ms, respectively, meaning that the impact tip touches the rotor surface over arcs of 4 and 25 deg, respectively. The second factor is the time delay between the impact and the start of the response at the transducer. Although the test rotor is relatively short, the largest transmission path time is of the same order of magnitude as the impulse length and one should have expected a phase delay. However, neither of the mentioned factors showed up in the FFT analyzer's frequency response calculation.

From Fig. 2 it is seen that the transducer sensitivity varies greatly from the displacement probe to the accelerometer, in particular near the first critical speed and also near the second critical speed. The sensitivity of the force probe is between the two other probes and is not as frequency dependent as the displacement and acceleration probes. Thus it appears advantageous to use force probes whenever possible, but the present tests confirmed also that the widely used probes for displacement and acceleration will produce acceptable results. If displacement probes are used some care must be exercised in selecting the running speed of the rotor such that the higher harmonics of the rotor frequency do not coincide with the selected response frequencies. The higher harmonic components originate from the shaft's out-of-roundness, and as can be seen from Fig. 2 these components can actually be larger than the response one tries to measure. Based on this, it should now be evident why a rotor speed of 13.5 Hz was chosen such that the response frequencies at 111.5 Hz to 117 Hz were well away from, in this case, the eighth and ninth harmonics, marked 8f and 9f on Fig. 2.

The influence of a large imbalance in the rotor on the calculated impact influence coefficients has also been investigated and it was found that the method is not sensitive to this within the measurement tolerances, but again, attention must be paid to the selection of the rotor running speed versus the response frequency to the effect that the synchronous and higher harmonics, if any, must not have a pronounced influence on the components at the response frequencies.

In an extreme case it was tried to impact the rotor using a handheld hammer and, considering the employed method, the results obtained were usable.

The balancing results shown in Table 4 confirm that the proposed method is as good, on the average, as the conventional trial weight method. Although it appears that when acceleration probes are used the result is poorer, this is really not so. The result shown in the column "impact influence coefficient method" is good enough if the absolute values are compared with vibration standards. In all cases the first and second critical speeds could be passed comfortably and a typical result of the final balancing is shown in Fig. 3. The force probes were used to produce the results and the dotted curves indicate the imbalance condition before installing correction weights allowing the rotor to pass the first and second critical speeds. Whether further refinement is required must depend on the individual rotor application and its place in the balance groups mentioned in various standards (API 1979, ISO 1983, VDI 1981).

Conclusion

The investigation has demonstrated that the proposed method of calculating the influence coefficient for balancing purposes by impacting a rotor at a speed below a critical speed is of some practical value and should be considered as a supplementary method to the conventional methods: trial weight and modal balance methods.

As shown, a wide range of measurement transducers can be employed and the measured values agree sufficiently well with the directly obtained influence coefficients.

The principal shortcomings of the method are that access is required to impact the rotor where the balancing planes are positioned, although interpolation techniques may be tried, and that the rotor has a fine machined surface at the points of impact. However, because of the established close agreement in the present experiments, the approach merits confidence and could be developed into a practical method of balancing.

References

American Petroleum Institute, 1979, "Centrifugal Compressors for General Refinery Services," API Standard 617, Washington, DC, pp. 11-12.

Glienicke, J., 1966-67, "Experimental Investigation of the Stiffness and Damping Coefficients of Turbine Bearings," *Proc. IMechE*, Vol. 181, Part 3B, pp. 116-129.

Goodman, T. P., 1964, "A Least-Squares Method for Computing Balance Corrections," ASME *Journal of Engineering for Industry*, Vol. 86, No. 3, pp. 273-279.

International Organization for Standardization, 1983, "Criteria for Evaluating Flexible Rotor Balance," ISO Standard No. 5343, pp. 1-9.

Lund, J. W., and Tonnesen, J., 1972, "Analysis and Experiments on Multiplane Balancing of a Flexible Rotor," ASME *Journal of Engineering for Industry*, Vol. 94, No. 1, pp. 148-158.

Morton, P. G., 1974, "The Derivation of Bearing Characteristics by Means of Transient Excitation Applied Directly to a Rotating Shaft," *Dynamics of Rotors*, IUTAM Symposium, Lyngby, Denmark, Springer-Verlag 1975, pp. 350-379.

Nordmann, R., and Scholhorn, K., 1980, "Identification of Stiffness and Damping Coefficients of Journal Bearings by Means of the Impact Method," *Proc. Second International Conf. on Vibrations in Rotating Machinery*, IMechE, Cambridge, England, pp. 223-230.

Verein Deutscher Ingenieure, 1981-1983, "Shaft Vibrations of Turbomachinery," VDI 2059, parts 1-4, Düsseldorf, Federal Republic of Germany.

Current Status and Future Trends in Turbine Application of Thermal Barrier Coatings

K. D. Sheffler

D. K. Gupta

United Technologies,
Pratt & Whitney,
East Hartford, CT 06108

This paper provides an overview of the current status and future trends in application of thermal barrier coatings (TBC) to turbine components, and in particular to high turbine airfoils. Included are descriptions of the favorable results achieved to date with bill-of-material applications of plasma-deposited TBC, and recent experience with developmental coatings applied by electron beam-physical vapor deposition.

Introduction

The modern commercial gas turbine engine typically utilizes turbine airfoil alloys with melting points on the order of 2250 to 2400°F (about 1230 to 1315°C) in a combustion exhaust gas environment in excess of 2500°F (1370°C). To avoid structural failure by melting or by some other less severe degradation mode such as creep, oxidation, thermal fatigue, etc., turbine airfoils are made hollow and are cooled by internal injection of compressor discharge air.

Extraction of this compressor discharge air from the primary gas path reduces cycle efficiency. Efficiency thus may be improved by reducing the amount of cooling air required to maintain airfoil structural integrity. Major strides have been made in recent years in increasing the cooling efficiency of turbine airfoils, both through clever design of internal cooling geometries and through the introduction of an external cooling film by bleeding air out of tiny holes drilled through the airfoil wall. Unfortunately, the rate at which new gains in airfoil cooling efficiency are being achieved is decreasing as airfoil design technology matures, and new innovations are required to allow further efficiency improvements.

Thermal barrier coatings represent a material innovation, which has the potential to provide quantum increases in effective cooling efficiency by application of a ceramic insulating layer on the external surface of cooled turbine airfoils (Duvall and Ruckle, 1982; Miller and Lowell, 1982), as illustrated in Fig. 1. Calculations indicate that a 0.01 in. (0.25 mm) thick layer of zirconia can reduce metal temperature by as much as 300°F (about 170°C), depending on the local heat flux. As shown in Fig. 2, this amount of metal temperature reduction is greater than the cumulative gains made in temperature capability of airfoil alloys over the past twenty years (Gell et al., 1987). It is estimated that efficiency gains resulting from the application of TBC to all high turbine airfoils in a typical modern gas turbine engine could result in annual fuel savings as high as ten million gallons for a 250 aircraft fleet.

Barriers to TBC Incorporation

While potential TBC payoffs are large, incorporation has been slow because the technological barriers are not insignificant. The greatest concern involves thermally driven spallation of the brittle ceramic (Miller and Lowell, 1982; Grisaff and Levine, 1979; Ruckle, 1979). Recent work (DeMasi et al., to be published) shows that spallation of current coatings results from progressive accumulation of fatigue cracking damage in the ceramic adjacent to the ceramic–metal interface. Cracking is driven by cyclic thermal strains resulting from differences in thermal expansion between the ceramic and the underlying base metal. Phenomenological evidence indicates that cracking is augmented, through an as yet undetermined mechanism, by metal oxidation at the metal–ceramic interface. As discussed below, improvements to ceramic coating processing and consequent structure have dramatically increased ceramic spallation resistance in the past several years (Duvall and Ruckle, 1982; Sumner and Ruckle, 1980; Grot and Martyn, 1981).

Another major technological concern is the need for development of a thermal barrier coated airfoil design system and the coating life prediction methodology needed to support it. Once reliable coatings are identified, a design system must be developed to take maximum advantage of potential TBC benefits in airfoil design. To assure both coating and component reliability, this sytem must include a methodology to predict TBC spallation life. The subject of TBC life prediction was dealt with in another paper at this conference (Miller, 1988).

Other technological barriers include increased surface roughness of certain types of TBC, potential alteration of cooling hole geometry and flow as a result of ceramic deposition, alteration of turbine aerodynamics as a result of increased airfoil thickness and increased centrifugal loading of

---

Contributed by the International Gas Turbine Institute and presented at the 33rd International Gas Turbine and Aeroengine Congress and Exhibition, Amsterdam, The Netherlands, June 5–9, 1988. Manuscript received by the International Gas Turbine Institute January 8, 1988. Paper No. 88-GT-286.

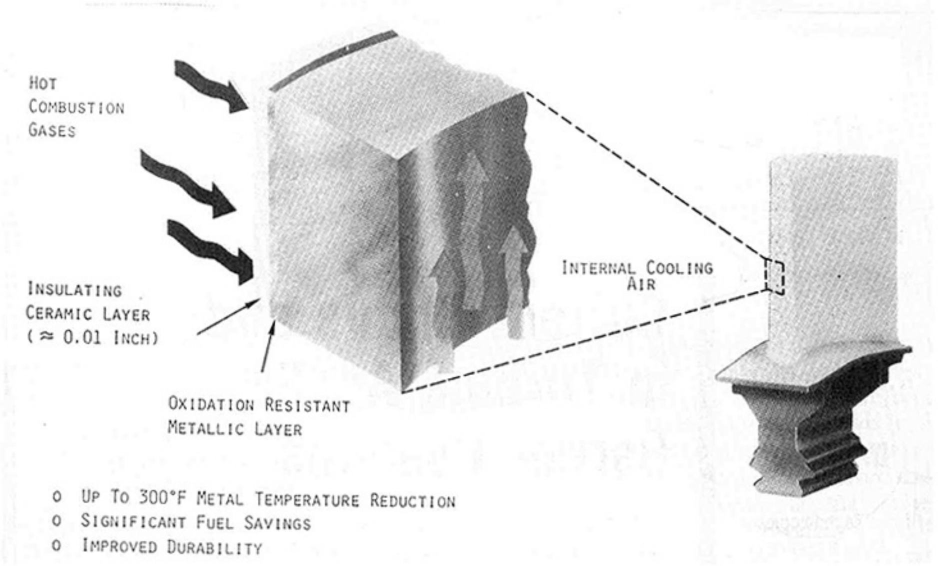

Fig. 1 Thermal barrier coating benefits

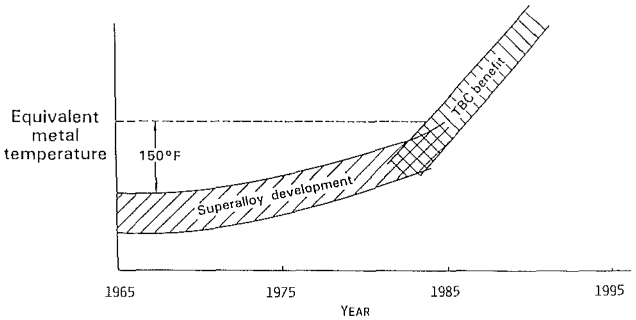

Fig. 2 Potential turbine temperature benefits offered by thermal barrier coating compared with increases of metal temperature capabilities achieved through superalloy development over the past 20 years

rotating airfoils. While all of these technological barriers have technological solutions, some of these solutions increase coating cost. The dollar value of durability and/or performance benefits provided by the coating must be greater than total coating cost for TBC use to be justified.

Recent Advances in Thermal Barrier Coatings

Dramatic improvements in cyclic thermal spallation life have been achieved over the past several years through use of stronger and tougher ceramic compositions, residual stress control, and, most importantly, through careful control of ceramic microstructure to enhance ceramic compliance and thus reduce the level of stress induced by expansion mismatch strains (Duvall and Ruckle, 1982; Sumner and Ruckle, 1980; Grot and Martyn, 1981). Illustrated in Fig. 3 are three ceramic microstructures representing progressive improvements in cyclic thermal strain tolerance. Figure 3(A) shows a relatively dense ceramic, which exhibits typical brittle ceramic behavior as shown in Fig. 4, Curve A. Shown in Fig. 3(B) is the microstructure of an optimized plasma deposited ceramic thermal barrier coating which exhibits the behavior shown in Fig. 4, Curve B. The difference in ceramic compliance, as evidenced by the level of stress induced at a given strain, and the total strain to failure, is clearly evident in Fig. 4. The cyclic thermal durability benefit provided by the Fig. 3(B) microstructurally optimized plasma sprayed ceramic is shown in Fig. 5.

The most recent breakthrough in ceramic coatings is shown in Fig. 3(C). This structure is produced by Electron Beam-Physical Vapor Deposition (EB-PVD), and consists of individual, free-standing ceramic columns, each of which is very tightly bonded to the metal substrate but is essentially free to separate from adjacent columns as the underlying substrate thermally expands relative to the ceramic. While the cyclic strain tolerance benefits of this structure have been known for some time (Duvall, 1980), it is only recently that EB-PVD process technology has advanced to the point of producing this coating with reproducibly high levels of relative cyclic thermal durability. Early efforts to fabricate EB-PVD ceramic were plagued with "infant mortality" failure problems where one coating run would produce coatings with outstanding durability and the next run would produce coatings that spalled very early in testing or sometimes even during pretest handling. As a result of improved basic understanding of EB-PVD ceramic failure modes, the cause of this infant mortality failure has been clearly identified, and improved reactive evaporation processing (Bunshah, 1974) has been developed to eliminate the problem. Laboratory burner rig screening tests indicate that the relative durability increase for the improved EB-PVD can be about eight times bill-of-material plasma sprayed coating durability, as shown in Fig. 5.

Engine Application of Thermal Barrier Coatings

(A) Design Considerations. Thermal barrier coating benefits described in the introduction represent the maximum performance increase that could be achieved through increasing turbine inlet temperature (or reducing airfoil cooling air) after all technological barriers have been overcome in a cost-effective way. In the meantime, thermal barrier coatings are being utilized in flight service to achieve substantial increases in component durability at current performance levels.

Two key requirements for full exploitation of the TBC potential are development of a thermal barrier coated airfoil design system and demonstration of a "prime reliable" thermal barrier coating; that is, a coating whose *assured* cyclic thermal durability equals or exceeds the design life of the airfoil to which it is applied. These two requirements are closely interrelated, in the sense that the definition of "assured" coating life depends on the nature of the airfoil design system, and in particular on how the system treats coating life requirements and life prediction.

The core of this problem lies in how the design and life prediction system treats variability of material performance, and the extent to which average properties must exceed

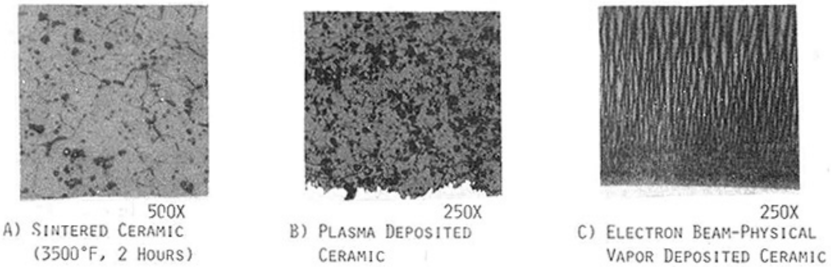

Fig. 3 Evolution of ceramic microstructures with increasing levels of resistance to thermally induced spallation

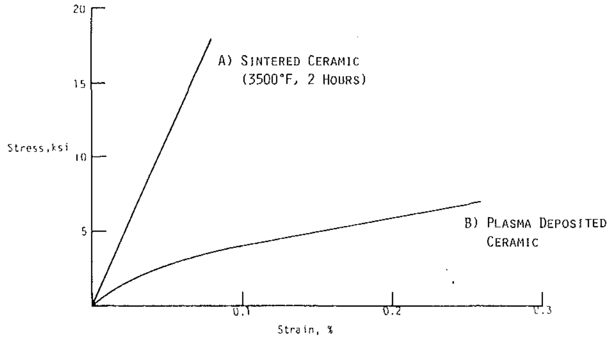

Fig. 4 Stress-strain curves for ceramic microstructures shown in Figs. 3(A) and 3(B)

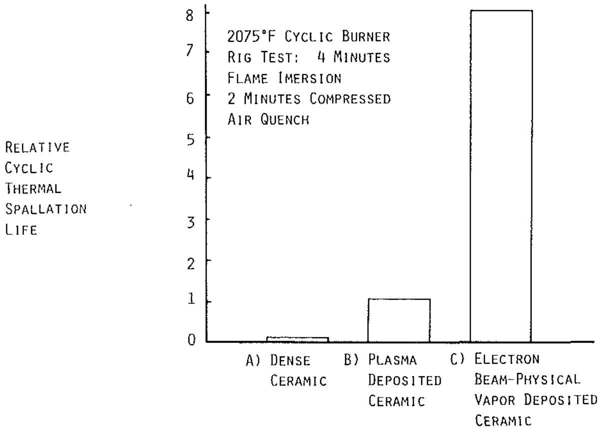

Fig. 5 Results of laboratory cyclic burner rig tests to determine relative spallation resistance of various ceramics

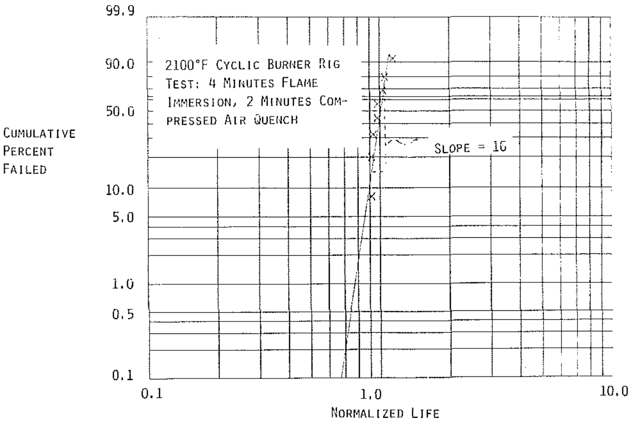

Fig. 6 Normalized Weibull plot of plasma-deposited TBC laboratory burner rig test results

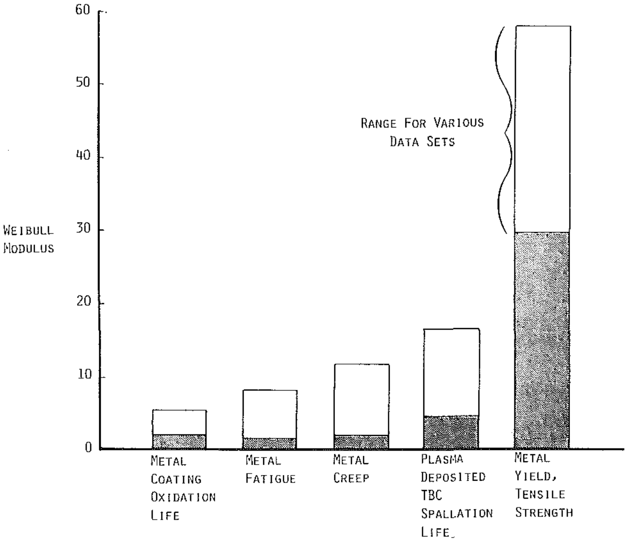

Fig. 7 Typical Weibull modulus ranges for various properties of gas turbine engine materials

minimum life requirements to "assure" vanishingly small probability of coating failure during component design life. The emerging discipline of structural ceramic design treats this subject of reliability using the method of Weibull statistics. This method is familiar to the gas turbine engine designer, being used routinely to treat the subject of reliability for time and/or cycle-dependent metal properties such as creep and especially fatigue.

Using the Weibull method, we have attempted to address the subject of ceramic coating reliability using laboratory test results. Shown in Fig. 6 is a normalized Weibull plot of laboratory burner rig test life data for our current bill-of-material plasma deposited ceramic coating. (Details of this coating are given in a later section.) The slope of this plot, or "modulus," is taken as a measure of reliability. The data shown in Fig. 6 exhibit a Weibull modulus of 16. Data generated at different test conditions have shown TBC Weibull moduli as low as 5. The question is, what do these numbers mean? We posit that the best way to answer this question is to compare TBC moduli with moduli of other typical gas turbine engine materials. This has been done in Fig. 7, which shows that for time and cycle-independent properties such as tensile and yield strength, the Weibull modulus typically is on the order of 30 to 60. However, for time or cycle-dependent properties such as creep and fatigue, typical Weibull moduli are in the range of 2 to 12. Based on these data, we conclude that the inherent reliability of thermal barrier coating life, which has been shown to be both time and cycle dependent, is at least comparable to the reliability of other gas turbine engine materials that have time and/or cycle-dependent failure modes.

The question remains, how do we relate laboratory properties such as those shown in Fig. 6 to engine life requirements? The answer lies in a sequence of critical steps. The first in-

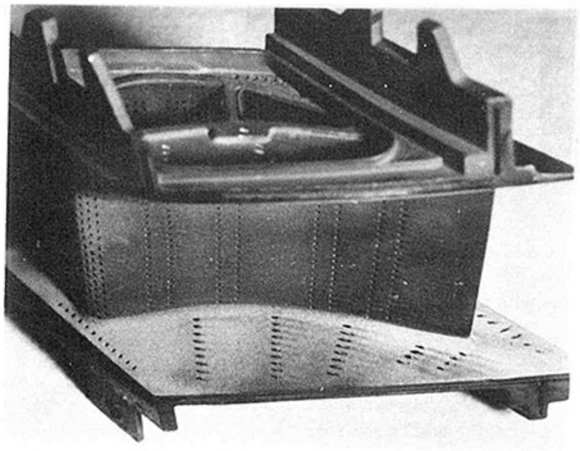

Fig. 8 Photograph showing plasma-deposited JT9D first turbine vane platform TBC in excellent condition after 9300 hours in commercial flight service

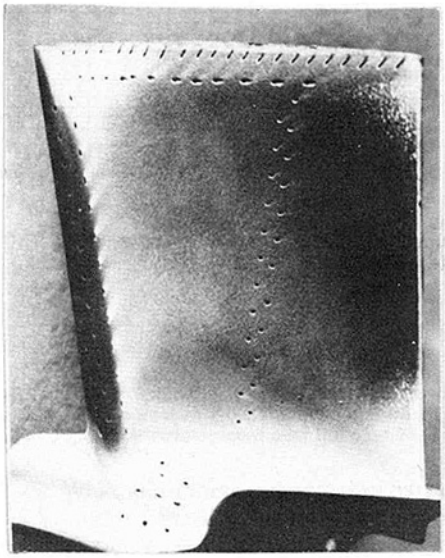

Fig. 9 Electron beam-physical vapor deposited ceramic coated PW2040 first turbine blade exposed in 150 hour endurance test. Note that color variation, and especially mottled appearance near trailing edge tip, are the result of engine deposits.

volves development of a TBC life prediction system based on lab data, which will relate imposed time–temperature cycles to spallation life as measured under known laboratory conditions. The second will be generation of quantitative engine life data with various time–temperature, or "mission cycles," both to calibrate the laboratory based model and to substantiate the suitability of both the model and the coating for the intended engine application. In essence, we must rely on engine experience to calibrate our design system and to tell us how much "excess" average life (i.e., how much safety margin) is required to assure acceptably small probability of ceramic failure during component design life.

Based on initial efforts in both of these areas, we feel that we are beginning to satisfy the requirements for prime reliable TBC design and application. We have developed a life prediction system for our current plasma deposited coating (Miller, 1988), we have identified an advanced, EB–PVD deposited system that we feel has the potential to fulfill prime reliable life requirements, we are in the process of adapting the existing life prediction system to the advanced coating, and, most importantly, we have accumulated substantial engine experience with the current generation plasma coating in bill-of-material durability extending applications and are starting to accumulate an engine experience base with the more durable EB–PVD coating. Highlights of this engine experience are described in the following sections.

(B) Current Engine Applications. Current bill-of-material applications of TBC utilize a plasma-deposited ceramic. This coating system incorporates of a 0.01 in. (0.25 mm) thick insulative outer layer of plasma-deposited 7 weight percent yttria partially stabilized zirconia containing a highly developed network of compliance enhancing microstructural features such as porosity and microcracking (shown previously in Fig. 3B), and a 0.005 in. (0.127 mm) thick inner "bond coat" of low-pressure chamber plasma sprayed NiCoCrAlY, which enhances ceramic adherence and provides oxidation protection for the base metal. This coating currently is being used to enhance durability of high turbine vane platforms in high thrust models of the JT9D-7R4, and in all models of the PW2000, PW4000, and V2500 engines, and on the PW4000 first and second turbine vane airfoils.

The degree of durability enhancement provided by plasma deposited ceramic has been demonstrated in comparative engine tests, which showed thermal barrier coated JT9D first turbine vane platforms to be in good condition after 2778 endurance cycles in a ground-based test engine, as compared to substantial damage on adjacent vanes that ran for only 1500 cycles in the same engine with a protective metallic coating but no ceramic insulating layer. The durability enhancement provided by the ceramic coating was clear and dramatic. Whereas the ceramic-coated vanes exhibited no significant platform damage, the non-TBC coated platforms exhibited substantial cracking along rows of cooling holes and two major burn locations on either side of the leading edge where hot gas burned almost completely through the platform wall. Combined JT9D and PW2037 field service experience with plasma ceramic on vane platforms currently exceeds two million cumulative engine flight hours and over six hundred thousand engine flight cycles and has been highly favorable, with only minor spallation typically observed at edge and hole associated hot spots after flight times up to 18,000 hours. Shown in Fig. 8 is a JT9D vane, which exhibits no spallation after 9300 hours of airfline flight engine service. Recent observations at an airline overhaul facility, where we were unable to take photographs, showed plasma-deposited TBC still to be in highly serviceable condition after more than 18,000 flight hours in another engine of the same model.

(C) Engine Evaluation of EB–PVD Ceramic. As shown previously, laboratory test data indicate that EB–PVD ceramic offers the potential for a substantial increase in cyclic thermal spalling life as compared to current bill-of-material plasma deposited coating. The specific coating, which has been evaluated in recent engine tests, is similar to the previously described plasma coating except for substitution of EB–PVD ceramic. Recent engine test results have provided dramatic evidence of the durability of this ceramic. Shown in Fig. 9 is an EB–PVD ceramic-coated PW2040 first turbine blade that is in good condition after operation for 150 endurance test hours in a ground based engine. Previous engine test experience had shown spalling of plasma-deposited ceramic after less severe testing on the same component (Anderson, 1986). Additional substantiation is provided by flight testing on JT9D first turbine blades. Airfoils coated with plasma-deposited ceramic were spalled after only 1500 hours of flight service, whereas EB–PVD ceramic was still in good condition when testing was terminated after almost 5000 hours, indicating the relative durability benefit of EB–PVD ceramic to be greater than three times that of plasma-deposited ceramic.

Future Directions

We expect that in the near future we will be using EB–PVD ceramic as bill-of-material in the durability extending mode. As indicated earlier, we are begininng to demonstrate the necessary combination of durability, reliability, and predictability for prime reliable application of EB–PVD ceramic, and are embarked on a vigorous but carefully planned program to substantiate our early findings further. This program involves an evolutionary series of tasks that are moving progressively from development of a TBC airfoil design system and laboratory substantiation of reliability, durability, and predictability through ground-based and flight engine substantiation and calibration of the coating and design system. At that point we will be in a position to create our first "clean-sheet-of-paper" design for a prime reliable TBC airfoil that provides the full performance benefits potentially available from TBC. We expect that we will accomplish this goal in the early 1990s.

A second area of substantial TBC development activity involves investigation of advanced ceramic compositions, focusing primarily on increased temperature capability and reduced density. Our first generation EB–PVD coating is based on the yttria partially stabilized zirconia incorporated in the current bill-of-material plasma-deposited ceramic. Future directions in engine design suggest that as turbine inlet temperature and heat flux increase beyond current levels, ceramic surface temperature may exceed the phase stability temperature limit for yttria partially stabilized zirconia (Miller et al., 1981; Suhr et al., 1984). In addition, reduced density is desirable for rotating airfoil applications where increased centrifugal loading from the structurally parasitic coating is a significant issue. We are investigating alternative ceramics to address both of these requirements. We expect that this work also will come to fruition in the early 1990s, so that the availability of higher temperature systems will be well coordinated with the design system development and coating performance substantiation efforts discussed in the preceding paragraph.

Acknowledgments

Advances in the state of the art of thermal barrier coating processing, characterization, and application discussed in this overview paper have come about as a result of sustained effort and occasional inspirations on the part of many persons, most especially Neal Anderson, Chuck Bevan, Bob Cone, Jeanine DeMasi, Charlie Giggins, Ernie Littlefield, Sue Manning, Rich Mullin, Vinnie Nevins, Don Nordstrom, Walt Olson, Milt Ortiz, Tom Radzavich, Ray Vine, Nick Ulion, and Merritt Wight. The dedication and diligence of all of these people is gratefully acknowledged.

Also, we wish to acknowledge the financial support of some of this work by NASA under Contract No. NAS-3-23944, and especially the technical guidance and encouragement of the NASA Project Monitor, Dr. Robert A. Miller.

References

Anderson, N. P., 1986, "Program for Development of Strain Tolerant Thermal Barrier Coating Systems," Informal Report, Contract NAS-3-22548.

Bunshah, R. F., "Reactive Evaporation," *Science and Technology of Surface Coatings*, B. N. Chapman and J. C. Anderson, eds., Academic Press, London–New York.

DeMasi, J. T., Ortiz, M., and Sheffler, K. D., to be published, "Thermal Barrier Coating Life Prediction Model Development," Final Report, NASA Contract NAS3-23944 (Pratt & Whitney Aircraft).

Duvall, D. S., and Ruckle, D. L., 1982, "Ceramic Thermal Barrier Coatings for Turbine Engine Components," ASME Paper No. 82-GT-332.

Duvall, D. S., 1982, "Processing Technology for Advanced Metallic and Ceramic Turbine Airfoil Coatings," *Proceedings from the Second Conference on Advanced Materials for Fuel Capable Heat Engines*, Electric Power Research Institute, Palo Alto, CA, EPRI-RD-2396-SR, pp. 6-102.

Gell, M., Duhl, D. N., Gupta, D. K., and Sheffler, K. D., 1987, "Advanced Superalloy Airfoils," *J. of Metals*, p. 11.

Grisaff, S. J., and Levine, S. R., 1979, *Proceedings of First DOE/EPRI Conference on Advanced Materials for Alternative Fuel Capable Directly Fired Heat Engines*, Castine, ME, p. 680.

Grot, A. S., and Martyn, J. K., 1981, "Behavior of Plasma-Sprayed Ceramic Thermal-Barrier Coating for Gas Turbine Applications," *American Ceramic Society Bulletin*, Vol. 60, No. 8, p. 807.

Miller, R. A., 1988, "Life Modeling of Thermal Barrier Coatings for Aircraft Gas Turbine Engines," presented at the 33rd ASME International Gas Turbine and Aeroengine Congress and Exposition, Amsterdam, The Netherlands, 8 June, 1988; published in: *Toward Improved Durability in Advanced Aircraft Engine Hot Sections*, ASME, New York.

Miller, R. A., and Lowell, C. E., 1982, "Failure Mechanisms of Thermal Barrier Coatings Exposed to Elevated Temperature," *Thin Solid Films*, Vol. 99, p. 265.

Miller, R. A., Smialek, J. L., and Garlick, R. G., 1981, "Phase Stability in Plasma Sprayed Partially Stabilized Zirconia-Yttria," in: *Science and Technology of Zirconia I: Advances in Ceramics*, Vol. 3, A. H. Heuer and L. W. Kobbs, eds., American Ceramic Society, Columbus, OH, p. 241.

Ruckle, D. L., 1979, "Evaluation of Plasma-Sprayed Ceramic Coatings for Turbine Engine Components," *Thin Solid Films*, Vol. 64, p. 327.

Suhr, D. S., Mitchell, T. E., and Keller, R. J., 1984, "Microstructure and Durability of Zirconia Thermal Barrier Coatings," in: *Science and Technology of Zirconia II: Advances in Ceramics*, Vol. 12, N. Claussen, M. Ruhle, and A. H. Heuer, eds., American Ceramic Society, Columbus, OH, p. 503.

Summer, I. E., and Ruckle, D. L., 1980, "Development of Improved-Durability Plasma Sprayed Ceramic Coatings for Gas Turbine Engine," AIAA Paper No. 80-1193.

Thermal Barrier Coating Life Prediction Model Development

T. A. Cruse

S. E. Stewart
Southwest Research Institute,
Department of Engineering Mechanics,
San Antonio, TX 78284

M. Ortiz
Pratt & Whitney,
Commercial Engineering,
East Hartford, CT 06108

Ceramic thermal barrier coating tests show that the coating fails by ceramic spallation. Analysis of life data indicates that cyclic thermal loading and thermal exposure play synergistic roles in controlling the spallation life of the coating. A life prediction algorithm has been developed, based on a damage accumulation algorithm that includes both cyclic and time-dependent damage. The cyclic damage is related to the calculated cyclic inelastic strain range in the ceramic coating; the time-dependent damage is related to the oxidation kinetics at the bond–ceramic interface. Cyclic inelastic strain range is calculated using a modified form of the Walker viscoplastic material model. Calculation of the oxidation kinetics is based on traditional oxidation algorithms using experimentally determined parameters. A relation between oxide growth and cycle parameters was derived from test data. The life prediction model was evaluated by predicting the lives of a set of thermal cyclic tests whose heating and cooling rates were significantly greater than those used to correlate the life parameters. Correlation between the actual and predicted spallation lives is within a factor of 3. This is judged to be satisfactory, relative to fatigue life prediction scatter in metals.

Introduction

Overview. Thermal barrier coating (TBC) systems are currently being developed to protect gas turbine hot section components. Because of the thermal insulating properties of the coatings, protected engine parts may be designed for a less severe loading environment, and the gas turbine may then have enhanced durability, performance and efficiency characteristics. Spallation of a coating that leads to exposure of the underlying component to the hot-gas environment may lead to premature component and system failure. Therefore, before thermal barrier coating systems can be used in critical flight systems, engine designers must be able to predict the coating spallation life with reasonable confidence.

To this end, Southwest Research Institute (SwRI) supported the Pratt & Whitney Engineering Division of United Technologies Corporation (PW) in a program for NASA's Hot Section Technology (HOST) effort (Di Masi, 1986). The project goal was to develop an analysis-based life prediction model for a candidate thermal barrier coating system. The technical approach to the life prediction problem consisted of an initial series of cyclic thermal tests of the TBC to identify principal damage mechanisms; then, from these data, to develop a preliminary TBC life model. The life model was then refined using data from a second experimental series and a mechanical testing program of the coating material. The design of the second experiment series and the mechanical testing program addressed life prediction and material behavior issues raised during the preliminary phase. The refined life model was then used to predict the results of a verification experiment series.

Physical Description of the Thermal Barrier Coating. The coating system evaluated was a two-layer material system consisting of a 7 percent yttria, partially stabilized zirconia ceramic insulator over a NiCrCoAlY bond coat. The substrate material selected for all experiments was a nickel-based cast superalloy commonly used in modern gas turbines known as B1900 + Hf.

For all experimental specimens, the bond coat and ceramic were applied to the substrate by low-pressure and atmospheric pressure plasma spray techniques, respectively. Adjustment of plasma spray parameters allowed the ceramic's porosity, microcracking and residual stress levels to be controlled during specimen fabrication. Figure 1 is a photomicrograph of a section through an untested laboratory specimen coated with the selected TBC system.

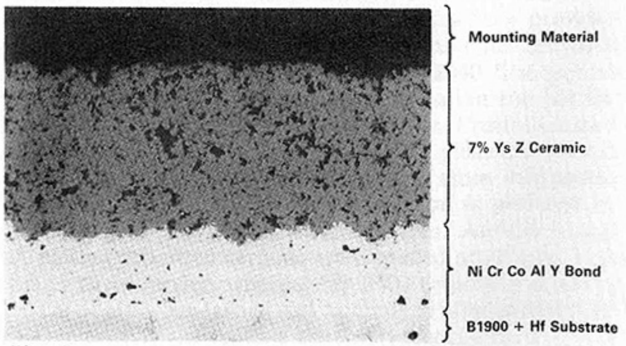

Fig. 1 Photomicrograph of TBC material system

Contributed by the International Gas Turbine Institute and presented at the 33rd International Gas Turbine and Aeroengine Congress and Exhibition, Amsterdam, The Netherlands, June 5–9, 1988. Manuscript received by the International Gas Turbine Institute September 15, 1987. Paper No. 88-GT-284.

Preliminary Life Prediction Correlation

Preliminary Life Prediction Model. The objective of the first experimental series, designated Task I, was to identify the relative importance of various TBC degradation and failure modes. These tests recognized that two damage mechanisms, damage caused by thermal cycling and damage caused by oxidation at the bond–ceramic interface, may significantly affect TBC life. Hence, the set of Task I experiments included cyclic thermal tests and furnace tests. In the former, specimens were repetitively heated to and cooled from typical turbine temperatures; in the latter, specimens were raised to turbine temperatures under isothermal conditions and held at this temperature for various lengths of time.

The Task I experiments identified two important modes of coating degradation. The first of these is mechanical, and is assumed to involve an accumulation of cyclic damage resulting from thermally induced mechanical strains. The second degradation mode involves prolonged thermal exposure, and appears (on the basis of phenomenological evidence) to involve oxidative degradation of the metal coating system component.

Following the approach of Miller (1984), the TBC life prediction model is based on a Manson–Coffin type relationship and equates the coating life to the ratio of cyclic plastic[1] strain to single cycle failure strain.

$$N = A\,(\Delta\epsilon_p/\Delta\epsilon_t)^{-b} \tag{1}$$

where N is the number of inelastic strain cycles to failure and A is a constant. The exponent b typically has a value on the order of 1.5 for metallic materials. For the specimen geometries used in this program, the hoop or in-plane component of plastic strain was used; radial strains in the thin coatings are relatively small.

Since TBC damage is postulated to be driven by in-plane plastic strain and oxide layer growth, the strain required to fail the coating in one additional cycle must depend on the amount of oxide and the magnitude of plastic strain. The single-cycle failure strain is therefore taken to be a linear combination involving the amount of oxidation, relative to a critical amount, and a static failure strain $\Delta\epsilon_{to}$ that would fail a nonoxidized TBC in one cycle

$$\Delta\epsilon_t = \Delta\epsilon_{to}\,(1-\delta/\delta_c) + \Delta\epsilon_p\,(\delta/\delta_c) \tag{2}$$

Substituting the single-cycle failure strain, equation (2), into the life algorithm, equation (1), and taking $A=1$ results in the following expression for cyclic life:

$$N = \left[\frac{\Delta\epsilon_{to}}{\Delta\epsilon_p}\,(1-\delta/\delta_c) + (\delta/\delta_c)\right]^b \tag{3}$$

Note that this algorithm predicts life for a particular amount of oxide and cyclic inelastic strain. During each cycle, however, the amount of oxide increases, so the algorithm must be applied repetitively to determine remaining life in the TBC. This is done by inverting equation (3) so as to obtain the "damage" performed per cycle. The damage per cycle is accumulated until the damage equals one. Oxide thickness in equation (3) is updated from cycle to cycle.

For this preliminary analysis, the cyclic inelastic strain $\Delta\epsilon_p$ in equation (3) was estimated from simple strength of materials considerations of the thermal strain response of the experimental specimen. A more advanced model of plastic strain per cycle is presented in the next section.

The total strain of the specimen is set by the thermal growth of the metallic substrate during the thermal cycle. The coating was initially assumed to be elastic–perfectly plastic, with equal yield strength in both tension and compression. The coating was assumed to have no creep response. Following one thermal cycle, a shakedown condition is achieved for the coating, due to the fact that the imposed total strain far exceeds the elastic strain capability of the coating. As a result of shakedown, the coating initial state is at the compressive yield strength. As the coating heats up, relative to the substrate, a transient plastic strain $\Delta\epsilon_n$ is imposed. The expansion of the substrate then imposes a tensile plastic strain of $\Delta(\alpha\Delta T) - 2\sigma_y/E$, which is the differential thermal growth (substrate - coating) minus the full elastic strain capability of the coating. The coating is then in a state of tensile yield. When the system is cooled the coating sees a further transient tensile plastic strain $\Delta\epsilon_c$ as the ceramic tries to shrink before the substrate. The cyclic plastic strain is then given by

$$\Delta\epsilon_p = \Delta\epsilon_n + \Delta\epsilon_c + \Delta(\alpha\Delta T) - 2\sigma_y/E \tag{4}$$

While the idealized cycle with balanced tensile and compressive behavior turns out to be a poor representation of actual coating response (see Section 5), the identification of plastic strain as the fatigue driver is seen to be an important new insight gained in Task I. The use of plastic strain allows for the recognition of some of the transient loading effects on coating durability.

The relationship between oxide growth and cycle characteristics for Task I experiments was based on weight gain experiments performed at NASA using the TBC and substrate system (Miller, 1986). Specimens were isothermally heated to 1373 or 1473 K (2012 or 2192 °F) and weighed periodically to measure the accumulation of oxide. Regressing the results gave the following expression for the increase in oxide thickness with time:

$$\delta = 5.35\times10^{-4}\bullet[2.057\times10^{15}\bullet g^{-52771/\mathrm{T}}\bullet t]^{0.2952} \tag{5}$$

In this relation, T is the specimen temperature in K, and t is the furnace exposure time in hours. The oxide thickness is returned in centimeters. To apply this expression to the prediction of cyclic thermal tests, each thermal cycle was divided into time increments, each small enough that the temperature could be assumed constant over the increment. Equation (5) was then used successively after each increment to calculate the total accumulated oxide thickness. After each completed

---

[1] In this paper the authors borrow terms like "plastic" strain and "creep" from the notions of metallic material response. The mechanisms of nonrecoverable and time-dependent strain are, of course, different for ceramic coatings. However, the general notion is conveyed by adopting the metallic terminology herein.

Nomenclature

b = life equation exponent
E = Young's modulus
K = drag stress
K_1 = drag stress parameter
K_2 = drag stress parameter
N = number of cycles to failure
n = Walker model inelastic strain rate exponent
R = gas constant
S_0 = stress parameter
T = temperature
t = time
$\Delta(\alpha\Delta T)$ = thermal mismatch strain
δ = current value of oxide thickness
δ_c = critical oxide thickness
$\Delta\epsilon_c$ = transient cooling strain
$\Delta\epsilon_t$ = single cycle failure strain
$\Delta\epsilon_{to}$ = no oxide failure strain
$\Delta\epsilon_k$ = transient heating strain
$\Delta\epsilon_b$ = cyclic inelastic strain
σ = applied directional stress
σ_y = yield stress
Ω = back stress

cycle, the newly established oxide thickness was used in conjunction with the life algorithm, equation (3), to establish the accumulated fatigue/oxidation damage at the end of that cycle. Damage per cycle is defined as the inverse life of the cycle, and this damage is summed linearly. The number of cycles to achieve a sum of unity is defined as the predicted cyclic lifetime.

The oxide relationship, equation (5), was later found to overpredict the experimentally observed cyclic oxide growth by a factor of nearly two. A revised oxide growth model, based on measured oxide thicknesses, was used in the refined model.

Correlation of Task I Experimental Results. To establish values of the model parameters, b and $\Delta\epsilon_{to}$, the spallation life data generated in the Task I experiments were regressed using the preliminary life correlation model, equation (3). The critical oxide thickness δ_c was taken as the thickness at the time for failure of a furnace specimen isothermally heated to about 1422 K (2100 °F). The parameters giving the best correlation between calculated and actual experimental lives were $b = 10.8782$ and $\Delta\epsilon_{to} = 0.02496$.

Figure 2 plots correlated versus experimental lives for the Task I experiments. In the figure, pre-exposed specimen results are indicated by solid symbols, non-pre-exposed by open symbols. The high value of the life exponent, $b = 10.8782$, indicates that, compared to metals, the fatigue life of the coating is quite sensitive to changes in cyclic strain. For metals, a slope of about 4 is typical. Scatter in the correlation of this data is consistent with what one would expect for metals, where the ratio of actual to predicted is typically spread over a range of seven. The scatter in Fig. 2 is about 9 (±3).

It is readily apparent from the plot that little differentiation is made by the preliminary life model between the D1 and E1 cycles although the experiments indicated a substantial variation in life. This batch effect has not been traced to any specific production variable, but perhaps is an indication of the level of scatter that can be seen between nominally identical coatings. The E1 tests, which should have increased life (reduced time at elevated temperature and reduced oxide growth), have shorter average lives than the D1 tests. On the other hand, differences between D1 and D2 cycles (which have different peak temperatures) are well correlated by the preliminary model. Further, D1 and F1 cycles (which have different cycle frequencies) are also well correlated. Pre-exposed specimens subjected to the D1 cycle are not well correlated, while D2, E1 and F1 pre-exposed results were better correlated by the model.

Viscoplastic Model Development

Constitutive Testing of Bulk Ceramic. Mechanical testing of the 7 percent yttria partially stabilized zirconia material was performed at SwRI to more clearly define the uniaxial stress–strain behavior of the material and hence improve the analytical modeling of the TBC in the life prediction models. Test conditions included uniaxial tension and compression testing to static failure, and tension and compression creep tests. The mechanical tests were conducted in a closed-loop, servo-hydraulically controlled testing machine with specimens radiatively heated by a susceptor, which was inductively heated. All loading was applied in parallel with the splat structure of the specimens. Figure 3 shows a typical test setup.

Intermediate and high-temperature compression tests were conducted on rods of ceramic in the "as-plasma-sprayed" condition. Tests were conducted at three temperatures: 811, 1144, and 1478 K (1000, 1600, and 2200 °F). Ultimate compressive strength values ranged from approximately 379 to 248 MPa (55 to 36 ksi) at 811 and 1478 K, respectively. The moduli for these tests were estimated to be nearly 13,790 MPa (2000 ksi). Failure strain values varied from 2 to 5 percent. Intermediate and high-temperature tension tests, on the other hand, indicated that the ultimate strength for this material was approximately 18 to 22 MPa (2.6 to 3.2 ksi), with little of the temperature dependence evidenced in the compression tests. Failure strain values varied from approximately 0.1 to 0.3 percent. Figure 4 indicates the stress–strain behavior of the bulk ceramic at various temperatures.

The compression-creep and tension-creep mechanical tests were conducted at a variety of loads and temperatures representative of both the test and turbine environment. In compression, the ceramic material showed a strong response in creep at both high (275 MPa; 40 ksi) and low (69 MPa; 10

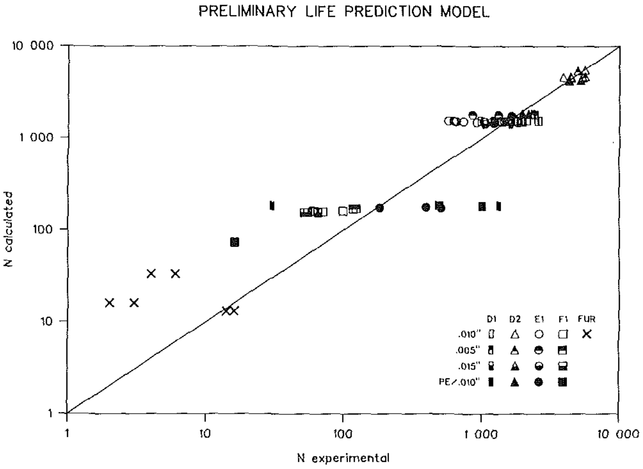

Fig. 2 Comparison of Task I experimental and calculated lives

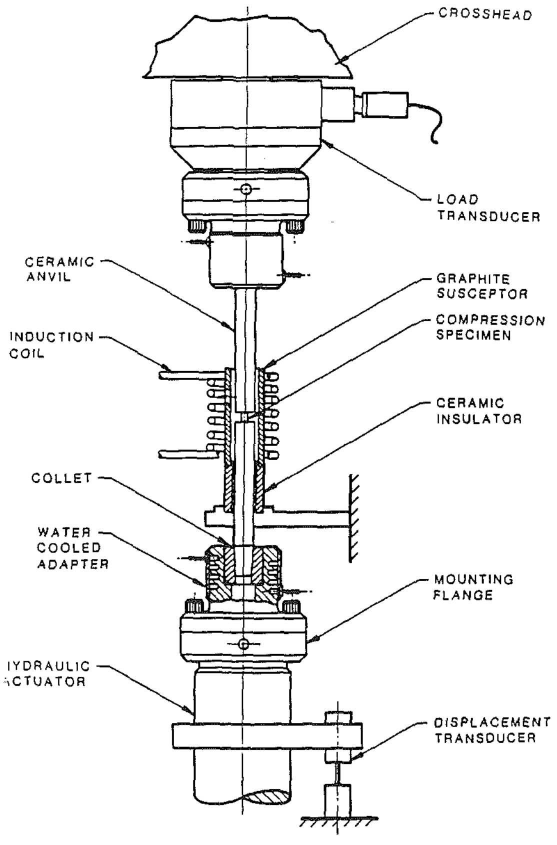

Fig. 3 Typical test setup for ceramic constitutive testing

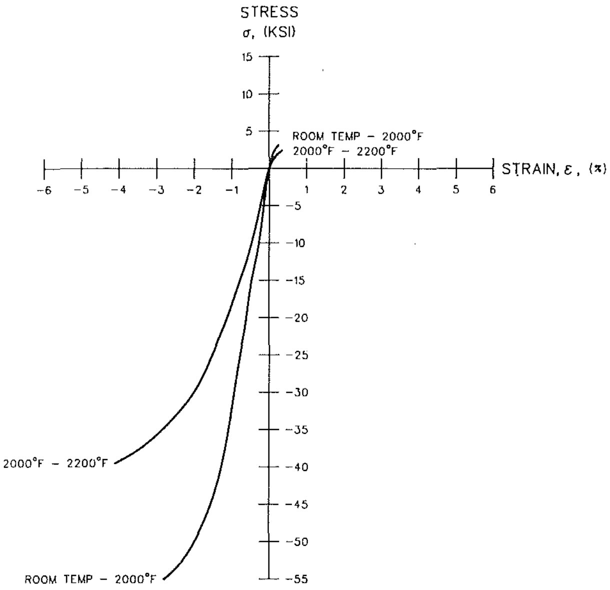

Fig. 4 Stress-strain behavior of ceramic at various temperatures

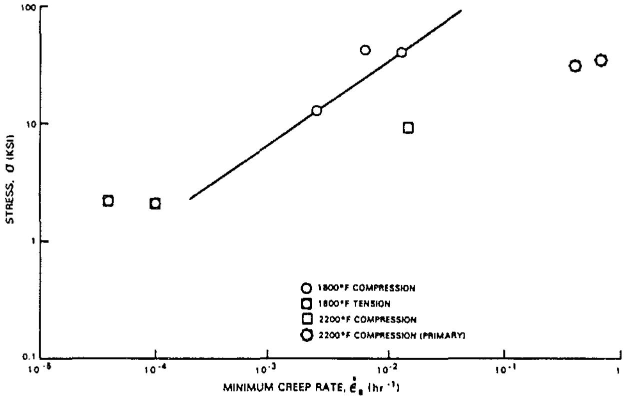

Fig. 5 Creep behavior of ceramic at various temperatures

ksi) load levels and over the range of temperatures: 1255-1478 K (1800-2200 °F). It was noted that the minimum creep rate appeared to increase with increasing stress. In tension, creep response was noted at temperatures above 1255 K (1800 °F). Figure 5 summarizes the creep test results.

The amount of inelastic strain capacity of the material, especially the creep response, was greater than had been expected and became an important consideration for the refined model development. The preliminary life model did not account for creep strains and was overly simplistic regarding the inelastic strain model.

Walker Viscoplastic Model of Ceramic Material. The mechanical tests showed that the simplified approach to ceramic inelastic response was too crude for accurate life prediction. More sophisticated modeling of the ceramic behavior to include the nonlinear, asymmetric, tensile, and compressive plastic response and creep was achieved using the Walker viscoplastic material model (Walker, 1981). The Walker model considers all inelastic strain to be time dependent, such that no distinction between plastic and creep strain is made. The governing equation for inelastic strain is

$$\dot{\epsilon}_{in} = \left(\frac{\sigma - \Omega}{K}\right)^n \tag{6}$$

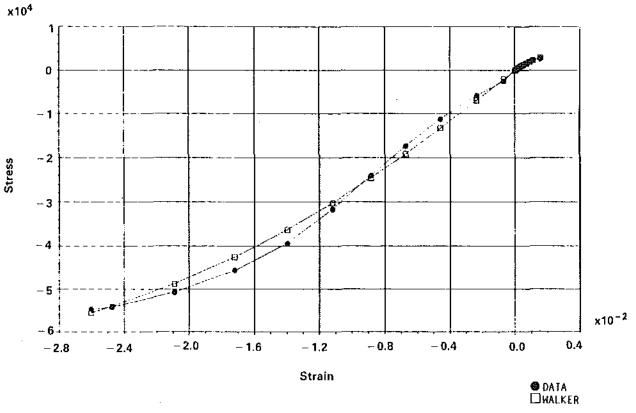

Fig. 6 Walker model prediction of ceramic uniaxial test data

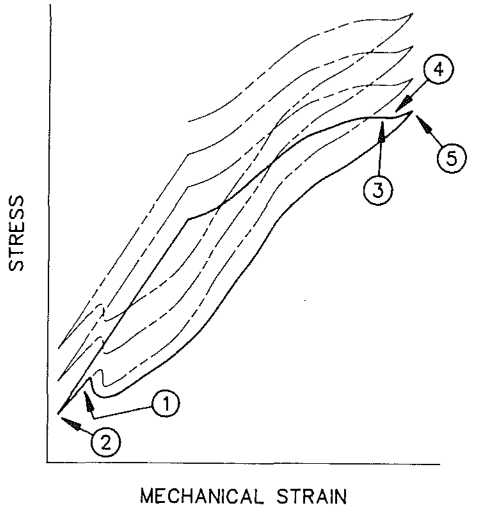

Fig. 7 Stress-strain response of ceramic to repeated thermal cycling

where n is a constant, Ω is the back stress, and K is the drag stress. The back stress term has been modified to account for the significant differences in tension and compression behavior in the ceramic TBC material. The modified back stress is given by

$$K = K_1 - K_2 \tan^{-1}(\sigma/S_0) \tag{7}$$

where σ is the applied (directional) stress and S_0 is a function of temperature. The effect of directionality of strength (tension versus compression) in the ceramic is obtained by the sign change of the stress term in equation (7).

In the evaluation of this model, all the 1478 K (2200 °F) tension, compression and creep mechanical test data were correlated using the Walker approach. Figure 6 shows that the uniaxial tension and compression behavior of the ceramic is well correlated by the Walker model. The time-dependent behavior was not well modeled by the parameters that gave the good time-independent correlation shown in Fig. 6. The lack of good creep correlation is seen as an item needing attention in any further work with this model. More will be said about this problem when discussing the Task II test results.

Figure 7 illustrates how the Walker model predicts the stress-strain behavior of the ceramic under a typical thermal cycle. Because of the stress-relaxation behavior of the ceramic material, a steady-state response of the material is not achieved until a few thermal cycles have elapsed. In the mature stress-strain cycle, the ceramic will be initially in compression (Point 1 in Fig. 7). When the ceramic is initially heated at the

Table 1 Characteristics of Task II experiments

Test Numbers	Test Emphasis	Nominal Max Temperature (deg K/deg F)	Nominal Min Temperature (deg K/deg F)	Nominal Cycle Length (sec)
1 - 2	Oxide	1380/2025	700/800	360
3 - 4	Oxide	1380/2025	700/800	720
5 - 6	Oxide	1380/2025	700/800	1440
7 - 8	Strain	1394/2050	294/70	360
9 - 10	Strain	1422/2100	294/70	360
11 - 12	Strain	1450/2150	294/70	360
13 - 14	Mixed	1353/1975	330/135	360
15 - 16	Mixed	1353/1975	330/135	720
17	Mixed	1380/2025	330/135	360
18	Mixed	1380/2025	330/135	720
19 - 20	Radius	1394/2050	294/70	360

Table 2 Results of Task II experiments

Test Numbers	Test Emphasis	Actual Life (cycles)	Predicted Life[1] (cycles)
1 - 2	Oxide	2036/3065	3899/3885
3 - 4	Oxide	818/1574	2131/2934
5 - 6	Oxide	784/798	986/539
7 - 8	Strain	2387/2079	1891/1635
9 - 10	Strain	414/484	804/305
11 - 12	Strain	28/260	25/[2]
13 - 14	Mixed	4198/4177	9583/2645
15 - 16	Mixed	2563/2332	2559/467
17	Mixed	2474	5204
18	Mixed	468	312
19 - 20	Radius	2754/2090	3304/1243

[1]Note: predictions made use of estimated (actual) temps.
[2]Note: no prediction made for this condition

beginning of the thermal cycle, the TBC is driven into further compression due to the constraint of the unheated substrate (Point 2). When the metal substrate then becomes heated later in the cycle, the ceramic is driven into tension elastically, and then plastically. When the TBC achieves the steady-state maximum cycle temperature (Point 3), some linear stress relaxation occurs, the amount of which will depend on the length of time the TBC remains at the maximum temperature (Points 3 and 4 in the figure). When the ceramic is initially cooled, additional inelastic tensile straining of the TBC occurs because the substrate, still hot, constrains deformation of the TBC. As the substrate does begin to cool, the TBC is driven into compression, first elastically, and then inelastically. At sufficiently low temperatures some stress relaxation is dictated by the model, and the predicted ceramic stress-strain state returns to the starting point (Point 1). The total inelastic strain response of the ceramic during the mature thermal cycle equals the maximum width of the stress-strain hysteresis loop shown in Fig. 7.

Life Prediction of Task II Experiments

Cyclic Thermal Testing. Task II experiments were designed more clearly to define the effect thermally induced cyclic strain, oxide growth, and radius effects had on the failure of the TBC material system. Radius effect tests examined the importance of the radial stress level induced by the coating curvature on specimen life. The 20-specimen test matrix is given in Table 1.

The test rig employed for these experiments was the same as used for Task I tests. Instead of a carousel of 12.7 mm (0.5 in.) diameter solid core specimens, however, each test was performed on a single, 23.88 mm (0.94 in.) hollow core specimen rotating on its own axis. The exception was a 20.83 mm (0.82 in.) specimen used to determine any effect on life of the specimen radius.

As in the Task I experiments, during the cool-down phase the burner rig was rotated away and the specimen was then cooled by an externally applied blast of air. For Task II experiments, the test procedure also included internal cooling of the specimen while it was exposed to the burner rig jet in order to increase the thermal gradient. The only exception to this cooling procedure was the set of tests referred to as the strain emphasis tests. In this set higher strains were achieved by reducing the gradient and increasing the bulk substrate temperature. Task II specimens were of the same material as the solid core specimens. Table 2 summarizes the results of the Task II experiments.

Refined Life Correlation Model. In the refined life prediction methodology, three fundamental changes were made. First, a more accurate relationship between oxide layer growth and cycle parameters was developed. Second, the Walker model was used to compute the cyclic inelastic strain for each of the Task II experiments. The Walker model directly accounts for both plasticity and creep effects. Third, in correlating the Task II experimental results, an hourly average inelastic strain, rather than a constant ceramic strain, was used in order to account for fluctuations in the thermal history. The life model accounts for these changes in the thermal history.

During the Task II phase of the program, photomicrographs of sectioned test specimens showed that the oxide growth rate equation (5) was overpredicting actual oxide thickness developed during the tests. The photomicrograph data were used to develop a new growth rate model. The new model assumes that the exponent in equation (5) is 0.5 and determines the constants based on a best fit to the data. The revised expression of oxide growth became

$$\delta = 1.20\times 10^{-4} \bullet [5.714\times 10^{11} \bullet g^{-104856/RT} \bullet t]^{0.5} \qquad (8)$$

The leading constant in equation (8) was selected to be a value that gave the best average correlation to the observed thicknesses from the Task II cyclic tests. The units for the activation energy in equation (8) are moles/calorie. To correlate the Task II experiments, the slope of the life model was taken to be the same as the Task I value, $b-10.878$. The critical oxide thickness δ_c, and the failure strain $\Delta\epsilon_{to}$, were then selected using a least-squares fit to the life data. The resulting values were δ_c-0.0094 mm (0.00037 in.) and $\Delta\epsilon_{to}$-0.004.

Task II experimental instrumentation showed some drift in measured parameters such as peak cycle temperature and cycle time. To improve the refined model correlations, the average Walker model inelastic strain was computed for each hour of each of the twenty Task II tests. In calculating the Task II experimental lives, the plastic strain variable in the life algorithm, equation (3), was updated to the current hourly average strain. Each change in strain corresponded to a new cyclic damage level for the life algorithm.

Task II Model Correlation. Figure 8 compares calculated and experimental lives of the Task II experiments, as reported in Table 2. The lives were calculated using the best estimate of the actual temperature conditions in the test rig. In general, the cycle times were well controlled, but the interface temperature conditions as estimated were off typically on the order of 25-50°F, although in some cases the error was over 100°F. This can be noted by comparing the calculated lives in Table 2 for the same nominal test conditions. The differences in the actual lives for the same nominal test conditions seemed to have less variation than the calculated lives; this may say something about the uncertainties in making temperature predictions for these kinds of tests!

The algorithm for calculating lives has no dependence on the stress normal to the spallation crack plane. This may seem to be an important missing term, except for the fact of Tests 19 and 20. In these tests the specimen radius is about 85 percent of that for the other tests. This change in radius results in

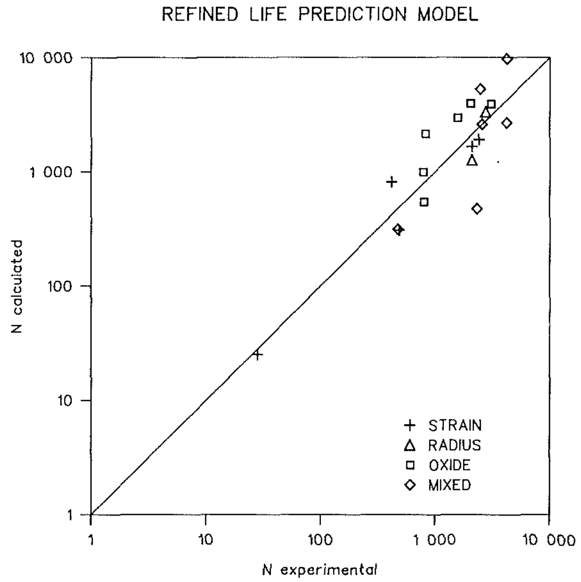

Fig. 8 Comparison of Task II experimental and calculated lives

an increase in radial stress of 15 percent. Given high crack growth rates in ceramics and low toughness values, one might expect a substantial effect on spallation life of this change in stress state. However, the experimental data does not show this. We thus concluded that cyclic hysteresis was the damage mechanism causing macrocracks, and that only in the last stages of life would the radial stress be important.

Generally, experimental lives for all tests are correlated within a factor of 3. All test types are correlated equally well, which represents an advance over the Task I tests and the preliminary model. This refined model is considered a usable correlation of the data. A better correlation cannot be expected without improving the mechanical damage model through the incorporation of more ceramic mechanical property data and a more accurate relation of oxide growth.

Verification Testing

One objective of the verification tests was to assess the usefulness of the refined life prediction model in engine design. Verification tests were designed to simulate engine exposure conditions to a greater extent than those of Tasks I and II. Table 3 summarizes the characteristics of the verification tests.

Tests 1 and 2 are the baseline strain emphasis and oxide emphasis tests. These tests were performed using the Task II burner rig procedure. Tests 3 and 4 (really four experiments on two specimens) subjected the specimens to blocks of high and low strains. In Test 3-I, the specimen accumulated damage at a low strain amplitude for 1310 cycles. In Test 3-II, the strain amplitude was increased by raising the peak cycle temperature and testing was continued until the specimen failed in an additional 665 cycles. In Test 4 the procedure was reversed. In 4-II, run first, the specimen accumulated damage at a high strain amplitude for 602 cycles, for which the predicted damage was equal to that of 3-II. The strain amplitude was then reduced and the specimen cycled to failure in an additional 267 cycles.

Tests 5 and 6 were conducted using a flat plate specimen and a quartz lamp heating rig. Quartz lamps were used to achieve the high heat fluxes more typical of the turbine environment. The flat specimens also eliminate radial stresses in the ceramic. Extensive cooling of the back of the substrate plate induced a large through-ceramic temperature gradient.

Figure 9 compares the correlated and experimental lives for the verification tests. The verification testing involved only six specimens. The scatter in the actual versus calculated lives is comparable to the scatter in Task I and Task II. However, the small number of specimens used would indicate that the correlation achieved in the verification testing was not as good as that in Task I and Task II. As Fig. 9 indicates, the refined life model is underpredicting all the strain emphasis test results and overpredicting all oxide emphasis test results. As previously mentioned, a probable source of improvement to the verification test predictions is an improved prediction of creep strains. The cyclic creep strains in the oxide and mixed mode tests are probably excessive, based on the lack of a good fit to the uniaxial creep data. A reduced amount of cyclic creep strain would be in a direction of improved life correlation. The second area of needed improvement is in the cyclic oxide growth model.

Table 3 Characteristics of verification experiments

Test	Test Emphasis	Test Specimen	Nominal Max Temp (deg K/ deg F)	Nominal Min Temp (deg K/ deg F)	Nominal Cycle Length (sec)	Actual Life (Cycles)
1	Strain	Hollow	1422/2100	311/100	360	1513
2	Oxide	Hollow	1422/2100	755/900	480	431
3	Mixed					1975
	Type I	Hollow	1366/2000	311/100	360	(1310+)
	Type II	Hollow	1422/2100	311/100	360	(665)
4	Mixed					869
	Type I	Hollow	1366/2000	311/100	360	(602+)
	Type II	Hollow	1422/2100	311/100	360	267
5	Strain	Flat Plate	1422/2100	311/100	360	570
6	Oxide	Flat Plate	1366/2000	811/1000	360	1000

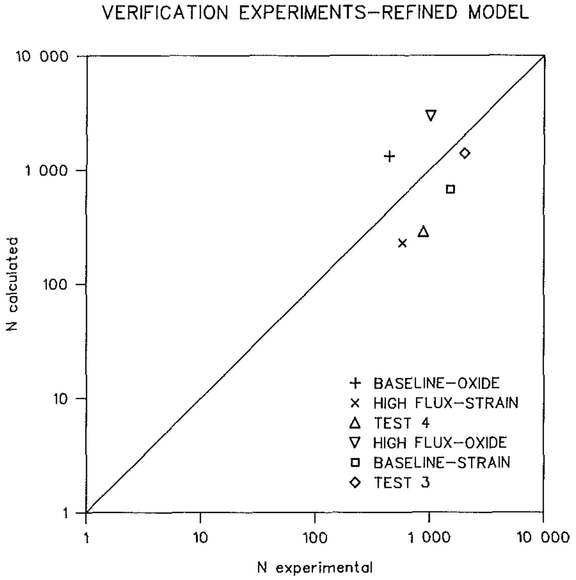

Fig. 9 Comparison of experimental and calculated lives for verification experiments

Summary

A series of progressively more challenging specimen tests was used to develop and refine a life prediction model for correlating spallation life in thermal barrier coatings. The model accounts for cyclic mechanical damage through time-independent hysteresis (plasticity) and time-dependent hysteresis (creep). The model also accounts for the fact that time at temperature degrades the coating life. This degradation mode is taken to be directly related to the presence of the oxide coating (more is worse); however, no direct physical link to the oxide coating has yet been made.

Correlation of the life model to cyclic data from one series of tests in each of two tasks was used to correlate the response of more severe tests. The correlation was carefully examined to assure a minimal bias in the life model for any particular mode of damage. However, it was found that the cyclic hot-time algorithm used to correlate oxide thickness did not achieve good correlation with static oxide growth data. Further work is needed to resolve this discrepancy.

One reviewer noted the possibility that oxide formation rate might be enhanced when the surface is under tension, as the oxide formation results in volume expansion relative to the displaced base metal. Some basis for cyclic oxide formation enhancement is clearly needed.

A viscoplastic material model from Walker was adjusted to account for the strong directionality of the ceramic coating damage. The model was fitted to the noncreep data but did not achieve a satisfactory fit to the creep data. As a result, those test conditions for which creep played an important role were not as well correlated by the model. More work to refine the creep fit in the Walker model is justified.

Finally, the comparison of actual and correlated fatigue lives has been quite satisfactory. This is especially so because the thermal rig tests were difficult to control and because of inherent scatter that should be expected in such limited ductility materials as the TBC material. Some batch effects were noted in the tests, but again these did not change the essential quality of the results.

Acknowledgments

The authors wish to acknowledge the support provided by the National Aeronautics and Space Administration under contract No. NAS3-23944. The authors would also like to acknowledge Pratt & Whitney for its support of the project and permission to publish the results. In particular, the authors wish to recognize the significant technical assistance and advice provided by Dr. Robert Miller, NASA, and Mr. Keith Sheffler, Mr. Tom Hajek, Ms. Jeanine DeMasi, and Mr. Merritt Wight of PW. The experimental effort to obtain material constitutive data used in this project was separately provided at SwRI by Mr. Andrew Nagy and Mr. Forrest Campbell, with financial support from PW.

References

DeMasi, J. T., 1986, "Thermal Barrier Coating Life Prediction Model Development; Second Annual Report," Technical Report, NASA CR-179508, Pratt & Whitney, East Hartford, CT.

Miller, R. A., 1984, "Oxidation-Based Model for Thermal Barrier Coating Life, *Journal of the American Ceramic Society,* Vol. 67, No. 8, pp. 517–521.

Miller, R. A., 1986, "Weight Gains of a Low Pressure Plasma Sprayed Bond Coat in a $ZrO_2 7\% Y_2O_3$/NiCrCoAlY/B1900+Hf TBC," Informal Technical Report, NASA Lewis Research Center, Cleveland, OH.

Walker, K. P., 1981, "Research and Development Program for Nonlinear Structural Modeling With Advanced Time-Temperature Dependent Constitutive Relationships,"Technical Report, NASA-CR-165533.

Processing Aspects of Plasma Sprayed Ceramic Coatings

R. C. Novak
United Technologies Research Center,
East Hartford, CT 06108

Experimental studies are described that demonstrate that variation in plasma spray process parameters has a substantial effect on the fundamental mechanical, thermal, and physical properties of ceramic coatings. This property variation is shown to influence the behavior of the coatings under rig tests that simulate exposure in gas turbine engines. Illustrative examples are given to demonstrate the value of the designed experiment approach to understanding the coating process/coating behavior interaction. Finally, statistical process control methods are discussed and shown to be useful for identifying process control limits utilizing sophisticated in-process sensors.

Introduction

The key to developing thermal barrier ceramic coatings that will reliably meet all technical requirements, and that can be reproducibly fabricated with high yields in a production environment, is to take a systems approach to the problem. The successful coating begins with a definition of the thermal requirements, and the stresses generated due to thermal, mechanical, and other environmental factors, such as wear interactions, corrosion, erosion, etc., all of which combine to form design criteria for the coating. The next step involves identification of materials that meet the criteria and a process for fabricating them into the desired configuration. In this latter step, particular care must be taken to insure that the process is one that can be sufficiently controlled such that proper interpretation can be made of experimental results, the coatings will have the desired properties when fabricated in a production environment, and the process is one suitable for production and not just laboratory personnel.

Plasma spraying of zirconia-based materials is widely recognized as a generic approach to accomplishing these objectives. Thin (0.038 cm) thermal barriers have been utilized on production gas turbine components by United Technologies' Pratt & Whitney Division for many years. Recently, a very demanding ceramic coating also reached production status for Pratt & Whitney following the development approach outlined above. Based on this successful program, first and second-stage plasma sprayed zirconia-based turbine blade outer air seals are bill-of-material on the newest P&W engine models. These sprayed coatings are greater than 0.25 cm thick and operate at surface temperatures and through-thickness thermal gradients substantially in excess of those present in traditional thermal barrier coatings. More recently, this technology has been applied to developing thick thermal barriers for diesel engine components by Matarese (1987).

United Technologies Research Center (UTRC) participated in this development program in the area of materials and process technology. This paper describes the depth of understanding that has been achieved in plasma spraying thick ceramic coatings for the gas turbine and diesel applications, emphasizing the role of process understanding and control.

Process/Coating Behavior Relationships

The initial work in developing the material technology for the ceramic turbine seal involved defining the range of properties that could be produced by plasma spray, and determining how those properties could be controlled to meet the design requirements. One of the most critical criteria involved the definition of coating mechanical properties, and an early study was conducted to evaluate the effects that the plasma spray parameters have on the strength, modulus, and microstructure of plasma-sprayed zirconia discussed by Eaton and Novak (1986). The approach taken was to fabricate specimens by statistically selecting and varying the spray parameters. Free-standing samples were prepared and tested, then phenomenological modeling in combination with empirically derived mathematical functions were used to relate spray parameters to the measured properties. This resulted in a preliminary understanding of the fundamental mechanisms involved in the spray process that affect the material properties.

Figure 1 presents a summary of the results of this study. The open circles represent four point bend strengths of free standing ZrO_2/20 percent Y_2O_3 coatings sprayed under different conditions. The strengths are plotted against a combined plasma spray parameter that relates to the heating and velocity of the powder particles in the plasma stream. This parameter, which combines the process variables of power, arc gas flow, gun-workpiece distance, and gun-workpiece relative speed, was empirically formulated based on a model that strength of the plasma-sprayed ceramic was controlled by mechanical interlocking of molten powder splats. Thus, uniformly melted powder producing a tightly fitting, low-porosity microstructure would be stronger than a poorer fit-

---

Contributed by the International Gas Turbine Institute and presented at the 33rd International Gas Turbine and Aeroengine Congress and Exhibition, Amsterdam, The Netherlands, June 5–9, 1988. Manuscript received at ASME Headquarters March 7, 1988. Paper No. 88-GT-289.

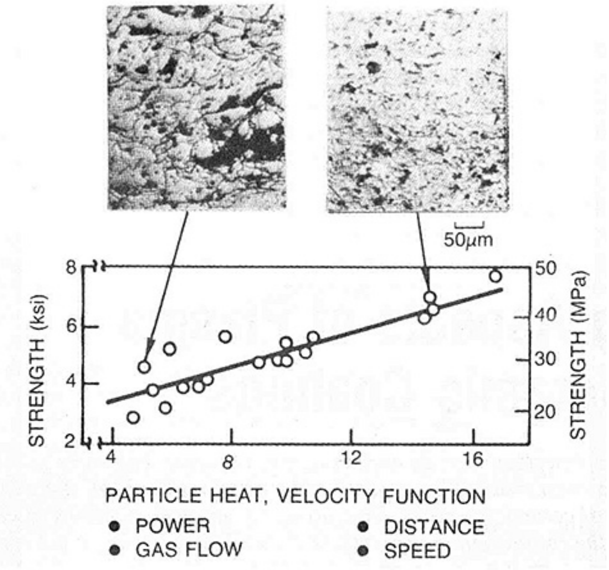

Fig. 1 Coating strength depends on process parameters

ting nonuniformly melted microstructure. The photomicrographs in the figure show that this was the case.

The calculated dependency of strength on the process variables is shown by the curve in Fig. 1. The correlation coefficient of the measured versus the predicted strength was 0.938, indicating that 88 percent of the measured variation was explained by the prediction. Although this was considered quite acceptable for providing developmental direction, there was still substantial variation in strength observed for supposedly identical conditions, especially for parameters which produced lower strength coatings.

In addition to the direct role of coating strength in resisting the thermally induced stress in the turbine seal, other critical behavior was found to be dependent on strength, as discussed by Eaton and Novak (1987). Resistance to erosion is important in maintaining the smallest possible clearance between the blade tips and the outer seals, and, therefore, an understanding of erosion behavior is key to the successful performance of the seals.

Data presented in Fig. 2 show that at 1315°C the erosion rate of plasma-sprayed zirconia, in terms of grams of material removed per kilogram of erodent particles, is dependent on the strength of the material. In this case, the strength was measured at first failure in the specimens rather than at the maximum load as in Fig. 1, but strength was again varied by changing the processing parameters. It was found that two mechanisms of erosion existed, dependent on coating strength. Below approximately 14 MPa, entire splats were removed by the erodent particles and the amount of material removed was strongly dependent on the strength. This mode of erosion was termed "fracture" since it involved fracture and removal of coating building blocks. At higher strength, the stress produced by impacting particles was insufficient to overcome the intersplat bonding. The mode changed to a plowing mechanism where much less material was removed and erosion rates were lower.

Another critical processing variable for plasma-sprayed ceramic coatings applied to metallic substrates is control of the substrate temperature during fabrication. Work by UTRC under subcontract to Cummins Engine on DOE/NASA Contract DEN3-331 has demonstrated that substrate temperature control can be used to manage the residual stress in the coating. This, in turn, can influence the performance of the coating for better or worse depending on the nature of the residual stress and the operating conditions.

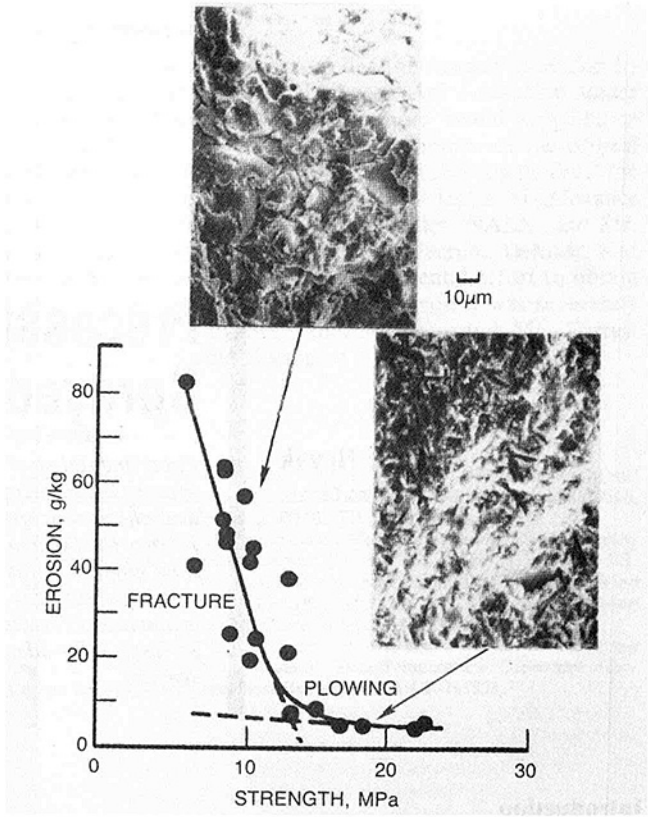

Fig. 2 Ceramic erosion controlled by strength

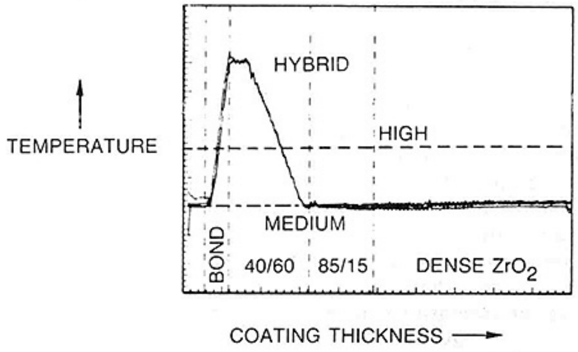

Fig. 3 Fabrication temperature used to control residual stresses.

Figure 3 shows three fabrication temperature profiles used in the development of a four-layer thermal barrier coating for diesel applications. The layers consist of a metallic bond coat, a 40 percent MCrAlY/60 percent ZrO_2 intermediate layer, an 85/15 intermediate layer, and a top layer of ZrO_2 (stabilized by 20 percent Y_2O_3). Medium and high profiles maintained a constant temperature over the entire thickness, while the hybrid profile involved a high temperature during the initial portion of the coating process; a constant temperature was then maintained for the remainder.

Thermal shock testing of samples fabricated using each of the three temperature profiles was conducted in a high-velocity, high-temperature air/kerosene combustor capable of generating gas temperatures up to 1815°C. Samples were exposed to increasingly severe surface-to-substrate thermal gradients, and it was found that the hybrid profile specimens could withstand gradients of up to 705°C with only slight cracks generated in the coating, while the other systems exhibited much greater cracking.

Processing Considerations

These examples of strength, erosion, and thermal shock

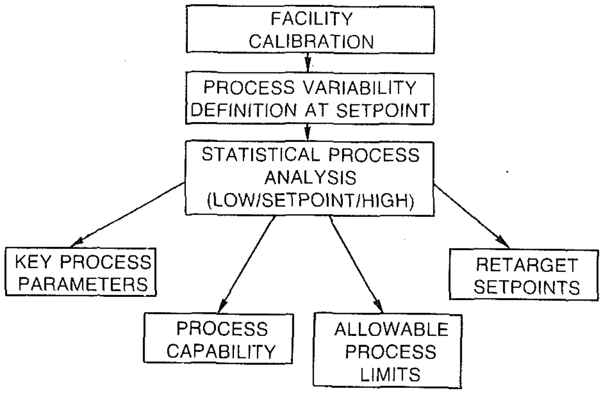

Fig. 4 Statistical process analysis for reliable spray manufacturing

behavior are illustrative of the general finding that the properties and performance of plasma-sprayed zirconia for the seal application are critically tied to an understanding and control of the plasma spray process. In response to this need, Controlled Process Plasma Spray (CPPS) fabrication methodology was developed by Matarese and Novak (1985). CPPS fabrication philosophy requires that all important spray process parameters be closed-loop controlled and/or recorded during fabrication, with subsequent review for assurance of conformity to desired standards. This assures the reliability and repeatability of coating quality necessary for proper interpretation of experimental results in development, and can serve as the foundation for statistical process control in production.

The plasma spray technology base, which relates plasma spray parameters to resultant mechanical and thermal properties of zirconia coatings, was utilized to define critcal spray parameters that most influence the desired material properties. To accomplish the necessary process monitoring and control, a unique plasma spray facility has been developed. The UTRC facility has been equipped with state-of-the-art equipment in commercially available sensors to monitor and/or control process variables such as gun power, gas flows, gun and part motion, and temperatures. All process data are computer monitored and stored, and are plotted at the end of the run to provide a record of the process.

Two sensors developed by UTRC were added to the system to provide additional process control. Both are built around the principle of radio isotope transmission gaging. The first measures the thickness of the coating while it is being sprayed and allows the spray operator to determine when to change from one material to the next in multilayer coatings without shutting down the gun, and also determines when the total intended thickness has been deposited. A similar radiation transmission gage was developed to measure the mass flow of powder delivered by the powder feeder to the plasma gun. This system is capable of closed-loop control such that the powder flow gage can continuously measure powder flow and adjust powder feeder delivery speed to maintain flow constant or varied throughout the spray run.

With this well-controlled and highly instrumented facility in place, a statistical process control (SPC) study is underway for the fabrication of gas turbine ceramic coatings. This information can be used both to insure the best possible performance of the coating, and to maximize the yield of acceptable quality parts. The overall methodolgy of the SPC study is given in Fig. 4. The initial phase involved calibration of all sensors in order to document their inherent accuracy. The second phase involved a definition of the variability of the baseline process, either through experience or by performing spray runs at set point conditions. Analysis of these data provided a definition of the mean values and limits of each of the process variables being monitored (amps, volts, gas flows, etc.). This information was then used to define processing conditions for the experimental phase of the study. In the final phase, the process was intentionally run at the statistically defined upper and lower operating limits ($\pm 3\sigma$) for the measured parameters, as well as at the set point conditions. This led to a definition of the most important process parameters and the inherent process variability, specification of the allowable limits on each of the parameters in order to fabricate acceptable parts, and a possible retargeting of selected parameters to improve yields and quality of the parts.

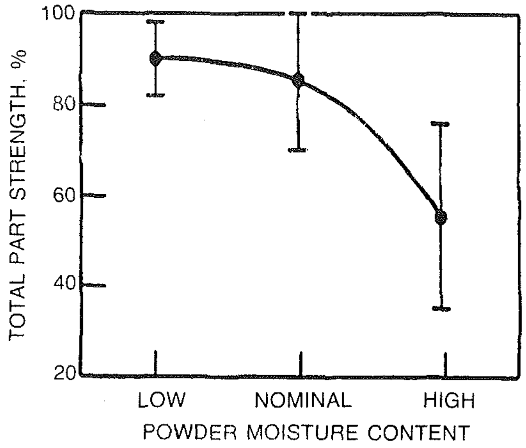

Fig. 5 Powder moisture content ranked as most influential parameter

Based on prior experience, ten processing parameters were selected as those most important in controlling the coating quality. These were:

Gun-part distance
Part speed
Gun speed
Powder carrier gas flow
Cooling jet gas flow
Powder feed rate
Gun power
Gun primary gas flow
Gun secondary gas flow
Powder preheat

A modified Taguchi test matrix was established to examine the ten variables, with the result that those parameters affecting the flow of powder into the plasma had the largest influence on the coating quality as measured by porosity, thickness, composition, and thermal shock resistance. Figure 5 shows how coating thermal shock behavior, measured by the percentage of parts which passed the test, was influenced by the moisture content of the powder prior to spray. Moisture content was varied by pretreatment of the powder by heat (low moisture), laboratory exposure (nominal), or humidity oven storage (high). High moisture content produced very erratic powder flow and a high standard deviation of flow during the run. This may have produced poor resistance to thermal shock. In general, it was found that conditions that produced erratic behavior (high standard deivation) of a process variable had a more harmful effect than well-controlled changes of the mean.

An example of how the SPC data can be used is shown in Fig. 6. Under the designed experiment phase of the program, ten runs were conducted at nominal set point conditions. The final run failed to meet the thermal shock quality criterion as shown by the post-test photomicrograph. A review of the SPC data showed that powder flow was the only parameter that fell outside the established control limits. The powder flow data for the ten runs are given on the left side of Fig. 6 for both the

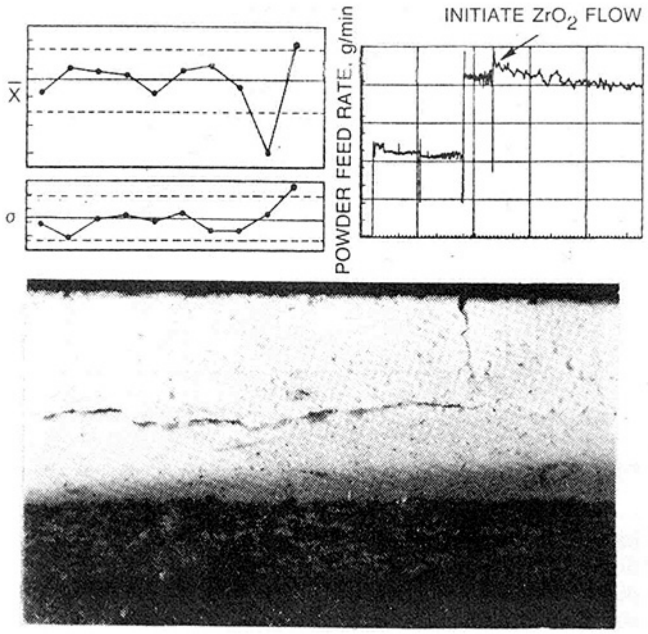

Fig. 6 SPC screening used to detect poor performing parts

mean $\bar{x}$, and the standard deviation σ. Both runs 9 and 10 fell outside the control limits for $\bar{x}$, but only 10 had a σ higher than expected. A review of the run 10 ZrO_2 feed rate data for pure ZrO_2 (right side of Fig. 6) indicated that the powder flow started too high, then drifted downward during the run. Subsequent examination of the powder feeder revealed a mechanical failure had occurred during the run causing the erratic performance. With SPC methodology in place in production, such parts, which violate control limit criteria, would be flagged and subjected to detailed inspection for a determination of acceptability.

Conclusions

Engineering performance and manufacturing producibility of plasma-sprayed ceramic coatings are closely tied to the processing parameters. In order successfully to develop coatings with the desired properties and to produce them in a reliable manner at high yield, it is necessary to understand the process/property relationships and to utilize processing technology that is capable of exerting the proper level of control.

Acknowledgments

The author wishes to acknowledge the contributions of the following individuals: H. E. Eaton, coating erosion and strength behavior; A. P. Matarese, statistical process control study; L. L. Packer, radio isotope gaging.

References

Eaton, H., and Novak, R., 1986, "A Study Concerning the Effects of Parameter Variations on the Strength and Modulus of Plasma Sprayed Zirconia," *Surface and Coatings Technology*, Vol. 27, pp. 257–267.

Eaton, H., and Novak, R., 1987, "Particulate Erosion of Plasma Sprayed Porous Ceramic," *Surface and Coatings Technology*, Vol. 30, pp. 41–50.

Matarese, A. P., and Novak, R., 1985, "Controlled Process Plasma Spray, CPPS, Techniques Produce Porous Metallic Coatings With Improved Properties," Internatioanl Conference on Metallurgical Coatings, San Diego, CA., Apr.

Matarese, A. P., 1987, "Thermal Barrier Coatings for Diesel Engines," Coatings for Advanced Heat Engines Workshop, Castine, ME, July.

A New Approach to Evaluating the In-Service Performance of Marine Gas Turbine Air Filters[1]

J. S. Hobday

J. Havill

Royal Navy,
Admiralty Test House,
Royal Aerospace Establishment Pyestock,
Farnborough, Hampshire, United Kingdom

Early work by the Naval Engineering Department of NGTE Pyestock, now RAE Pyestock, sought to define the Marine Aerosol through simple relationships between wind speed and aerosol size and distribution. Experience has shown the resulting Standard Aerosols to be unrepresentative of the actual conditions found in service. This paper describes a new approach using available ship and meteorological data and proven analytical techniques to generate a multivariable mathematical model of the Marine Aerosol embracing a wide envelope of operating conditions. It further describes how a simple model of a gas turbine air filter can be used in conjunction with the Marine Aerosol model and a model describing a ship propulsion system to predict the performance of the filter in terms of probable salt ingestion by the ship's engines. This versatile design tool can be used for direct or comparative assessments of separator applications for marine gas tubine propulsion engines and generating sets.

Introduction

With the pressure to reduce warship top weight and to make more space on the upper deck for weapons it is becoming increasingly important to keep the size and weight of marine gas turbine downtake systems to a minimum. To achieve this as complete an understanding as possible of downtake systems and marine gas turbine air filtration is required. The comparative trial of gas turbine air filters carried out for the Type 23 Frigate by the Naval Engineering Department at RAE Pyestock gave an opportunity for a reappraisal of the whole area of marine gas turbine air filtration. It also provided an opportunity for the updating of the filter test rig and its instrumentation.

The comparative trial highlighted the shortcomings in the definitions of the NGTE Standard Marine Aerosols against which the gas turbine air filters are tested. It also prompted the development of techniques to generate multivariable mathematical models of the Marine Aerosol and a ship's Gas Turbine Air Filtration systems. By simulating the ship's operating profile and the meteorological conditions the ship is likely to meet in service and by combining the mathematical models of marine aerosol, filtration, and ship propulsion systems, a very powerful investigative design tool can be produced, outlined in Fig. 1, able to predict the amount and concentration of salt that will be ingested by a marine gas turbine. A simulation of this type based on empirical data, and known or proposed ship configuration, provides a very flexible means of assessing, directly or comparatively, air filtration systems.

This paper describes the building of such a simulation and discusses its uses and merits.

Previous Work—Comparative Trial

Following the requirement to carry out a comparative trial of air filters for the Type 23 Frigate it was decided to update the instrumentation used for testing and the test rig itself. The main improvement was the acquisition of the Forward Scattering Spectrometer Probe (FSSP-100). This instrument replaced the Cassella Cascade Impactor as the means of measuring aerosol droplet size and distribution, dramatically improving measurement accuracy and resolution. The use of light-scattering rather than impaction techniques to measure droplet size and distribution has increased our knowledge and

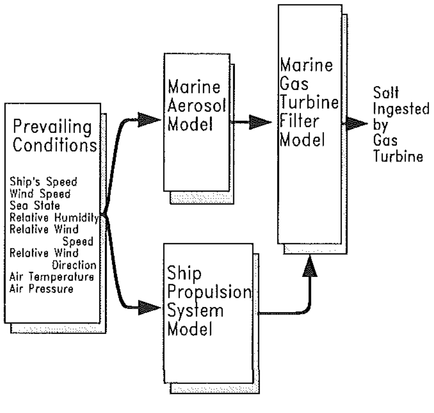

Fig. 1 Outline of simulation

---

[1] This paper expresses the views of the authors and not Ministry of Defence policy.

Contributed by the International Gas Turbine Institute and presented at the 33rd International Gas Turbine and Aeroengine Congress and Exhibition, Amsterdam, The Netherlands, June 5–9, 1988. Manuscript received by the International Gas Turbine Institute November 1987. Paper No. 88-GT-268.

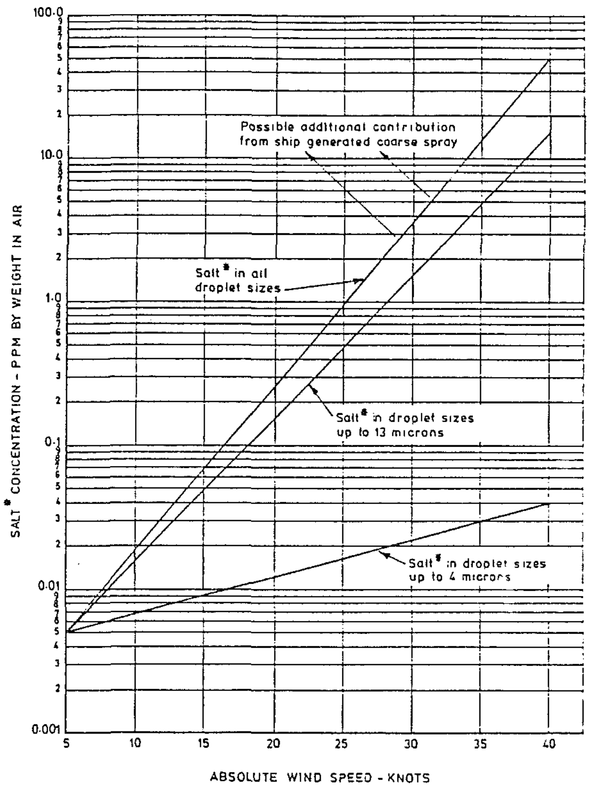

Fig. 2 NGTE Standard Marine Aerosols

understanding of filtration. The light scattering instrument's vastly improved resolution has given a much more complete and practical description of a filter's performance. The comparative trial also provided the opportunity to review previous work carried out in the gas turbine air filtration field. It revealed the work carried out by Featherstone (1979), which formed the basis for this paper. This review also raised two interesting and important questions, which are fundamental to understanding how the testing of marine gas turbine air filters has evolved.

The first question concerns the levels of salt that are acceptable downstream of the marine gas turbine air filter. Rolls-Royce stipulated a concentration of 0.01 ppm NaCl by weight in air as the maximum allowable salt ingestion limit from the inlet air. That limit determines the performance of the filters. How was the 0.01 ppm salt limit for Rolls-Royce engine derived?

The second question concerns the test used to check that filters are allowing through no more than 0.01 ppm salt. Obviously we would wish to test the filters against salt levels that are expected to be met in service in the marine environment. At the moment this is described by a range of three aerosols called the NGTE Standard Marine Aerosols. How were the NGTE Standard 20, 30, and 40 knot aerosols derived?

(*a*) **The Rolls-Royce 0.01 PPM Salt Ingestion Limit.** The Admiralty Test House in the 1960's carried out a series of trials on Proteus (Young and Attard, 1967) and Tyne (Clark, 1967) gas turbines in preparation for their use for marine propulsion and power generation. This pioneering work included an investigation into the effects that the presence of salt, both in the marine atmosphere and in the fuel, had on the engines. It soon became apparent that the materials used in aircraft engines were unsuitable when the engine was subjected to even modest concentrations of salt. Following these trials Rolls-Royce set the limits for salt ingestion for their engines, the airborne part of which was set at 0.01 ppm NaCl by weight in air.

(*b*) **NGTE Standard Marine Aerosols.** In an attempt to provide adequate filtration against salt in the marine atmosphere, standards were devised against which gas turbine air filters were to be tested. These were called the NGTE Standard Marine Aerosols (Randles and Ansari, 1972) and were intended to reflect the range of salt concentration levels and particle size distributions that the filters would be expected to deal with in service. The NGTE standard marine aerosols, proposed in 1971, were originally based on extrapolated data taken on board the USS MEREDITH as part of the Gas Turbine Combustion Air Salt Aerosol Separation Programme undertaken by NAVSECPHILADIV in 1965 (Kaufman and Pollini, 1968). They consist of three aerosols defined by sea-salt concentration and particle size in relation to wind speeds of 20, 30, and 40 knots (the 40 knot aerosol has not been used for some time however due to a lack of confidence in the aerosol composition). No humidity data are contained in the descriptions. The NGTE standard marine aerosol sea-salt concentration and particle size data are shown in Fig. 2.

The MEREDITH results were later discounted by NAVSECPHILADIV (Mihalek and Shen, 1977) as being incorrectly sampled following a further sampling trial carried out on board the Danish Frigate PEDER SKRAM (Young, 1966). In view of this, and a general lack of reliable marine aerosol data, two sampling studies were initiated by MOD (Navy). The first of these studies was carried out by Lovett (1975) on board UK weatherships stationed in the North Atlantic. The second far less extensive study was carried out by Westwood (1976) on board HMS TORQUAY shortly afterward. The results of the two studies confirmed the work of earlier researchers, such as Woodcock (1953), and highlighted various anomalies in the NGTE standard aerosols.

It can be seen from the data in Table 1 that there is good agreement between the relationships of sea salt to windspeed obtained by Lovett (1975), Westwood (1976) and the earlier work of Woodcock (1953). Table 1 also shows that the concentration of sea salt contained in the NGTE standard aerosol is some 12 times the mean value measured by Lovett at 20 knots and 87 times greater than at 30 knots. However the NGTE standard marine aerosols were not amended to reflect the change in understanding of the marine aerosol. The MEREDITH data were regarded as an overestimate of sea-salt concentration and would therefore serve as a severe testing standard for air intake sea salt separators.

In 1978 further work was done by Featherstone (1979) who investigated the techniques of regression analysis and Monte Carlo simulation to try to describe the Marine Aerosol and assess filter performance more accurately.

Nomenclature

ATM = air pressure
FFV = filter face velocity
H = inlet height
MMD = mass mean diameter
m = meter
P = penetration
ppm = parts per million
RH = relative humidity
RWD = relative wind direction
RWS = relative wind speed
s = second
SS = sea state
T = air temperature
TCDN = total salt concentration downstream of the filter
TCUP = total salt concentration upstream of the filter

Table 1 Comparison of the NGTE Standard Aerosols with Lovett, Westwood, and Woodcock models

Source	Regression Model	Concentration at 20Kt wind speed ppm ($\mu g/m^3$)	Concentration at 30Kt wind speed ppm ($\mu g/m^3$)
NGTE	–	0.22 (269.5)	3.6 (4422)
Lovett (all results)	$\mathrm{Ln}\,\theta = 0.16u + 1.45$	0.018 (22.0)	0.041 (50.3)
Westwood (all results)	$\mathrm{Ln}\,\theta = 0.14u + 1.7$	0.02 (24.5)	0.042 (51.6)
Woodcock	$\mathrm{Ln}\,\theta = 0.16u + 0.94$	0.011 (13.1)	0.025 (30.7)
	u= wind speed m/s θ= salt concentration ($\mu g/m^3$ NaCl)		

Mathematical Modeling

Aerosol Model—The Revised Marine Aerosol. A review of the measurements taken by both NGTE and the U.S. Navy has led to the conclusion that a revision of the standard aerosols for testing filters is required, not only with respect to the sea-salt concentration and particle size data but also whether those aerosol characteristics are solely dependent on the parameter of windspeed. When the first sampling trials were undertaken it would have been a very difficult and time-consuming task to analyze the way in which various parameters combined to influence the Marine Aerosol. It was recognized that wind speed played the major role in determining the salt concentration and particle size distribution and this determined the manner in which the marine aerosol was to be defined. With the advent of the computer more exotic and labor-intensive analytical techniques became available for general use, including multiple regression.

The data collected by Westwood (1975) and Lovett (1974) were used to produce regression models relating salt concentration to windspeed alone in the form

$$Y = A1 + A2 \cdot X \qquad (1)$$

where $A1$ and $A2$ are constants, Y is the dependent variable, and X is the independent variable.

Multiple regression allows the relationship between one dependent variable and many independent variables to be described mathematically. It gives models of the form

$$Y = A0 + A1 \cdot X1 + A2 \cdot X2 + A3 \cdot X3 + \ldots An \cdot Xn \qquad (2)$$

which describes the relationship between the dependent variable Y and the independent variables $X1$, $X2$, $X3, \ldots, Xn$.

Using the analytical technique of multiple regression it is possible to investigate the influence of any number of factors on the concentration of sea salt in the marine aerosol. Analyzing the data collected by Westwood (1976) in this way, it was found that 80 percent of the variation in sea-salt concentration could be accounted for by the inclusion of relative humidity, ship's speed, air temperature, relative wind speed, and relative wind direction in the windspeed model, an improvement of 30 percent over the Westwood windspeed model shown in Table 1.

Having determined the relationships between these variables using multiple regression, a mathematical model of the marine aerosol was produced. It has the form:

$$\begin{aligned} \mathrm{LnTCUP} = {} & A1 + A2 \cdot \mathrm{WS} + A3 \cdot S + A4 \cdot \mathrm{RH} + \\ & A5 \cdot \mathrm{RWS} + A6 \cdot \mathrm{RWD} + A7 \cdot \mathrm{SS} + \\ & A8 \cdot T + A9 \cdot \mathrm{ATM} + A10 \cdot H \qquad (3) \end{aligned}$$

where $A1$-9 are the regression coefficients; TCUP is the total salt concentration upstream of the filter (i.e., contained in the marine aerosol); S = ship speed; WS = wind speed; RWS = relative wind speed; RWD = relative wind direction; RH = relative humidity; T = air temperature; ATM air pressure; SS = sea state; H = inlet height, constant for specific intake.

By substituting values for each of the variables in equation (3) a value of the concentration of salt in the marine aerosol can be calculated. The mathematical model of the Marine aerosol produced by this method from observed data gives a far more realistic description than the NGTE Standard Aerosols because it describes the influence of many factors, not just the single one of windspeed.

Different sets of such values can be put into the mathematical model in order to determine the variations in salt concentration upstream of the gas turbine air filter over a wide range of conditions. It is also possible to determine the affect one particular variable has on the downstream salt levels. This can be achieved by taking nominal mean values for all variables except the one under investigation.

The majority of the parameters used in the equation describing the marine aerosol are weather dependent; the others are influenced by the way the ship is being operated. Mean values of these parameters may be used to determine how much salt the ship is likely to meet in service, but this would merely give a fairly crude answer. It would be far better to calculate the answer using the whole range of variation of each parameter and incorporating the proportion of time each parameter was at a particular value. In such a way a simulation of what a ship can be expected to meet in practice will be produced. This can be achieved using Monte Carlo techniques.

Monte Carlo Simulation. Monte Carlo methods were first used in 1908 for determining the statistical t distribution, but their present uses have evolved with the electronic computer from about 1947. The simulation of natural processes that are subject to continuing random disturbances is one application. It allows the use of chance to construct a simulation of a process under analysis in the same way that chance operates in the original system. All that is required is a mathematical model of the system under analysis and some sort of gambling device such as a roulette wheel weighted to simulate the input conditions of the model.

Rather than use weighted roulette wheels, one for each variable, to simulate the inputs to the model, it is much more efficient to use the random number generator of a computer. A value for each of the independent variables used in the mathematical model is generated at random within the limits and probabilities of each variable's known occurrence. Each set of values generated in this way is substituted in the mathematical equation describing the model and the answer calculated and stored. This process can be repeated as many times as required (the accuracy of the simulation increasing as the square of the number of iterations). Once this has been completed the results can be presented graphically for easy analysis and comparison.

The input data required to carry out a Monte Carlo simulation of a ship air filtration system can be obtained as follows:

Wind speed, air temperature, air pressure, relative humidity, and sea state are all weather dependent. The Meteorological Office can supply data from all over the world's oceans describing how these values vary over a particular month or the whole year. The data can be presented in histogram form indicating the proportion of time at each value.

The proportion of time a ship sails at a particular speed is determined by the way a ship is employed, and will either be known for a ship type or estimated for a new class of ship.

Relative wind speed and direction could be estimated for new classes of ship from data collected from existing ships carrying out similar duties.

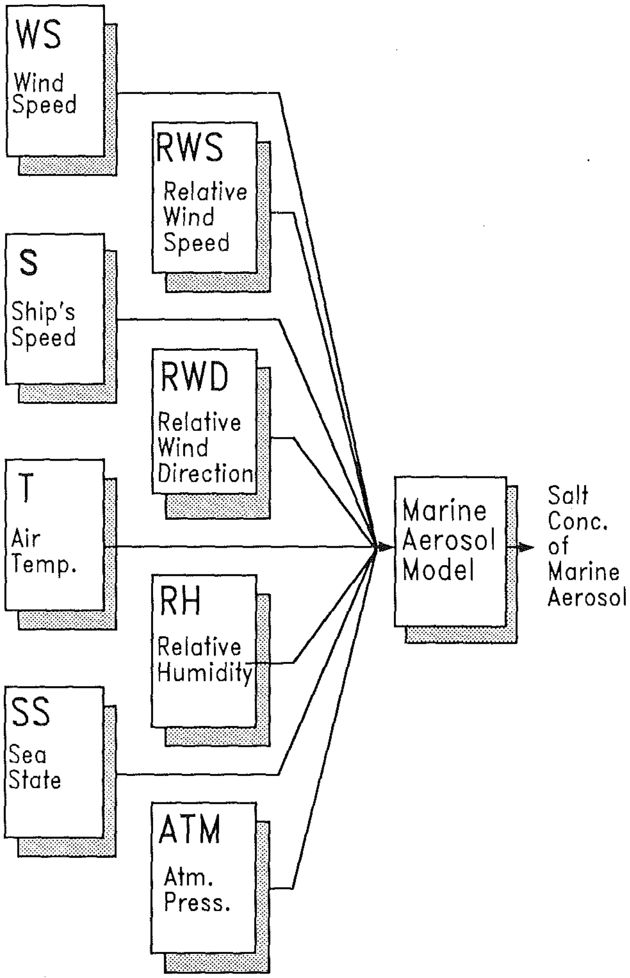

Fig. 3 Marine Aerosol Model

The process of calculating the concentration of salt in the marine aerosol is illustrated in Fig. 3. Statistical data describing the range of values for each parameter and their frequency of occurrence is sampled at random to give one value for each parameter. The values are used in the equation describing the marine aerosol to calculate the salt concentration. This process is repeated many thousands of times to ensure as accurate a result as possible. Each value of salt concentration calculated is stored. The frequency of occurrence of a particular salt concentration as a percentage of the total number of occurrences (or iterations) is plotted against salt concentration. The fraction of the total number of iterations is equivalent to the fraction of the total time; thus if for 50 percent of the iterations the salt concentration was below 0.1 ppm then the ship is likely to meet salt concentration less than 0.1 ppm for 50 percent of the time it is on patrol.

The Monte Carlo approach allows a far more realistic and accurate means of describing the marine aerosol. It is a dynamic definition of a dynamic natural phenomenon. It gives the ability to predict the outcome of the interaction of many variables. In this case it can be used to determine:

(*a*) the range of salt concentrations that can be expected in the marine aerosol; and

(*b*) the proportion of time that a ship will experience each level of salt concentration, in a particular geographic location, at a particular time of year, following a specific operating profile.

This can be expanded even further to simulate a ship's passage from A to B, patrol in area B, and return to A over a time span of months.

Predicting Engine Salt Ingestion. The Monte Carlo simulation of the Marine Aerosol allows a prediction to be made of the salt concentrations a ship's gas turbine air filtration system must be designed to cope with. This defines the performance required of the filtration system so that the ship's gas turbines are adequately protected.

In addition to estimates of salt concentration upstream of a gas turbine air filter, it would be very desirable to determine the salt concentration levels downstream of the filters, i.e., the levels of salt ingested by a gas turbine during its operation.

This information would be of great benefit in ship design; it would allow the selection of a filter, for a particular ship's propulsion system, to be made with much greater confidence. The possibilities of over or underdesign could be eliminated much earlier in the design process. Underdesign increases salt ingestion, reducing engine life, availability, and reliability. Overdesign may result in increased fuel consumption or increased ship topweight and reduced available space on the upper deck. Under and overdesign or inaccurate specification of filter performance can have very expensive consequences when a fleet of ships is considered.

In order to provide the designer with practical information, which describes how the filter performs in the overall ship system, some means of including the filter performance in a model of engine and ship operation is required.

The model of the marine aerosol has already been described. The models of the ship filtration and propulsion systems are outlined below.

Ship Filtration System Model. To be able to model a ship filtration system a mathematical description of how the gas turbine air filters operate is required.

The filter performs the function of removing salt water droplets and dry particles of salt from the gas turbines intake air. The performance of a filter can be described in terms of the effectiveness with which it removes salt from the inlet air (the efficiency of salt removal) or the proportion of the salt in the inlet air which is not removed (the penetration).

Penetration is a very useful parameter for modeling a filter because simple multiplication with the upstream concentration will give the downstream concentration using the following equation:

$$\mathrm{TCDN} = \mathrm{TCUP} \cdot P \qquad (4)$$

where TCDN is the total salt concentration downstream of the filter (i.e., ingested by the engine); TCUP is the total salt concentration upstream of the filter (i.e., the salt concentration of the marine aerosol); P is the air filter value of penetration (the proportion of the upstream salt concentration it allows through).

If the concentration of salt in the marine aerosol and the filter penetration are known at a particular instant, it is a simple operation to determine the salt concentration ingested by the engine. The problem arises, however, that the concentration of salt in the Marine Aerosol and the filter value of penetration both vary. In order to calculate the salt ingested by the engine over a period of time the first task is to obtain an accurate description of both of these two variables. The means of obtaining these descriptions in the form of mathematical models is outlined below.

The value of penetration for a filter is not a constant; it is affected by the filter face velocity, by the size distribution of the upstream aerosol spray (usually characterized by the Mass Mean Diameter (MMD)) and relative humidity.

The three-stage filters the Royal Navy uses remove virtually 100 percent of droplets/particles larger than 10μm. The efficiency of removal of smaller droplets/particles reduces with size until at 1-2 μm the removal efficiency could be as low as 50 percent in some circumstances. This means that when the

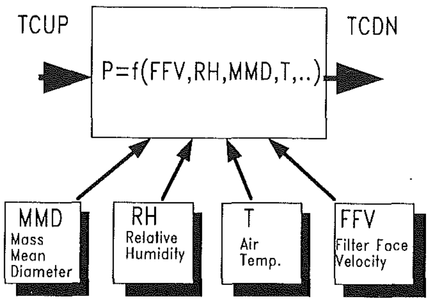

Fig. 4 "Overall" filter model

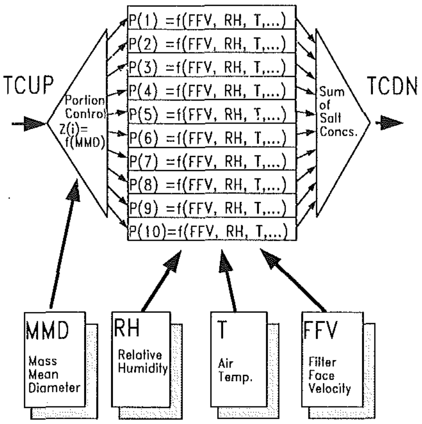

Fig. 5 "Composite" filter model

mass mean diameter of the upstream spray is small, meaning that a large proportion of the spray is made up of small droplets, more of the droplets and therefore more salt will pass through the filter than if the same concentration of salt were contained in an aerosol with a larger mass mean diameter.

Bearing in mind the above, there are two ways of modeling a filter:

(*a*) an overall view;

(*b*) a composite model made up of descriptions of the filter performance in distinct size bands.

Both of these models use the parameter of penetration.

(*a*) *The "Overall" Filter Model.* In this model the filter is considered to be a black box as shown in Fig. 4. The total concentration downstream is calculated as the product of the penetration and the total concentration of salt upstream as in equation (4). However as the value of penetration is dependent upon relative humidity, mass mean diameter, filter face velocity, etc., all these parameters must be taken into account to give the best answer.

This is achieved using multiple regression to produce a mathematical model from experimental data. The model will be in the form

$$P = A1 + A2 \cdot \mathrm{FFV} + A3 \cdot \mathrm{RH} + A4 \cdot \mathrm{MMD} + A5 \cdot T + A6 \cdot \mathrm{ATM} + \ldots \qquad (5)$$

The experimental data would be collected from rig testing under controlled conditions providing a wide variety of data.

(*b*) *The "Composite" Filter Model.* The composite model does not consider the overall penetration of the filter. It is composed of separate penetration functions for each particle size band width. Thus for each particle size band width there is a mathematical equation describing how the penetration varies with filter face velocity, relative humidity, etc., but, of course, not mass mean diameter. The concentration of salt downstream of the filter is calculated by summing the products of the concentration of salt and the penetration in each particular size band. This model is made complex by the need to apportion the appropriate amount of the concentration of salt to each size band. This is achieved by relating mathematically the mass mean diameter of the upstream aerosol to the proportion of the upstream concentration in each size band. This is illustrated in Fig. 5.

For any given upstram aerosol with a known concentration of salt and mass mean diameter, it is possible to calculate the concentration of salt downstream of a particular filter, given values for the variables which were used to produce the filter model, such as: filter face velocity (FFV); relative humidity (RH); air temperature (T); air pressure (ATM).

The Propulsion System Model. In describing the mathematical models of the Marine Aerosol and the filter we have found that both are functions of multiple variables. A list of them follows:

Filter Fact Velocity
Ship Speed
Relative Wind Speed
Relative Wind Direction
Relative Humidity
True Wind Speed
True Wind Direction
Air Temperature
Air Pressure
Sea State

Some of these variables can be considered to be independent of one another; others are interdependent.

Wind speed, wind direction, air pressure, air temperature, sea state, and relative humidity are all weather-dependent parameters. The geographic location and the time of year will have an overall affect on their range of values; however within that caveat the parameters are largely independent of one another (with the possible exception of wind speed and sea state).

Ship speed is also taken to be an independent variable. In practice the ship is unlikely to proceed at 25 knots in a force 10 gale; however this could be taken into account if required.

The filter face velocity of gas turbine air filters is a function of the ship speed. The speed of a ship dictates the power required to propel it through the water and this in turn will determine a range of acceptable engine states and conditions. A propulsion system model describing these interrelations has been produced based on the following.

Marine gas turbine air filters are designed to operate with filter face velocities between 3 and 9 m/s. The filter is matched to the engine by relating the swallowing capacity of the engine to the filter area to give approximately 3 m/s filter face velocity at idle and 9 m/s at full power. The relationship between engine power and ship speed is a cube law determined during the ship's design. Thus it is possible to determine, for a specific ship speed, the power generated by each of the ship's engines and therefore the filter face velocity of a particular engines filter system.

The ship's operating profile may also be described, i.e., how the ship is going to be used to perform a particular duty. A model of the propulsion system can be produced that gives a realistic description of how the engines would be run in service by relating the ship's operating profile to the rules governing the use of particular engines.

A propulsion system model of this sort allows us to determine the filter face velocity for a particular engine intake filter at a particular ship speed.

The Complete Model and Whole Ship Simulation. Combining the three models of marine aerosol, filter, and propulsion system it is possible to calculate the concentration of salt

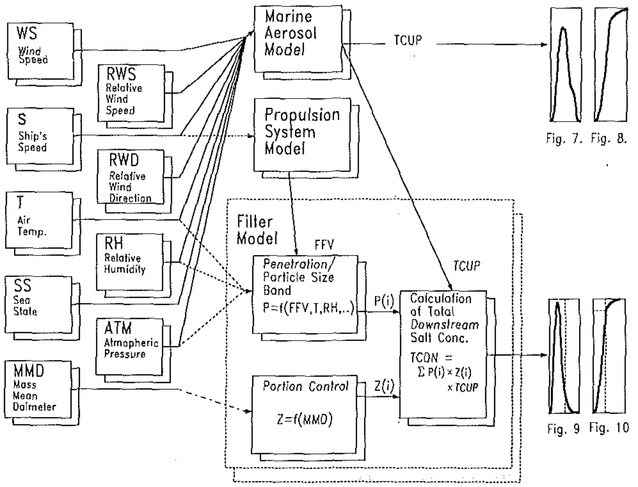

Fig. 6 Complete model

Predicted Salt Concentrations Upstream of Filter

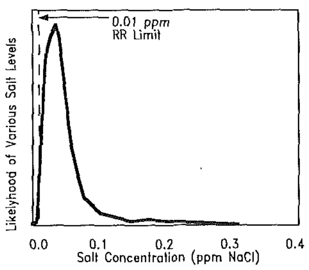

Fig. 7

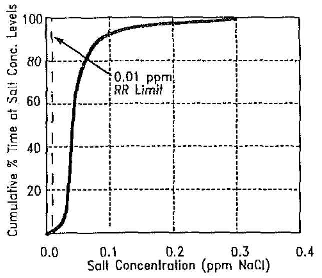

Fig. 8

Predicted Salt Concentrations Downstream of Filter

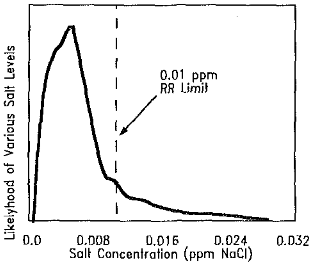

Fig. 9

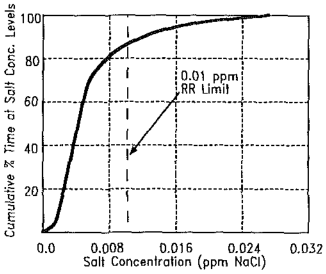

Fig. 10

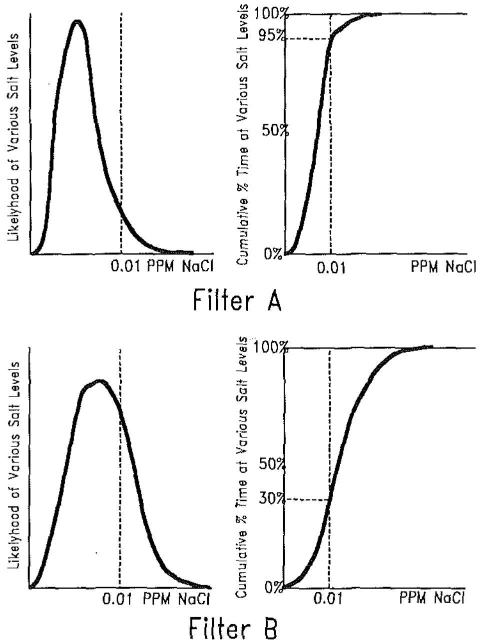

Fig. 11 An example of comparative filter performance

downstream of the filter for any combination of factors that may be found to have an effect. Such a model is illustrated in Fig. 6. Typical graphic representations of results produced using this simulation are shown in Figs. 7-10. Figures 7 and 8 show what can be expected upstream of the air filters, i.e., the marine aerosol. Figures 9 and 10 show how effective the filters are at keeping the salt ingestion limit below 0.01 ppm.

By using the model to simulate various situations it is possible to make a prediction of the salt levels each of the ship's engines are likely to encounter. The situations would differ due to many factors such as geographic location and time of year (both of which would determine prevailing weather conditions), ship's operating profile or type of duty (which will affect ship's speed, and if helicopter operations are a significant factor, relative wind speed and direction). It is also possible to compare the modeled "in-service performance" of different designs of air filter by keeping the geographic location, time of year, and operating profile constant. This is illustrated by comparing the downstream results from one filter, Filter A, with the downstream results from a rival filter, Filter B, shown in Fig. 11. It can easily be seen that Filter B if used in this propulsion system would allow the 0.01 ppm salt limit to be breached 70 percent of the time whereas with Filter A the limit is breached only 5 percent of the time.

Filtration systems may be tailored to suit different operating situations using information from this model. One filter may perform better in conditions of low humidity; another may be better suited to North Atlantic duties.

Perhaps the greatest benefit of this type of modeling is that the extent to which our ship gas turbine filters are over or under designed may be determined. For many years we have been testing air filters against rough approximations of the marine aerosol. We have marine gas turbine air filters that perform adequately. But can we say with confidence that the 0.01 Rolls Royce salt ingestion limit is never breached? Can we quantify by how much the filter is more efficient than the minimum requirement? If such information were available we would be able to see by how much our filters are overdesigned. An excessive margin of safety may be exchanged for a decrease in pressure drop across the filter with consequent saving in fuel costs.

The future should also be of concern. The next generation of marine gas turbines may have air filtration requirements that are altogether different from today's. Certainly reducing the size and weight of the filtration and intake systems will become even more important; the need to reduce warship top weight and provide more room on the upper deck for weapons and sensors will increase. This may involve the development of radically different air filters. The Monte Carlo simulation method described in this paper would provide a very flexible and powerful design tool, which could be used to assess and match any filtration system to an engine, thus avoiding the costly mistakes of over or underdesign.

Conclusion

The Standard NGTE Aerosols are questioned as accurate descriptions of the Marine Aerosol. It is proposed that a multiple regression model of the Marine Aerosol based on empirical data would give a much more accurate description.

By adopting multiple regression models of the marine aerosol and a marine gas turbine filtration system and combining them with a mathematical model of a ship propulsion system a whole ship model can be produced.

By using the whole ship model in a Monte Carlo simulation it is possible to predict the levels of salt ingested by a ship's gas turbines while carrying out its duties.

This whole ship simulation provides a flexible and powerful design tool, which can be used in the following ways:

(*a*) comparison of performance of filters of different design;

(*b*) the matching of filters to ship's propulsion system and ship's operating profile;

(*c*) providing information on whether and by how much filters are over or underdesigned for the protection they are installed to provide.

References

Clark, A. J., 1967, "Endurance Testing of a Rolls-Royce Tyne Engine in a Marine Environment," Naval Marine Wing Note No. 7/67, National Gas Turbine Establishment Pyestock, Hants, United Kingdom.

Featherstone, C. C., 1979, "The Application and Analysis of Marine Aerosol Data in the Evaluation of Marine Gas Turbine Air Intake Sea-Salt Separators," National Gas Turbine Establishment Memorandum M179120(M).

Kaufman, R. E., and Pollini, R. J., 1968, "Gas Turbine Combustion Air Salt Aerosol Separation Program," NAVSECPHILADIV Project T-454, Naval Ship Engineering Center, Philadelphia Division, Philadelphia, PA.

Lovett, R. F., 1975, "The Occurrence of Airborne Sea-Salt and Its Meteorological Dependence," M.Sc. Thesis, Heriot-Watt University, United Kingdom.

Mihalek, E. W., and Shen, C. N., 1977, "Real Time Test Techniques for Sea-Salt Aerosol-Separator Evaluation," ASME Paper No. 77-GT-29.

Randles, R. H., and Ansari, Z., 1972, "Evaluation of the Peerless Mark 1 Spray Eliminator for Protection of Marine Gas Turbine Air Intakes," Naval Marine Wing Note No. 30/71, National Gas Turbine Establishment Pyestock, Hants, United Kingdom.

Westwood, S. P. C., 1976, "An Investigation Into the Effects of Ship Movement on the Concentration and Particle Size and Distribution of the Marine Aerosol," M.Sc. Thesis, Royal Naval Engineering College, Manadon, Plymouth, United Kingdom.

Woodcock, A. H., 1953, "Salt in Marine Air as a Function of Altitude and Wind Force," *Journal of Meteorology*, Vol. 10, pp. 362–371.

Young, L. J., 1967a, "Proteus Salt Ingestion Trial," Naval Marine Wing Note No. 2/67, National Gas Turbine Establishment, Pyestock, Hants, United Kingdom.

Young, L. J., 1967b, "A Report of the Salt in Air Sampling Trials Carried out in HDMS Peder Skram, October/November 1966," NGTE Note No. NT. 648, National Gas Turbine Establishment Pyestock, Hants, United Kingdom.

H. Taniguchi

K. Kudo

Department of Mechanical Engineering,
Hokkaido University,
Sapporo, 060 Japan

W. H. Giedt

Department of Mechanical Engineering,
University of California,
Davis, CA 95616

I. Park

Department of Mechanical Engineering,
Hokkaido University,
Sapporo, 060 Japan

S. Kumazawa

Mayekawa Manufacturing Co., Ltd.
(MYCOM),
Tokyo, 135 Japan

Analytical and Experimental Investigation of Two-Phase Flow Screw Expanders for Power Generation

An analytical procedure for calculating the performance of a two-phase flow screw-type expander is presented. Predicted results are compared with experimental measurements made with a recently developed prototype expander. This expander was designed for investigating the applicability of this type of machine as the expansion device in refrigeration or heat pump cycles with the objective of taking advantage of the power-producing capability of the expanding fluid. It has two rotors each with a diameter of 81.6 mm and a length of 135 mm, and was operated with Freon-12 entering at a pressure of 1.588 MPa (230.4 psia) and subcooling of between 2 and 12 K. Maximum power generated was 10 kW at a rotor speed of 3000 rpm. The internal (machine) efficiency is predicted to increase from about 30 to 70 percent as the rotor speed increases from 500 to 3000 rpm. Experimental results over this same speed range increase from 30 to 60 percent. The lower experimental values at the higher rotor speeds are attributed primarily to frictional losses not included in the analysis. Estimates of the performance of machines with larger diameter rotors yielded internal efficiencies reaching 80 percent and increases in power output proportional to the square of the rotor diameter.

Introduction

In the usual vapor compression cycle used for heat pumps or refrigerators, the refrigerant undergoes an irreversible constant-enthalpy change as it is expanded through a throttling device from the condenser pressure to the evaporator pressure. Although this change has the potential for producing power, a simple, reliable, efficient, and economical machine through which a subcooled or saturated liquid would expand isentropically is needed. Recent investigations (reviewed in Steidel et al., 1982) of the use of a screw-type expander for generating power from low quality (~10-20 percent) geothermal fluids indicated that this type of machine should be suitable for use in heat pump and refrigeration systems. Since they operate on the principle of volumetric expansion, such machines can be expected to function without erosion and slip losses between liquid and vapor under two-phase flow conditions.

In regard to anticipated performance, Steidel et al. (1982) reported a maximum efficiency of 58 percent at 8000 rpm when using steam-water mixtures with inlet quality varying from 0.08 to 0.27. The possibility of efficiencies on the order of 60 percent was further supported by the experiments of Hijikata and Mori (1982) with a Wankel type rotary engine and Fujii et al. (1983) with a radial outflow reaction-type turbine, both driven by steam-water mixtures.

On the basis of these results, the desirability of using a screw expander in a district heating system incorporating a heat pump cycle was investigated in a design study (Taniguchi et al., 1983). Calculations showed that the heat rate that could be supplied would be increased by around 10 percent if the expansion device were replaced with a power-producing expander. A pilot plant of the proposed system was constructed and tested (Kudo et al., 1985). Results showed that the power recovered by the expander increased the heat rate supplied by the system by 2.4 percent. Although not a dramatic increase, this improvement was estimated to make the addition of an expander to the system cost effective.

In view of the satisfactory operation of the prototype machine in the district heating pilot plant tests, and interest in other applications, the present analytical study of the performance of a screw-type expander powered by subcooled or saturated liquid was undertaken. The objective was to develop and verify experimentally a calculational procedure with which (1) the performance of a particular machine could be estimated and (2) the effects of rotor size and speed could be investigated. The screw-type machine is simulated by two pistons in a cylinder with the working fluid expanding between them. Special attention was given to characterizing the flashing of the liquid as it enters and to accounting for the numerous leakage paths that exist in a screw machine. The

---

Contributed by the Advanced Energy Systems Division for publication in the JOURNAL OF ENGINEERING FOR GAS TURBINES AND POWER. Manuscript received by the Advanced Energy Systems Division June 27, 1986.

latter were found to have a very significant effect on performance.

Screw Expander Development and Operation

The original development of the screw machine is credited to A. Lysholm (see Steidel et al., 1982, for an interesting review). Today Lysholm gas compressors are widely used. Their performance has been analyzed by Fujiwara et al. (1984, 1985). Analysis and tests of a gas-driven screw expander (frequently referred to as a Lysholm engine) have been carried out by Shigekawa (1984) and Kaneko and Hirayama (1985). Peak adiabatic efficiencies of 70-73 percent were reported. In recent tests of gas-powered expanders conducted by Myers et al. (1985), a peak efficiency of 84 percent was obtained, with higher values projected for larger machines.

The components and the operation of a screw expander are illustrated in Fig. 1. The counterrotating male and female rotors mesh like parallel mounted helical gears. Work is produced by the expansion of fluid contained in V-shaped volumes between the lobes of both rotors and the casing. Starting with one set of lobes of the male and female rotors just separating at the intake end, saturated or subcooled working fluid flows through the intake port into the volume formed between these two lobes and the casing. The force of the fluid (and the vapor formed as flashing begins) against the rotors causes them to rotate and do work. As indicated in Fig. 2, this inflow process occurs as the male rotor rotates from 10 to 120 deg. At this point, the trailing lobes shut off the intake port and the working fluid continues to expand as the volume between the lobes increases (see Fig. 2). When the angle of rotation reaches 400 deg, the forward lobes of the two rotors reach the exhaust port and the working fluid begins to flow out. This process continues through a rotor rotation angle of 400 to 720 deg.

Because of necessary clearance tolerances between moving parts, the screw expander has several inherent internal leakage paths, which are shown in Fig. 3. These are classified into two categories: (1) The first accounts for leakage between adjacent expansion or working volumes and includes the leakage paths at B (through the seal line between rotor and casing), at D (through the triangular opening formed by the rotors and casing), and at C and F (clearance between the rotor ends and the casing end plate); (2) the second accounts for leakage between expansion volumes and the discharge port and includes the leakage paths at A (clearance between male and female rotors), and at E and G (clearances between the rotor ends and

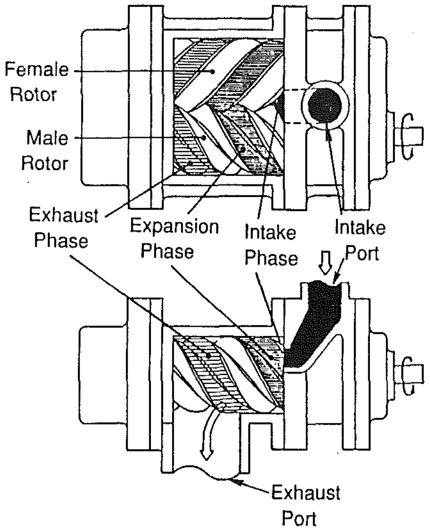

Fig. 1 The operating processes of a screw expander

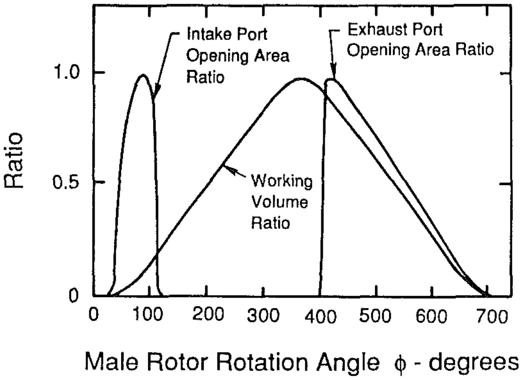

Fig. 2 Variations of intake and exhaust port areas and working volume with rotor angle

Nomenclature

A = area
D = rotor diameter
E = bulk modulus of working fluid in liquid state $= v/(\partial v/\partial p)_T$
G = mass in expansion volume
H, h = enthalpy, specific enthalpy
M = mass flow rate
N = rotational speed of male rotor
p = pressure in expansion volume
$t, \Delta t$ = time, small time step for calculations
T = temperature
u = specific internal energy
v = specific volume
V = expansion volume between consecutive lobes and machine casing
ΔV = change in V in time Δt
W = work output per cycle of fluid in an expansion volume
W_e = work output per unit mass of fluid in an expansion volume
W_i = predicted work output per unit mass of fluid in an expansion volume
x = quality of working fluid
α = flow coefficient
η_i = internal efficiency
η_v = flow ratio
ξ = adiabatic expansion efficiency
ρ = density
τ = bubble formation delay time
ϕ = male rotor angle

Subscripts

a = analytical
e = experimental
fb, fa = before, after flashing
g, l = gas, liquid
n = iteration number
in, out = incoming, outgoing
int, ex = intake, exhaust
is, ie = start, end of intake phase
lk = leakage
sat = saturated
sc = subcooled
— = average value during Δt

the casing end plates). The estimated change (based on machine design clearances) of these leakage areas with the male rotor angle is shown in Fig. 4.

Physical Model and Solution Procedure

For the analysis the operation of a screw expander was simulated by the expansion of a two-phase fluid between two pistons with appropriate leakage paths. The model is illustrated schematically in Fig. 5. The variation of the volume contained between two consecutive lobes and the casing (i.e., the expansion or working volume) is known as a function of rotor rotation angle (Fig. 2). This determines the volume between the pistons in Fig. 5 and their relative locations as a function of time.

As indicated by this model the work output of a screw expander is produced by an adiabatic (close to isentropic) expansion of the working fluid. However, the performance is significantly influenced by leakage between working volumes and directly to the exhaust. This leakage depends on pressure differences, which vary as the working fluid progresses through the expander. To account for this leakage a numerical solution was developed to carry out the analysis in small time steps. The solution procedure is divided into intake, expansion, and exhaust phases, and is described in the following sections and illustrated schematically in Fig. 6. The basic governing relations are conservation of mass and energy and the equation of state of the working fluid.

Numerical Solution Procedure. Operating conditions selected were the intake and exhaust pressures, p_{int} and p_{ex}, the degree of subcooling of the working fluid ΔT_{sc}, and the male rotor rotational speed N. These are specified as input data along with a time step Δt, and an exhaust port flow coefficient α_{ex}. A bubble formation time τ is included to investigate the effect of delay time in flashing.

Calculations were initiated with estimated constant values for the intake port flow coefficient α_{int} and an average leakage path flow coefficient α_{lk}. These were the only quantities varied for a given set of operating conditions. At the end of each cycle calculation the values of α_{int} and α_{lk} were changed and the calculation repeated until there was effectively no change in the final calculated pressure in the working volume. This condition was satisfied by specifying that $|p_{\text{change}}|/p \leq ER_{\max}$, where p_{change} is the difference between the final pressures of the last two iterations and $ER_{\max}$ is a specified convergence requirement.

Intake Phase. During the intake phase before flashing of the working fluid is initiated, the net mass increase in the working volume for a small time step Δt^1 can be calculated as

$$\rho_l \Delta V = \Delta G_{int} + \Delta G_{lk,\,in} - \Delta G_{lk,\,out} \tag{1}$$

where ΔV is obtained by differentiating the expansion volume ratio shown in Fig. 2. The intake mass flow is given by

$$\Delta G_{int}/\rho_{int} = \Delta t \bar{A}_{int} \alpha_{int} [2(p_{int} - p)/\rho_{int}]^{1/2} \tag{2}$$

The leakage flow terms $\Delta G_{lk,\,in}$ and $\Delta G_{lk,\,out}$ are calculated from

$$\Delta G_{lk}/\rho_{lk} = \Delta t \bar{A}_{lk} \alpha_{lk} [2\Delta p/\rho_{lk}]^{1/2} \tag{3}$$

where the $\bar{A}_{lk}$ are obtained from Fig. 4. Since accurate values for Δp are not known initially, the ΔG_{lk} are set equal to zero during the first iteration. Appropriate values for the pressures during subsequent cycle calculations were then automatically selected from the previous cycle results.

The liquid working fluid begins to flash when the pressure drops below the saturation pressure p_{sat}. The time at which this occurs is denoted by t_{sat} and will depend on the degree of subcooling. To account for the possible delay in vapor formation after p_{sat} is reached, a bubble formation time τ was introduced. Values of τ investigated are listed in Table 2. Assuming thermodynamic equilibrium as the liquid working fluid begins to flash during the intake phase, property values are calculated as follows:

$$\Delta V_{fb-fa} = -\Delta p_{fb-fa} V_{l,fb}/E \tag{4}$$

$$V_{fa} = \{x_{fa} v_g(p_{fa}) + (1 - x_{fa}) v_l(p_{fa})\} G_{fa} \tag{5}$$

$$u_{fa} = x_{fa} u_g(p_{fa}) + (1 - x_{fa}) u_l(p_{fa}) \tag{6}$$

where ΔV_{fb-fa} is the volume decrease of liquid working fluid due to the pressure increase Δp_{fb-fa} resulting from flashing. The expression $v_g(p_{fa})$ indicates that the specific volume of the vapor is a function of p_{fa}. The pressure is determined from the equation of state data for the working fluid.

During the intake phase after the initiation of flashing, conservation of mass in the expansion volume is expressed by

$$(V + \Delta V)/(G + \Delta G_{int} + \Delta G_{lk,\,in} - \Delta G_{lk,\,out})$$
$$= (x + \Delta x) v_g(p + \Delta p) + \{1 - (x + \Delta x)\} v_l(p + \Delta p) \tag{7}$$

in which

$$\Delta G_{int}/\rho_{int} = \Delta t \bar{A}_{int} \alpha_{int} [2\{p_{int} - (p + \Delta p)\}/\rho_{int}]^{1/2} \tag{8}$$

and the leakage flow terms $\Delta G_{lk,\,in}$ and $\Delta G_{lk,\,out}$ are evaluated using equation (3). Assuming the expansion to be isentropic, conservation of energy is expressed by the following relation:

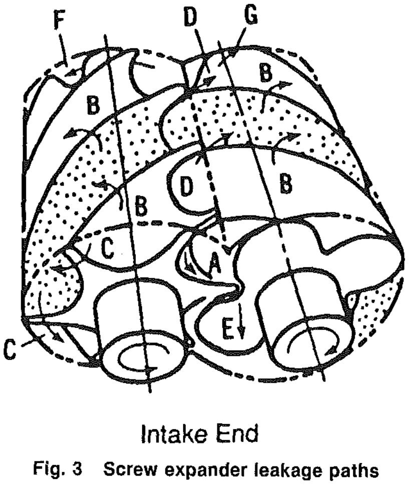

Fig. 3 Screw expander leakage paths

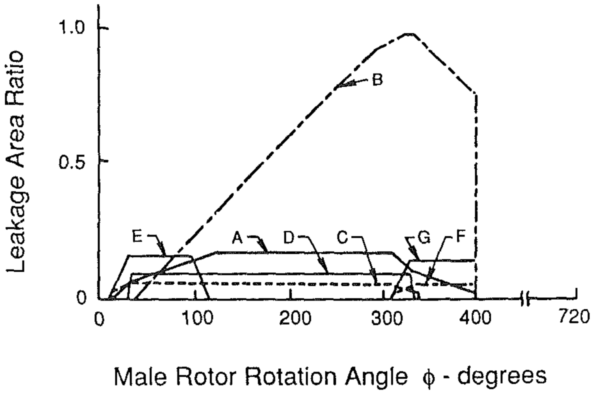

Fig. 4 Variations of leakage areas with rotor angle

---

[1] Final calculations were made with the time step Δt specified as the time for the rotor to turn through an angle $\Delta\phi$ of 1-2 deg during the intake and exhaust phases and 5-10 deg during the expansion phase. These values were found to yield the same results as shorter time steps, indicating that possible second-order effects not included in the finite difference solution procedure were negligible.

$$\Delta G_{int} h_{int} + G\{xu_g(p) + (1-x)u_l(p)\} + \Delta G_{lk,\,in} h_{lk,\,in} - \Delta G_{lk,\,out} h_{lk,\,out} = (G + \Delta G_{int} + \Delta G_{lk,\,in} - \Delta G_{lk,\,out}) \bullet [(x+\Delta x)u_g(p+\Delta p) + \{1-(x+\Delta x)\}u_l(p+\Delta p)] + \bar{p}\Delta V \quad (9)$$

in which $\bar{p}$ is the average pressure during the time increment Δt. Computed results provided the starting values for a new time step Δt. This procedure is continued until the end of the intake phase ($\phi = 120$ deg).

Expansion Phase. After a working volume is closed off from the intake port, the governing equations during the expansion or working phase are obtained by simply setting $\Delta G_{int} = 0$ in equations (7)–(9). If the time for bubble formation τ is relatively long, it is possible that initiation of flashing of the liquid working fluid will not occur during the intake phase. In this case the working volume will contain only liquid at the end of the intake phase. Hence, as the intake port closes and the expansion phase begins, the initial increase in working volume will cause the pressure of the working fluid to drop effectively to zero. After the time for bubble formation has elapsed, flashing begins and conservation of mass and energy are expressed as follows, assuming that thermodynamic equilibrium conditions are realized after the flashing initiation:

$$\left[V_{ie} + \sum_{t_{ie}}^{t_{fa}} \Delta V\right] \Big/ \left[G_{ie} + \sum_{t_{ie}}^{t_{fa}} \Delta G_{lk,\,in} - \sum_{t_{ie}}^{t_{fa}} \Delta G_{lk,\,out}\right] = x_{fa} v_g(p_{fa}) + (1 - x_{fa}) v_l(p_{fa}) \quad (10)$$

$$\sum_{t_{is}}^{t_{ie}} \Delta G_{int} h_{int} + \sum_{t_{is}}^{t_{fa}} \Delta G_{lk,\,in} h_{lk,\,in} - \sum_{t_{is}}^{t_{fa}} \Delta G_{lk,\,out} h_{lk,\,out} - \sum_{t_{is}}^{t_{fa}} \bar{p}\Delta V = \left(G_{ie} + \sum_{t_{ie}}^{t_{fa}} \Delta G_{lk,\,in} - \sum_{t_{ie}}^{t_{fa}} \Delta G_{lk,\,out}\right) u_{fa} \quad (11)$$

in which ΔG_{int} is calculated using equation (2) and $\Delta G_{lk,\,in}$ and $\Delta G_{lk,\,out}$ using equation (3).

Exhaust Phase. The exhaust volume flow during a time increment Δt is then given by

$$\Delta G_{ex}/\rho_{ex} = \Delta t \bar{A}_{ex} \alpha_{ex} [2(p - p_{ex})/\rho_{ex}]^{1/2} \quad (12)$$

Conservation of energy requires that

$$G\{xu_g(p) + (1-x)u_l(p)\} - \Delta G_{ex}\{xh_g(p) + (1-x)h_l(p)\} = (G - \Delta G_{ex})[(x+\Delta x)u_g(p+\Delta p) + \{1-(x+\Delta x)\}u_l(p+\Delta p)] + \bar{p}\Delta V \quad (13)$$

These calculations are continued until the pressure in the working volume falls below the exhaust pressure p_{ex}. The convergence criterion is then checked. This is to compare the fractional change of the final calculated pressures in the working volume for the last two iterations ($|p_n - p_{n-1}|/p_n$) with a specified convergence requirement $ER_{\max}$. If this was not satisified, values for α_{int} and α_{lk} were modified and the working fluid cycle recalculated.

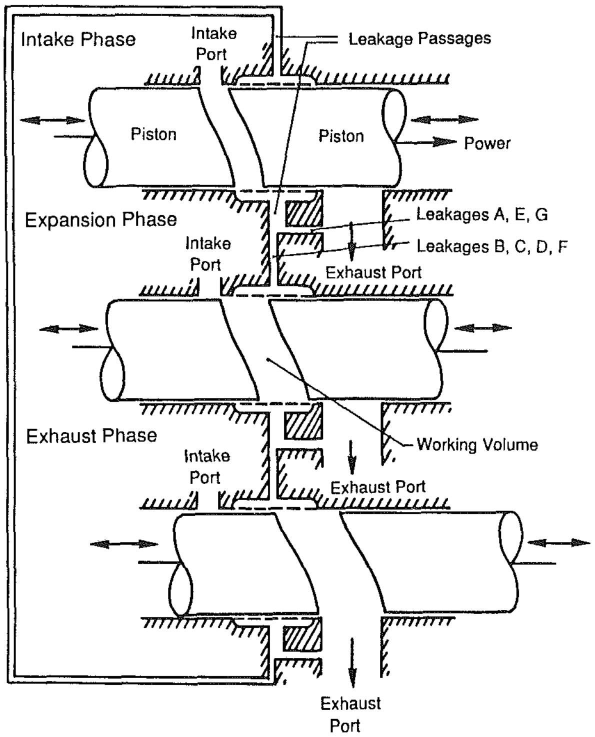

Fig. 5 Model of screw expander

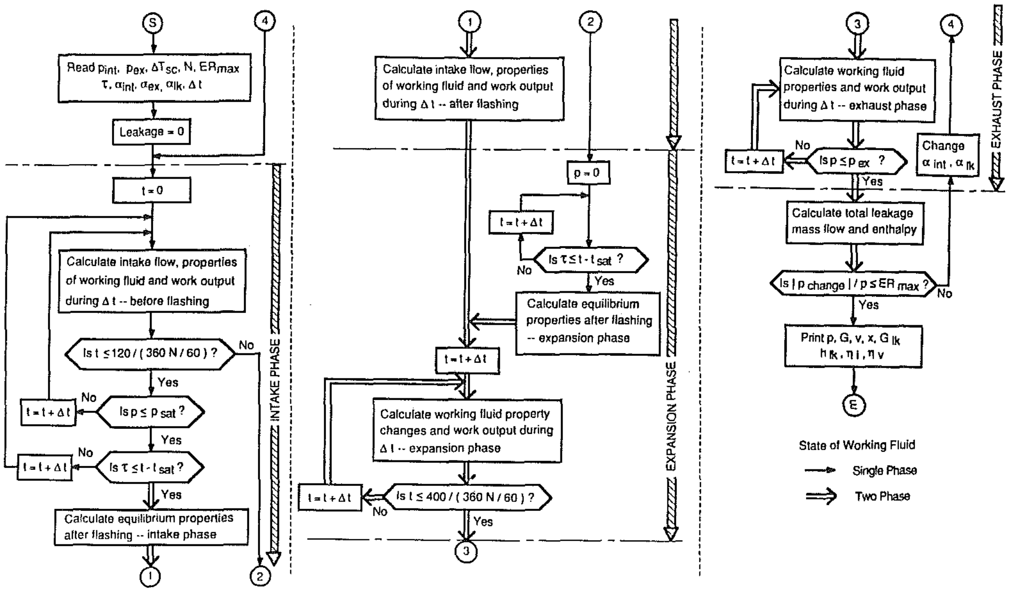

Fig. 6 Flow chart of numerical solution procedure

Leakage Calculations. It was recognized that appropriate values for the α_{lk} could be different depending on whether the leaking working fluid was in the liquid or in the two-phase state. They could also be affected by the different velocities of the walls forming the leakage paths (the possibility of choking was considered negligible since all the leakage paths, except between the rotor ends and the casing, can be regarded as sharp-edged orifices). However, since specific information about the individual leakage paths is not available, it was decided to use single average values for α_{int} and α_{lk} for any set of operating conditions. It was anticipated that this would be satisfactory because a substantial amount of leakage will occur in two paths, E and B, and that flow through both would be in the liquid phase. From Fig. 4 note that the path with the largest area during intake is E through which liquid from the working volume escapes to the exhaust port. Path B, which is between the rotor tips and the casing, is much larger. The thickness of the liquid film formed on the inner surface of the casing near the exit due to centrifugal force was estimated to be 2.5 mm. The clearance between rotor tips and the casing is less than this. Hence, the fluid flowing through these two paths should be in the liquid phase.

Process Efficiencies. The experimental internal efficiency[2] of the expander η_{ie} is defined as the ratio of the measured useful work output per unit of mass flow W_e to the isentropic specific enthalpy drop Δh. This will be compared to a predicted internal efficiency η_{ia}, which is the ratio of the predicted work output W_a per unit of mass flow (net expansion work) to Δh. The value of W_e is measured experimentally; W_a is determined from the summation the $\bar{p}\Delta V$ outputs in equations (9) and (13) over the time for a complete working volume cycle. An experimental flow ratio η_{ve} is defined as the quotient of the measured intake mass flow per cycle to the ideal intake mass flow per cycle M_{ideal}. An analytical or predicted flow ratio η_{va} is determined as the quotient of the calculated mass flow per cycle M_{cal} to the ideal intake mass flow per cycle M_{ideal}. The calculated M_{cal} is the summation of the intake mass flows

$$\left(\sum_{t_{is}}^{t_{ie}} \Delta G_{int}\right)$$

from equations (2) and (8), and M_{ideal} is the intake mass flow that would occur if there were no leakage and no pressure drop across the intake port during the intake phase. That is, M_{ideal} would be the mass of liquid at p_{int} required to fill the working volume completely at the end of the intake phase. If there were no leakage, this condition would be approached at low rotor speeds.

Experimental Apparatus and Procedure

A schematic diagram of the experimental apparatus is shown in Fig. 7. Saturated or subcooled R12 Freon at a pressure of 1.588 MPa (230.4 psia) was supplied as the working fluid. After flowing through the screw expander it is discharged to a vapor–liquid separation tank. The vapor from the tank is compressed and then liquefied as it passes through a condenser. From the condenser the liquid flows to a low-pressure tank. Liquid from the gas–liquid separation tank and from the low-pressure tank is compressed and heated to a subcooled or saturation condition as it is returned to the screw expander. The expander outlet pressure was regulated by controlling the volumetric output of the compressor. The mass flow rate of the working fluid entering the expander was measured with a turbine meter.

An experimental program was carried out to validate the screw expander model and performance calculation procedure developed. Rotor characteristics and dimensions are listed in Table 1. Ranges of experimental and analytical conditions investigated are given in Table. 2. Martin's equation of state (Downing, 1974) was used to determine the thermodynamic properties of the working fluid (Freon R12).

Discussion of Analytical and Experimental Results

Indicator Diagrams and Flow Coefficients. The pressure variation of the working fluid as it passes through the expander, as predicted from the analytical procedure described previously, is shown in Fig. 8 for intake and exhaust conditions used during tests. These curves are referred to as indicator diagrams, since they are similar to such records obtained from reciprocating engines. Diagrams are shown for three cases: (1) with no pressure drop across the intake port and no leakage (ideal case), (2) with pressure drop across the intake port without leakage, and (3) with pressure drop across the intake port and leakage (real case). The flow coefficients for the intake port and the leakage paths are empirical con-

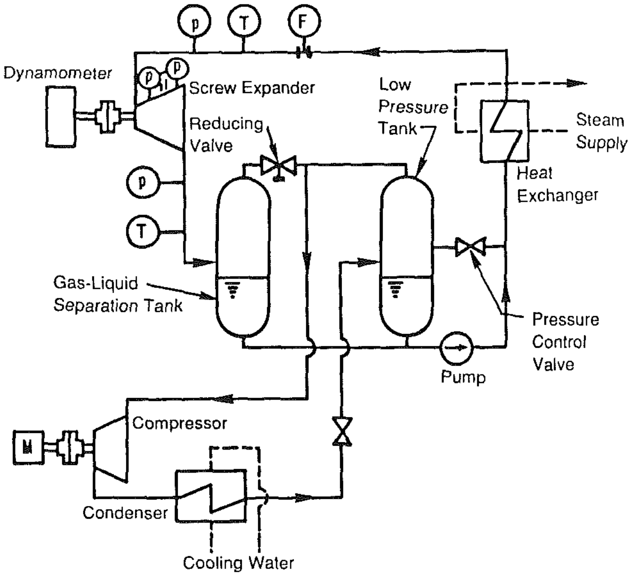

Fig. 7 Screw expander test system

Table 1 Characteristics and dimensions of test expander rotors

Male rotor	4 lobes
Female rotor	6 lobes
Rotor diameters	81.6 mm
Rotor lengths	135 mm
Volume ratio*	5
Wrap angle	300 deg
Lobe profile	Asymmetric

* Ratio of maximum volume between lobes during expansion phase to intake phase volume.

Table 2 Ranges of operating conditions and characteristics; working fluid: R12

p_{int}	1.588 MPa	α_{int}	0.72–0.76
p_{ex}	0.490 MPa	α_{lk}	0.35–0.65
ΔT_{sc}	2–12 K	α_{ex}	0.85
N	500–3000 rpm	τ	0–3 msec

---

[2] The terms "adiabatic efficiency" or "machine efficiency" are also used.

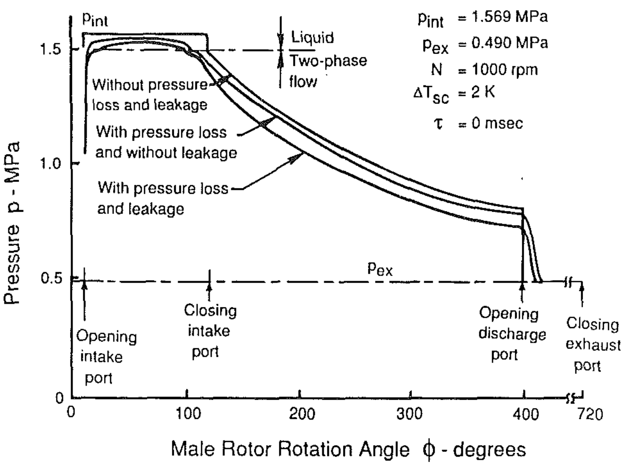

Fig. 8 Typical predicted working volume pressure variation

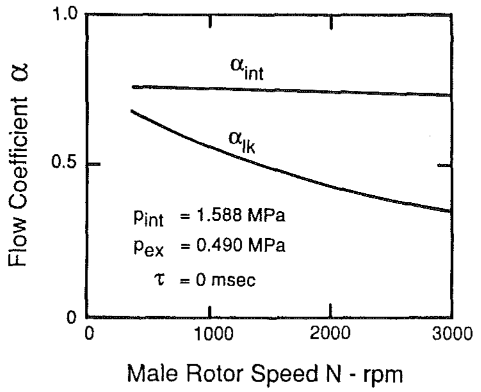

Fig. 9 Variations of flow coefficients with male rotor rotational speed

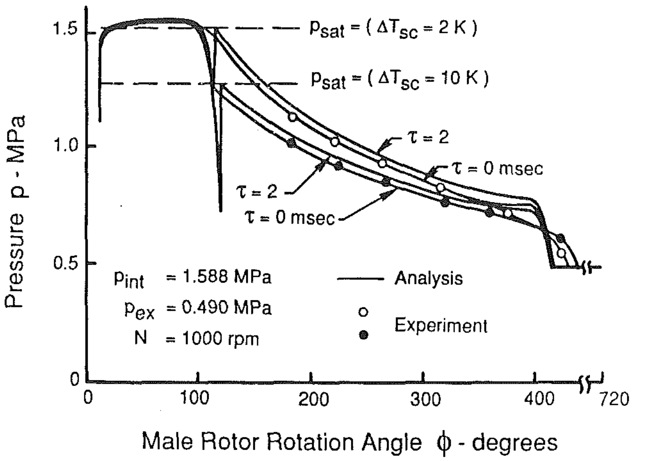

Fig. 10 Effect of bubble initiation delay time on working volume pressure variation

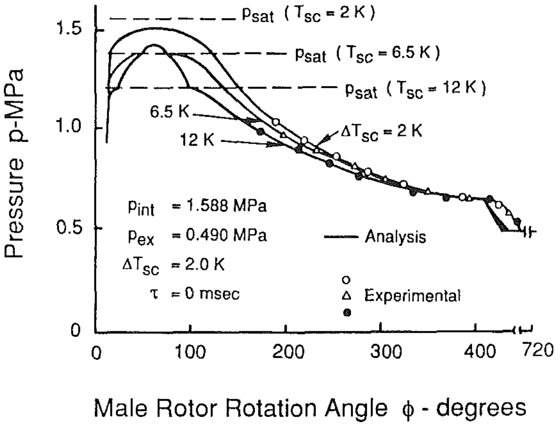

Fig. 11 Effect of subcooling on working volume pressure variation

stants in the analysis. Values for these two coefficients were determined by trial and error to obtain the best fit of the analytical results for the flow ratio, internal efficiency, and indicator diagram, to the experimental results. Figure 9 shows the final values selected for these flow coefficients. Note that the coefficient for the intake port α_{int} is almost constant with the male rotor rotational speed N. The value of 0.8 is considered reasonable in that the intake flow passage is essentially a converging nozzle with a small area change. In contrast the flow coefficient α_{lk} for the leakage paths decreases significantly (from 0.7 to around 0.4) with increasing N. This trend is also reasonable because the leakage paths are formed between the moving rotors and the rotors and casing. The direction of the leakage flow is generally opposite to the motion of the rotor surfaces which form part of the flow channels. Hence, flow resistance will increase with increasing rotor speed.

Bubble Formation Delay Time. When the pressure on a subcooled or saturated liquid is suddenly decreased below its saturation value, vapor formation (flashing) is usually initiated at nucleation sites within the liquid. Vapor bubbles then develop around these sites. Since this process is not instantaneous, a vapor bubble formation delay time τ was incorporated into the analysis. The effect of $\tau = 2$ ms compared with no delay time on the machine indicator diagram is shown in Fig. 10 for two different saturation pressures and degrees of subcooling.[3] Differences in predicted pressures are seen to be small, indicating that delay in bubble formation would have only a minor influence. Furthermore, it is also obvious in Fig. 10 that the predicted curves for zero delay time are in excellent agreement with experimental results. This was also found to be true at higher rotational speeds. Vapor formation during the expansion process thus appears to occur essentially instantaneously with decreasing pressure, probably due to vigorous mixing in the expansion volume.

Subcooling. Figure 11 shows the effect of subcooling ΔT_{sc} on the indicator diagram. As can be seen, the indicator work decreases with increasing ΔT_{sc}. The effects of ΔT_{sc} on the experimental internal efficiency η_{ie}, predicted internal efficiency η_{ia}, and flow ratios η_{ve} and η_{va}, are shown in Fig. 12. Increasing the amount of subcooling ΔT_{sc} at the inlet of the expander increases the flow ratio η_v; however, there is no effect on η_i over a wide range of ΔT_{sc}. The validity of the analysis is supported by the good agreement of predicted with experimental results shown in Figs. 11 and 12.

Male Rotor Rotational Speed. The effect of male rotor speed N on the pressure variation during expansion is shown in Fig. 13. Figure 14 shows the variations with rotor speed of the experimental internal efficiency η_{ie}, predicted internal efficiency η_{ia}, and the experimental and predicted flow ratios η_{ve} and η_{va}. The effect of the deviation from an isentropic expansion was investigated by multiplying the $\bar{p}\Delta V$ term in equations (9) and (13) by an adiabatic expansion efficiency ξ. Results are included in Fig. 14 for values of $\xi = 1.0$, 0.95, and 0.90. As the rotor speed approaches 3000 rpm the difference between η_e and η_i for an isentropic expansion increases to

---

[3] With Δt specified as the time for 2 deg of rotation at 1000 rpm, a τ of 2 ms corresponds to six time steps during the intake and exhaust phases, and to about one time step during the expansion phase.

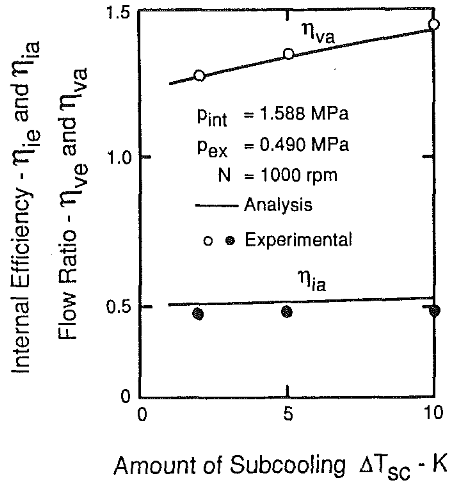

Fig. 12 Effect of subcooling of working fluid on performance

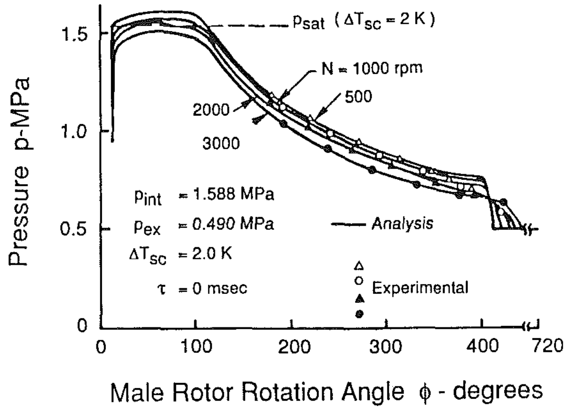

Fig. 13 Effect of rotor speed on working volume pressure variation

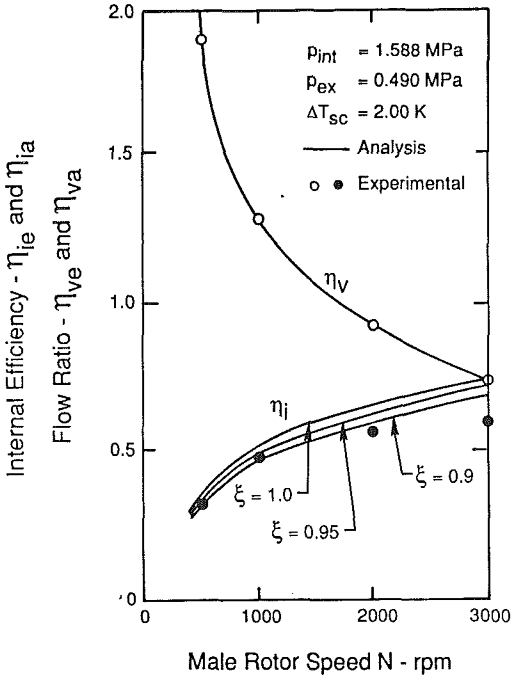

Fig. 14 Variations of efficiencies and flow ratio with rotor speed

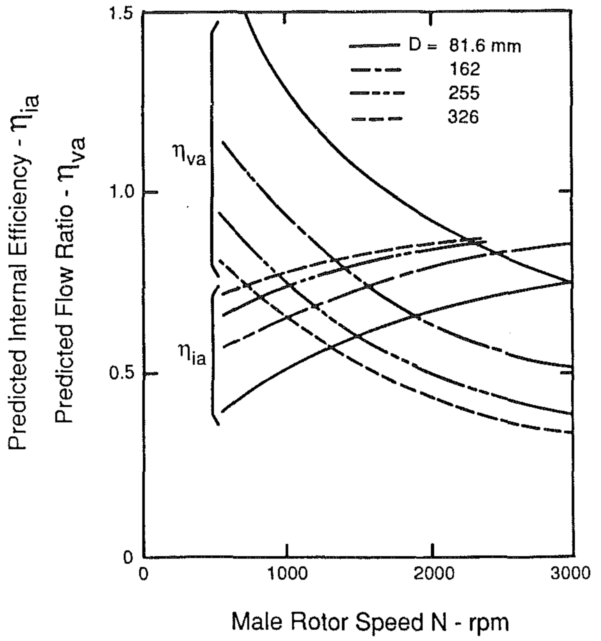

Fig. 15 Effect of rotor diameter on internal efficiency and flow ratio

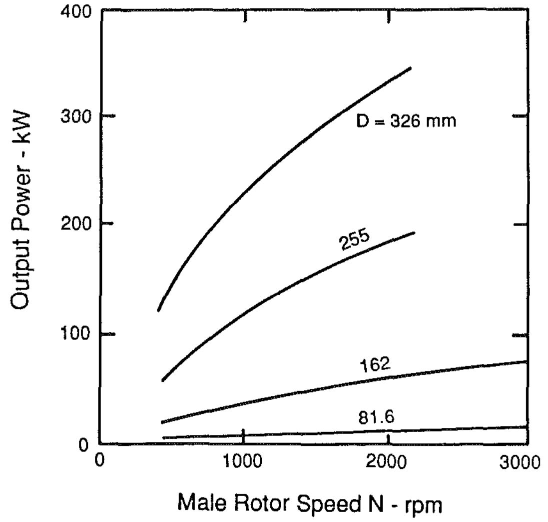

Fig. 16 Effect of rotor diameter on power output

about 20 percent. This difference is decreased by around 9 percent for an adiabatic expansion efficiency of 0.90. Mechanical losses due to bearing friction, timing gears, and shaft seals and oil pump power were estimated at 3000 rpm to be about 5 percent. The power output loss due to Coriolis acceleration of the liquid forced toward the casing is on the order of 1 percent. Viscous friction at the rotor tips was estimated to be less than 1 percent. Hence, these effects would reduce the predicted results by around 7 percent. Adding this reduction to the predicted loss for an adiabatic expansion efficiency of $\xi = 0.90$ yields excellent agreement between the analytical and experimental results.

The rapid decrease of the flow ratio η_v with increasing rotor speed (Fig. 14) is primarily due to the decreasing of the mass flowing into the working volume during the intake phase. Although the pressure drop across the intake port increases, this enters to the one-half power, while the time for inflow decreases linearly with speed. The decrease in leakage mass flow with increasing speed also contributes to the decrease in η_v.

Performance of Larger Screw Expanders

The excellent agreement of analytical results with experimental measurements established the applicability of the model proposed and the calculational procedure developed. It was then used to investigate the performance of larger two-phase flow screw expanders. The calculations were based on the following additional assumptions:

1 the expansion volume is proportional to the cube of the rotor diameter;

2 the areas of the intake and exhaust ports are proportional to the square of the rotor diameter; and

3 leakage gap widths are constant so that the leakage path areas are proportional to the rotor diameter.

Results for rotor diameters varying from 81.6 to 326 mm (2, 3, and 4 times the test machine dimension) are presented in Figs. 15 and 16 as a function of rotor speed for $\xi = 1.0$. Note that (Fig. 15) the predicted internal efficiency η_{ia} increases with increasing rotor diameter D (attributable to proportionately less leakage). However, it appears to be approaching a maximum as the diameter is increased to 326 mm. In the range of 2000-3000 rpm this maximum is around 80 percent. Actual performance is expected to be a little lower in that these results are based on an adiabatic expansion efficiency $\xi = 1.0$ and mechanical friction losses have not been included.

In contrast the predicted power output increases more rapidly as the rotor diameter is increased. For the dimensions and conditions considered the predicted power output (Fig. 16) is approximately proportional to the square of the rotor diameter. This trend results from the leakage increasing proportionally with the first power of the rotor diameter, while the expansion or working volume increases in proportion to the cube of the rotor diameter.

Conclusions

An analytical method was developed for estimating the performance of power-producing two-phase flow screw expanders. The applicability of the method was established by comparison of predicted with experimental results. Analytical and experimental results established the following performance characteristics and trends of screw expanders under two-phase flow operation:

1 The internal efficiency increases and the flow ratio decreases, both toward asymptotic values, as the rotor speed increases. These trends are attributable to the decrease in leakage mass flow and the decrease in intake mass flow with increasing rotor speed.

2 The internal efficiency is not affected by the degree of subcooling ΔT_{sc}.

3 The delay time τ for the initiation of flashing can be taken to be zero for design calculations.

4 The internal efficiency approaches a maximum of about 80 percent with increasing rotor diameter, while the power output increases in proportion to the square of the rotor diameter.

References

Downing, R. C., 1974, "Refrigerant Equations," *ASHRAE Trans.*, Vol. 80, Part II, pp. 158–169.

Fujii, T., Akagawa, K., Takagi, S., and Takeda, M., 1983, "Performance of a Hero's Turbine Using Two Phase Mixture as a Working Fluid," ASME-JSME *Thermal Engineering Joint Conference Proceedings*, pp. 199–206.

Fujiwara, M., Kasuya, K., Matsunaga, T., and Watanabe, M., 1984, "Analysis of Screw Compressor Performance (1st Report, Calculation of Geometrical Characteristics)," *Trans. JSME*, Vol. 50, pp. 1027–1033.

Fujiwara, M., Kasuya, K., Matsunaga, T., and Watanabe, M., 1985, "Analysis of Screw Compressor Performance (2nd Report, Simulation Program)," *Trans. JSME*, Vol. 51, pp. 1816–1824.

Hijikata, K., and Mori, Y., 1982, "Fundamental Performance of Two-Phase Flow Rotary Expander," *Trans. JSME*, Vol. 48, pp. 160–167.

Kaneko, T., and Hirayama, N., 1985, "Study on Fundamental Performance of Helical Screw Expander," *Trans. JSME*, Vol. 51, pp. 134–142.

Kudo, K., Giedt, W. H., Taniguchi, H., Park, I., Kasahara, K., and Kawamura, K., 1985, "Energy-Conserving Heat Pump-Boiler System for District Heating—Pilot Plant Test Results," *Proceedings, 20th Intersociety Energy Conversion Engineering Conference*, Vol. 2, pp. 2223–2228.

Myers, B., Deis, G. A., and Shell, T. E., 1985, "Operating Efficiencies of a Lysholm Helical Expander for Brayton-Cycle Heat Engines," UCRL-53478/6001-70, Lawrence Livermore National Lab, Livermore, CA.

Shigekawa, K., 1984, "Performance Characteristics of a Screw Expander," *R & D Kobe Steel Engineering Reports*, Vol. 34, No. 1, pp. 32–35.

Steidel, R. F., Weiss, H., and Flower, J. E., 1982, "Performance Characteristics of the Lysholm Engine as Tested for Geothermal Power Applications in the Imperial Valley," ASME JOURNAL OF ENGINERING FOR POWER, Vol. 104, pp. 231–240.

Taniguchi, H., Giedt, W. H., Kudo, K., Kasahara, K., Ohta, J., and Kawamura, K., 1983, "Energy-Conserving Heat Pump-Boiler Systems for District Heating," *Proceedings, 18th Intersociety Energy Conversion Engineering Conference*, Vol. 4, pp. 1862–1868.

R. Bons

J. Hanlon

S. Spencer

Department of Engineering Sciences,
Allied-Signal Aerospace Company,
Fluid Systems Division,
Tempe, AZ 85282

Predicting the Behavior of Solar Dynamic Closed Brayton Cycle Power Conversion Systems

Since space power conversion systems must operate both in the sun and in the earth's shadow, they seldom encounter design operating conditions. As a consequence, consideration of off-design performance is essential in the preliminary design of these systems. To illustrate the necessity and utility of an off-design system model, this paper presents the results of a study of the solar dynamic closed Brayton cycle power conversion system for use on the NASA Space Station.

Introduction

The Phase 2 configuration of the NASA Space Station will utilize a hybrid power conversion system consisting of a combination of photovoltaic and solar dynamic power conversion systems. Fluid Systems Division, in support of Rocketdyne, has conducted a preliminary design of a solar dynamic closed Brayton cycle (CBC) power conversion system.

Solar-powered energy conversion systems must operate over a wide range of conditions that result from variations in insolation and the length of the solar day. In addition, the sink temperature and the power requirements fluctuate, and the system performance changes as the components age. This combination of design considerations provides a series of challenges in characterizing system performance. The need for accurate analysis of system performance mandates the development of off-design models, including a model for time-dependent heat storage.

The NASA Space Station system is required to produce 25 kW_e while operating in a low earth orbit. In addition, a peaking power requirement of 27.75 kW_e can occur as frequently as once every orbit. Each peaking period is followed by a recovery period when the power requirements are reduced. The reduction is such that the total energy output for the orbit is unchanged.

CBC Power System Description

The heart of the power conversion system is a recuperated CBC. A schematic of the system is shown in Fig. 1. The cycle working fluid is a mixture of xenon and helium with a molecular weight of 40.8. The energy source (sunlight) is focused by a mirror (concentrator) into a receiver.

A manifold system ducts the cycle gas to the aperture end of the receiver where the gas is channeled into 82 parallel tubes, shown in Fig. 2. The tubes are jacketed with donut-shaped canisters filled with phase-change material (a eutectic salt). The latent heat of fusion of the salt, along with the sensible heat of the tube assembly, provides the mechanism for thermal energy storage. Stored energy not recovered by the recuperator is rejected by a flat plate radiator via a single-phase liquid loop.

The pumped-liquid (a fluorocarbon) loop brings the working fluid into contact with this flat plate radiator. The coolant leaving the radiator first passes through a heat exchanger in order to cool the electronic controls package. The flow is then split into three parallel loops. The majority of the liquid is routed to the heat rejection heat exchanger. The rest of the liquid is used to cool the alternator and the bleed gas. The bleed gas (2 percent of the main flow) removes energy from the alternator rotor and the bearings.

Other than the coolant pumps, the combined rotating unit (CRU) is the only continuously moving part in the engine. The CRU consists of a centrifugal compressor, the alternator rotor, and a radial inflow turbine mounted on a common shaft riding on compliant gas foil bearings.

The CBC system is controlled by a combination of inventory management and a parasitic load radiator (PLR). The engine gas inventory is slowly adjusted to accommodate variations in the total energy absorbed by the receiver and quickly adjusted to produce peaking power when required. To decrease the cycle gas inventory, working fluid is bled from the high-pressure side of the compressor into an accumulator. To increase the cycle inventory, gas is introduced into the compressor inlet from the accumulator. The rotating speed of the engine is controlled by using the PLR to modulate the load on the alternator. The PLR is also used to dissipate power not used by the Station.

Off-Design Drivers

As discussed earlier, the fluctuating nature of the operating environment combines with the variable-power requirement to introduce transients into the system response.

The most significant transient results from the Station's passing into and out of the shadow of the earth. During this movement, the receiver either stores or releases energy, resulting in variations in the turbine inlet temperature (see Fig. 3).

Contributed by the International Gas Turbine Institute and presented at the 33rd International Gas Turbine and Aeroengine Congress and Exhibition, Amsterdam, The Netherlands, June 5–9, 1988. Manuscript received by the International Gas Turbine Institute June 22, 1987. Paper No. 88-GT-195.

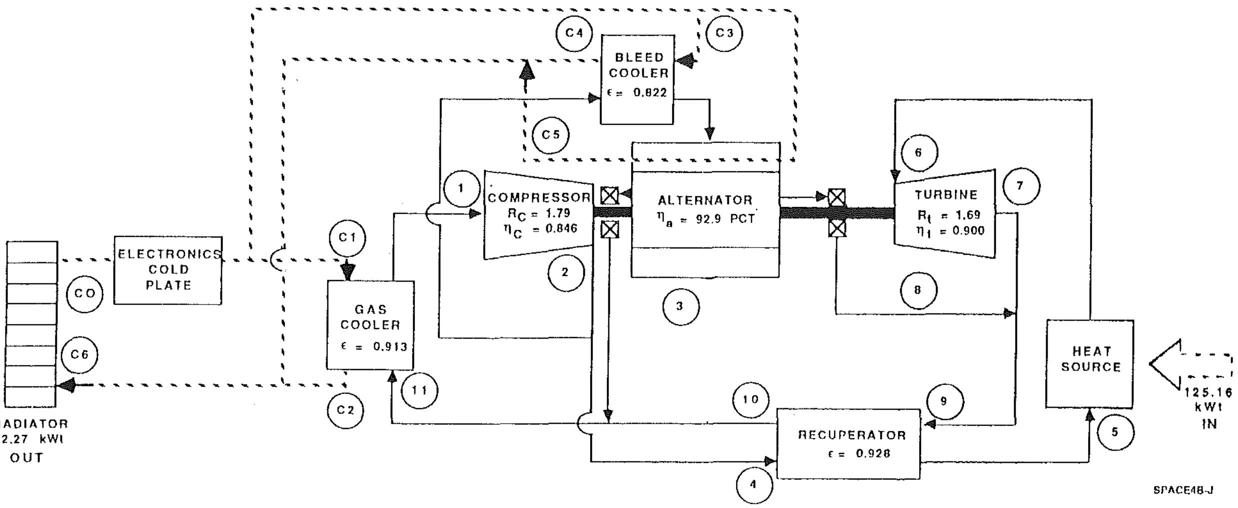

STATE POINT	TEMPERATURE		PRESSURE		FLOW RATE	
	DEG K	DEG F	KPA	PSIA	KG/S	LB M/S
1	320.01	116.35	286.06	41.49	1.2194	2.6884
2	419.45	295.34	512.64	74.35	1.2194	2.6884
3	504.54	448.50	288.59	41.86	0.0244	0.0538
4	419.59	295.58	511.92	74.24	1.1890	2.6212
5	799.88	980.11	508.81	73.79	1.1890	2.6212
6	1002.19	1344.27	493.86	71.63	1.1890	2.6212
7	832.01	1037.95	292.90	42.48	1.1890	2.6212
8	347.46	165.75	292.90	42.48	0.0061	0.0134
9	829.52	1033.46	292.55	42.43	1.1950	2.6346
10	451.17	352.44	288.59	41.86	1.1950	2.6346
11	452.24	354.36	288.59	41.86	1.2194	2.6884
C 0	275.81	36.79			0.6055	1.3349
C 1	280.87	45.89			0.5080	1.1200
C 2	437.33	327.53			0.5080	1.1200
C 3	280.87	45.89			0.0180	0.0396
C 4	379.79	223.95			0.0180	0.0396
C 5	328.32	131.30			0.0795	0.1753
C 6	422.11	300.13			0.6055	1.3349

ELECTRICAL OUTPUT = 35.79 kWe

BETA = 0.941
BEARING LOSS = 1.24 kW
WINDAGE LOSS = 2.33 kW
NET CYCLE EFFICIENCY = 28.62 PCT
ROTOR SPEED = 32,000 RPM
SINK TEMPERATURE = 186K (-125F)
EMISSIVITY = 0.9

Fig. 1 Minimum insolation peaking orbit at sunrise

In addition to the environmental factors discussed earlier, transients are induced by peaking power requirements. The system is required to make the transition from nominal to peaking power within 60 s. The transitions among peaking, recovery, and nominal power induce similar transients.

Time-Dependent Heat Storage Model

Development of an accurate time-dependent heat storage model for the CBC system required the modeling of all the components that introduce significant transients within the system. The transients encountered during normal operation are such that the thermal responses of the receiver and radiator dominate the system response, a logical effect since these two components constitute 70 percent of the engine mass. As a consequence, dynamic thermal models were developed for the radiator and receiver only. The remaining components were represented by steady-state models. For the cold-start analysis, the dynamic response of the recuperator was also modeled.

The receiver was modeled using a finite element code. Symmetry permitted a model of one of the receiver's 82 working fluid tubes to characterize the entire receiver. This tube, assumed to have circumferential symmetry, was based on results from a more sophisticated receiver program. The resulting model has three dimensions: radial distance, axial distance, and time. The computational domain is a matrix of eight axial by nine radial nodes, as shown in Fig. 4. Since the canisters are physically separated from one another, the only axial conduction is at the interior tube wall.

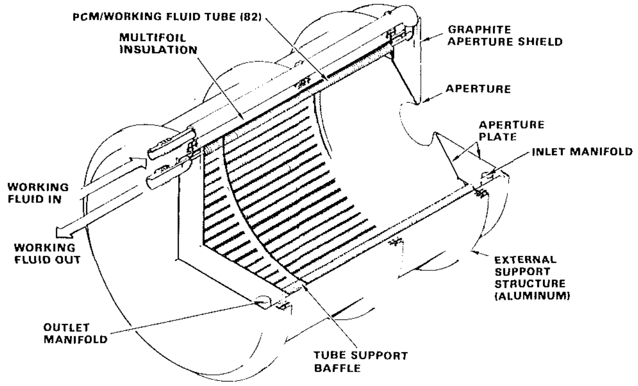

Fig. 2 Cross section of receiver showing key features

The receiver model includes energy transfers through the outer shell, within the canisters, and to the working fluid. These energy transfers are illustrated in Fig. 5. The outer shells of the canisters are subject to both radiative and conductive heat transfer. In addition to the incident solar radiation, radiation occurs between the tubes, with the end walls, and out the aperture of the receiver. Several mechanisms are at work in the interior nodes: The thermal/physical properties of the salt are functions of both temperature and the phase of the salt. A large variation in the salt density results in the formation of voids within the canister. Constant mass, rather than fixed-volume, nodes were used to account for the variation. The energy transfer with the working fluid was also modeled using a finite-element basis that included accounting for entrance effects and variations in the heat transfer coefficient along the length of the tube.

The radiator was modeled as a simple finned tube surface

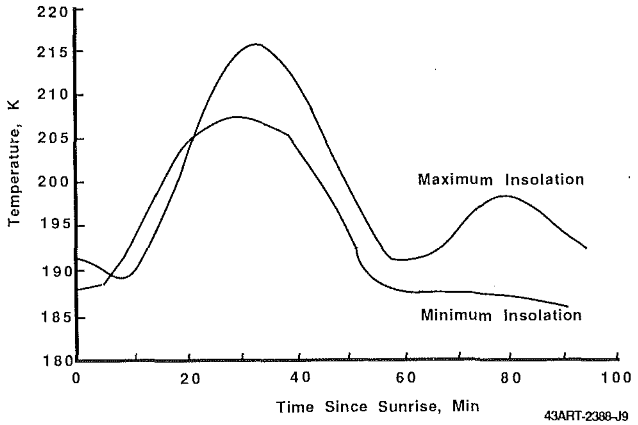

Fig. 3 Sink temperature for maximum and minimum insolation orbits

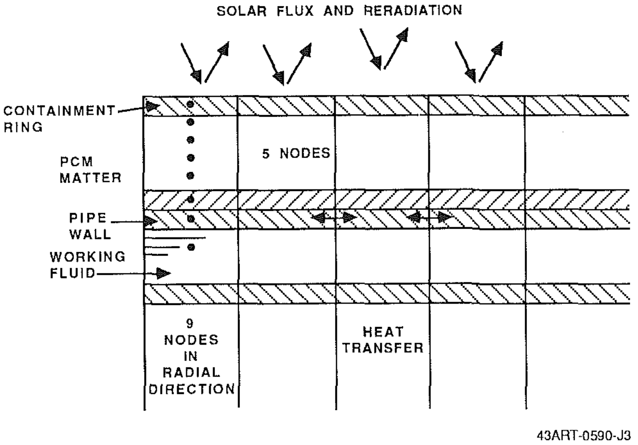

Fig. 4 Node distribution

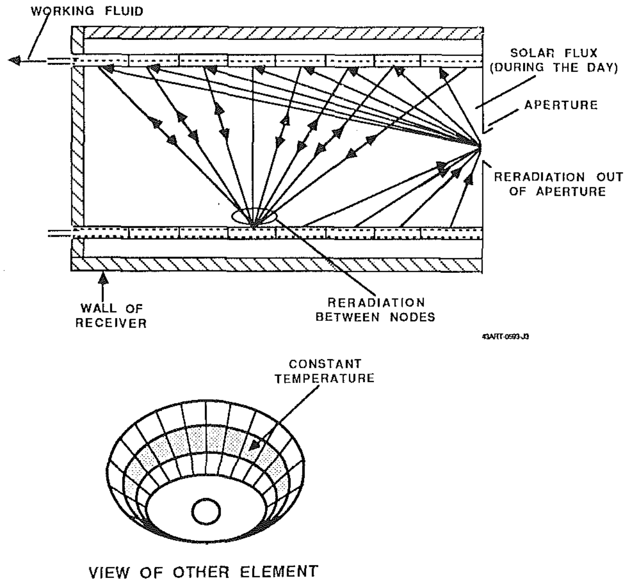

Fig. 5 Receiver reradiation

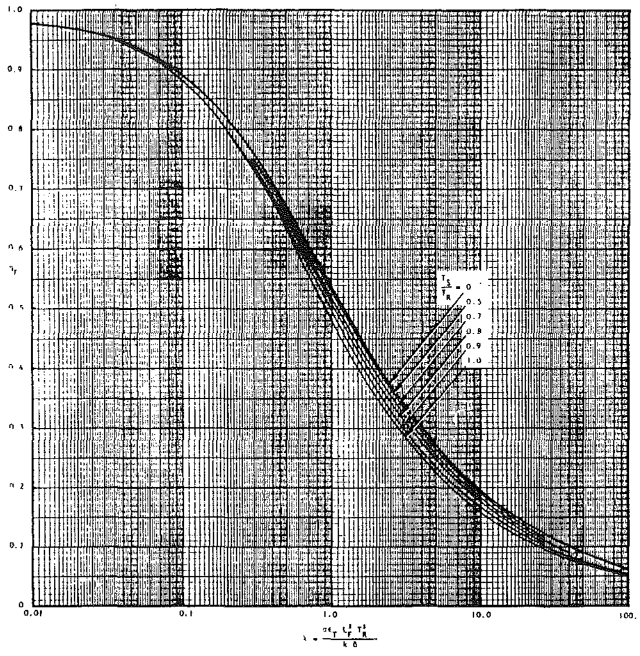

Data taken from: Bartas and Sellers, Trans. ASME, Series C, Journal of Heat Transfer 82, 73-75 (1960)
S. Lieblein, NACA TN D-196
D.B. Mackay, ASD 61-30, NAA SID 61-66

A-6235

Fig. 6 Radiation fin effectiveness η_F for rectangular fins

with heat rejection from both sides. The model developed was a combination of a two-dimensional (length and time) finite-element representation and closed-form solution. The closed-form solution addresses radiation heat transfer from extended surfaces. The finite-element portion of the model accounts for the variation in temperature along the length of the tubes.

A limiting case solution to the governing differential equation for the fin temperature distribution made this approach to radiator modeling possible. The limiting case solution was obtained by allowing the ratio of sink temperature to fin-root temperature to equal 1.0. This approximation linearizes the governing equation. Consequently, a closed-form solution to the problem of temperature distribution can be attained.

Although meaningless in a physical sense, the limiting case solution produces very accurate results if the radiator is designed with sink-to-fin-root temperature ratios of 0.75 or greater and a fin effectiveness of 0.8 or greater. Figure 6, showing the error inherent in this technique, was used to develop the correction factor applied to the fin effectiveness predicted by the closed-form solution.

The system model was run by breaking each orbital period into discrete time increments. Due to the thermal complexity of the receiver, its condition was evaluated over a much smaller increment than the remainder of the system. At each of the longer intervals, the operator could adjust control variables including power level, rotational speed, amount of recuperator bypass, and cycle gas inventory. This adjustment provided the operator with the flexibility necessary to develop and test control strategies. At each of these breaks in the simulation, a complete summary of the system performance and operating conditions was recorded. A summary file containing selected cycle information from a break in the simulation is shown in Fig. 7.

General Results

The model was used to predict system performance for various control and operating strategies by selecting a control mode; sizing the concentrator and setting the cycle gas inventory; and then running the model in order to observe system performance. The minimum insolation orbit at sunrise, which presents the most difficulty in satisfying the power requirements, was the first orbit exercised. For the purposes of this paper, a "maximum insolation" orbit refers to an orbit with maximum solar flux, longest orbital period, minimum shadow time, and operation with a new concentrator. The opposite set of conditions corresponds to a "minimum insola-

```
MINIMUM INSOLATION ORBIT

FLUX THROUGH APERTURE = 188.0 KW       INVENTORY = .7908 KG      DATE RAN   1986-11-22

Time Since  Melt     T1      T5      T6P     TMAX     TSINK   W5       GAO    P1      P2        QIN  E-STORED HOLE WAL WHOL WAL
Sun Rise  Fraction (K)      (K)     (K)     (K)      (K)    (KG/S)   (KW)   (MPA)   (MPA)     (KW)  (KW-MIN)  (K)      (K)
      0   0.0785   287.5   796.8   1011.9  1040.8   186.4  0.8521   32.14  0.1859  0.3539     95.2        0   968.4   1045.9
   4.55   0.0921   287.8   802.1   1018.8  1045.5   185.7  0.8546   32.74  0.1868  0.3555     96.2      347   996.0   1056.5
    9.1   0.1402   288.5   806.6   1024.3  1046.5   188.3  0.8553   33.04  0.1876  0.3567     96.8      684  1012.8   1062.2
  13.66   0.2172   289.1   808.3   1026.1  1047.5   190.8  0.8557   33.06  0.1881  0.3572     96.8     1021  1021.7   1064.5
  18.21   0.2859   290.4   809.6   1026.8  1048.6   196.7  0.8549   32.82  0.1888  0.3576     96.5     1357  1026.5   1066.1
  22.76   0.3495   291.7   810.8   1027.4  1051.0   201.7  0.8545   32.59  0.1894  0.3581     96.2     1694  1030.0   1067.4
  27.31   0.4072   292.6   811.5   1027.7  1052.0   205.2  0.8542   32.41  0.1900  0.3585     95.9     2033  1031.9   1068.0
  31.86   0.465    293.1   812.1   1028.1  1053.5   206.9  0.8543   32.34  0.1904  0.3588     95.9     2371  1033.7   1069.2
  36.42   0.5196   293.2   812.3   1028.2  1056.1   207.0  0.8546   32.35  0.1905  0.3590     95.9     2710  1034.7   1069.7
  40.97   0.577    292.9   812.2   1028.4  1057.1   205.8  0.8549   32.44  0.1903  0.3589     96.0     3049  1035.7   1070.5
  45.52   0.6337   292.2   812.0   1028.6  1059.6   203.2  0.8550   32.59  0.1900  0.3586     96.2     3387  1036.6   1071.4
  50.07   0.6758   291.3   815.6   1033.9  1073.8   198.9  0.8559   33.18  0.1899  0.3592     97.1     3719  1040.4   1075.6
  54.62   0.7122   290.2   821.3   1042.3  1087.2   193.3  0.8581   34.08  0.1901  0.3606     98.6     4043  1046.7   1083.1

  TIME = 54.678      POWER TO WORKING FLUID (KW) = 97.156    TOTAL POWER ABSORBED (KW)= 168.15

TEMP        1002.9  1046.9  1061.2  1085.3  1087.3  1078.6  1062.9  1046.9

TEMP         998.7  1042.2  1059.6  1084.2  1086.5  1077.9  1062.3  1045.3          RADIAL NODES
QUAL           0.0  .74666       1       1       1       1       1       1

TEMP         997.7  1041.0  1056.9  1082.4  1085.1  1076.9  1061.3  1043.8
QUAL           0.0     0.0       1       1       1       1       1       1

TEMP         996.4  1039.9  1053.8  1080.5  1083.6  1075.8  1060.3  1042.2          AXIAL NODES
QUAL           0.0     0.0       1       1       1       1       1  .97966

TEMP         995.1  1038.8  1050.2  1078.3  1081.9  1074.5  1059.3  1042.2
QUAL           0.0     0.0       1       1       1       1       1     0.0          FRACTION OF SALT MELTED

TEMP         993.6  1037.4  1045.9  1075.9  1080.0  1073.2  1058.3  1042.1
QUAL           0.0     0.0       1       1       1       1       1     0.0

TEMP          991.8  1035.8  1042.2  1073.0  1077.8  1071.6  1057.2  1042.1
QUAL            0.0     0.0  .11234       1       1       1       1     0.0

TEMP          990.6  1034.7  1041.3  1071.2  1076.4  1070.7  1056.7  1042.1          NODES WITHOUT PHASE CHANGE
                                                                                            MATERIAL
TEMP          990.0  1034.2  1040.9  1070.8  1076.1  1070.4  1056.6  1042.0

FLUID      821.3   871.6   918.6   954.1   987.8  1013.5  1030.1  1037.9  1039.1


  54.68   0.7126   290.2   821.3   1042.5  1087.3   193.2  0.8581   34.11  0.1901  0.3606     98.6     4047  1046.8   1083.2
  59.23   0.6672   289.2   811.3   1029.9  1048.9   190.5  0.8567   33.35  0.1886  0.3581     97.3     3531  1020.7   1038.9
  63.78   0.594    288.7   808.0   1026.0  1042.0   188.7  0.8554   33.11  0.1878  0.3570     96.9     3019  1008.3   1034.1
  68.33   0.5032   288.4   807.0   1024.9  1042.0   187.7  0.8559   33.11  0.1877  0.3570     96.9     2506  1001.8   1032.7
  72.89   0.4054   288.4   806.6   1024.3  1042.0   187.9  0.8550   33.02  0.1875  0.3566     96.7     1994   997.9   1031.9
  77.44   0.3182   288.3   804.8   1022.0  1041.9   187.6  0.8545   32.85  0.1872  0.3561     96.4     1485   990.2   1029.4
  81.99   0.227    288.1   803.0   1019.7  1041.4   187.3  0.8540   32.69  0.1870  0.3557     96.2      980   982.8   1026.9
  83.52   0.196    288.0   802.6   1019.2  1041.3   187.1  0.8539   32.67  0.1868  0.3555     96.1      811   980.9   1026.2
  88.07   0.1255   287.7   798.9   1014.6  1041.0   186.7  0.8526   32.33  0.1862  0.3544     95.5      307   970.7   1021.7
  91.02   0.0808   287.6   796.9   1011.9  1040.8   186.4  0.8525   32.15  0.1859  0.3540     95.3      -15   964.9   1018.9

MELT FRACTION = FRACTION OF SALT IN RECEIVER THAT IS LIQUID
T1            = TEMPERATURE INTO COMPRESSER (K)
T5            = TEMPERATURE INTO RECERVER
T6            = TEMPERATURE OUT OF RECEIVER
TMAX          = HOTEST PART OF TUBE SHELL
W5            = CYCLE GAS MASS FLOW RATE THROUGH RECEIVER
GAO           = GROSS ALTERNATOR OUTPUT (KW)
P1            = PRESSURE INTO COMPRESSER
P2            = PRESSURE OUT OF COMPRESSER
QIN           = ENERGY INTO WORKING FLUID
E-STORED      = NET ENERGY STORED IN RECEIVER SINCE SUN RISE
HOLE WAL      = TEMPERATURE OF THE RECEIVER FRONT WALL (APERTURE END), ON THE INSIDE.
WHOL WAL      = TEMPERATURE OF THE RECEIVER BACK WALL
```

Fig. 7 Summary sheet

tion" orbit. Provided the results for a minimum orbit were satisfactory, the system was next run for the maximum insolation orbit. The maximum insolation orbit is the most difficult case for energy dissipation and, as such, determines the size of the PLR and of the alternator.

The combination of operating parameters which would result in an orbital steady-state condition while meeting the operational requirements was not apparent. In particular, the system must produce the minimum power, yet maintain sufficient energy storage to handle a peaking load. A key operational indicator used was the relative amount of energy stored in the receiver at the beginning of an orbit (sunrise). If excess energy was stored initially, then by sunset, the system would experience prohibitively high temperatures in the receiver. If insufficient initial energy was stored, the system would be unable to produce peaking power toward the end of an eclipse.

The amount of energy stored is an important parameter in another sense: It directly influences the average receiver exit/turbine inlet temperature, which in turn impacts the cycle efficiency and the total power output of the alternator. The alternator efficiency, in turn, affects the required concentrator size for a minimum insolation orbit.

Exercising the model demonstrated that relatively simple control strategies would best satisfy the system requirements and allowed the discarding of more elaborate control strategies such as controlling receiver inlet temperature through bypassing the recuperator and minimizing the compressor inlet temperature by maintaining the heat capacity ratio of the cooler. The adopted control strategy is based on allowing the alternator output to vary above a minimum power level while maintaining a constant rotating speed. This approach uses a PLR and cycle gas inventory management scheme, as discussed earlier, to compensate for variations in power demand and alternator output.

Specific Cases Examined

System performance was examined for four conditions: maximum insolation, minimum insolation, peaking orbits, and cold start. For each case, the model was run for sufficient orbits to establish a quasi-steady-state condition. A quasi-steady state is achieved when the receiver parameters at the end of an orbit have the same values as those at the beginning of the orbit. The receiver parameters monitored were the gas

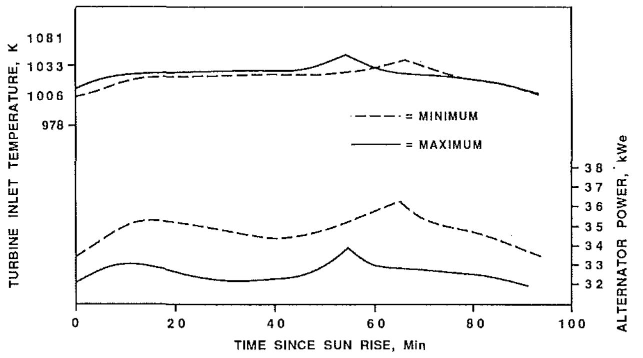

Fig. 8 Power output and turbine inlet temperature compared for minimum and maximum isolation orbit

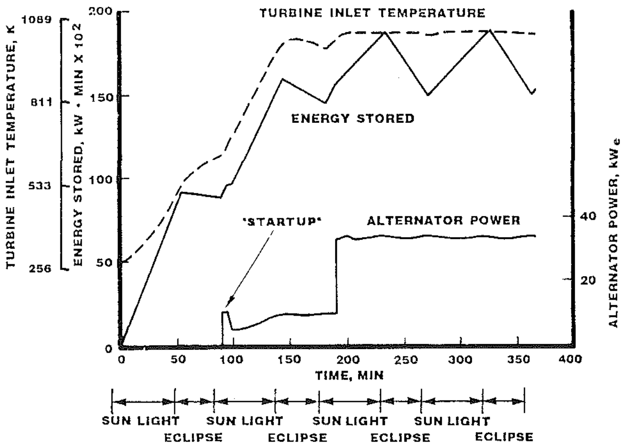

Fig. 9 Energy versus time plot showing the CBC startup

exit temperature, the net energy stored in the receiver, and the percentage of eutectic salt melted.

The minimum insolation nominal power orbit was studied first since it determines the size of the concentrator. The simulation began with assumed receiver conditions and cycle gas inventory. Once steady state was achieved, the results were compared with system requirements before appropriate adjustments were made to the initial conditions. This process was repeated until a set of acceptable operating conditions was established, as shown in Fig. 8. The sunrise conditions were then stored and used as the starting point for evaluating system performance on minimum insolation orbits involving peaking and recovery. This process established the initial receiver conditions necessary for successful system operation over all the minimum insolation cases (nominal, peaking, and recovery). The receiver initial conditions for the minimum insolation orbits are characterized by 6 percent of the salt being in the liquid phase.

A process similar to the one used for the minimum insolation orbit was used to determine the cycle gas inventory and the initial energy stored in the receiver. Since the concentrator size was based on the minimum insolation orbit, the cycle gas inventory and the initial energy stored in the receiver were the only remaining parameters to be determined. Figure 8 also presents these results. Since the maximum insolation orbit has the shortest eclipse period and highest solar flux, its initial receiver energy is the lowest and its cycle gas inventory the highest.

The model was also used to examine a cold startup, with the goal of starting the system without thermally stressing the receiver. The analysis assumed an initial system temperature of 0°C. Figure 9 depicts the method developed for starting the engine: at sunrise, the concentrator was pointed at the sun (as during normal operation) and the temperature in the receiver was monitored. When sufficient energy was stored, the alternator was used to motor the CRU, circulating cycle gas through the loop. Once the CRU reached a self-sustaining speed, the motoring current was cut and the CRU was allowed to accelerate to the normal operating speed. At this point, the inventory level was reduced as much as possible and the rotational speed of the CRU reduced to idle. This action minimized the energy transfer throughout the system. Running with the minimum possible gas flow minimized the thermal shock to the system while allowing the receiver to charge. The receiver reached its normal temperature and thermal charge after approximately 230 min (2.5 orbits). The cycle inventory was then increased, and normal operation began.

Conclusions

Prior to this study, the need for a time-dependent system model was only dimly recognized. In fact, this model was essential in verifying the viability of the system design, developing control and operating strategies, and understanding the interrelationships among of the system variables. The model enabled us to devise a system and demonstrate its ability to satisfy the design requirements under all operating conditions. It also enabled us to devise a simple control scheme based on varying the working fluid inventory and PLR load. The emergence of the receiver energy level as a system parameter was the direct result of using the model to establish the relationship between working fluid inventory, receiver energy level, and concentrator size. In addition, the model helped to generate a cold-start scenario that proved to be much simpler than had been anticipated.

This study demonstrated that time-dependent, off-design modeling is essential in verifying the performance of a system under varying operating conditions. Modeling of this type is also essential to understanding the behavior of a system and offers the insight required to optimize a system further and to explore potential tradeoffs.

A Four-Year Investigation of Brayton Cycle Systems for Future French Space Power Applications

Z. P. Tilliette

E. Proust

F. Carre

Commissariat à l'Energie Atomique,
I.R.D.I./D.E.D.R./D.E.M.T.,
Centre d'Etudes Nucléaires de Saclay,
91191, Gif-sur-Yvette, Cedex, France

Within the framework of a joint program initiated in 1983 by the two French Government Agencies C.N.E.S. (Centre National d'Etudes Spatiales) and C.E.A. (Commissariat a l'Energie Atomique), in order to study space nuclear power systems for future ARIANE 5 applications, extensive investigations have dealt with the Brayton cycle, which has been selected as the energy conversion system. Several aspects can be mentioned in this field: matching of the power system to the available radiator dimensions up to 200 kWe, direct or indirect waste heat transfer to the radiator, the use of a recuperator, recent work on moderate (25 kWe) power levels, simulation studies related to various operating conditions, and general system optimization. A limited experimental program is starting on some crucial technology areas including a first contract to the Industry concerning the turbogenerator. Particular attention is being paid to the significance of the adoption of a Brayton cycle for space applications involving a nuclear heat source, which can be either a liquid-metal-cooled or a gas-cooled reactor. For a gas-cooled reactor, direct-cycle system, the relevance to the reactor technology and the concept for moderator thermal conditioning is particularly addressed.

Introduction

The European space program is presently based on the use of the ARIANE 2, 3, and 4 launch vehicles for communication and television satellites. The earth observation is also considered, the first application being SPOT 1 shown in Fig. 1 and in operation since 1985. After 1995, the availability of the heavy launcher ARIANE 5 (Fig. 2) will permit more ambitious missions.

Higher on-board energy levels will be needed at the turn of the century for long periods, which is the reason why nuclear energy will probably be required. Several papers [1-12] report on the main aspects of this program. They deal with program considerations [1, 2, 5], reactor and system concepts [3, 6, 10, 12], Brayton cycle conversion [4, 7, 8, 11], and radiators [9].

The selection of the Brayton cycle conversion system has been confirmed; it takes into account common reasons and in particular French and European space technical considerations. Several investigated aspects can be mentioned in this field: a first assessment of a reference 200 kWe system with a view to the matching of the power system to the available radiator dimensions, the direct or indirect waste heat transfer to the radiator, the recent work on moderate power levels on the order of 25 kWe, the simulation studies related to transient and various operating conditions, and some activity on a general system optimization and on the parameters sensitivity to modified conditions. In addition to the studies carried out up to now, a limited experimental program is starting in some crucial areas. As far as the turbogenerator is concerned, a first contract has been awarded to the Industry for a preliminary definition.

With regard to moderate power level (20–30 kWe) systems, the current study refers to both liquid-metal-cooled fast spectrum and gas-cooled epithermal spectrum reactors for comparison purposes.

The interest in a gas-cooled reactor direct-cycle concept stands to reason if a Brayton cycle is used. This close, natural combination with the heat source prompts an investigation on the utilization of the closed-cycle gas turbine conversion system. There are naturally consequences of the selection of a gas cycle on the reactor technology and concept. An additional approach is being considered. It concerns thermal spectrum gas-cooled reactors and particularly ways of achieving satisfactory temperature conditions, making it possible to use efficient moderator and reflector materials like the ZrH and Li_7H metal hydrides for a long period. Only the Brayton cycle aspects of the topic are addressed in this paper.

Waste Heat Rejection, Radiator

The heat rejection studies relate to the transfer of the Brayton cycle waste heat to the radiating area. This is a point of prime importance, given the length of the cooling circuit, as illustrated by Fig. 3, the extension of the radiator heat exchange surface, and the resulting greater sensitivity of these components to a possible aggressive environment, and to an inadequate structural behavior. It is wise to keep the length of the working fluid circuit of dynamic conversion systems as short as possible in order to lower the gas pressure drop, to

---

Contributed by the International Gas Turbine Institute and presented at the 33rd International Gas Turbine and Aeroengine Congress and Exhibition, Amsterdam, The Netherlands, June 5–9, 1988. Manuscript received by the International Gas Turbine Institute November 30, 1987. Paper No. 88-GT-157.

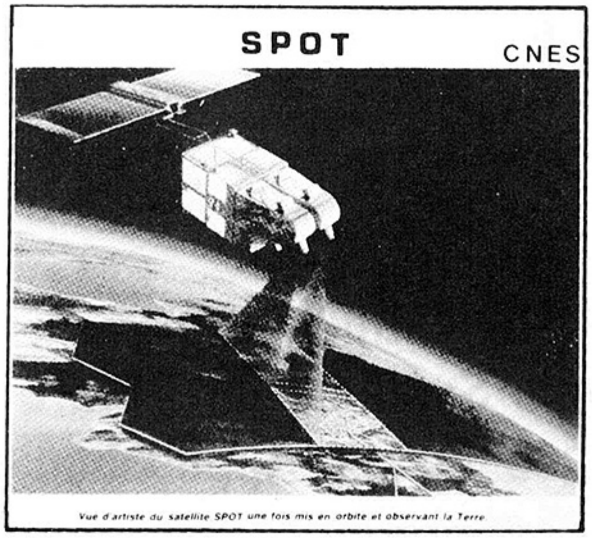

Fig. 1 "SPOT" observation satellite launched by "ARIANE" (1985)

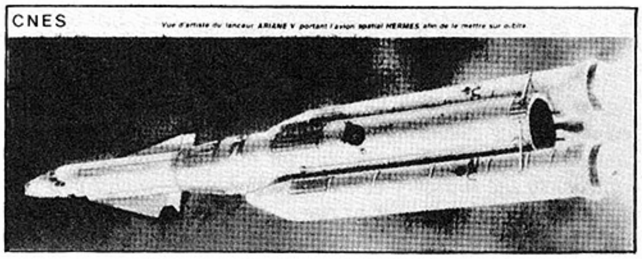

Fig. 2 Future "ARIANE 5" launch vehicle with the "HERMES" space plane

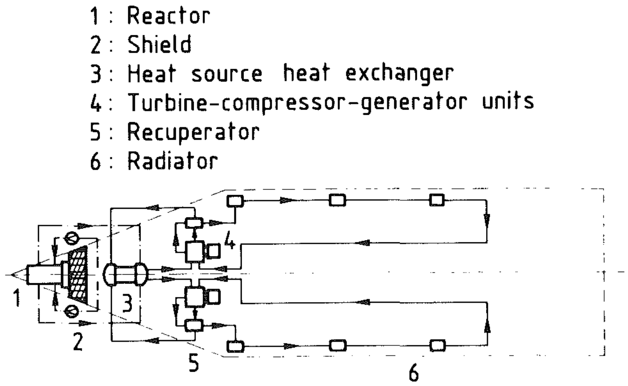

Fig. 3 Schematic arrangement of an "ARIANE 5" gas-cooling circuit, Brayton cycle nuclear power system

make the gas pressure control and the achievement of an absolute leak tightness easier, to make the radiator heat exchanger much more compact, and to prepare the way to possible satisfactory deployable radiator techniques.

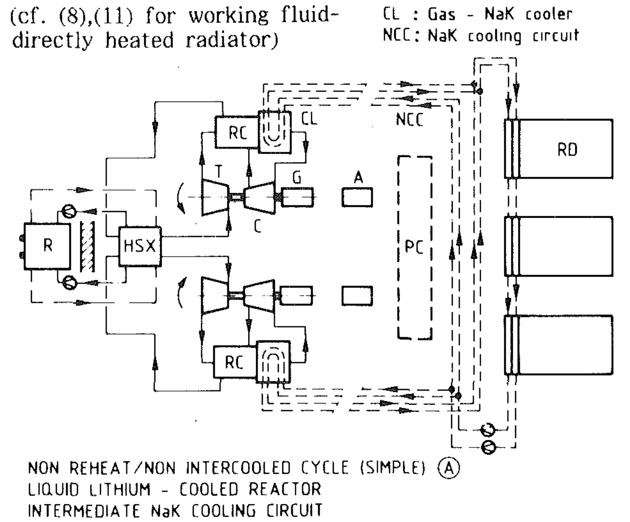

Fig. 4 Power system diagram; intermediate waste heat circuit and heat pipe radiator

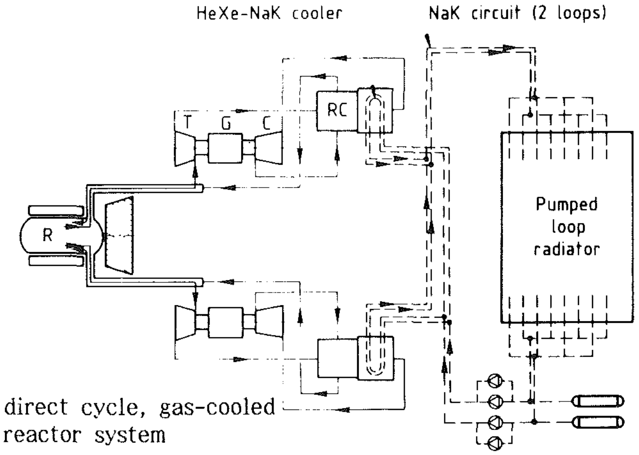

Fig. 5 Power system diagram: intermediate waste heat circuit and pumped-loop radiator

In parallel with the transfer of the waste heat to the radiator heat pipes directly by the working fluid, a version featuring an intermediate cooling liquid under a very low pressure is considered (Fig. 4). Two cooling loops are provided for redundancy, and either the eutectic NaK(78) or an organic fluid could be utilized, according to the temperature range. The use of an intermediate cooling circuit makes it convenient to adopt a pumped-loop radiator, as shown in Fig. 5. These two techniques are compatible with a Brayton cycle conversion system because heat is transferred through a large temperature change, which involves limited fluid mass flows.

The preliminary studies carried out so far in this field lead to sufficiently positive conclusions for pursuing this investigation [8, 11].

Low-Power-Level Applications

Presently, moderate power levels of around 25 kWe are being investigated. Some first results were presented in [8, 11]. Three turbine inlet temperature (TIT) values are being considered recently:

Nomenclature

NaK = eutectic sodium–potassium
TIT = turbine inlet temperature
CIT = compressor inlet temperature
ZrH = zirconium hydride
LiH = lithium hydride
HP = high pressure
Pt = thermal power

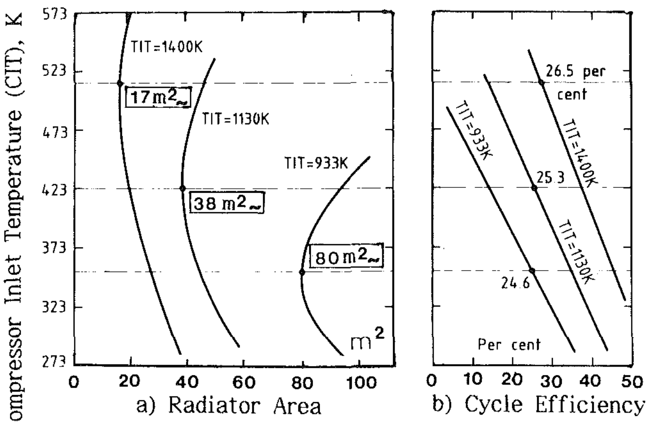

(TIT: turbine inlet temperature, Pe (net): 25kWe)

Fig. 6 Radiator area and cycle efficiency variation of 25 kWe systems

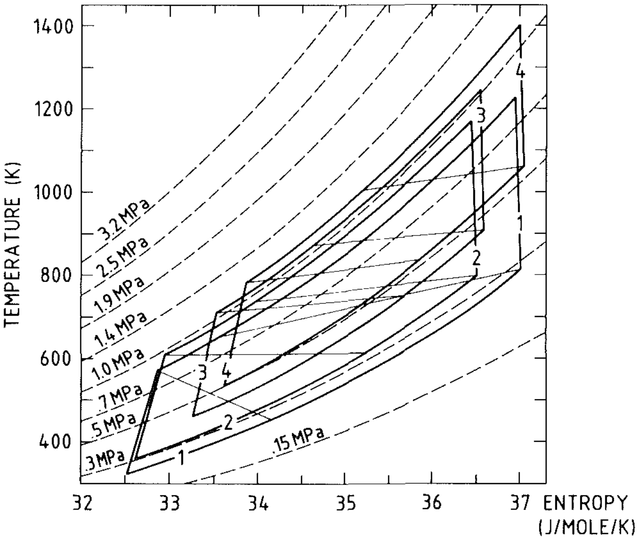

Fig. 7 Brayton cycle evolution during the runup of one pair of converters

- 933 K (short-term liquid sodium or NaK-cooled reactor),
- 1130 K (medium-term direct cycle, gas-cooled reactor),
- 1400 K (long-term high-temperature lithium-cooled reactor).

Figure 6(*a*) shows the variation of the radiator area of these 25 kWe systems as a function of the compressor inlet temperature (CIT). For the 933 K, 1130 K, and 1400 K cycles, the minimum radiator area, respectively, corresponds to 80 m^2, 38 m^2, and 17 m^2. The minimum of the curves is all the more marked as the TIT is lower. Figure 6(*b*) presents the corresponding variation of the cycle efficiency, the value of which changes only from 24.6 percent to 26.5 percent for the minimum radiator area conditions. Additional results are given in Table 1. The total power system mass is worth mentioning; it is of the order of 2400 kg, 2000 kg, and 1700 kg, respectively, for the 933 K, 1130 K, and 1400 K TIT cycles.

These low-power-level applications are being studied more in depth.

Simulation Studies

The first applications of this work concern the previous 200 kWe reference project. The analysis of the transient behavior of the system, via computer simulation, is intended to validate, detail, or modify preliminary selected basic options regarding:

- the operating transient scenarios and the associated regulation;
- the reactor control and the protective actions in the case of abnormal transients.

In the 200 kWe project, power is generated by two pairs of 50 kWe Brayton rotating units. Several operating procedures for the successive runups of both pairs of 2 × 50 kWe converters have been analyzed (Fig. 7).

The energy needs and time scale involved in the startup scenario with frozen coolant were estimated by the numerical

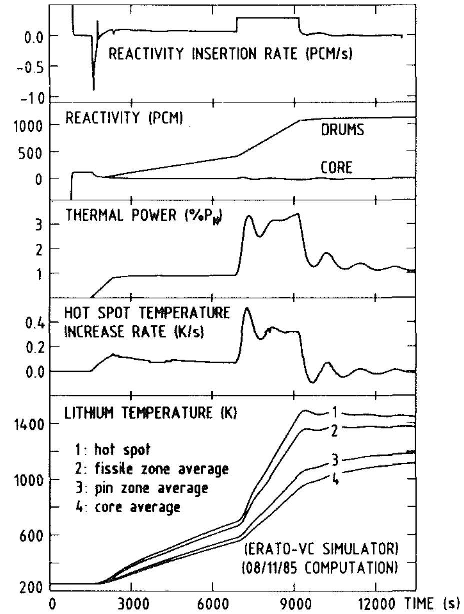

Fig. 8 Reactor response to the start-up procedure

Table 1 Key data of 25 kWe systems (values for minimum radiator area)

Turbine inlet temperature	K	1400	1130	933
Compressor inlet temperature	K	513	423	353
Pressure ratio (compressor)		←	1.90	→
Cycle efficiency	per cent	26.5	25.3	24.6
Net efficiency	per cent	21	20	19.5
Reactor thermal power	kWt	119	125	128
He-Xe (40) mass flow	kg/s	0.73	0.97	1.20
Recuperator dimensioning factor		1.33	2.18	3.20
Radiator thermal power	kWt	83.5	89	92
Radiator area	m^2	17	38	80
Radiator specific area	m^2/kWe	0.68	1.52	3.20
Total power system mass (round)	kg	1700	2000	2400

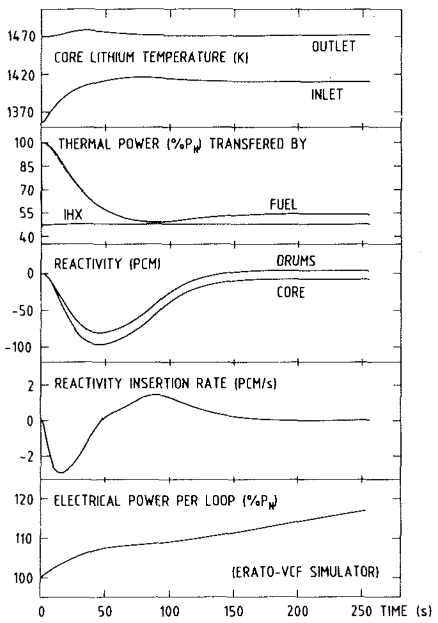

Fig. 9 Regulation response to the failure of one pair of converters

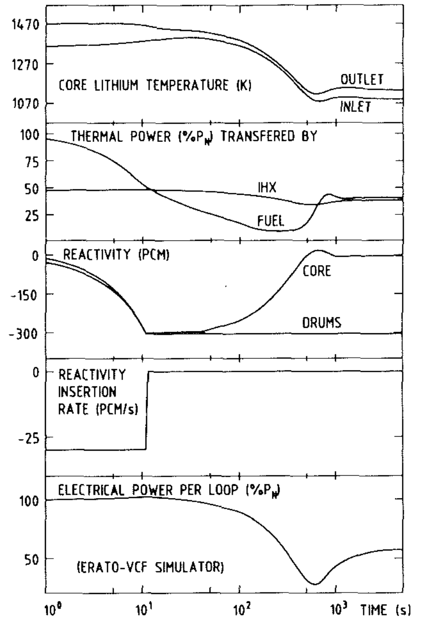

Fig. 10 Protective response to the failure of one pair of converters (automatic power reduction down to 50 percent Pn)

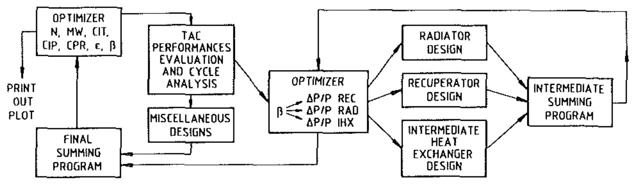

Fig. 11 Conversion subsystem optimization program architecture

simulation of the primary loop thermal response to a monitored reactivity insertion (Fig. 8).

As the restart procedure is expected to be long and difficult, control and protective actions have been developed that aim at avoiding the complete stopping of the rotating units. The capacity of the proposed regulation system for stabilizing the reactor operation and for damping the power and temperature

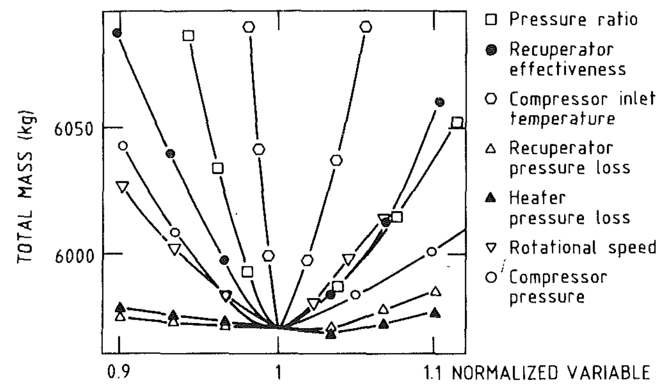

Fig. 12 Sensitivity of the power system mass to the departure of some key parameters from their optimum values

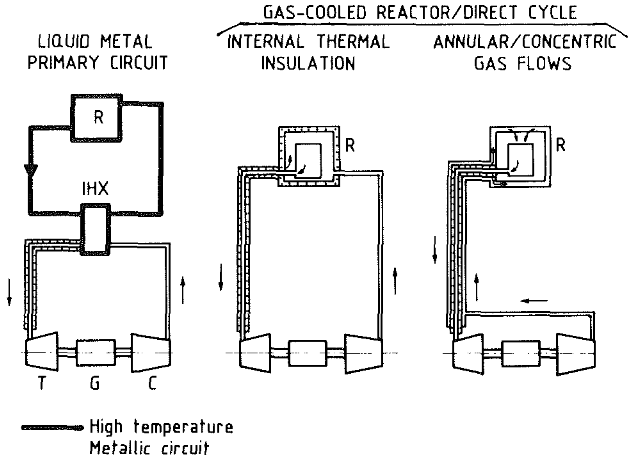

Fig. 13 High-temperature, Brayton cycle space nuclear power system concepts

swings has been demonstrated by the numerical simulations of various cooling accidents scenarios (Fig. 9). Simulation studies are currently applied to check the possibility of reversible protective actions, and to define the procedure of automatic reactor power reduction in particular, so as to keep at least one of the two pairs of converters running (Fig. 10).

These studies will be extended to future sensitivity analyses, in order to assess the advisability of departure from the reference design and operating conditions.

Power System Mass Optimization

Within the scope of the studies on the 200 kWe reference system, computer programs and procedures are being developed for performing an automated optimization of components and system design parameters. This optimization aims at minimizing the total mass under the constraints set by the integration into the ARIANE 5 launch vehicle.

In order to make the procedure more flexible, the global system is split into three weakly coupled subsystems, namely:

1 reactor + shield
2 primary circuit
3 conversion system + primary heat exchanger

Figure 11 presents the architecture of the program optimizing the third subsystem. Figure 12, drawn from results obtained with a preliminary version of the program, illustrates the consequences, on the reference system mass, of a slight departure from their optimum values of the major thermodynamic cycle parameters.

This work is expected to be extended in the near future to

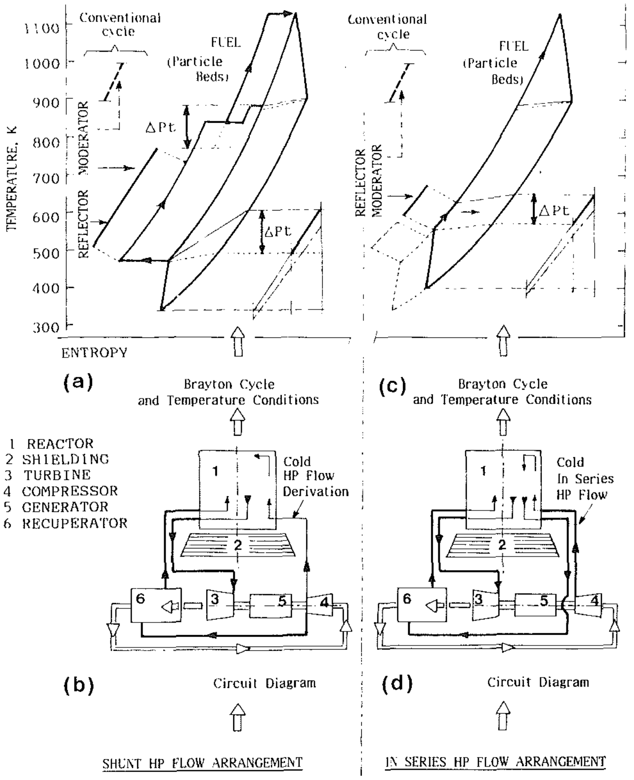

Fig. 14 Two examples of Brayton cycle adaptation for moderator, reflector, structure cooling

the optimization of low-power (20–30 kWe) space systems associated with both a liquid-metal-cooled nuclear reactor and a gas-cooled one with a gas turbine conversion system.

Reactor Technology and Concept

When going more closely into the significance of the utilization of the Brayton cycle for space power systems, it is essential to consider the possible consequences on the nuclear heat source technology and concept.

Reactor Technology. Figure 13 makes it possible to compare three investigated concepts.

A liquid-metal-cooled reactor implies an intermediate liquid-gas heat exchanger and an almost isothermal high-temperature primary circuit, including the structural materials.

The direct-cycle gas-cooled reactor is naturally suited to a Brayton cycle conversion system. In that case, the thermal conditions of most of the structures under pressure turn out to be quite different. Internal thermal insulation can be used in a gaseous environment in such a way that the piping and pressure vessel temperatures can be maintained at a moderate level. Another solution features a concentric flow technique, which keeps the main part of the circuit at the reactor inlet temperature. This point is worth noting because it is a question of technology readiness and also of the technical capability of European countries, given the moderate temperature level of the pressurized vessel and piping.

Attractive developments in this field can result from the temperature conditioning of moderated reactors discussed in the next section.

Reactor Concept. Another aspect has to be emphasized. In a direct cycle arrangement, it amounts to the investigation of a utilization of the conversion system that is as adequate as possible, supposing that a satisfactory space system should probably feature a right match and an actual symbiosis between the heat source and the conversion subsystem. This aspect concerns the possibility of contemplating a thermal spectrum gas-cooled reactor for moderate power level, long lifetime space applications. Consequences would be of the utmost importance from the points of view of fissile material inventory, safety, shielding, weight, control, and structure irradiation. Conditions must be fulfilled so that the temperature level allows use of efficient moderator and reflector materials like ZrH and Li_7H metal hydrides for a long period; it must be relatively low. In a first approach, the gas cycle makes it possible to use a convenient moderator by maintaining it at the reactor inlet temperature in normal operating conditions. But, in addition, more promising arrangements can be suggested and this topic is addressed in the following section.

Table 2 Comparison of two moderator, reflector, structure cooling arrangements

Moderator, Reflector, Structures Cooling Arrangements	SHUNT	IN SERIES
Turbine Inlet Temperature	1130 K	
Recuperator Effectiveness	0.93	
Compressor Inlet Temperature	345 K	400 K
Cooling HP Gas Flow Percentage	30 % (1)	100 %
Cooling HP Gas Inlet Temperature (2)	475 K (3)	550 K (4)
Reflector, Moderator, Temperature Range	520 - 760 K	600 - 670 K
Power System Relative Pressure Loss	7 %	8,4 % (+20%)
Pressure Loss Conversion Efficiency Penalty	NIL	- 1,6 pt. (-5%)
Reference Radiator Area (Conventional Cycle)	1,2 Sr	Sr (5)
Radiator Thermal Power Increase	+ 70 %	+ 36 %
Radiator Area Increase	+ 22 %	+ 13 %

(1) Hypothesis for a given moderator+reflector thermal power.
(2) Compressor exit.
(3) Lower than the required value for a minimum radiator area.
(4) Close to the required value for a minimum radiator area.
(5) Pressure loss penalty taken into account. – (optimum C.I.T.)

Moderated Reactor Temperature Conditioning

As far as thermal spectrum nuclear reactors are concerned, the required long lifetime use of the needed efficient ZrH and Li_7H moderator and reflector materials depends upon sufficiently low temperature and power levels. This section is devoted to the Brayton cycle aspects of the problem. The reactor design is a key factor of the study, but its presentation is beyond the scope of this paper. Ways of controlling the moderator and reflector temperature can be offered by a Brayton cycle directly combined with a gas-cooled reactor, typically a particle bed one. The two means presented in this paper imply the use of the high-pressure (HP) flow at the compressor exit, either partially or totally.

In the first arrangement, a certain amount, roughly 25 to 35 percent, of the HP flow leaving the compressor shunts to the HP side of the recuperator and cools the reflector and the moderator before being mixed with the remaining part of the flow, which has been preheated through the recuperator, as shown by Fig. 14(*a*). There is obviously a penalty in energy conversion efficiency because the increase in the heat source thermal power ΔPt must be rejected by the radiator. However, a significant comment has to be pointed out: the thermodynamic loss does not at all correspond to the characteristics of a conventional cycle of the same derated efficiency. As a matter of fact, in the shunt cycle arrangement, the working fluid mass flow and pressure drop are not modified and, what is of prime importance for space applications, the additional radiator thermal power ΔPt is rejected at a temperature higher than the one of the usual configuration and, consequently, the radiator size penalty is limited. For the example given in Table 2 the amount of heat transferred by the radiator increases by 70 percent but the corresponding radiating area extension does not exceed 22 percent.

The basic findings of Fig. 14(*a*) consist of the resulting much lower moderator and reflector temperature range in comparison with the conventional conditions. This temperature range goes from about 900–1000 K down to 520–760 K.

The power system circuit diagram of the shunt arrangement is shown by Fig. 14(*b*), the main feature of which is a small, cold, relatively short pipe connecting the compressor outlet to the reactor inlet.

Figure 14(*c*) shows the cycle and temperature conditions of the second arrangement, which features utilization of the whole HP flow coming from the compressor for cooling the reflector and the moderator. In this in-series configuration, the HP working fluid is directed to the reactor, cools the reflector and the moderator separately, and has to leave the reactor in order to flow through the recuperator before being finally heated in the core. As illustrated by the circuit diagram of Fig. 14(*d*), a double pipe has to be added between the reactor and the recuperator but it is a cold one and it can be of a concentric design.

It is more important to emphasize the consequences from thermal and thermodynamic points of view. The reflector and moderator temperature range is reduced, lowered, and extends from 600 K to 670 K only, compared with the previous case. The temperature drop reaches 300 K, as shown by Fig. 14(*c*), where a conventional cycle is shown for comparison. Because of this cooling upstream of the recuperator, the corresponding amount of heat ΔPt must be additionally rejected by the radiator, but only in the higher temperature region. For the example of Table 2, which concerns the same power level as previously, the increase in radiator thermal power is 36 percent but the extension of the radiator area is limited to 13 percent. These values take an increase in circuit pressure drop into account. As already mentioned, the working fluid mass flow is not modified at all. A further feature of this in-series arrangement is that the compressor inlet temperature is not lower than the value corresponding to the minimum radiator area for moderator temperature reasons.

Both shunt and in-series arrangements make it possible to condition the main pressurized structures like the reactor pressure vessel at an appreciably low temperature.

As far as the reactor is concerned, it can be said for the moment that the multiple particle bed concept offers ways of separating reflector, moderator, and fuel cooling areas.

The thermal and thermodynamic aspects of the separate moderator and reflector cooling are proven attractive given the basic advantages it offers for the adequate utilization of ZrH and Li_7H and for the necessary hydrogen containment. Related reactor design studies, which are presently in progress, tend to confirm the practicability and the interest of such moderated space nuclear power systems, at least for low or intermediate power levels. The in-series arrangement could be preferred.

Conclusions and Summary

In addition to the extended, corresponding development carried out in this field during many years in the USA, the four-year investigation of Brayton cycle power systems reported in this paper can be considered as conclusive for space applications. Results are estimated satisfactory from efficiency, compactness, weight, power level range, waste heat rejection conditions, flexibility, heat source adaptation, and technology points of view.

There are reasons for carrying on with the study of this conversion system. However, it is judicious to try to determine a utilization of the Brayton cycle that is as satisfactory as possible through an adequate association and match with the heat source. The temperature conditioning of a moderated reactor is an example of what could be accomplished in this domain.

Acknowledgments

The French space nuclear power systems studies are cosponsored by the Government Agencies "Centre National d'Etudes Spatiales" (C.N.E.S.) and "Commissariat à l'Energie Atomique" (C.E.A.). The sponsoring agencies and the authors wish gratefully to acknowledge the Garrett Corporation, Tempe, AZ, and particularly Mr. A. Pietsch, for information about various advanced Brayton cycle power systems.

References

1 Poher, C., et al., "Space Electronuclear Generators: Comparison Between Different Kinds of Energy Conversion Methods," I.A.F. Conference, Lausanne, 1984.

2 Poher, C., et al., "French Activity on Space Nuclear Power Systems," *2nd Symposium on Space Nuclear Power Systems*, Paper No. MS-2, Albuquerque, NM, Jan. 14–17, 1985.

3 Carré, F., Proust, E., and Schwartz, J. P., "Liquid Metal Versus Gas-Cooled Reactor Concepts for a Turbo-Electric Powered Space Vehicle," *2nd Symposium on Space Nuclear Power Systems*, Paper No. RS-1, Albuquerque, NM, Jan. 14–17, 1985.

4 Tilliette, Z. P., "Utilization of a Brayton Cycle Energy Conversion System in Space Nuclear Power Applications," *2nd Symposium on Space Nuclear Power Systems*, Paper No. EC-8, Albuquerque, NM, Jan. 14–17, 1985.

5 Poher, C., and Delaplace, J., "Space Electronuclear Generators; the French Approach," *3rd Symposium on Space Nuclear Power Systems*, Paper No. RS-6, Albuquerque, NM, Jan. 12–16, 1986.

6 Carré, F., et al., "Status of C.E.A. Reactor Studies for a 200 kWe Turbo-Electric Space Power System," *3rd Symposium on Space Nuclear Power Systems*, Paper No. RS-2, Albuquerque, NM, Jan. 12–16, 1986.

7 Tilliette, Z. P., "Advances in Defining a Closed Brayton Conversion System for Future Ariane 5 Space Nuclear Power Applications," ASME *Journal of Engineering for Gas Turbines and Power*, Vol. 109, 1987, pp. 92–98.

8 Tilliette, Z. P., and Cacheux, J., "Extended Brayton Cycle, Radiator Investigation for Future Ariane 5 Space Nuclear Power Applications," *21st Intersociety Energy Conversion Engineering Conference*, San Diego, CA, Vol. 3, 1986, pp. 1985–1992.

9 Alleau, T., and Lecocq, P., "Heat Pipe-Cooled Radiator for a Brayton Cycle Space Power System," *3rd Symposium on Space Nuclear Power Systems*, Paper No. TM-2, Albuquerque, NM, Jan. 14–17, 1986.

10 Carré, F., et al., "Status of C.E.A. Design and Simulation Studies of a 200 kWe TurboElectric Space Power System," *4th Symposium on Space Nuclear Power Systems*, Albuquerque, NM, Jan. 11–16, 1987, pp. 55–60.

11 Tilliette, Z. P., Proust, E., and Carre, F., "Progress in Investigating Brayton Cycle Conversion Systems for Future French Ariane 5 Space Power Applications," *22nd Intersociety Energy Conversion Engineering Conference*, Vol. 1, Philadelphia, PA, Aug. 10–14, 1987, pp. 438–443.

12 Carré, F., et al., "Conceptual Design Studies of 20 kWe Nuclear Power Systems. Impact of Reactor Temperature and Technology upon Design and Performances," *5th Symposium on Space Nuclear Power Systems*, Albuquerque, NM, Jan. 11–14, 1988.

R. Radermacher
Department of Mechanical Engineering,
University of Maryland,
College Park, MD 20742

An Example of the Manipulation of Effective Vapor Pressure Curves by Thermodynamic Cycles

The performance of a two-stage Rankine cycle employing a working fluid mixture and solution circuits has been computed with reference to heat pump applications. Its performance is compared to the single-stage version of this cycle and one operating with pure refrigerants. It is found that the two-stage cycle operates along an "effective" vapor pressure curve of very flat slope, resulting in pressure ratios that are reduced to about one third compared to conventional cycles. For large temperature differences between heat sink and source the Coefficient of Performance (COP) can be increased by up to 50 percent.

Introduction

It is well known from many applications of the Rankine cycle that its performance depends strongly on the thermodynamic and transport properties of the working fluid involved. Thus for given temperatures of heat sink and source each working fluid provides a certain pressure ratio according to its vapor pressure at these temperatures. It is common knowledge that the vapor pressure curves of all technically applied fluids show very similar slopes on an ln (p), $1/T$ diagram. This implies that all available pressure strains, even for a wide variety of fluids, are found to be not in drastic variance. It cannot be expected, at least according to today's knowledge of thermodynamics, that a fluid can be found whose vapor pressure curve would "cross" through all others on an ln (p), $1/T$ diagram, providing a low pressure ratio for given temperature differences between heat sink and source. However, for technical applications a fluid of such behavior would be of great interest. It would allow, for example in heat pumping, to overcome large differences in heat sink and heat source temperatures while encountering only very moderate pressure ratios. This would result in a dramatically increased temperature lift for any given compressor. The same reasoning is followed for two-stage absorption heat pumps as well. In this paper a certain version of the Rankine cycle will be discussed that effectively works along such more moderately sloped vapor pressure lines, although it may employ common and well-known working fluid mixtures. For the sake of simplicity the following consideration is concerned with a heat pump process only. However, the results can be transferred easily to power generation processes.

First the Rankine cycle using mixtures will be explained. The commonly known Rankine cycle, which uses a pure substance, can be generalized by using working fluid mixtures. The use of mixtures means with respect to thermodynamic the introduction of a new degree of freedom. One consequence of this is the following feature:

The saturation temperature of the mixture is no longer a constant during phase change, although the process is still isobaric. This leads to a so-called gliding temperature interval, which accompanies the change of quality from 0 to 100 percent. Its size depends on the mixture selected.

In order to accommodate the cycle described later, a working fluid mixture will be used in which the constituents have boiling points far apart from each other. If for a such a mixture a quality change from 0 to 100 percent would be required, the gliding temperature range would become inconveniently large. To limit this temperature interval, the mixture is partially evaporated. While the vapor is compressed by the compressor, the remaining liquid is pumped by a liquid pump into the condenser to absorb the compressed vapor. This arrangement of evaporator, condenser, and two liquid lines (one from the condenser to the evaporator, as usual, and one with the pump from the evaporator to the condenser) is called a (single-stage) solution circuit. Here this cycle is only of concern as a building block for the two-stage cycle, which accomplishes an effective vapor pressure curve of very flat slope as described next.

Two-Stage Rankine Cycle With Solution Circuit

In order to obtain a new "effective" vapor pressure curve the following configuration of heat exchangers is employed, as shown in Fig. 1. All heat exchangers are arranged in a pressure–temperature diagram, similar to the ln (p) $1/T$ graph. Thus the temperature and pressure values in heat exchangers (which accommodate a phase change) are obvious. This cycle operates with a working fluid mixture composed of components with boiling points far apart from each other. Figure 1(a) shows the vapor pressure curve for the two components, in this case refrigerants 1 and 2, and the two solution circuits, each of which is following the vapor pressure curves of mixtures of 1 and 2 with certain compositions. Heat exchanger A in Fig. 1(b) is an evaporator, or more correctly, a desorber from which vapor containing the predominantly low boiling component of the working fluid mixture is generated and fed into the compressor. The remaining liquid mixture is circulated by means of a pump into a second heat exchanger B in

---

Contributed by the Advanced Energy Systems Division for publication in the JOURNAL OF ENGINEERING FOR GAS TURBINES AND POWER. Manuscript received at ASME Headquarters June 27, 1988.

which the liquid absorbs the high-pressure vapor delivered by the compressor. The heat of absorption from B is released and used entirely to generate additional low-pressure vapor from a second desorber, component C, which also is supplied to the same compressor while the remaining liquid is pumped to absorber D, where again compressed vapor is absorbed. Here the heat of absorption is released to a heat sink medium. Note that absorption and desorption are occurring at constant pressure, but due to the inherent composition change a temperature interval is encountered during absorption and desorption (here referred to as "gliding temperature").

This cycle incorporates one compressor and two solution circuits. While the pressure and temperature values within each solution circuit are determined by the circulating mixture and its composition, the combined system represents a cycle that operates between the lowest temperature (heat source) and a highest temperature (heat sink). But the compressor encounters a much smaller pressure difference. In fact the pressure difference is just the same as for the single-stage cycle, which would pump heat only across half the temperature lift, for example, between the heat source temperature and the intermediate temperature level (Fig. *1*). This cycle thus effectively allows operation across a large heat sink and source temperature difference at very moderate pressure ratios, a feature that could be achieved by a working fluid with a vapor pressure curve with very low slope. The equivalent "effective" vapor pressure curve is indicated in Fig. 1(*a*) by line E.

The slope of vapor pressure curves is proportional to the latent heat of evaporation, a property that directly influences the mass flow rate and, since the compressor is a device providing a constant volume flow rate, also the capacity. This is also the case for the two-stage cycle. For each unit of vapor generated by introducing heat from the heat source, the compressor has to compress approximately two units of vapor, since the additional quantity is delivered from the internal heat exchange process between heat exchangers B and C.

Therefore, the advantage of a low pressure ratio of the moderately sloped effective vapor pressure curve is achieved by reduced capacity or increased mass flow rate. This is according to basic thermodynamic principles.

Although this process has been published (Alefeld, 1982), it has not yet been applied. Yet the single-stage version, which has only one set of heat exchangers (A and B for example) is currently being applied in a district heating system and is under investigation in a laboratory (Mucic and Sheuerman, 1983; Stockar and Trepp, 1987). Another description is found in Vobach (1983) and it was first described in 1920 (Altenkirch, 1950). The advantages inherent in the single-stage cycle are that capacity control over a wide range can be easily achieved by controlling the composition of the circulating mixture, and that gliding temperatures in absorber and desorber are available. This increases the coefficient of performance in most applications where counterflow heat exchange can be employed. The two-stage cycle introduced here offers the same features, but the available composition change is reduced in most cases.

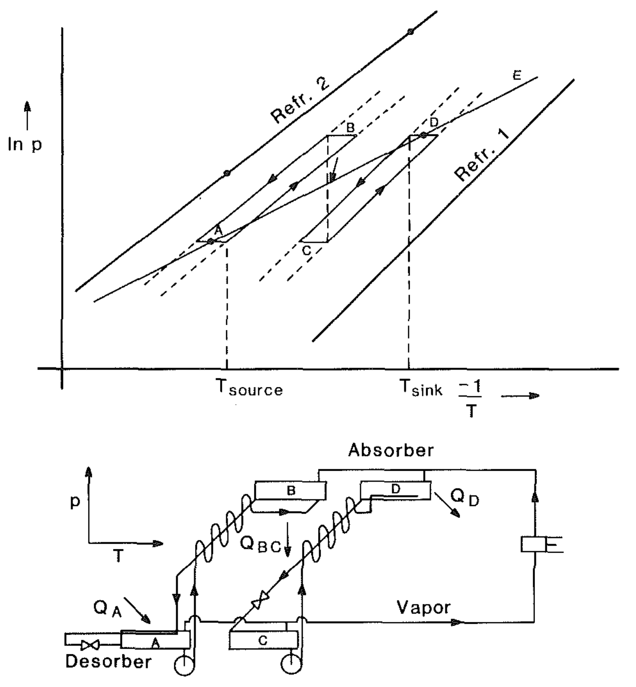

Fig. 1 Vapor compression heat pump with two-stage solution circuit: (*a*) The vapor pressure curves of the two constituents of the mixture are shown superimposed on a pressure-temperature diagram. Between them the liquid concentrations of the fluid circulating within the respective pairs of desorber and absorber are indicated. When all heat released in B is transferred to C, then heat pumping is performed from A to D. This results in an "effective" vapor pressure curve E, which has a considerably flatter slope than those of the real fluids. (*b*) Again superimposed on a pressure-temperature diagram all major heat exchangers are shown.

In order to study and compare the two cycles introduced here, calculations have been performed using halogenated hydrocarbon mixtures as working fluids. Note that in general those mixtures are to be preferred where the boiling points are as far apart as possible.

Calculations

All computations have been performed for the mixture R13B1/R11 using an equation of state developed at NBS (Morrison, 1985) for halogenated hydrocarbons. For environmental impact considerations, the working fluid mixture selected here will be banned in the relatively near future. Although it is not expected that a particular unit will operate with the mixture chosen for the calculations, it serves, nevertheless, as a good example for the potential of working fluid mixtures. This equation of state requires the adjustment of one parameter in order to represent mixture data accurately. Since no measured mixture data are available, a value of 0.03 was chosen, which is an average found to be valid for most

Nomenclature

COP = Coefficient of Performance
p = pressure
T = temperature
m = fraction of clearance volume to total cylinder volume
V = volume
ΔT = temperature change between beginning and ending of absorption or desorption process
η = volumetric efficiency

Subscripts

suc = suction
dis = discharge

Components

A = low-temperature desorber, receives heat from source
B = low-temperature absorber, supplies heat to C
C = high-temperature desorber, receives heat from B
D = high-temperature absorber, rejects heat to heat sink
E = indicates the effective vapor pressure line

halogenated hydrocarbon mixtures known. A sensitivity study revealed that the results presented here are not significantly changed by adjusting this factor over the entire range encountered so far.

The calculations have been performed for a lower heat sink temperature of 50°C and a gliding temperature interval of 10 K in the absorber, while the highest heat source temperature were 8°C and −20°C in order to cover the entire range to be encountered in many heat pump applications. The compression was assumed to be isentropic. A volumetric efficiency for reciprocating compressors has been accounted for according to the following equation (Stoecker and Jones, 1982):

$$\eta = 1 - m\cdot\left(\frac{V_{\text{suc}}}{V_{\text{dis}}} - 1\right) \qquad (1)$$

where m is the ratio of clearance volume over total cylinder volume, and V_{suc} and V_{dis} are the specific volumes of suction and discharge vapor, respectively. Further, it was assumed that saturated liquid leaves the desorber and absorber, and that the heat exchange in the liquid heat exchanger is complete. The efficiency of the pumps was assumed to be 0.7.

For comparison, the calculations have been performed for the pure components under proper consideration of the gliding temperature intervals, and for the one- and two-stage cycles as described above.

Figure 2 shows the gliding temperature range ΔT_c for the absorber rejecting its heat to the heat sink fluid, versus the composition of the mixture leaving the low temperature desorber, component A. This gliding temperature interval does stay around 10 K for the two-stage cycle (continuous line), which was calculated assuming that the composition change in the absorber is 0.1. In the case of the single-stage version (dashed line) the temperature difference ΔT_c was kept at 10 K by adjusting the composition difference of the mixture in the two liquid lines accordingly. In this case the corresponding gliding interval in the desorber, ΔT_D, was found to be on the order of 4 K.

Figure 3 shows the pressure ratios for the given conditions again versus composition as described above for Fig. 2. While for the pure components (squares) the pressure ratios become excessively large (especially for the lower heat source temperature at high R11 compositions) the pressure ratio does remain moderate for the single-stage cycle. However in the case of the two-stage cycle the pressure ratio is reduced by almost a factor of three compared to the more favorable pure component R13B1, which is in accordance with the discussion above.

Figure 4 shows the heating capacity per unit of suction slide volume over composition. The capacity changes almost linearly with composition for all mixture cycles. But the capacity of the single-stage cycles is higher than what would be expected by linear interpolation between the pure components. The capacity of the two-stage cycle is reduced by a factor of about two, as expected. In addition, from Fig. 4 it can be seen that for a given temperature difference between heat sink and source the capacity of single-stage cycle can be changed by a factor of three by mere adjustment of the circulating composition. Still a factor of two is possible when the desorber temperature changes from 8°C to −20°C. This implies that with decreasing outdoor temperature the heating capacity of a heat pump can be doubled, a feature no commonly employed heat pump cycle exhibits using constant displacement rate compression.

Figure 5 shows the heating COP versus composition. The power consumption of the pumps is considered in the COP

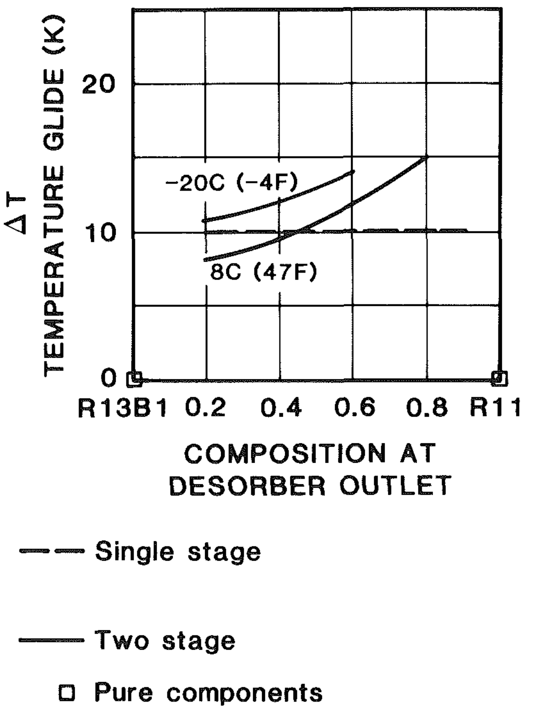

Fig. 2 The temperature change during phase change is shown as a function of the composition of the liquid stream leaving A. For the two-stage cycle two curves are indicated, corresponding to two heat source temperatures of −20°C and 8°C. The curves do not span the whole concentration range because the cycle ceases to operate under the specified conditions when the concentration range approaches its limits.

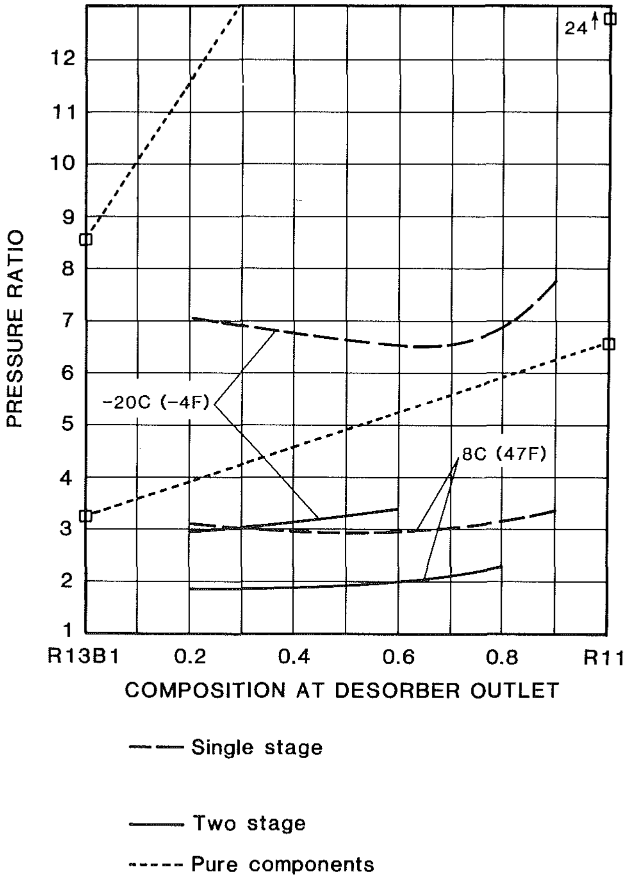

Fig. 3 Pressure ratio is plotted versus the liquid composition at the outlet of component A. The curves represent two cases corresponding to two heat source temperatures.

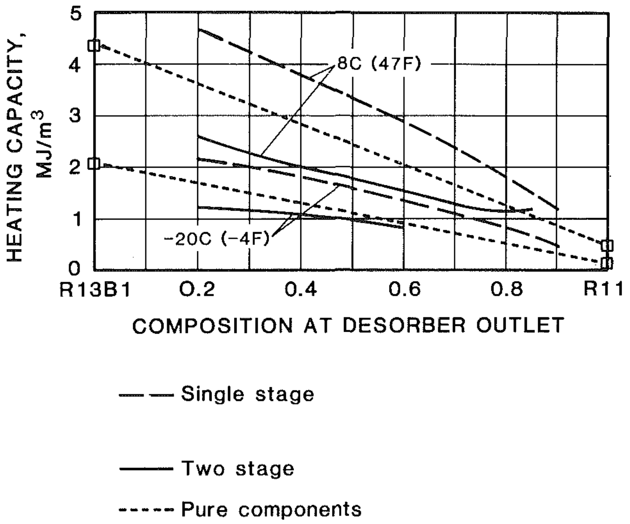

Fig. 4 Heating capacity of the cycle plotted versus the liquid composition at the outlet of component A

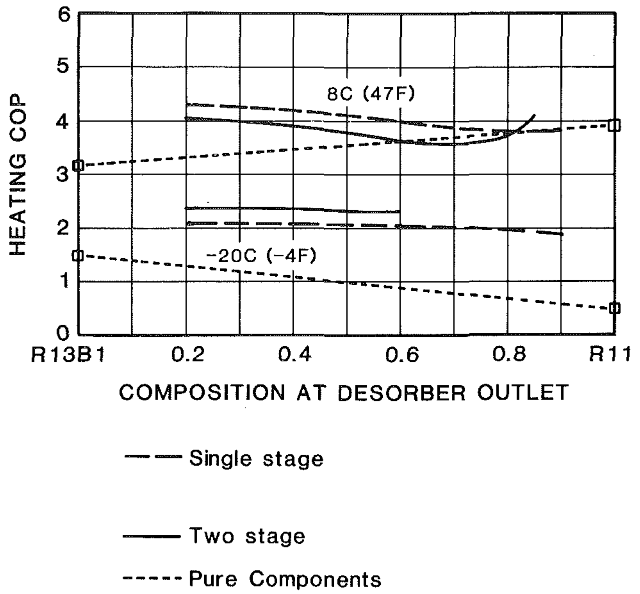

Fig. 5 Heating COP shown as a function of the liquid composition of the outlet of A

calculations. The COP of the conventional nonazeotropic mixture cycle drops significantly with increasing R11 content due to the excessively large gliding temperature intervals. In accordance with thermodynamics, the COP of the single- and two-stage cycles stays relatively constant with composition. At the higher heat source temperature the two-stage cycle performs poorer than the single-stage version. This is mainly due to the power consumption of the second solution pump. However, at the lower heat source temperature, the two-stage cycle achieves a COP that is 10 percent higher than that of the single-stage version, and more than 50 percent higher than the better of the pure components, R13B1. This increase is caused by the low pressure ratio, resulting in increased COP by itself and supported by the fact that due to the low pressure ratio the efficiency remains high.

So far the COP for heating has been considered. For the cooling performance the same arguments hold, and the differences between cycles would be quite similar with one important exception. All COP values for cooling are obtained from those for heating by subtracting 1.0, according to the First Law.

Technical Implications

The results show that the cycles discussed here offer new options in capacity control and a dramatically expanded range of application of vapor compression heat pumps employing one single-stage, constant volume flow-rate compressor. This can have a significant technical impact. While capacity control at constant temperatures can be achieved up to a factor of about ten by choosing an appropriate mixture, a significant capacity increase with increasing temperature lift becomes possible as well. This constitutes a feature no heat pump offers so far with a fixed volume flow-rate compressor.

The two-stage cycle offers as its main feature a pressure ratio of about a third of what would be found for the single-stage cycle or one with pure components for a given temperature lift. Said feature provides a significantly increased COP. This has two implications. Single-stage compressor units can be employed to overcome large temperature lifts (in cases where two-stage compressors are employed commonly) reducing head pressures drastically, and expanding the climatic ranges for heat pump applications. Secondly, since the mass flow rate is significantly increased for a given set of conditions and the pressure ratio reduced, this cycle offers an extended range of applicability for centrifugal and screw compressors in conditions otherwise served by reciprocal ones only. The same consideration holds of course for other low-pressure heat compressors.

The price of these advantages is the introduction of one or more circulating pumps, the power consumption of which is found to be always significantly below 10 percent of the compressor power even when more realistic pump efficiences of 0.5 are chosen, and significantly enlarged heat transfer areas for internal heat transfer. A rough estimate yields that for a single-stage cycle the refrigerant side heat transfer area will increase by 50 percent due to the liquid heat exchanger, while it triples for the two-stage version (both compared to a system for a single pure component). However, these increases would be much smaller for any high latent heat-low specific heat working fluid mixture like ammonia/water. Currently a laboratory proof-of-concept unit is under construction that will allow test and verification of the claims made here (Radermacher et al., 1988).

Finally, it should be noted that the cycle introduced here is a special case of a so-called *blend cascade*, which is used for the liquification of natural gas (Missimer, 1973).

Conclusions

Heat pump cycles employing one or more solution circuits employ a more complicated design, requiring more internal heat transfer surface and one or more liquid pumps, but offer in exchange several advantages: wide range of capacity control by composition shift, significant extension of the range of applicability of vapor compression heat pumps by overcoming large temperature lifts at very low pressure ratios; and significantly increased COPs, as compared to cycles using fixed volume displacement compressors and no degradation of heat transfer for the refrigerant mixture (as compared to the pure components that constitute the mixture).

Acknowledgments

This study is part of a larger refrigerant mixtures program under the joint sponsorship of the National Bureau of

Standards, Electric Power Research Institute, and the Department of Energy through Oak Ridge National Laboratory.

References

Alefeld, G., 1982, "Heat Conversion Systems," Lecture Notes, Physics Department E19, Technical University of Munich, Garching, Federal Republic of Germany.

Altenkirch, E., 1950, "Vapor Compressor Refrigerator With Solution Circulation," *Kaetechnik*, Vol. 2, pp. 151, 279, 310.

Missimer, D., 1973, "Self-Balancing Low Temperature Refrigeration System," US Patent No. 3,768,273.

Morrison, G., 1985, "Two Refrigerant Mixtures and the Hard Sphere Fluid," *ASHRAE Transactions*, Vol. 91, pt. 2.

Mucic, V., and Sheuermann, B., 1983, "Two Component Vapor Compressor Heat Pump With Solution Circuit," Pilot Pant Mannheim-Waldhof, BMFT-FB-03E-588A.

Radermacher, R., Zheng, J., and Herold, K., 1988, "Vapor Compression Heat Pump With Two-Stage Solution Circuit: Proof-of-Concept Unit," Int. Workshop on Absorption Heat Pumps, London, United Kingdom, Apr. 12-14.

Stockar, M., and Trepp, Ch., 1987, "Compression Heat Pump With Solution Circuit. Part 1: Design and Experimental Results," *International Journal of Refrigeration*, Vol. 10, pp. 87-96.

Stoecker, W., and Jones, J., 1982, *Refrigeration and Air Conditioning*, 2nd ed., McGraw-Hill, New York.

Vobach, A. R., 1983, "Development of a Chemically Assisted Mechanical Refrigeration Cycle," DOE/R6/12081—T1.

Temperature Transformation for High-Temperature Heat Pumps

R. Radermacher

L. A. Howe

Department of Mechanical Engineering,
The University of Maryland,
College Park, MD 20742

A heat pump cycle is introduced that allows heat pumping between two very high temperature levels, while the suction temperature of the working fluid vapor passing through the compressor is considerably lower. This effect of "Temperature Transformation" is achieved by using a working fluid mixture instead of a single pure component and by employing an unconventional cycle design. The proposed cycle allows the extension of heat pump applications to high temperature levels without encountering operating problems for conventional compressors. This cycle and its features are explained. Its performance has been calculated and the results are presented and discussed.

Introduction

Advanced energy conversion cycles that use working fluid mixtures can offer quite surprising features, the technical implications of which may be far reaching (Alefeld, 1982). For example, some versions can accomplish a tilting of an "effective" vapor pressure curve, so that its slope is reduced to half of the usual value (Missimer, 1973; Radermacher, 1986; Pourreza-Djourshari and Radermacher, 1986). Another version also taken from Alefeld (1982) is discussed here. Its main feature is called "Temperature Transformation." This term refers to a vapor compression heat pump, with a compressor operating on one temperature level, while the heat pump process may occur at two completely different temperature levels, which may be significantly higher or lower. In fact all moving parts are exclusively on the low temperature level. On the high temperature levels there are just heat exchangers. The heat pumping temperature levels may, for example, be chosen so high that conventional compressors (in conventional heat pumps) would not be operational because of oil breakdown. Therefore the cycle proposed here seems to be very well suited to lift waste heat to higher temperature levels. How this is accomplished is described in more detail below.

Description of the Cycle

Figure 1 shows the process scheme. All heat exchangers that accommodate a phase change are arranged in a pressure–temperature diagram so that the prevailing pressures and temperatures are obvious. The scales of the axes are chosen so that vapor pressure curves of the pure working fluids and their mixtures are straight lines. In this representation, the function and properties of a basic component of all Rankine cycles, the so-called "solution circuit," become obvious. The simplest example for a solution circuit is a paired evaporator and condenser, which are connected by a liquid line. This liquid line can be provided with a pump when the pressure level of the evaporator is higher than the condenser, thus feeding liquid working fluid from the condenser into the evaporator, as is the case in a power plant. The liquid line can also be provided with an expansion valve, as is encountered in heat pumps. When a working fluid mixture is used, one may distinguish two cases. When all the liquid evaporates in the evaporator (case one), the solution circuit remains the simplest possible version as described above. However, if the mixture does not evaporate completely (case two), then we have to add a second liquid line in order to convey the remaining liquid portion into the condenser. This second line must be provided with either a pump or an expansion valve to appropriately overcome the pressure difference. When mixtures are used, the evaporator is frequently termed the desorber and the condenser the absorber. Since desorber and absorber are on different temperature levels, it is advisable to arrange for heat exchange between the two liquid streams.

A complete and more general solution circuit therefore is composed of two heat exchangers that accommodate a phase change of at least part of the working fluid mixture, two liquid lines that are exchanging heat with each other (which requires a third heat exchanger), and either line is fitted with either an expansion valve or a pump. Such a solution circuit can be viewed as a building block for more complex Rankine cycles. For example, two solution circuits (one simple and one with two liquid lines) represent a conventional absorption heat pump. In this case one solution circuit is operated as a heat pump, the other as a power plant. Therefore the latter is sometimes referred to as a thermal compressor. Three solution circuits can be combined for (a variety of) two-stage absorption heat pumps (Alefeld, 1982).

Here we combine two solution circuits (one of them simple) with a compressor in order to achieve temperature transformation. In contrast to an absorption heat pump, the main input of energy is now in the form of work, not heat. It is essential to note that the proposed cycle will only work if the same mixture (with different compositions) is used in both solution circuits.

According to Fig. 1, the absorber and desorber belong to a

Contributed by the Advanced Energy Systems Division for publication in the JOURNAL OF ENGINEERING FOR GAS TURBINES AND POWER. Manuscript received by the Advanced Energy Systems Division April 20, 1987.

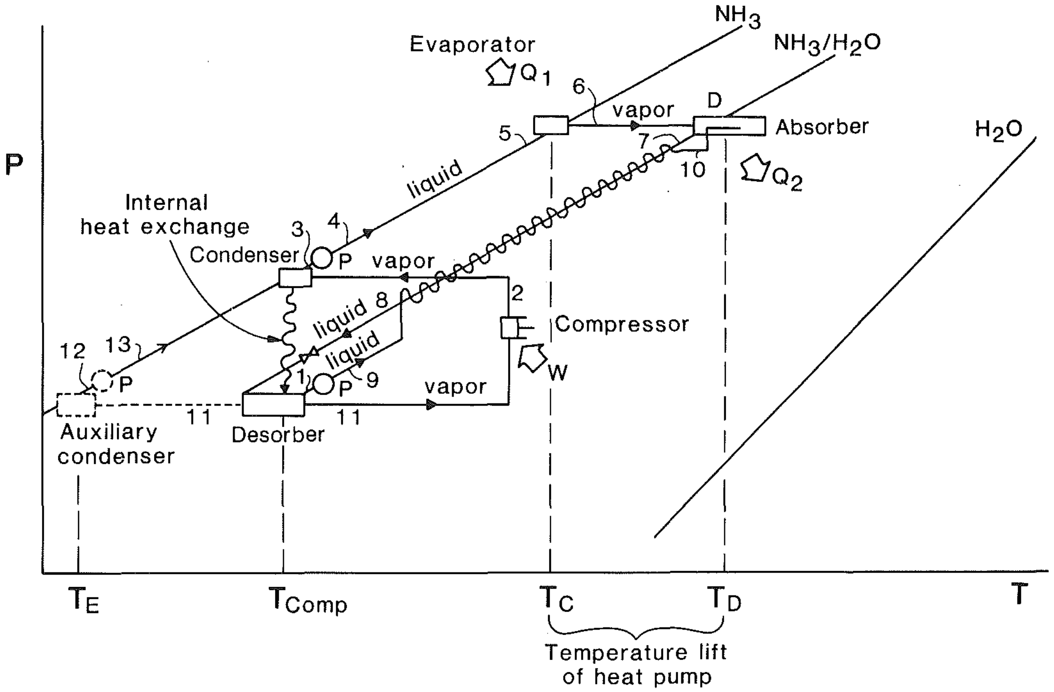

Fig. 1 Heat pump cycle with temperature transformation: The compressor operates between the desorber and condenser with the condenser supplying the heat of desorption. The heat pump process occurs between the evaporator, absorbing low-temperature heat, and the absorber, rejecting high-temperature heat. The compressor is never faced with the high temperatures of the evaporator and desorber. The numbers indicate the state points listed in Table 1.

complete solution circuit and the evaporator and condenser to a simple one. The second one could have been a complete one too, but was chosen to be a simple one for the sake of simplicity.

Vapor is generated in the desorber out of a working fluid/absorbent mixture (e.g., ammonia/water) and compressed by means of the compressor. The high side pressure is selected so that the heat of condensation of the vapor within the condenser can be used to generate further vapor in the desorber. The remaining solution is pumped through a liquid/liquid heat exchanger into the absorber, while the condensate leaving the condenser is pumped into the evaporator. The system is designed so that the pressure in the evaporator and absorber is the same (Fig. 1). The actual value of this pressure is determined by the composition of the mixture and the desired temperature levels of the acutal heat pump process. The evaporator of the heat pump absorbs heat from an outside high-temperature source, while the absorber rejects heat by absorbing vapor supplied by the evaporator into the liquid mixture pumped from the desorber through the liquid/liquid heat exchanger. The solution with the high working fluid concentration leaves the absorber and returns through the other side of the liquid/liquid heat exchanger and the expansion valve into the desorber. In a conventional heat pump, the compressor conveys vapor from the evaporator to the condenser of the same solution circuit, the same one that does the heat pumping. We face a different situation here. The compressor now conveys vapor from one solution circuit to the next, while the acutal heat pump process returns the vapor to the original solution circuit. Through this measure, the compression process and the heat pump process are decoupled This enables us to choose the temperature levels for the actual heat pump process (almost) independently of the temperature level of the compressor suction gas. The temperature level of the evaporator and absorber is only limited by the pressure head the pumps are able to provide.

The temperature lift of the heat pump, i.e., the temperature difference between the evaporator and absorber, is determined by the difference between the average composition of the mixture circulating between the desorber and the absorber and the composition of the liquid being pumped from the condenser to the evaporator. This in turn determines the pressure ratio the compressor has to overcome (Fig. 1). Any change in the average composition will move the solution circuit comprised by the desorber and absorber, the pump, expansion valve, and liquid/liquid heat exchanger, closer to the solution circuit comprised of the condenser and evaporator in terms of pressure and temperature, or farther away, thus affecting the pressure ratio for the compressor and at the same time the temperature lift (Fig. 1).

So far it has been assumed that the amount of heat provided by the condenser is just sufficient to generate vapor in the desorber under steady-state conditions. However, as shown later, it turns out that this does not have to be the case. Actually the condenser may reject excess heat to an external sink or the desorber may require additional heat from an outside source.

It turns out that for the cases discussed here the condenser supplies excess heat. It is therefore most beneficial to circulate through the compressor only enough working fluid to the condenser to meet the heat requirement of the desorber. The excess vapor is rerouted from the desorber directly into an auxiliary condenser (Fig. 1, dashed lines). Here the excess vapor is condensed and also pumped into the evaporator. In this way the overall efficiency of the system is increased, and also the requirement of a low-temperature heat sink is introduced.

For the reader familiar with absorption systems, it may not be surprising to realize the following: If the auxiliary condenser is in operation and the compressor and the condenser were removed or inoperational, and if heat were supplied to the desorber from an outside source, then the configuration of Fig. 1 would represent an absorption heat transformer (or temperature amplifier). Thus the cycle investigated here can be considered a compressor-driven heat transformer.

Calculation Procedure

It is assumed for the investigation presented here that the fluid mixture is ammonia/water. The reasons for this selection are the following:

- availability of thermodynamic data,
- favorable high-temperature stability, and
- favorable heat and mass transfer properties.

Any other fluid mixture can be used in such a cycle as long as the boiling points of the pure components are sufficiently far apart.

In addition, the cycle presented here assumes that the vapor generated in the desorber is pure working fluid (containing only a negligible amount of absorbent). This does not have to be the case. The only change required for the cycle in order to accommodate any otherwise suitable mixture is the introduction of a complete solution circuit rather than a simple one between the condenser and evaporator. Thus the entire cycle would have two complete solution circuits.

The data and subroutines for ammonia/water are taken from Ziegler and Trepp (1984) in the form of computer subroutines. These were used to calculate the properties of NH_3/H_2O mixtures based on a Gibbs free energy function, which allows us to calculate phase equilibrium and single-phase properties using an iterative scheme. The actual equations used are discussed in detail in the cited reference.

A computer code was written to calculate all thermodynamic properties at all in- and outlets of all heat exchangers and the mass flow rates. The information entered consisted of the temperature and composition at the outlet of the desorber (Fig. 1) and the temperature at the outlet of the evaporator. The difference in composition between the two mixture streams between the absorber and desorber was set to a given value. It was further assumed that the heat exchange in the liquid/liquid heat exchanger is complete, i.e., there is a zero temperature difference at one end. In addition, it was assumed that the vapor leaving the desorber is in equilibrium with the fluid entering (after the expansion valve) and that the compression process was isentropic. The saturation temperature in the condensor was selected so that it was equal to the highest temperature required in the desorber.

Accuracy

The property subroutines used reproduce the experimental data for ammonia/water as stated by Ziegler and Trepp (1984) within the following limit: vapor pressure data ±3 percent and enthalpy data ±10 kJ/kg. Since the calculations are based on an ideal cycle, the numerical results can be considered accurate within the limits stated above and the precision of the computer. The lack of closure of the energy balance was always less than 0.1 percent. The most severe limitations are introduced by the assumptions described in the previous section. The calculations for the Rankine cycles with pure fluids are based on the assumption of ideal cycles and the data are taken from ASHRAE (1985) and from Keenan et al. (1969).

Results and Discussions

Calculations have been performed for various ammonia compositions, but the temperature at the outlet of the desorber (point 1, Fig. 1) has been fixed at 45°C and at the outlet of the absorber (point 7) at 120°C. The temperature level of the heat pump evaporator is thus a function of the composition of the mixture circulating in the complete solution circuit. The temperature range was selected so that waste heat is used to produce low-pressure steam. Table 1 shows the results obtained for the calculations of one particular set of conditions. The pressures, temperatures, enthalpies, and compositions are listed for each state point, the numbers of which correspond to the numbers in Fig. 1. In Table 2, the heat exchanged by each component, the work requirement of compressor and pumps, and the heating COP are listed. All values are listed twice, with and without the auxiliary condenser in operation.

Table 1 Values of thermodynamic variables at various state points (numbers refer to Fig. 1) throughout the cycle; case 2 of Table 3 has been chosen as an example

Point	P(bar)	T(°C)	H(kJ/kmol)	x(mol-fract.)
1	5.6	45	-733	.500
2	17.7	122	25827	.998
3	17.7	45	3658	.998
4	44.1	46	3770	.998
5	44.1	46	3770	.998
6	44.1	87	22044	.998
7	44.1	120	5898	.600
8	44.1	96	986	.600
9	44.1	45	-614	.500
10	44.1	120	5530	.500
11	5.6	30	22689	.998
12	5.6	7	560	.998
13	17.7	8	607	.998

Table 2 Amount of heat and work exchanged by components according to case 2 (Table 3)

Amount of Heat Rejected by Component	without auxiliary condenser kJ/(kmol vapor at 6)	with auxiliary condenser kJ(kmol vapor at 6)
Desorber	-14852	-14852
Condenser	21527	14852
Evaporator	-18274	-19219
Absorber	14679	14679
Auxiliary Condenser	0	6861
Compressor Work	2495	1722
Pump Work	583	598
COP_h (incl. pump work)	4.8	6.3
COP_c (incl. pump work)	5.9	8.3

Since the calculation is based on one kmol of vapor at point 6, the amount of heat released or absorbed by the desorber and evaporator is independent of the auxiliary condenser. It is further expected that the condenser is affected by the operation of the auxiliary condenser, because some of the amount of vapor leaving the desorber is rerouted to the auxiliary condenser, so the amount of vapor condensing in the condenser is reduced. The evaporator shows a minor influence, which results from the fact that part of the liquid entering is supplied from the auxiliary condenser, i.e., at a lower temperature, increasing the enthalpy difference across the evaporator. It should be noted that the amount of heat absorbed by the evaporator of the heat pump is larger than the amount of heat released by the absorber. This is due to the fact that part of the evaporator heat is required to preheat the liquid entering the evaporator and that heat rejected by the cycle at the auxiliary condenser is not suitable for heating. Thus the evaporator capacity seems to be increased, compared to the absorber capacity. Another consequence of this fact is that the difference between heating and cooling COP is no longer 1 as is frequently the case for conventional heat pumps.

Whether the auxiliary condenser is in operation or not af-

Table 3 Calculated results for the performance of a temperature transformation heat pump cycle for five different operating conditions

			Case		
Variable	1	2	3	4	5
T_{comp} (°C)	45	45	45	45	45
T_C (°C)	85	87	90	92	96
T_D (°C)	120	120	120	120	120
T_E (°C)	-7	7	17	20	25
T_{sup} (°C)	148	122	106	96	83
x_1 (mol fract.)	.40	.50	.58	.60	.65
x_7 (mol fract.)	.60	.60	.60	.65	.70
Ax (mol fract.)	0.2	0.1	0.02	0.05	0.05
COP_{heat}	3.5/4.8	4.8/6.3	3.5/4.2	5.5/6.8	6.2/7.4
W_{pump}/W_{comp}	0.08	0.19	1.12	.56	0.74
Pressures (bar)	3.3/17.8/44.1	5.6/17.8/44.1	7.9/17.8/44.1	8.5/17.8/50.0	10.0/17.8/55.8
P/P	5.4	3.18	2.25	2.09	1.78

fects the pump work slightly due to the additional need for pumping liquid from the lowest pressure level into the evaporator. The work requirement of the compressor is reduced quite profoundly by using the auxiliary condenser, because part of the vapor generated in the generator is no longer passing through the compressor, but rather condensed in auxiliary condenser directly. The compression process for this portion of the fluid is transferred from the vapor to the liquid state.

The results obtained for five cases, which are selected as examples, are summarized in Table 3. This table shows in rows the values for the following parameters: T_{comp} is the temperature on the suction side of the compressor; T_E is the temperature of the saturated liquid leaving the auxiliary condenser; T_D and T_C are the temperatures of the saturated liquid leaving the absorber and the evaporator, respectively; T_{sup} is the temperature of the compressor discharge gas; x_1 and x_7 are the compositions of the two liquid streams between desorber and absorber, while Δx is their difference. Two further values for the COP are given. The lower is calculated assuming that all excess heat of the condenser is rejected at T_{comp}, while for the higher one it is assumed that the auxiliary condenser is in operation. Finally the ratio of pump work over compressor work input is given, along with the values of the three pressure levels.

The first three cases have the composition x_7 fixed to 0.60 while Δx is given the values 0.2, 0.1, and 0.02. Since the outlet composition is fixed, and also the compressor temperature level, the two higher pressure levels are fixed as well, and any change in Δx affects the lowest pressure level only (Table 3). Thus the temperature level required for heat rejection of the auxiliary condenser changes accordingly. It is found that for the smallest Δx, i.e., the highest low-side pressure, the temperature level of the auxiliary condenser is highest (17°C), and the pressure ratio across the compressor lowest. This case also has the lowest superheat temperature of the vapor leaving the compressor. Nevertheless, the COP is best for the intermediate Δx. The reason for this behavior is the pump work. The smaller Δx becomes, the higher is the mass flow rate through the pump. At the very extreme, the pumpwork increases to a value that is, for example, 1.12 times higher than the work input to the compressor when $\Delta x = 0.02$ (Case 3, Table 3). Consequently the best performance is obtained by a Δx of 0.05. The last two columns of Table 3 show the best results. The COP is found to be the highest and the pressure ratio to be lowest.

When the overall composition is shifted toward higher ammonia concentrations, it can be observed that the lowest pressure and highest pressure increase in order to meet the prescribed conditions, while the intermediate pressure, fixed through the compressor suction temperature, remains constant (Case 4 and 5, Table 3). The temperature of the heat pump evaporator increases accordingly. As should be expected, the COP increases as well.

Table 4 Results of performance calculations for vapor compression heat pump with a single complete solution circuit

				Case		
Variable	1	2	3	4	5	6
T_{comp} (°C)	85	90	95	85	90	95
T_{desor} (°C)	85	90	95	85	90	95
T_{absorb} (°C)	120	120	120	120	120	120
T_{sup} (°C)	186	177	169	156	151	146
x_1 (mol fract.)	0.2	0.2	0.2	0.5	0.5	0.5
x_7 (mol fract.)	0.15	0.15	0.15	0.45	0.45	0.45
Ax (mol fract.)	0.05	0.05	0.05	0.05	0.05	0.05
COP_{heat}	5.3	5.7	6.2	6.5	7.2	8.2
W_{pump}/W_{comp}	0.002	0.002	0.002	0.14	0.15	0.15
Pressures (bar)	2.4/8.6	2.8/8.6	3.3/8.6	12.9/32.6	14.6/32.6	16.3/32.6
P/P	3.6	3.07	2.6	2.5	2.2	2.0

Comparison With Conventional Cycles

The performance of the cycle described above is now compared to three competitors, which are more advanced. First we consider a single-stage heat pump with a single complete solution circuit, using ammonia/water as the working fluid. At least four of these are currently investigated in Europe on a laboratory or pilot plant scale (Mucic, 1986). The calculations were performed under the same assumptions specified under the headline, CALCULATION PROCEDURE, to the extent they apply.

Table 4 shows the results of the performance calculations for the vapor compression heat pump with a single solution circuit. Since the average composition of the working fluid mixture can be chosen, two cases are selected here, one with 45 weight percent of ammonia and one with 15 weight percent ammonia. The first composition is preferred performancewise, but the second is actually used in high-temperature applications in a pilot plant (Mucic, 1986) primarily because of its considerably lower pressure levels. As can be seen from Table 4, the higher ammonia content leads to higher pressure levels, lower pressure ratios and superheat, and higher COPs compared to the lower ammonia concentrations. All the differences are a consequence of the fact that in a solution of only 15 weight percent of ammonia the properties of steam dominate. The high ammonia content leads to COPs that for the high desorber temperature (we have now a desorber in-

Table 5 Results of performance calculations for ideal vapor recompression with steam

T_{comp} (°C)	85	90	95
T_{evap} (°C)	85	90	95
T_{cond} (°C)	120	120	120
T_{sup} (°C)	240	215	205
Fluid	Steam		
COP_{heat}	9.9	12.3	14.3
Pressures(bar)	0.58/1.98	0.70/1.98	0.85/1.98
P/P	3.41	2.83	2.33

Table 6 Results of performance calculations for ideal vapor compression using refrigerated R11

T_{comp} (°C)	85	90	95
T_{evap} (°C)	85	90	95
T_{cond} (°C)	120	120	120
T_{sup} (°C)	121	121	121
Fluid	R11		
COP_h	8.5	9.8	11.4
Pressures (bar)	5.88/12.3	6.59/12.3	7.37/12.3
P/P	2.09	1.87	1.67

stead of an evaporator) are not as good as for the proposed cycle, but at lower desorber temperatures the values are considerably better. But one has to accept high superheat temperatures. While they range from 148°C down to 83°C for the proposed cycle, they are found to range from 156 to 146°C for the single-stage system with high ammonia content. The pressure level at the compressor outlet is very high (32.6 bar versus 17.8 bar for the proposed cycle). The case of low ammonia content provides considerably lower pressure levels (38 versus 8.6 bar for the proposed cycle). However very high superheat temperatures of up to 186°C and very low COPs are found. Thus using the single-stage system a system designer is faced with a tradeoff between high superheat temperatures and low COPs or better (but not at all sufficient) COPs at very high discharge pressures.

Another likely competitor is conventional vapor recompression. Table 5 shows results obtained when one assumes steam is isentropically compressed and condensed at 120°C. Table 5 shows the values obtained for a vapor recompression system. The high-side pressure is found to be 2 bar while the low-side pressure is in the vacuum range. The COPs are found to be very high, e.g., for a saturation temperature of 120°C, ranging from 9.9 to 14.3 for an ideal cycle. However the superheat temperatures are very high too. They range from 205°C to 240°C.

Finally we compare the performance of the temperature transformation cycle to an ideal Rankine cycle using R11 as the working fluid. Here we find essentially no superheat, moderate pressure levels, a discharge pressure of 12.3 bar, and COPs ranging from 8.5 to 11.4. The results are summarized in Table 6. Thus R11 is superior to the proposed cycle in the given temperature range. However, while R11 cannot be employed at considerable higher temperatures due to the proximity of the critical point, the ammonia/water system can be used up to 200°C.

It should be noted that the comparison between the mixture cycles and those employing pure components is somewhat hampered. While the pure components have constant phase change temperatures for a given pressure, it changes during the absorption process in a mixture. According to the conditions chosen, 120°C is the lower temperature while the higher temperature is for most cases about 130°C for a Δx of 0.05 for the ammonia/water mixture. A more appropriate approach would be to base the comparison on a given heat exchanger area, as discussed by McLinden and Radermacher (1987).

Some Implications Relating to a Technical Realization

The calculations performed have been idealized as described above and results were compared to ideal competing cycles. When the described cycle is to be reduced to practice, the following items should be kept in mind: The performance can be improved by preheating the liquid entering the evaporator by the lower end of the liquid stream leaving the absorber, which could be done by designing the liquid/liquid heat exchanger as a triple heat exchanger. Since the mass flow rate from the absorber to the desorber is larger than from the reverse liquid stream, excess heat is available. Further, we assumed that only pure working fluid is circulating through the compressor. This is not the case. One has always to assume that any amount of water contained in the ammonia vapor returns to its solution circuit. This can be achieved by a proper design of the evaporator, i.e., entraining accumulating water droplets in the vapor stream and/or by providing some rectification at the outlet of the desorber.

In the numerical example chosen, the pressures on the highest pressure level are quite high. This does not have to be the case. If a complete solution circuit were used the average compositions in both solution circuits could be selected such that all pressure levels would be in a more acceptable range. In this way, one can also move to higher heat pumping temperature levels only limited by the pressure head the pumps are capable of and eventually by the thermal stability and corrosivity of the working fluid. In the case of ammonia/water mixtures, this limit is reached at about 200°C.

Conclusions

The cycle introduced here offers the opportunity for high-temperature heat pumping while the compressor operates at lower and more suitable temperature levels.

This is accomplished by introducing two or three liquid pumps and additional heat transfer area for the internal heat exchange desorber/condensor, the liquid/liquid heat exchanger, and possibly an auxiliary condenser.

As shown by the calculations, the efficiency can be improved by using the auxiliary condenser as long as an appropriate heat sink is available. A further increase in efficiency is possible, when the refrigerant entering the evaporator is preheated in a triple liquid/liquid heat exchanger.

It is necessary to select and optimize operating parameters carefully, so that the task can be met in the most efficient way. Especially, the composition of the circulating mixture and the difference in compositions have to be carefully chosen. In addition, it should be realized that any contents of absorbent (water) in the refrigerant (ammonia) vapor can lead to large gliding temperature intervals.

In this paper only one possible application has been discussed: the raising of the temperature level of waste heat from 85-96°C to 120°C. Of course, other applications in different temperature ranges are possible too. Also other working fluid combinations can be used. Ammonia/water served only as an example.

The effect emphasized here is the "Temperature Transformation." It should be noted that this effect is acompanied by a corresponding change in pressure levels. The compressor is never faced with the high pressure levels prevailing in the evaporator and absorber for the cases discussed. Thus such a cycle can be seen as a means to operate the compressor at a suitable pressure level, while only the heat exchangers of the heat pump part have to take very high (or low) values.

For once, if all heat and mass flows are reversed, all pumps replaced by expansion values, expansion values replaced by pumps and the compressor replaced by a turbine, then the cycle will be a power generation cycle. Such a cycle could use a very high-temperature source at T_D, while the turbine temperature would be lower. Of course, this would be predicated on the development of very high-temperature working fluids and materials for the absorber.

Another opportunity would be to replace the low-pressure stage of a turbine in a power plant by an intermediate pressure stage turbine, using the low-pressure steam in a temperature transformation cycle, which produces intermediate pressure level steam. The working fluid in this case could be steam and an aqueous lithium bromide solution.

Although the cycle described may not have an immediate economic merit, it is yet another valuable example of what can be achieved by combining the basic building blocks of the Rankine cycle in creative ways.

Acknowledgments

This study is part of a larger refrigerant mixtures program under the joint sponsorship of the National Bureau of Standards, Electric Power Research Institute, and the Department of Energy through Oak Ridge National Laboratory.

The support by Dr. Trepp for providing the property subroutines is greatly appreciated.

References

Alefeld, G., 1982, "Rules for the Design of Multistage Absorption and Compression Heat Pumps" [in German], *Brennstoff-Warne, Kraft*, Vol. 34, p. 64.

ASHRAE, 1985, *Handbook of Fundamentals*, American Society of Heating, Refrigeration and Air Conditioning Engineers, Atlanta, GA.

Keenan, J. H., Kayes, F. C., Hill, P. G., and Moore, J. G., 1969, *Steam Tables*, Wiley, New York.

Missimer, D., 1973, "Self Balancing Low Temperature Refrigeration System," U.S. No. 3,768,273.

Mucic, V., 1986, Thermo-Consulting, Heidelberg, Federal Republic of Germany, Private Communication.

Pourreza-Djourshari, S., and Radermacher, R., 1986, "Calculation of the Performance of Vapor Compression Heat Pumps With a Two-Stage Solution Circuit," *International Journal of Refrigeration*, Vol. 9, pp. 245-250.

Radermacher, R., 1986, "Advanced Heat Pump Cycles Using Zeotropic Refrigerant Mixtures and Solution Circuits," *ASHRAE Trans.*, Vol. 92, Pt. 2, Paper No. 2977.

Radermacher, R., 1986, "Manipulation of Effective Vapor Pressure Curves Through Thermodynamic Cycles," *Energy-Sources Technology Conference*, New Orleans Technical Economics, Synfuels and Coal Energy, PD-Vol. 5, pp. 119-124.

Ziegler, B., and Trepp, C., 1984, "Equation of State for Ammonia-Water Mixtures," *International Journal of Refrigeration*, Vol. 7, No. 2, pp. 101-107.

D. A. Renfroe
Assistant Professor.
Assoc. Mem. ASME

M. Counts
Graduate Student.
Student Mem. ASME

Department of Mechanical Engineering,
University of Arkansas,
Fayetteville, AR 72701

Model of TPTC Stirling Engine With Adiabatic Working Spaces

A Stirling engine incorporating a phase-changing component of the working fluid has been modeled with the assumption that the compression and expansion space are adiabatic, and that the heat exchanger consists of a cooler, regenerator, and heater of finite size where the fluid follows an idealized temperature profile. Differential equations for the rate of change of mass in any cell and pressure over the entire engine were derived from the energy, continuity, state equations, and Dalton's law. From the simultaneous solution of these equations, all of the information necessary for calculation of power output and efficiency were obtained. Comparison of the results from this model with previous studies shows that the advantage of adding a phase-changing component to the working fluid may have been overstated.

Introduction

Over the past several years there has been some interest directed toward the incorporation of phase-changing components in the working fluid of a Stirling engine to enhance the power density of the machine. Typical Stirling engines, where an ideal gas such as air or hydrogen is used, have a very low power density at atmospheric pressure. Power density is improved by incorporating working fluids with a lower molecular weight and by increasing the mass of the fluid by pressurizing it. Power densities, approximately equivalent to a diesel engine, have been achieved by using hydrogen pressurized to 200 atm as a working fluid. In order to alleviate the problems caused by using high-pressure hydrogen, the addition of a phase-changing component of the working fluid has been proposed.

Several designs of Stirling-type engines using an evaporating or chemically reacting fluid have been built or modeled. West (1983a, 1983b) is the inventor of the Fluidyne engine in which columns of water act as power pistons with a fluid-filled tube acting as a tuned inertial mass connecting the two columns to keep the columns oscillating out of phase. The water in the heated column does experience evaporation but there is still some controversy over whether this is a positive or negative attribute (Martini, 1983; West, 1983a). West (1983b) has endeavored to model his engine with evaporation using the controlled evaporation technique. Athough water is incorporated in this engine configuration, it is not necessarily intended as a method of substantially increasing the power output of the engine, but to simplify the mechanical configuration of the engine.

Huffman built an engine called a tidal regenerator, which was a mechanically simple device to be used as a heart assist pump (Huffman, 1972; Hagen, 1974). It was essentially a power amplifier, which used a small amount of electrical power to move the water level in a canister up and down on a heated element, causing pressure fluctuations due to increased evaporation of the water. Although it had some of the attributes of a Stirling engine, such as the absence of valves, constant pressure throughout the engine, and a regenerative process, it was not an attempt to increase the power density of the traditional Stirling engine by incorporating a phase-changing component in the working fluid.

Iwasaki (1982) and Hirata (1984) analyzed and constructed an actual engine to operate as a two-phase two-component (TPTC) engine. They found that in order to get significant power impovements the mass ratio of evaporating fluid to carrier gas must be as much as 600. Their objective was to construct a bottoming cycle for a diesel or gasoline engine that would operate at relatively small temperature differences. They concluded that the heat transfer was greatly enhanced but did not emphasize the magnitude of expected power improvement.

In the 1930s, Malone (1931) constructed an engine that used only liquid water as a working fluid, incorporating a device that he called a thermodynamic pile instead of the traditional regenerator. The engine produced large amounts of power comparable to the diesel engine. Wheatley et al. (1980) discussed its operation and working fluid selection based on thermodynamic principles in a recent paper and suggested that the working fluid actually was operating in the supercritical region. Thus the advantage of increased specific volume during evaporation of water would not be seen in this engine.

Walker and Agbi (1973) and Metwally (1977) first approached the solution of the two-phase two-component format and the chemically reactive working fluid operating as a power enhancer in a typical Stirling engine using a first-order computation technique. The principal compromises that come with the use of this model were:

1 The expansion and compression processes were considered to be isothermal, where they are actually adiabatic, although the ideal cycle prescribes an isothermal process.

2 The regenerative process was considered to be ideal and occurs with an abrupt temperature change from the heater

---

Contributed by the Advanced Energy Systems Division for publication in the JOURNAL OF ENGINEERING FOR GAS TURBINES AND POWER. Manuscript received by the Advanced Energy Systems Division January 31, 1986.

temperature T_H to the cooler temperature T_C at a moving interface where the mass of working fluid on either side of this interface in the heat exchanger is arbitrarily set to be equal (Walker and Agbi, 1973).

3 Although dead volume was considered as a parameter in the optimization process, the order of the magnitude of heat exchanger volume was not accurately foreseen.

The first-order technique allowed trends to be evaluated while varying specific design parameters; however, the model was not meant to be comprehensive enough to allow for the design of an actual engine. Xia Zonglin (Srinivasan, 1983) later improved the model by eliminating some of the errors. A comparison of the two results is given in Fig. 9.

Renfroe (1981, 1983) endeavored to model the system using third-order techniques. This computational routine solved a set of simultaneous differential equations to model heat transfer, volume and pressure fluctuations, and fluid drag in an engine. The compression and expansion spaces were considered to be adiabatic and vary sinusoidally, while the fluid in the heater and cooler exchanged heat with a constant-temperature tube wall with an infinite heat capacitance, and the regenerator was a series of tubes with a finite heat capacitance but isolated thermally from the surroundings and the heater and cooler. Heat transfer and pressure losses for a fluid where boiling and condensation were occurring were also accounted for. Although the performance of such an engine appeared to be accurately depicted and valuable information on the regenerator heat transfer and design was gained, the computational time required on a mainframe computer was prohibitive for using such a model as a design tool.

The computational technique being presented here is an adiabatic analysis (Urieli, 1984) as opposed to the first-order isothermal analysis as proposed by Schmidt (1871) and used by Walker (Walker and Agbi, 1973; Walker, 1974; Metwally, 1977). Also the regenerator and heat exchangers were configured to have a definite volume, and vaporization occurred in the regenerator assuming a particular temperature profile as shown in Fig. 1. This impressed temperature profile is in anticipation of the development of a regenerator that uses hydrated salts as an energy storage medium in order to allow for the regeneration of the latent heat of the water. This idea is discussed in detail by Renfroe (1984). The present model assumes ideal regeneration of the working fluid, just as was done by Walker, Agbi, Zonglin, and Metwally. The experimentally determined performance of the regenerator may be incorporated into the model at a later date when more information concerning the hydrated salt regenerator is known.

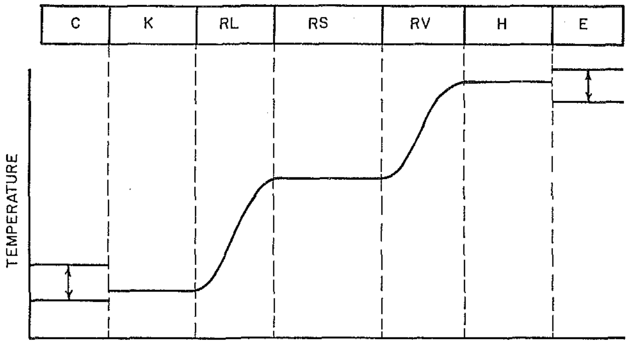

Fig. 1 Temperature profile across the heat exchanger of the engine

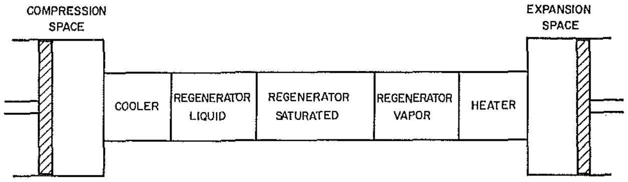

Fig. 2 Alpha engine configuration

Engine Configuration

The engine modeled is assumed to be in the linear alpha configuration as shown in Fig. 2. The compression and expansion spaces are adiabatic, vary sinusoidally in volume, and are out of phase by some angle a specified in the input data. The heat exchanger is divided into five sections, three of which are considered to be the regenerator. The temperature of the fluid in each section is assumed to be as shown in Fig. 1. This is the temperature of the fluid as it progresses from the compression to expansion spaces through the heat exchanger. It will be noticed that the temperatures in the compression and expansion spaces vary during the cycle due to the adiabatic characteristics of the chambers. The volume and surface of each section were initially approximated by using the heat transfer coefficients and fluid flow characteristics for a TPTC boiling and condensing fluid. The fluids considered for these particular calculations are assumed to be water and air due to the abundance of data on these fluids and the fact that previous research on this type of an engine used these materials. From the third-order model (Renfroe, 1981), which

Nomenclature

a = phase angle between compression and expansion spaces
B = mass ratio of water to air
CCV = compression space clearance volume
CSV = compression space swept volume
C_P = constant-pressure specific heat
C_V = constant-volume specific heat
D = differential operator $= d/dt$
ECV = expansion space clearance volume
ESV = expansion space swept volume
g = mass flux
k = specific heat ratio
m = mass
P = total pressure
Q = heat transfer
R_a = gas constant for air
R_m = gas constant for air/water
R_{rs} = gas constant for water
T = temperature
t = crank angle of the engine
V_c = compression space volume
V_e = expansion space volume
W = work

Subscripts

a = air
c = compression space
e = expansion space
g = air + water vapor
h = heater space
LHS = left-hand side
m = mix
RHS = right-hand side
rl = liquid portion of the regenerator
rs = saturated portion of the regenerator
rv = vapor portion of the regenerator

calculated the heat transfer in the heat exchanger using experimental correlations, Counts (1986) in Appendix C shows that the average heat transfer coefficient is 0.091 W/cm^2°C (151 Btu/hrft^2°F). The mass ratio of water to air is assumed to be constant throughout the engine. However the mass of water vapor varies depending on the position of a fluid particle in the engine and the engine pressure. When the water is condensed to liquid it is assumed to have no volume and thus no vapor pressure and when vaporized it behaves as an ideal gas. With the behavior of the fluid well characterized from experience with the third-order model, it is assumed that all of the spaces have been adequately sized to allow the temperature performance shown in Fig. 1. This is more comprehensive than the assumptions made in previous models of this type of engine (Walker, 1974; Metwally, 1977; Srinivasan, 1983) where regenerator and heat exchanger performance were disregarded. For the given temperature profile, all of the water is condensed in the compression space, cooler, and liquid portion of the regenerator. While the water is boiling in the middle portion of the regenerator, the temperature remains constant and the quality of the vapor is an average of 50 percent. As the liquid enters the boiling portion of the regenerator it is at zero quality and as it leaves it is fully vaporized or a quality of one. The average quality of this regenerator section, assuming constant heat flux, is then assumed to be 50 percent. As the fluid leaves the saturation portion of the regenerator it continues to be heated to the heater temperature in the vapor section of the regenerator, where the fluid is assumed to be a mixture of water vapor and air with a mass ratio of B. Finally the heater and expansion spaces contain a mixture of water vapor and air at the temperatures indicated on Fig. 1. Since the expansion and compression spaces are adiabatic and reversible, the temperature varies during the cycle. It does more accurately depict what occurs in an actual engine.

With the engine defined in this manner, equations may now be developed that will allow the calculation of the work output, heat transfer, efficiency, pressure excursion, and mass flux at each cell boundary for the TPTC engine.

Governing Equation Development

The equation of state, continuity, energy equations, Dalton's law, and the relations for volume fluctuation will be used to develop a set of differential equations that will be solved simultaneously to determine the pressure, mass in each cell, work, heat transfer, and efficiency for the engine throughout its cycle.

Volume Fluctuations. The volumes of the working spaces fluctuate sinusoidally. Hence

$$V_c = \mathrm{CCV} + (\mathrm{CSV})(0.5)(1+\cos(t)) \tag{1}$$

$$V_e = \mathrm{ECV} + (\mathrm{ESV})(0.5)(1+\cos(t+a)) \tag{2}$$

where CCV and ECV are the respective clearance volumes, and a is the phase angle between compression and expansion space volumes.

The angle rate of change of volume can be found by differentiating the above equations to obtain

$$DV_c = -(\mathrm{CSV})(0.5)(\sin(t)) \tag{3}$$

$$DV_e = -(\mathrm{ESV})(0.5)(\sin(t+a)) \tag{4}$$

Equation of State. The ideal gas equation of state is given by

$$PV = mRT \tag{5}$$

Taking logarithms and differentiating results in

$$DP/P + DV/V = Dm/m + DR/R + DT/T \tag{6}$$

where D is the differential operator d/dt. Since R is constant for a particular gas and the temperature and volume are constant in the heater, cooler, and saturated regenerated cells, then equation (6) reduces to

$$Dm = m \bullet DP/P \tag{7}$$

The temperature in the liquid and vapor portions of the regenerator varies linearly, assuming constant heat flux for a non-phase-changing fluid with constant heat capacitance, and therefore equation (7) can be applied to these cells at the average temperature of the cell.

The gaseous portion of the working fluid is considered to be an ideal gas. The gas constants for the air and mixtures of air and water vapor are:

R_a = gas constant for air

R_w = gas constant for water vapor

$$R_{rs} = (R_a + (B/2)R_w)/(B/2+1)$$

$$R_m = (R_a + BR_w)/(B+1)$$

where R_{rs} is the gas constant of the gas mixture in the portion of the regenerator where evaporation is occurring and R_m is the gas constant of the gas mixture in the vaporized portion of the regenerator, heater, and expansion spaces of the engine.

Energy Equation. The energy equation may be used to derive the relationship needed to calculate the rate of change of mass (Dm) in the expansion and compression spaces. From the first law of thermodynamics for an open system

$$Q + \Sigma m_i h_i = \Sigma m_e h_e + (m_2 u_2 - m_1 u_1) + W \tag{8}$$

The compression and expansion spaces are considered to be adiabatic and mass is either entering or leaving. Considering the above and putting the equation into differential form, the first law for the system becomes

$$-DW = Dm_B \bullet h_B + D(m\,u) \tag{9}$$

where the subscript B refers to the fluid properties at the interface between the compression/expansion space and the adjacent heat exchanger cell. These interface properties are dependent on the direction of flow and will be the properties upstream of the interface. Assuming ideal gas behavior the equation becomes

$$-DW = -Dm \bullet C_p T_B = D(mT)C_v \tag{10}$$

$$-P\,DV = -Dm \bullet C_p T_B + C_v D(mT) \tag{11}$$

where from the continuity equation, $Dm_B = -Dm$ for the flow into the space is considered negative. For an ideal gas

$$C_P = \frac{kR}{k-1} \tag{12}$$

and

$$C_V = \frac{R}{k-1} \tag{13}$$

Also from the ideal gas law

$$PV = mRT$$

the following can be derived

$$DV = V\left(\frac{Dm}{m} + \frac{DT}{T} - \frac{DP}{P}\right) \tag{14}$$

Substituting equations (12), (13), and (14) into equation (11) and rearranging, one obtains

$$Dm\left(\frac{RkT_B}{k-1}\right) = PV\left(\frac{Dm}{m} + \frac{DT}{T} - \frac{DP}{P}\right) + \left(\frac{R}{k-1}\right)(m \bullet DT + T \bullet Dm)$$

which upon expansion becomes

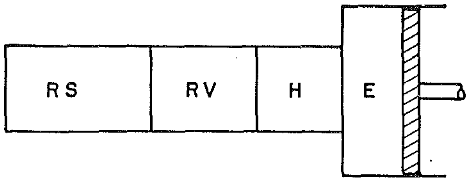

Fig. 3 Control volume of the side of the engine containing liquid water

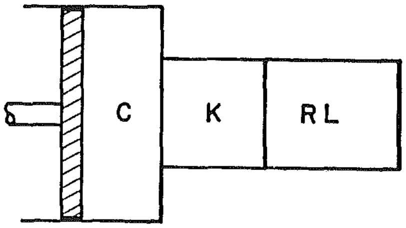

Fig. 4 Control volume of the side of the engine containing only vapor

$$Dm\left(\frac{RkT_B}{k-1}-RT-\frac{RT}{k-1}\right)=PV\left(\frac{DT}{T}-\frac{DP}{P}\right)$$

$$+\frac{Rm}{k-1}\bullet DT$$

Because of the nature of the machine, T_B is assumed to be approximately equal to T and both temperatures will be represented as the average of the compression/expansion space temperature and the adjacent cell temperature, which will be called T_c. Such an assumption was made by Berchowitz and Urieli (1984), which gave very good results when validated against the GPU-3 experimental data. The major point is that it predicted the behavior of the heat exchanger section of the engine. With this assumption the equation becomes

$$Dm\bullet RT_c\left(\frac{k}{k-1}-\frac{k-1}{k-1}-\frac{1}{k-1}\right)=PV\left(\frac{DT_c}{T_c}-\frac{DP}{P}\right)$$

$$+\frac{Rm}{k-1}\bullet DT_c$$

Upon further reduction the equation becomes

$$Rm\left(\frac{k}{k-1}\right)DT_c=V\bullet DP \tag{15}$$

Differentiating the equation of state gives

$$Dm=(V\,DP+P\,DV-mR\,DT_c)/(RT_c) \tag{16}$$

Substituting equation (15) into equation (16) and rearranging gives

$$Dm=(P\bullet DV+\frac{V}{k}\bullet DP)/(RT_c) \tag{17}$$

This equation will then represent the mass rate of change of the compression and expansion spaces.

Continuity Equation. Using the continuity equation and the previously derived equations, a differential equation for DP can be formulated. The total mass of air and water does not change within the engine system, but mass of water vapor or active gaseous working fluid does change with the crank angle of the engine. The engine will be divided into two control volumes: one where there is water vapor present (Fig. 3), and one where there is no water vapor (Fig. 4). Let m_g represent the mass of gaseous working fluid in the cells. The rate of mass change in the right-hand side (RHS) of the engine must be equal to the negative of the rate of mass change in the left-hand side (LHS) times the water vapor mass ratio B plus 1. Since the quality in the RHS cell is 50 percent, the vapor mass ratio will be $B/2$. From this relationship

$$Dm_{g\mathrm{RHS}}=-(B/2+1)(Dm_{g\mathrm{LHS}}) \tag{18}$$

The mass rate of change in the RHS control volume is

$$Dm_{g\mathrm{RHS}}=Dm_{grs}+Dm_{grv}=Dm_{gh}+Dm_{ge} \tag{19}$$

From equations (7) and (17), equation (19) becomes

$$Dm_{g\mathrm{RHS}}=DP(V_{rs}/(R_{rs}T_{rs})+V_{rv}/(R_mT_{rv})+V_h/(R_mT_h)$$
$$+V_e/(k_mR_mT_e))+P/(R_mT_e)DV_e \tag{20}$$

Similarly, for the left-hand side

$$Dm_{g\mathrm{LHS}}=DP(V_k/(R_aT_k)+V_{rl}/(R_aT_{rl})+V_c/(k_aR_aT_c))$$
$$+P/(R_aT_c)DV_c \tag{21}$$

Substituting equations (20) and (21) into equation (18) and solving for DP

$$DP=-P(DV_e/(R_mT_e)+(B/2+1)DV_c/(R_aT_c))/(X\ Y) \tag{22}$$

where

$$X=V_{rs}/(R_{rs}T_{rs})+V_{rv}/(R_mT_{rv})V_h/(R_mT_h)+V_e/(K_mR_mT_e)$$

and

$$Y=(B/2+1)(V_k/(R_aT_k)+V_{rl}/(R_aT_{rc})+V_c/(k_aR_aT_c)$$

Applying equation (17) to the expansion space to determine Dm_e and solving it simultaneously with equation (22), the pressure throughout the engine and mass in the expansion space may be determined. Using the continuity equations, the mass in each cell and the rate of change of mass in each cell may be determined.

Heat Transfer and Work. The heat transfer may be calculated for each heat exchanger space by applying the first law to obtain

$$DQ+(C_pT_{in}g_{in}A-C_pT_{\mathrm{out}}g_{\mathrm{out}}A)=C_V\ D(mT) \tag{23}$$

Rearranging and substituting the equation of state, DQ becomes

$$DQ=DP\ C_VV/R-C_PA\,(g_{\mathrm{in}}\mathrm{T}_{\mathrm{in}}-g_{\mathrm{out}}T_{\mathrm{out}}) \tag{24}$$

The temperature in and out are the temperatures of the fluid as it crosses the cell boundary, which are dependent on the direction of flow. It is assumed as a matter of convention that flow to the right is positive flow. For this case

$$T_{\mathrm{in}}=T_{i-1}\text{ if }g_{\mathrm{in}}>0;\text{ otherwise }T_{\mathrm{in}}=T_i \tag{25}$$

and

$$T_{\mathrm{out}}=T_i\text{ if }g_{\mathrm{out}}>0;\text{ otherwise }T_{\mathrm{out}}=T_{i+1} \tag{26}$$

where i denotes the cell where the mass is flowing in and out.

The mass flux at the boundary to the compression space is

$$g_{ck}=-Dm_c/A \tag{27}$$

For the other cell boundaries the mass flux is expressed as

$$g_{\mathrm{out}}=(g_{\mathrm{in}}-Dm_i)/A \tag{28}$$

The work done by the engine is the sum of the work done in the compression and expansion spaces. This is found by integrating

$$DW=P(DV_c+DV_e) \tag{29}$$

With these equations the power output and efficiency for a given engine with a phase-changing working fluid may be calculated.

Results

The effect of mass ratio, phase angle, swept volume ratio, and dead volume ratio were determined using the equations

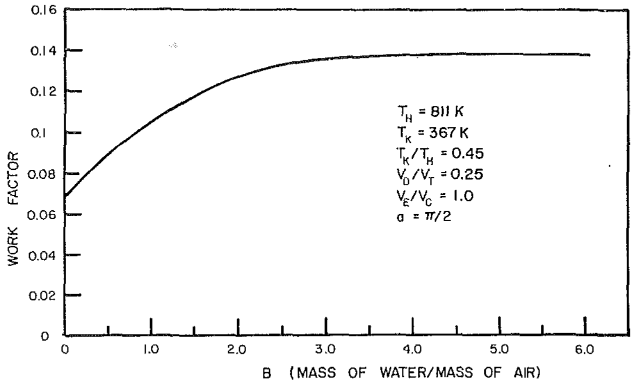

Fig. 5 Work factor versus mass ratio of water to air

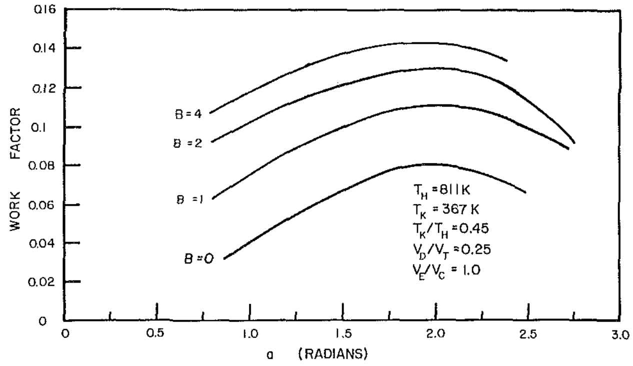

Fig. 6 Work factor versus phase angle between the compression and expansion spaces

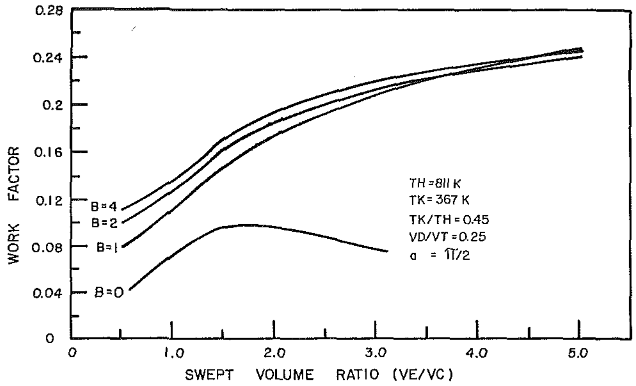

Fig. 7 Work factor versus the ratio *VC/VE*

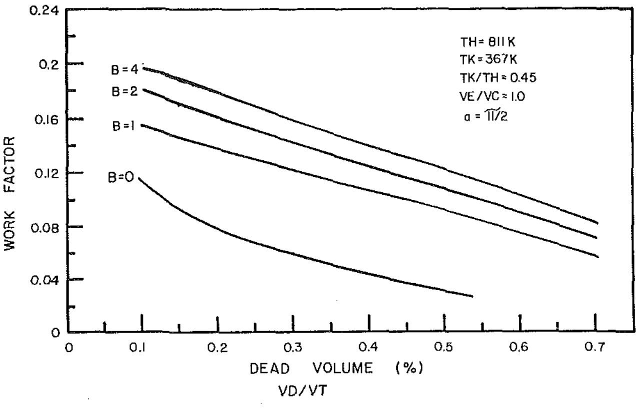

Fig. 8 Work factor versus the percent of dead volume, *VD/VT*

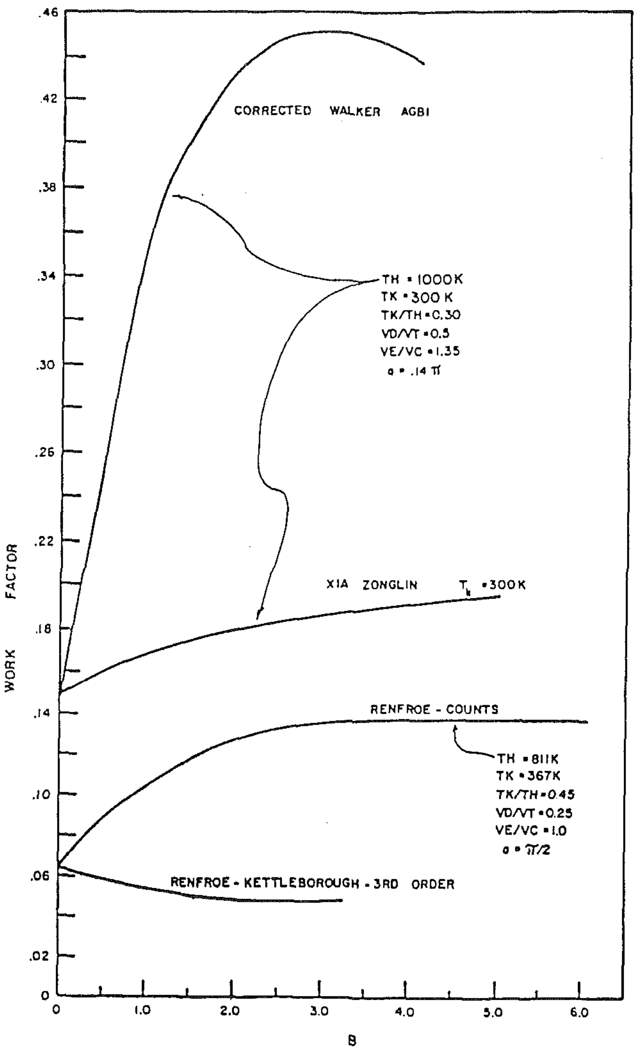

Fig. 9 Comparison of the results of different computational techniques

derived in the previous section. Equations (17) and (22) were solved simultaneously using a fourth-order Runge-Kutta technique with Gill's constants (Carnahan, 1969) to determine the pressure of the engine and mass in the expansion space for a given crank angle. From these two values the other values were calculated from the other equations.

This type of calculation technique is an initial value problem where the initial values are known and the model calculates the new values for succeeding crank angles. Unfortunately, the initial compression and expansion space temperatures are not known and thus must be guessed. Equilibrium is reached when the final temperatures are the same as the initial temperatures. Thus the model cycles through the process, checking initial and final temperatures, and stops when they are within some predetermined limit. This convergence process may be accelerated by adjusting the temperatures after each cycle, similar to what was done by Berchowitz and Urieli (1984).

Figures 5, 6, 7, and 8 show the variation of work factor with respect to mass ratio *B*, phase angle *a*, swept volume ratio (*VE/VC*), and dead volume. The work factor is what Walker called the power factor (Walker, 1980), which is the work output per cycle divided by the product of the maximum pressure times the maximum swept volume. This nondimensional factor allows the comparison of engine work output for a specific size and weight.

Figure 9 is a comparison of the results of different investigators using different techniques in calculating the effect of the addition of water to the working fluid of air in an alpha type of Stirling engine. The top two curves are the Walker–Agbi and Xia Zonglin curves. With the corrections from Zonglin the originally estimated improvement due to the addition of the water is much lower. The lower two curves for the present model and the third-order model are different operating conditions from the former analyses. The objective was to have the saturation temperature midway between the heater and cooler temperatures. The curve for the third-order model shows a decrease in the work factor with the addition of water. This is due to the nature of the model in modeling an actual piece of hardware, which was optimized for use with air, and the inability of the typical regenerator to regenerate the phase-changing working fluid. When equilibrium was reached in the third-order model, very little condensation was actually occurring. For this reason research on a hydrated salt regenerator is being conducted.

Conclusions

From the results presented here, it can be seen that the incorporation of a phase-changing component in the working fluid has a positive effect on the work factor and hence the power density of a Stirling engine. The trends are similar to what has been discussed before but the magnitude of the values is different to what Walker and Agbi (1973) had determined. It can be seen that as more real world factors are considered, the advantages of adding the phase-changing components are diminished. When an ideal regenerator is assumed to be feasible the maximum increase in power will be more on the order of a factor of two instead of a factor of three as was reported (Walker and Agbi, 1973). If the regeneration problem proves to be too difficult to overcome, water injection may be considered as a method of giving a power boost to a lower power density air engine such as the large Ringbom–Stirling engine being investigated for use on a locomotive in China. This would allow the construction of lower technology engines, which may operate efficiently over long periods of time with short bursts of low-efficiency high-power density power for starting and hill climbing in a locomotive. As with continued efforts toward increasing the regenerator effectiveness, potential engine operation in the water-injected mode should be investigated.

References

Carnahan, B., Luther, H. A., and Wilkes, J. O., 1969, *Applied Numerical Mdthods*, Wiley, New York.

Counts, M. A., 1986, "Computer Analysis of an Adiabatic Stirling Engine Using a Two-Phase Two-Component Working Fluid," Master's Thesis, University of Arkansas, Fayetteville, AR.

Hagen, D. G., Ruggles, A. E., and Huffman, F. N., 1974, "Themal Design of a Tidal Regenerator Engine for Circulatory Support Systems," AIAA/ASME Thermophysics and Heat Transfer Conference, July.

Hirata, M., Kasage, N., and Matsuno, Y., 1984, "Basic Cycle Analysis of Two Component Two-Phase Stirling Engine," 2nd International Conference on Stirling Engines, Shanghai, China.

Huffman, F. N., et al., 1972, "Performance of a Nuclear-Fueled Circulatory Assist System Utilizing a Tidal Regenerator Engine," 7th IECEC, Paper No. 729120, p. 771.

Iwasaki, E., and Hirata, M., 1982, "A Study on Two-Phase Two-Component Stirling Engine," *Proc. 17th IECEC*, p. 2169.

Malone, J., 1931, "A New Primer Mover," *Jnl. Royal Soc. Art*, Vol. LXXIX, No. 4099, pp. 679–709.

Martini, W. R., 1983, "Test on a 4U Tube Heat Operated Heat Pump," 18th IECEC, Paper No. 839142, p. 872.

Metwally, M. M., and Walker, G., 1977, "Stirling Engines With a Chemically Reactive Working Fluid—Some Thermodynamic Effects," ASME JOURNAL OF ENGINEERING FOR POWER, Vol.99, p. 284.

Renfroe, D. A., 1971, "A Computer Model of a Stirling Engine Using a Two Phase Two Component Working Fluid," Ph.D. Dissertation, Texas A & M University, College Station, TX.

Renfroe, D. A., 1983, "Effects of Using a Two-Phase Two-Component Working Fluid in a Stirling Engine," 18th IECEC, Paper No. 839148, p. 908.

Renfroe, D. A., and Counts, M. A., 1986, "Computer Analysis of an Adiabatic Stirling Engine Using a Two-Phase Two-Component Working Fluid," Master's Thesis, University of Arkansas, Fayetteville, AR.

Schmidt, G., 1871, "Theorie der Geschlossenen Calorischen Maschine von Laubroy und Schwartzkopff in Berlin," *Den. Pol. Journ.*, Vol. CLX, p. 401.

Srinivasan, V., Zonglin, X., Walker, G., and Fauvel, R., 1983, "A Review of Two-Phase Two-Component Working Fluids in Stirling Engines," Private Communication to Dr. Renfore, June.

Urieli, I., and Berchowitz, D., 1984, *Stirling Cycle Engine Analysis*, Adam Higler LTD, Bristol.

Walker, G., and Agbi, G., 1973, "Optimum Design Configurations for Stirling Engine With Two-Phase Two-Component Working Fluid," ASME Paper No. 73-WA/DGP-1.

Walker, G., 1974, "Stirling Cycle Cooling Engine With Two-Phase Two-Component Working Fluid," *Cryogenics*, p. 459.

Walker, G., 1980, *Stirling Engine*, Clarendon Press, Oxford.

West, C. D., 1983a, "Stirling Engines With Controlled Evaporation of a Two-Phase Two-Component Working Fluid," 18th IECEC, Paper No. 839149, p. 914.

West, C. D., 1983b, *Liquid Piston Stirling Engines*, Van Nostrand Reinhold Co., New York.

Wheatley, J. C., Allen, P. C., Knight, W. R., and Paulson, D. N., 1980, "Principles of Liquids Working in Heat Engines," *Proceedings of the National Academy of Sciences USA*, Vol. 77, No. 1, p. 39.

Design Experience in Minimizing Radiation Exposure to Personnel During Maintenance of BWR Power Plants

J. R. Punches
Manager, Servicing Equipment Design,
General Electric Company,
San Jose, CA 95125

As nuclear power plants become older, in-vessel maintenance to high radiation components will become more common. This paper describes General Electric's experience in making such repairs on Boiling Water Reactors and how the use of engineering and project management enhances the productivity of special maintenance projects. Design techniques employed to minimize personnel radiation exposure are discussed. Specialized remote, automatic, and semi-automatic equipment designs are presented. Included are sample descriptions of special tools developed, problems encountered, and lessons learned.

Introduction

Routine nuclear power plant maintenance has always been much more complex than conventional power plant maintenance. This is due mainly to the radiation environment, the necessity for remote handling, and the regulatory atmosphere. Major maintenance projects, which are *nonroutine*, require even more management and engineering attention because of the high cost of delays and the consequences of a mistake. In addition, the proliferation of major plant maintenance projects has taken its toll on maintenance costs and on plant availability. Concerns about individual radiation exposure have placed new emphasis on the need for industry to shorten outage times using fewer people, reducing exposure, and minimizing cost. Thus, there is a need for greater engineering support throughout a project in the areas of product design, installation tooling, and the installation process.

This presentation is about the design approach taken in a number of recent reactor maintenance projects. It describes how a disciplined approach to tool and hardware integration, functional testing, qualification, and operator training can and will lead to the successful completion of any project.

Equipment Development Process

In any nuclear power plant repair program, whether it be large or small, the development process for repair tools and hardware will include six distinct steps.

1 Definition of the Maintenance Task. What needs to be replaced; what is repairable; and what can be left in an as-is condition.

2 Definition of the Environment. Where is it located; what is the radiation field; what are the loads and design conditions; and what is the schedule.

3 Tool and Hardware Integration. What are the repair steps necessary; what tools are necessary for each step; and how can the tools and hardware be integrated to simplify each other.

4 Equipment Fabrication. Will all equipment, tools, and hardware meet the needs of 1 and 2 above; are there adequate spare parts; and are long lead items properly identified and ordered.

5 Functional Testing and Procedure Development. Will all tools and equipment meet the design requirements for intended use; are they functionally sound; is any rework required; and are any unexpected conditions uncovered.

6 Equipment Qualification and Personnel Training. Will all tools and equipment meet the requirements for intended use through *independent* testing; will they meet all requirements under full environmental conditions; are the procedures adequate for all steps of the maintenance task; and are all personnel fully trained on all steps of the procedure.

This disciplined approach to repair planning, with the close cooperation of engineering, project management, field supervision, and field technical support, is directly translatable to all current and future reactor maintenance projects.

Specific Application

In order to minimize radiation exposure, specialized remote, automatic, and semi-automatic equipment has been designed and qualified for numerous reactor repairs over the years. These repair programs include a wide range of programs from the very simple to the time consuming and complex.

Contributed by the Nuclear Engineering Division and presented at the Jt. ASME/IEEE Power Generation Conference, Miami Beach, Florida, October 4–8, 1987. Manuscript received at ASME Headquarters July 20, 1987. Paper No. 87-JPGC-NE-19.

For example, at a foreign BWR plant location, jet pump instrument line failures were observed on three different occasions. The first was a fracture of the instrument line itself and the last two were separation of the instrument line from one of its supports. Even though the three failures occurred at slightly different parts of the instrument line, the fracture location was essentially identical. In response to these failures, General Electric performed an extensive vibration analysis of the jet pump assembly. This evaluation concluded that instrument line excitation due to recirculation pump vane passing frequency was the most probable cause of the noted failures.

Using a full-size mockup of the jet pump assembly, the as-built configuration of the instrument lines was fabricated, vibration instrumentation installed, and the resulting mockup tested underwater to determine instrument line natural frequencies and the sensitivity to fabrication variables. This mockup testing confirmed the original hypothesis as to the cause of the failures. Also, using this mockup, it was demonstrated that mitigating supports that would provide near-midspan stabilization of the instrument lines would prevent the recurrence of the previously noted failures.

These tests led to a comprehensive repair program, which would both repair the observed fractured line and also mitigate the recurrence of future failures.

The instrument line repair required the replacement of a broken segment of instrument piping. The mitigation effort required the placement of custom-designed supports on all jet pump assemblies. The repair area was remote and inaccessible, located approximately 50 ft underwater below the vessel flange at the bottom of the jet pump annulus. In addition, a number of startup test instrument brackets had first to be removed by special electrical discharge machining (EDM) to allow access to even this narrow space adjacent to the jet pumps.

The design and qualification of the required repair and mitigation hardware and installation tooling was accomplished on an accelerated four-month schedule. Approximately 30 special installation tools were required to be designed, fabricated, and qualified to complete this effort. This included the development of a specialized three-axis manipulator assembly, which maneuvered EDM machining heads into place, positioned pipe finishing tools, and installed the permanent reactor hardware in place. In addition, required special vendor products were also developed during this period. Of special interest is a shrink metal alloy coupling, unique to this application, which was used to attach the repair hardware to existing in-vessel equipment.

Vibration testing, equipment qualification, and operator training were accomplished in work conducted around the clock in General Electric's Service Training Facility on full scale mockups. Site installation was accomplished by a team of two dozen engineers and technicians. While numerous difficulties had to be resolved in the course of around-the-clock work, the installation of mitigating devices and repair hardware was completed in 24 days without delay of the scheduled outage.

Equipment Qualification and Personnel Training

Although mockup usage is not new, the use of full-scale tooling and installation mockups has shown to be of ever-increasing importance as more complex repair programs are executed. These can include simple desk-size mockups during the conceptualization period to full-size mockups, which are used during equipment qualification and personnel training.

Much of this latter effort takes place in General Electric's Servicing Training Facility (STF), where full-scale simulation of nuclear plant refueling, maintenance, and repair activities can be duplicated. Located in San Jose, CA, this facility contains a BWR refueling floor mockup complete with an 85-ft-deep reactor vessel cavity, core section with major vessel internal components, spent fuel pool, refueling platform, overhead crane, and other associated servicing equipment.

There is, however, an always pressing need for local, site-specific mockups and training aids for equipment and worker qualification. In the case of the example repair program outlined above, two specialized mockups were constructed for this purpose. One was a Floor Fit-Up Mockup and the other was a full scale Reactor Annulus Mockup.

The Floor Mockup was constructed to simulate one jet pump diffuser and the lower portion of its immediate neighbors. This mockup was used in three phases of the program. During the first phase, the mockup was used to determine the fundamental cause of the problem. In this phase, the as-built configurations of the sensing lines were fabricated, vibration instrumentation installed, and the resulting mockup tested underwater to determine sensing line natural frequencies and the sensitivity to fabrication variables.

In the second phase, this same mockup was used during qualification of repair tooling and hardware as a floor mockup to assure tool and hardware fit-up during the functional fit-up stage of their development.

In the final third phase, the mockup was shipped to the site to aid in operator training, as a final checkout station for all equipment prior to reactor use, and as a simple mockup to verify all equipment operation as reactor as-built data became available.

The Reactor Annulus Mockup was fabricated to duplicate, in full scale, the reactor vessel shroud, shroud support, jet pumps, and vessel. This mockup was configured to duplicate an actual operating plant. It was fabricated with an adjustable shroud wall and, thus, can and has been used to replicate the fabrication parameters of other operating BWR units. This mockup, located in GE's Service Training Facility, has had extensive use during various reactor repair programs. Its use has included the conceptualization and design of repair tools, their functional and qualification testing, and in the area of personnel training prior to site work.

Summary

Through this and many similar programs, GE has demonstrated that even the most challenging in-vessel modifications and repairs can be successfully accomplished in a timely manner. However, meeting the challenges of plant aging and ever-increasing servicing needs requires a dedicated team with extensive experience, a disciplined approach to repair planning, and facilities for qualification and training.

Computerized Dose Estimates for Maintenance

F. L. Lau

J. Sejvar

Westinghouse Electric Corporation,
Pittsburgh, PA 15230

The minimization and control of radiation exposure usually starts with the determination of the total expected dose. Manual determination of an accurate value can require an extensive, error-prone amount of data manipulation. By computerizing the model for this determination the individual task and total dose values can be identified much more rapidly and accurately than by manual methods. Also, high-dose operations can be easily evaluated for ways to reduce exposure. The microcomputer also allows instantaneous updating of estimates as changes are made both in the planning stage and in the performance of the job.

Introduction

Minimizing radiation worker dose[1] has always been an important consideration when planning or performing nuclear power plant maintenance. The importance of this consideration was emphasized by the Nuclear Regulatory Commission in the late 1970s when they introduced the philosophy of "ALARA," or As Low As Reasonably Achievable. This philosophy is outlined in several Regulatory Guides [1-3]. As an aid in achieving ALARA doses the Institute of Nuclear Power Operations (INPO) has issued several Good Practice bulletins [4, 5].

In recent years the trend in radiation exposure management has been toward more stringent controls and reduced doses to assure that total Occupational Radiation Exposure (ORE) is minimized. In fact, most nuclear plants now have formal ALARA programs and recognize that they are a good business practice, which can reduce operational costs and improve plant reliability [6].

One aspect of a good ALARA program is the accurate prediction of worker doses. This should be accompanied by the evaluation and implementation of appropriate dose reduction actions. The success of an ALARA program for a particular job depends on many factors, including the accuracy of the radiation levels assigned to each work area and the accuracy of the stay times planned for the work. It may also be necessary to account for changes in the radiation level in some areas as the job progresses. For example, the radiation level increases in the area around a steam generator channel head after removal of the manway cover or above a steam generator tube bundle when the water level is decreased. Incorporating parameter changes into the dose estimates can require a significant amount of time and effort, especially when performed manually.

Manual Dose Estimating

Obtaining a dose estimate can be simple or cumbersome depending on the accuracy of input and the input details used by the estimator. A simple model can be developed by estimating the time for each of several large tasks and prorating the historical dose for a similar job to obtain the expected exposure. This approach can lead to misleading results because the "effective dose rate" may not be truly representative of the actual radiation levels that will be present. It also limits the ability to identify specific activities that will result in large dose expenditures. The approach is obviously less desirable when little or no historical data exist.

In contrast, a very detailed dose model can be developed where the job site is divided into many small areas and the dose rate at each area is calculated from individual runs of piping or components in the area. Measured dose rates are also used when available. The calculated or measured dose rate in an area, multiplied by the time spent by a worker in the area, is then summed for all areas and all workers to obtain the total expected dose. This process provides a great amount of flexibility and allows the estimator to examine the effect of adding shielding to a particular component or piping run or the effect of removing that piping from the area during the work. It also allows accounting for changes in the radiation level as the job progresses (e.g., draining of the primary loop).

Dose Modeling Problems

Regardless of the detail used for a dose model, the accuracy of the dose estimate for an individual task or for the total job depends on the accuracy of the source values in the piping components or on the dose rates assigned to the work area. The estimated accuracy also depends on the use of realistic worker stay times. As indicated, these values can be adjusted by the use of historical data or they can be varied to determine the effect of that particular value on the total estimate. When these manipulations are performed manually the use of a highly detailed model can be quite cumbersome and the total data manipulation process can be prone to error.

The compilation of historical data for use in dose model development or checking and in work procedure optimization

---

[1] "Dose" will be used to represent "radiation dose equivalent," which has units of "roentgen equivalent man" or "rem."

Contributed by the Nuclear Engineering Division and presented at the Joint ASME/IEEE Power Generation Conference, Miami Beach, Florida, October 4-8, 1987. Manuscript received at ASME Headquarters July 20, 1987. Paper No. 87-JPGC-NE-17.

requires that a system be developed that allows different people in a department to access, understand, and properly use the data. When a large amount of data is available the input to the system of new data is often postponed to perform more urgent work. When needed, the historical information may not be available or the data may not be understandable.

The effect of having to perform many routine calculations manually or to sort and organize historical data is generally to deter the dose estimator from making large models or storing the exposure results. These same concerns require that the estimator be skilled in the art of radiation analysis and dose reduction. Both of these concerns tend to reduce the accuracy of dose estimates and make it difficult to budget the dose for a particular type of plant operation or for the total station cumulative dose.

Problem Solution

The basic building blocks of a radiation exposure estimate are dose rates and work times; thus development of an estimate can become a relatively simple bookkeeping task. Summation of the product of dose rate and work time in each radiation zone provides an estimate of the collective dose for the entire operation as well as for each step, radiation zone, or worker classification. As already noted the process can be time consuming and prone to error when performed manually, thus providing an obvious opportunity for solution by computer.

The job of estimating collective exposure is particularly suited for solution by a microcomputer spreadsheet program. By using such a spreadsheet, the user can rapidly determine the effect of a change in any one parameter on a host of others and on the total job. Many other concerns expressed earlier can also be lessened through the computerization of both the collection and storage of the historical data and through the development of computerized dose models.

Acting on these conclusions, the Westinghouse Radiation Analysis Group has developed a collection of computerized dose exposure models. The general development of these models will be presented here.

The first step in the total program was to identify a plan for the development of the system. The basic plan included the following:

- Identify desirable attributes of the system
- Choose a spreadsheet or write one for the application
- Identify the input and output to be provided
- Determine the method of installing and using the data base
- Identify the tabular and graphic information to be provided.

A survey of health physics and other personnel involved in station ALARA programs [7] provides the following list of desirable attributes for any method of estimating collective dose:

- Easy to apply, requiring minimal analytical skills
- Flexible, accommodating alternate approaches and levels of detail
- Comprehensive, allowing for consideration of the installation, maintenance and operation phases of a project
- Compatible with existing ALARA practices (e.g., ALARA design checklists or radiation work permit dose estimates)
- Allows estimates to be easily updated with new or improved information
- Easy to incorporate adjustments for dose reduction measures
- Able to incorporate adjustments for unanticipated changes in conditions affecting dose rates
- Adequately document estimates for use to increase the accuracy of future estimates (adequately documenting the assumptions and adjustments for differing work scopes and plant conditions allows actual job conditions to be compared with the last estimate and with the historical records)
- Emphasize the accurate estimate of in-field man-hours

For our application the LOTUS^{TM} spreadsheet program was chosen because of the general availability of this program and the fact that it can be used to generate desired tables, graphics, and user-generated data conversions and comparisons. Each dose model utilizes a customized spreadsheet or template and extensive use was made of macro instruction routines referenced to single work menu items.

The input/output information that was chosen for display is as follows:

- Task No.
- Task description
- Work time
- Number of workers
- Worker type/job category
- Work area radiation fields
- Man-hours by radiation zone
- Dose by radiation zone
- Dose by task
- Cumulative dose
- Cumulative man-hours
- Schedule time

An extensive data base of radiation exposure information has been accumulated over the past several years through the actual performance of nuclear plant maintenance and inspection work. The information in this data base provides a reliable set of "benchmarks" against which actual plant performance can be measured. Information from this data base was included in the "default" case as part of each basic dose exposure model. Any single value or all of the data can be replaced as new or more appropriate information becomes available.

Template Development

The simplicity and flexibility of LOTUS^{TM} coupled with the extensive amount and the high confidence level in the data base provides a system that is comprehensive in the treatment of worker exposure for various tasks, yet is easy to use and requires minimal analytical skills. The logic diagram of the template model is illustrated in Fig. 1.

The template is geared toward use by the novice computer user through the use of keyboard macros and LOTUS^{TM} programming commands. Extensive use is made of user-defined menus, which appear in the control panel in a manner similar to standard LOTUS^{TM} commands. With this system the user operates the program with only the enter key and a pointer movement key except when it is necessary to enter data. Entering data is also a menu-driven process. Menu choices are generally displayed as single word options, which are supplemented by a line of explanatory information for each choice, as illustrated in Fig. 2.

This approach alleviates the need for tedious inputs and command syntax, thereby avoiding potential errors and confusion. Further, utilization of the programming capabilities of LOTUS^{TM} and invoking macros through the special menus that have been created means that the user need not have a familiarity with LOTUS^{TM} and/or its standard commands.

Formulas used in generating the models are inherent in the spreadsheet owing to LOTUS^{TM} formula calculation capability. For example, locating the cell pointer at a particular cell provides the user with both the calculated value as well as the formulation used in arriving at the value. Hence, saving a particular spreadsheet on disk provides complete documentation of the exposure estimate, including final results, structure of the estimate, and method used in preparing the estimate.

Table 1 Antivibration bar field experience

Job No.	Plant I.D.	S/G No.	Date	Man-Rem Estimated	Man-Rem Actual	Actual/Estimated
1	A		9/83	55.0	92.0	1.67
2	B	B	4/85	59.6	15.2	0.26
3	C	21	9/85	8.3	3.4	0.41
4		22		8.3	3.4	0.41
5	D	11	3/86	3.6	3.8	1.06
6		12		3.6	3.8	1.06
7	E	A	4/86	10.5	5.1	0.49
8		B		10.5	4.8	0.46
9	F	1	8/86	8.7	6.5	0.75
10		2		8.7	6.5	0.75
11		3		8.7	6.5	0.75
12	B	C	10/86	17.3	11.0	0.75
13		A		17.3	6.3	0.64
14	G	1	4/87	10.4	8.4	0.81
15		2		10.4	8.4	0.81
16		3		10.4	8.4	0.81
17		4		10.4	8.4	0.81
Average*				9.8	6.3	0.64

*Note: Averages excluding first two jobs

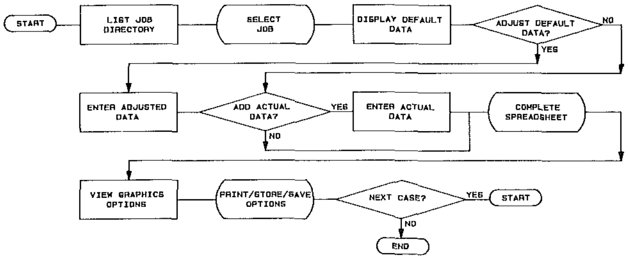

Fig. 1 Logic diagram for dose exposure models

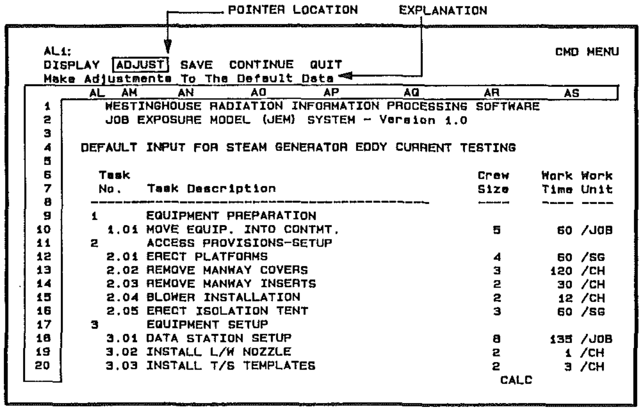

```
AL1:                                                       CMD MENU
DISPLAY [ADJUST] SAVE  CONTINUE  QUIT
Make Adjustments To The Default Data
       AL  AM     AN      AO      AP       AQ       AR       AS
 1      WESTINGHOUSE RADIATION INFORMATION PROCESSING SOFTWARE
 2      JOB EXPOSURE MODEL (JEM) SYSTEM - Version 1.0
 3
 4   DEFAULT INPUT FOR STEAM GENERATOR EDDY CURRENT TESTING
 5
 6    Task                                           Crew   Work Work
 7    No.   Task Description                         Size   Time Unit
 8   ----------------------------------------------  ----   ---- ----
 9   1      EQUIPMENT PREPARATION
10    1.01 MOVE EQUIP. INTO CONTMT.                    5      60 /JOB
11   2      ACCESS PROVISIONS-SETUP
12    2.01 ERECT PLATFORMS                             4      60 /SG
13    2.02 REMOVE MANWAY COVERS                        3     120 /CH
14    2.03 REMOVE MANWAY INSERTS                       2      30 /CH
15    2.04 BLOWER INSTALLATION                         2      12 /CH
16    2.05 ERECT ISOLATION TENT                        3      60 /SG
17   3      EQUIPMENT SETUP
18    3.01 DATA STATION SETUP                          8     135 /JOB
19    3.02 INSTALL L/W NOZZLE                          2       1 /CH
20    3.03 INSTALL T/S TEMPLATES                       2       3 /CH
                                                          CALC
```

Fig. 2 Example of user-defined menu

Experience

Manual job exposure models have been used at Westinghouse for Radiation Exposure Management/ALARA Programs for over ten years. These job exposure models are the basis for computerized models, which provide an improved tool for the minimization of radiation exposure during plant maintenance.

The original models and the computerized versions have been used extensively in job planning, dose budgeting, ALARA evaluation of procedures, and equipment/tooling design. The models have also been used to identify tasks for exposure reduction action, as a source of data required for plant managed maintenance programs and in the plant licensing process [8]. The models reflect a significant data accumulation and evaluation process based on feedback from Westinghouse service crews and utility personnel. They also reflect the results of time-and-motion studies performed at mockup facilities and during field operations at plant sites.

Table 2 Field experience for eddy current testing

Steam generator	Estimated dose (Man-Rem)	Actual dose (Man-Rem)	Actual estimated
A	13.1	14.6	1.11
B	14.1	14.1	1.00
C	9.3	7.9	.85

Comparisons of predicted and actual occupational radiation exposure (ORE) for several plant maintenance activities are presented in Tables 1 and 2. Total job exposures associated with modifications to antivibration bars (AVBs), which are located at the top of U-tube steam generators, are illustrated in Table 1. As shown by the data for the first two jobs of this type there can be significant discrepancies between estimated and actual exposures due to unanticipated problems, uncertainties in projecting the actual work area radiation fields, differences in worker efficiency/productivity, and other factors. Even though the degree of agreement between the estimate and the actual exposure was not high a primary function of the model, i.e., evaluation of the job and identification of dose reduction measures in the preplanning phase, was easily fulfilled.

For those maintenance activities that are performed on a more regular basis, the data base and experience level are such that good agreement between estimated and actual job exposures is generally observed. An example of estimated versus actual doses for a frequent activity is illustrated in Table 2, which presents results for nuclear plant steam generator eddy current inspection programs. Such programs are performed annually at nuclear stations and the required personnel exposure continues to decrease over time as improved equipment and procedures are developed and implemented.

Use and Benefits

The specific benefits of computerized exposure models are as follows:

- Provide a benchmark against which actual performance can be measured. Such comparisons are possible for an entire operation, for specific tasks within the operation, or for a combination of subtasks
- Ready availability of work time and dose information, by worker classification, for the personnel involved in the various

tasks makes it possible to budget both manpower and dose prior to performing the actual operation

- Facilitates easy identification of tasks within a work activity with the largest potential for dose reduction
- Provides the capability for quickly evaluating alternative methods of dose reduction, and thus provides a basis for cost/benefit evaluation
- The system provides a convenient documentation and tracking system for job exposures and work times, which is valuable in preplanning for future outages and for post-outage report preparation
- Enables personnel more effectively to develop improved equipment and procedures to reduce radiation doses.

The computerized dose estimate models developed at Westhinghouse are intended for use by individuals with various levels of experience in dose estimation and ALARA assessment. The system is designed to be easily used by personnel with little or no computer experience and is of particular value to personnel who lack experience in assessment of job exposures and/or to utilities who have limited historical data upon which to base dose estimates.

References

1 "Information Relevant to Ensuring that Occupational Radiation Exposures at Nuclear Power Stations Will Be As Low As Reaonably Achievable," U.S. Nuclear Regulatory Commission, Washington, D.C., Regulatory Guide 8.8, Revision 4, Mar. 1979.

2 "Operating Philosophy for Maintaining Occupational Radiation Exposures As Low As Reasonably Achievable," U.S. Nuclear Regulatory Commission, Washington D.C., Regulatory Guide 8.10, Revision 1-R, May 1977.

3 "Occupational Radiation Dose Assessment in Light-Water Reactor Power Plant Design Stage Man-Rem Estimate," U.S. Nuclear Regulatory Commission, Washington D.C., Regulatory Guide 8.19, Revision 1, June 1979.

4 "Guidelines for Radiological Protection at Nuclear Power Stations," Institute of Nuclear Power Operations, Good Practice, INPO 85-004.

5 "Use of Goals in Reducing Personnel Radiation Does," Institute of Nuclear Power Operations, Good Practice, INPO 86-011.

6 Fero, A. H., "Westinghouse Experience: Radiation Exposure Management Makes Sense," Proceedings of the ANS Executive Conference, *There Are Dollars and Sense in Good Radiation Protection Management*, San Diego, CA, Dec. 9-12, 1984.

7 Mann, B. J., et al., "Estimating Collective Dose in Nuclear Facilities, With Emphasis on the Design Process," National Environmental Studies Project/Atomic Industrial Forum, SC and A, Inc., Dec. 1986, pp. 2-1, 2-2.

8 "Standard Format and Content of Safety Analysis Reports for Nuclear Power Plants, LWR Edition," U.S Nuclear Regulatory Commission, Washington, D.C., Regulatory Guide 1.70, Revision 3, Nov. 1978.

Advanced Research and Technology Development Fossil Energy Materials Program

R. R. Judkins

R. A. Bradley

Oak Ridge National Laboratory,
Metals & Ceramics Division,
Oak Ridge, TN 37831

The Advanced Research and Technology Development (AR&TD) Fossil Energy Materials Program is a multifaceted materials research and development program sponsored by the Office of Fossil Energy of the U.S. Department of Energy. The program is administered by the Office of Technical Coordination. In 1979, the Office of Fossil Energy assigned responsibilities for this program to the DOE Oak Ridge Operations Office (ORO) as the lead field office and Oak Ridge National Laboratory (ORNL) as the lead national laboratory. Technical activities on the program are divided into three research thrust areas: structural ceramic composites, alloy development and mechanical properties, and corrosion and erosion of alloys. In addition, assessments and technology transfer are included in a fourth thrust area. This paper provides information on the structure of the program and summarizes some of the major research activities.

Introduction

The AR&TD Fossil Energy Materials Program is directed toward obtaining a fundamental understanding of materials and their behavior in fossil energy systems. Long-range needs of fossil energy systems are addressed on the program, and funded projects should have general applicability to most fossil energy technologies. Three research thrust areas are included in the program: structural ceramic composites, alloy development and mechanical properties, and corrosion and erosion of alloys. A fourth thrust area, assessments and technology transfer, is included to identify needed research and to transfer materials developments to industrial organizations for implementation and use (Judkins and Carlson, 1987).

Funding is presently divided among the three materials research thrust areas as shown in Table 1. There are 55 active projects on the program. The research is being performed at national and other government laboratories, universities, and industrial research centers.

Principal activities on the structural ceramic composites research thrust area include the development of processes for making silicon carbide whiskers, incorporating whiskers into ceramic matrix composites, development of fiber-reinforced ceramic composites produced by chemical vapor infiltration and deposition of a ceramic matrix in a fibrous preform, joining of reinforced ceramic composites, studies of mechanical properties of advanced structural ceramic composites, and development of nondestructive examination techniques for green and densified ceramics.

Two major alloy development projects are being conducted. The first of these is the development of nickel–iron and iron aluminides. This project includes separately funded activities at Oak Ridge National Laboratory and at two other laboratories. The primary development effort on the nickel–iron aluminides was concluded in FY 1987 (ended Sept. 30, 1987), and efforts are now directed toward larger-scale production of materials, indentification of specific applications of the alloys, and transfer of the technology to industry. The iron aluminides project is in the initial development phase.

The second alloy development project is the development and evaluation of iron-base alloys for advanced (650°C, 35 MPa) combustion superheater and reheater tubes. This project was initiated in FY 1985 and is scheduled to continue through FY 1990. The goal of the project is the selection by 1990 of not more than four alloys for final development and commercialization by industry. At about this time, the Electric Power Research Institute and its member utilities are scheduled to address the issue of demonstration of advanced steam cycles operating at 650°C and 35 MPa.

Corrosion research centers on studies of the formation and breakdown of protective oxide scales, particularly in sulfur-containing atmospheres. Our goal is to understand the com-

Table 1 Summary of FY 1988 funding for the AR&TD Fossil Energy Materials Program by thrust area

Thrust area	Funding ($ in thousands)
Structural ceramic composites	2588
Alloy development and mechanical properties	1391
Corrosion and erosion of alloys	1942
Assessments and technology transfers	559
Total	6480

Contributed by the International Gas Turbine Institute and presented at the 33rd International Gas Turbine and Aeroengine Congress and Exhibition, Amsterdam, The Netherlands, June 5–9, 1988. Manuscript received by the International Gas Turbine Institute January 15, 1988. Paper No. 88-GT-234.

position and characteristics of alloys that are necessary for the formation of adherent protective oxide films and scales. Most of this work is concerned with materials degradation in coal combustion and coal gasification environments.

Erosion and wear research on the AR&TD Fossil Energy Materials Program is directed to the understanding of modes of materials erosion and their relationships to materials properties. We believe that with this understanding, improvements can be made to materials to improve their erosion resistance. Erosion and wear research on the program includes fundamental studies of materials erosion, fluid dynamics studies of erosive systems, and a study of galling and abrasive wear.

The determination of materials research needs and the transfer of developments on the program are accomplished in the assessments and technology transfer thrust area. Activities in this thrust area are continuously changing, but presently we have subcontract efforts to investigate the causes of failure of ceramic filters and to assess the potential applications of ceramic composites in gas turbines. Our technology transfer activity includes the formation of an industrial consortium to fund the development of a user-friendly and intelligent computer software system based on a thermomechanical model of refractory liners for coal gasifiers. This software system will permit the use of this rather complex computer model by engineers who may or may not be familiar with finite-element analysis techniques.

Structural Ceramic Composites

Fiber-reinforced ceramic composites are being developed as potential candidates for high-temperature structural materials. Ceramic fibers incorporated into brittle matrices prevent catastrophic failure by improving frature toughness through energy dissipation processes such as fiber pull-out and crack deflection. Ceramic composite systems have been reported that have improved strength and fracture toughness over monolithic ceramics, but many of the conventional ceramic manufacturing techniques used to produce ceramic composites degrade the fibers.

In one of the major activities on this program, scientists at Oak Ridge National Laboratory (Stinton et al., 1986) are using a chemical vapor infiltration and deposition process to produce fiber-reinforced ceramic composites. In this process, reactant gases such as methyltrichlorosilane (MTS) are entrained in a carrier gas such as hydrogen and are passed through a fibrous preform of some desired product shape. By controlled heating of the preform, the reactant gases decompose and deposit a matrix of silicon carbide around and on the preform fibers. A schematic of the process is shown in Fig. 1. In a recently completed statistically designed experiment, densities up to 2.65 g/cm^3 or 91.2 percent of the theoretical density of silicon carbide were obtained by this technique. Material with uniform physical properties was produced, and trends that are controlled by process conditions were determined. Room temperature flexure strengths of over 480 MPa were obtained for specimens produced in this experiment. The flexure strengths were measured by four-point bending, and all specimens exhibited typical composite behavior during testing. That is, all specimens failed noncatastrophically with fiber pull-out, and the appearance of the load-crosshead displacement curves was similar for all specimens tested.

The ability of this process to produce lower-density and higher-porosity ceramic composites suitable for use as hot-gas cleanup filters has also been demonstrated. Tests of disk-shaped filter specimens indicated that they were very efficient ($>$99 percent of particles removed) in filtering fluidized-bed combustor fly ash and coal gasifier char from hot-gas streams. The filter specimens also proved to be quite durable in cyclic cleanability tests.

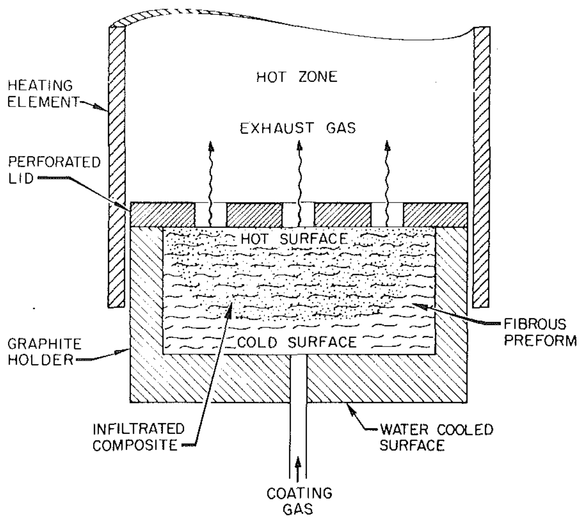

Fig. 1 Schematic of infiltration system

In a supporting project (Starr, 1987) at Georgia Tech Research Institute, a microstructural model for the fibrous preform and the intermediate, partially densified composite is used to predict gas flow and temperature throughout the body. Combined with kinetics data, the model allows calculation of the density distribution during the infiltration process. The model aids optimization of the processing conditions, structure, and properties by predicting the effect of modifications to the process and of changes in preform structure.

Projects at Pacific Northwest Laboratory and ORNL are addressing the issue of fiber-matrix interaction in an attempt to understand the roles that fiber-matrix interfaces play in relationship to properties of the composite materials (Bates et al., 1987; Lowden and Stinton, 1987).

At Los Alamos National Laboratory, a vapor-liquid solid whisker growth process (Milewski et al., 1985) has been developed and optimized for the production of short (10 mm) silicon carbide whiskers. Modifications to this process have been made to permit production of longer ($>$25 mm lengths) whiskers. The short whiskers may be incorporated into a ceramic matrix to provide toughening of the ceramic matrix. The development of staple yarns from the long whiskers for use as a fiber reinforcement in ceramic composites is a major goal of this project, as is the transfer of the technology to industry.

Two closely related projects (Ellingson et al., 1987; Singh, 1986) at Argonne National Laboratory (ANL) are developing methods to detect and characterize flaws in and to determine the effect of these flaws on the fracture behavior of structural ceramics. As an example of the activities on these projects, fracture studies and nondestructive evaluation (NDE) were performed to detect and assess the effect of flaws on the fracture behavior of hot-pressed SiN with iron inclusions. Through-transmission and backscatter ultrasound and low-kV contact radiography NDE were used to detect the iron-inclusion-induced internal flaws. The critical flaw sizes in the specimens were always larger than the fractographically measured flaw sizes. In a comparison of the fractography and NDE results for the location of critical flaws, the backscatter ultrasound method may be more suitable than through-transmission ultrasound or low-kV contact radiography for the detection of the near-surface flaws that lead to fracture.

In addition to the NDE work at ANL, ultrasonic methods for evaluating ceramic fiber-ceramic matrix composites are being developed (Walter and Lott, 1987) at the Idaho National Engineering Laboratory (INEL). Through-transmission techniques, including the use of time delay spectrometry and laser generation of ultrasound, for measuring ultrasonic properties are being used. These techniques appear to be adequate bases for developing effective ultrasonic NDE methods for the analysis of composites.

Silicon nitride composites with random, short-fiber reinforcement have been fabricated at the Georgia Tech Research Institute using reaction sintering techniques (Starr and Harris, 1987). Large diameter fibers yield high-density composites but degradation of fibers during nitriding limits property gains. Small diameter whiskers with better high-temperature stability yield low-density composites using currently available powders.

A research project at INEL is identifying and developing techniques for joining silicon carbide fiber-reinforced ceramic composites of tubular geometries, primarily through the use of glass joining materials (Coon et al., 1987). Major tasks on the project include identifying, preparing, and characterizing glass compositions suitable for joining ceramic fiber-ceramic matrix composites; developing joining methods and evaluating the effects of process parameters on joint characteristics; fabricating and characterizing joints; and determining the properties and fracture behavior under simulated service conditions.

Complementary projects at INEL and ORNL are investigating the production and fabrication of superconducting ceramic materials. The INEL project is focusing on the production of superconducting ceramics by sol-gel techniques and ORNL is investigating powder processing and fabrication of these materials by microwave sintering.

Alloy Development and Mechanical Properties

This research thrust area consists of two major projects. The first project (Liu et al., 1987; McKamey et al., 1986) at ORNL, development of nickel-iron and iron aluminides, is designing and characterizing new, improved high-temperature materials based on Ni_3Al+Fe and Fe_3Al for structural use in coal conversion and utilization systems. One of the most exciting properties of this class of alloys is the increase in strength with temperature that they exhibit. Figure 2 illustrates this behavior and compares it with the behavior of the superalloy, Hastelloy X. Although temperature limits for this behavior exist, there are many fossil energy applications at temperatures less than that at which strength starts to decrease rapidly with further temperature increases. It was this property that prompted the initiation of this activity. Although strength is vitally important in most high-temperature structural applications, corrosion resistance is also of prime importance in fossil energy systems.

Chromium has been found to be a key alloying element for the nickel-iron aluminides that promotes the rapid formation of protective oxide scales and improves the corrosion resistance of these alloys. Alloying with 3 to 7 at. percent Cr also dramatically reduces dynamic embrittlement in oxidizing environments at 400 to 800°C. Both chromium and iron increase the stability of the bcc-ordered B2 phase, which is brittle at room temperature and weak at elevated temperatures. Chromium is also a key alloying element for the iron aluminides. Additions of chromium have been shown to increase room-temperature ductilities of these alloys up to about 10 percent elongation.

Corrosion studies have demonstrated that chromium additions of 7 at. percent were very effective in minimizing sulfur attack on the nickel-iron aluminides. Oxide films produced in air are very effective in preventing sulfidation attack; however, the air oxidation temperature should be 1000 to 1050°C, and the alloys still must contain at least 3 at. percent chromium. Corrosion resistance of the iron aluminides is outstanding even without additions of chromium.

In addition to the primary development work at ORNL, support activities have been conducted or are in progress at other laboratories. A recently completed project at INEL involved a study of the weldability of advanced aluminides (Clark, 1987). This work showed that solidification segregation during base metal production decreases weldability by creating melting regions susceptible to hot cracking. This problem is eliminated by extrusion, hot rolling, and annealing, which homogenize the base metal microstructure. The effects of zirconium, preheat temperature, and weld travel speed on weldability were evaluated using a gas tungsten arc welding process and heat-affected zone simulation. Tendency toward cracking increased with zirconium content at low zirconium levels and welding speed, but decreased with increasing preheat. Hot cracking was more severe at higher zirconium levels. An interdendritic phase enriched in zirconium was present in weldments made at higher welding speeds.

The Center for Welding Research at Colorado School of Mines is investigating the weldability and hot ductility of aluminides. This work concerns the improvement of weldability and hot ductility of these alloys through microstructural refinement of the grain structure and production of an antiphase domain structure.

A project in progress at INEL is studying the consolidation of rapidly solidified nickel and nickel-iron aluminide powders (Wright and Flinn, 1987). Vacuum gas and centrifugal atomization both produce clean powders with a thin oxide that does not hinder bonding consolidation by hot extrusion and hot isostatic pressing. Extruded materials have very fine grain sizes, which resist coarsening at elevated temperatures. The powder metallurgy materials have good room temperature strength and ductility and exhibit relatively little flow stress increase with increasing temperature. Properties of the hot isostatically pressed material are very sensitive to consolidation parameters and heat treatment.

A project was initiated at ORNL in 1985 to develop or modify alloys for use as advanced (650°C, 35 MPa) combustion superheater and reheater tubing. The project was conceived as a support activity to an Electric Power Research Institute program aimed at developing advanced combustion systems operating at 650°C and 35 MPa. The candidate alloys selected for investigation are modifications of steels in four groups: type 316 stainless steel, type 310 stainless steel or alloy 800, aluminum-containing (4 to 8 percent) steel, nickel-chromium alloys such as alloys 617, 690, and 671. A plan was developed (Swindeman et al., 1986) with the goal of providing by about 1990 the information needed to select an

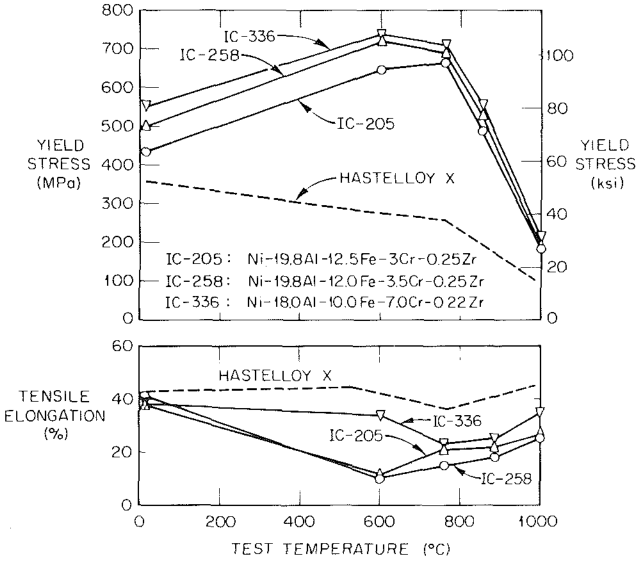

Fig. 2 Comparison of yield stress and tensile elongation of some nickel-iron aluminides with Hastelloy X

alloy for final development and commercialization by industry. The first phase of the plan, which reduced the candidate alloys from 40 to 16, has been completed.

In implementing the plan, performance criteria and evaluation methods were defined. Performance criteria for fireside corrosion, steamside corrosion, mechanical properties, fabricability, and compositions and microstructure were established. Evaluation methods to verify that the performance criteria could be met were used.

Most of the work to date has concentrated on the so-called lean austenitic stainless steels, which contain less than 20 percent chromium. Based on the results obtained to date, fabricability of these alloys is satisfactory; weldability depends on proper selection of filler metal; and mechanical properties that meet the performance criteria can be attained. One of the most important considerations for the alloys is their creep behavior. A comparison of creep curves at 170 MPa and 700°C is made in Fig. 3. Data for several standard alloys including 17-14CuMo stainless steel, alloy 800H, and type 316 stainless steel are included in the curves for comparison.

Fabricability of the alloys is being evaluated by Babcock and Wilcox. This work is intended to demonstrate that these alloys can be fabricated by standard industry methods. The evaluation will include clad and unclad tubes.

The lean austenitic stainless steels will likely require coatings, claddings, or some kind of surface treatment to provide the necessary steamside and fireside corrosion protection. Foster Wheeler Development Corporation is studying the fireside corrosion of these alloys. At the operating temperatures, molten salts, which are highly corrosive, are formed. Specimens included in the tests will include both bare and surface-modified materials. Appropriate coatings to provide the necessary resistance to this corrosive material should be identified in this project.

The high-temperature deformation and microstructural stability of these alloys are being investigated (Carolan et al., 1987) at Cornell University. Several of the lean austenitic stainless steels have been evaluated in terms of high-temperature flow strength. The effects of thermomechanical pretreatment on alloy flow strength have also been investigated to optimize alloy strength before use. Load relaxation testing has been the primary technique used in this investigation. Several important conclusions have been reached as a result of the Cornell work. A copper-modified and Ti-Nb-V stabilized 316 stainless steel is the strongest alloy tested when used with an optimum pretreatment. This optimum pretreatment involves solution treatment at 1150°C followed by 2 percent cold work and a stabilization aging treatment of two days at 850°C. The effects of copper are to increase the stacking fault energy of the austenite lattice that favors enhanced nucleation of MC-type precipitates on the dislocation structure developed during cold work when the material is given a stabilization aging treatment before use.

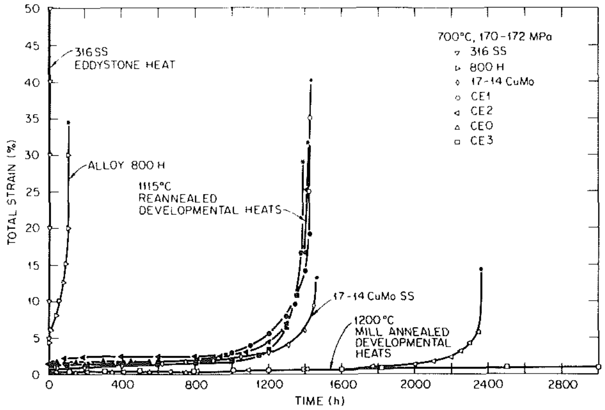

Fig. 3 Comparison of the creep behavior of the developmental alloys with some commercial alloys

Corrosion and Erosion of Alloys

The goal of the research on corrosion of alloys is to obtain an understanding of the formation and breakdown of protective oxide scales in atmospheres typical of fossil energy process environments. The basis for the research is that if the formation and breakdown of these protective scales is understood in a mechanistic sense, alloys can be selected, modified, or developed that will perform well in these environments.

In late FY 1986, a competitive procurement was completed with awards to Battelle Columbus Division, Case Western Reserve University, and Universal Energy Systems, Inc., to investigate the effects of microalloy constituents, surface treatment, and oxidation conditions on the development and breakdown of protective oxide scales (Wright and Colwell, 1987; Vedula et al., 1987; Srinivasan, 1987). The objectives of this work are to gain an improved understanding of the effects of alloying constituents present at low levels on the development and mode of breakdown of protective oxide scales in conditions representing those encountered in coal combustion and gasification processes, and to achieve better control over the growth of scales, which will contribute to improvements in long-term high-temperature corrosion resistance.

Three base alloys, Fe-25Cr, Fe-25Cr-20Ni, and Fe-25Cr-6Al, were chosen for study. The 25 percent chromium level was selected to ensure that continuous, protective scales of Cr_2O_3 are reliably formed. The aluminum-containing alloy is intended to be an alumina former, but literature data indicate that a continuous film of alpha alumina does not form at temperatures below about 800°C. These studies are directed toward applications in the 500 to 700°C range. Alloying additions are being studied to determine what beneficial effects can be obtained. In addition, the techniques used to incorporate the alloying elements into the base alloys are being studied. Several different methods are being investigated, and they include both bulk alloying and surface modification techniques.

There is, in the total program activity, some overlap in the work being performed at these three organizations. For example, the same base alloy compositions are being used. However, each subcontractor selects the minor alloying elements and method of incorporation into the base alloy. This approach provides the necessary freedom to explore many possibilities and also prevents too much overlap and duplication of effort.

A project at Argonne National Laboratory over the past ten years has evaluated the compatibility of engineering materials and model alloys in oxygen-sulfur mixed-gas environments that are relevant to both coal gasification and coal combustion (Natesan and Bakker, 1985; Natesan, 1986). Present research is examining the roles of several factors such as cation and sulfur transport through the scales, mechanical effects, sulfur segregation, and time-dependent morphological changes in the scale, in the onset of breakaway corrosion in structural alloys. These studies indicate that molecular transport of SO_2 inward through a porous oxide scale is responsible for sulfidation attack of materials exposed to SO_2-containing atmospheres, but the transport of base-metal cations outward through the scale, and subsequent sulfidation of them, seems to initiate breakaway corrosion in H_2S-containing atmospheres.

Corrosion tests at 800°C were conducted at ORNL on iron-based alloys in a H_2-H_2S-H_2O-Ar gas mixture with $P_{S_2} = 10^{-6}$ and $P_{O_2} = 10^{-20}$ atm that simulate severe coal gasification environments (Hsu, 1986). Alumina-forming iron-based alloys were more corrosion resistant than chromia-forming iron-based alloys in this environment. Rapid sulfidation of the alumina-forming alloys with and without preoxidation proceeded initially by nucleation and growth of chromium-rich sulfides and later by formation of iron-rich sulfides. The formation of fast-growing sulfides such as CrS and FeS should be minimized or avoided to increase the corrosion resistance of alumina-forming iron-based alloys. This is the approach being taken in the development of some new alloys that should be very sulfidation resistant.

In a project at the University of Pittsburgh, the corrosion of several ferrous alloys (Fe-18Cr-6Al, Fe-18Cr-6Al-1Ti, Fe-18Cr-6Al-1Hf, Fe-25Cr, and Fe-20Si) was studied between 700 and 1100°C in oxidizing atmospheres (Kim et al., 1987). The breakdown of preformed oxide scales on these alloys was studied in a sulfidizing-oxidizing atmosphere at the same temperatures. Several important conclusions were reached based on this work. The resistance to isothermal oxidation and thermal cycling in air at 950°C increases in the order SiO_2-former > Al_2O_3-former > Cr_2O_3-former. The addition of titanium to the aluminum-containing alloy improves its resistance to cyclic oxidation and to sulfidation-oxidation at 950°C. Hafnium improves the cyclic oxidation resistance of the aluminum-containing alloy but provides rapid transport paths for sulfur through the scale. Chromia scale breakdown in the Fe-25Cr alloy in high P_{S_2} and low P_{O_2} atmospheres is initiated at the scale-gas interface. Silica scales are resistant to sulfur penetration, but the outward transport of iron through the scales raises questions concerning their long-term stability in high P_{S_2} and low P_{O_2} atmospheres.

Erosion and wear research in the AR&TD Fossil Energy Materials Program is, like research in the other thrust areas, directed to the understanding of materials behavior. The philosophy of this approach is that if the modes of material erosion and their relationships to materials properties are understood, improvements to materials to improve their erosion resistance can be made. Erosion and wear research includes fundamental erosion studies and studies of particle flow effects on erosion.

Projects at ORNL and Lawrence Berkeley Laboratory (LBL) are addressing the fundamental aspects of erosion in fossil energy systems (Keiser and Ficalora, 1986; Levy and Man, 1985). In the work at ORNL, a unique device has been developed to study damage to the surfaces of materials as a result of individual particle impacts. The device consists of a scanning electron microscope with a chamber modified to perform in-situ erosion and erosion-corrosion studies. Modifications include a miniature gas gun (see Figs. 4 and 5) that is capable of firing individual particles at a target specimen at velocities up to 100 m/s. Atmosphere, temperature, and impingement angle can all be controlled to provide a very broad range of experimental conditions. Figure 6 shows overlapping craters in 304L stainless steel resulting from successive impacts at 30 deg incidence. Table 2 provides information on impact craters produced in three different alloys. The goal of this project is to relate the surface damage of materials to their physical and mechanical properties.

Results to date support the theory that particle impacts change the surface properties of the target material. For example, work hardening appears to occur in nickel-base alloys. However, in alloys with lower melting temperatures, particle impacts may anneal the surface region and result in a softening of the alloys. These and other surface phenomena will continue to be investigated in this work.

At LBL, the erosion of material surfaces by small solid particles in gaseous carriers is being investigated. The materials are tested over a range of conditions that simulate portions of the operating environments of surfaces of containment materials in coal gasification and fluidized-bed combustion systems. Both alloys and cermets are being investigated on this project. Attempts are made to correlate, or establish trends of, materials properties with their erosion resistance. For example, some evidence has been reported for improvement in erosion resistance by solid-solution strengthening. The erosion behavior of alloys and cermets with a wide range of second-phase carbides has also been investigated at LBL. Several important observations were made in this work. For alloys containing less than about 30 vol percent carbides, erosion rates increased with carbide volume fraction. This behavior is apparently related to the size of the carbide particles. These low-volume-fraction carbide materials had large (> 10 μm) carbide particles. Displacement of the binder material as a result of particle impact is limited by the large carbide particles and results in an increase in the ability of subsequent impacts to remove material. For the carbide cermets containing 60 to 80 vol percent carbides, erosion is controlled by the binder. The binder is severely constrained by the carbides, and its ductility is greatly reduced. This results in a decrease in the ability of subsequent impacts to remove material.

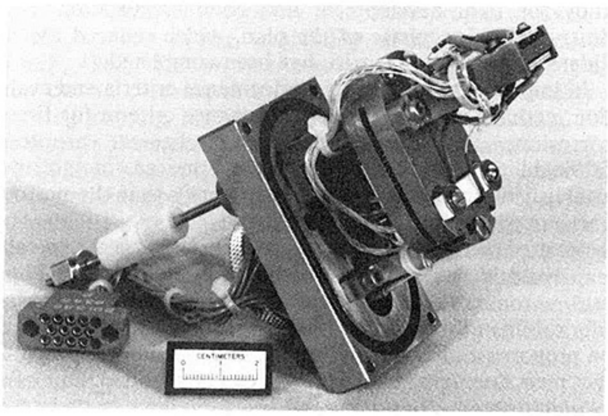

Fig. 4 Erosive-particle gun

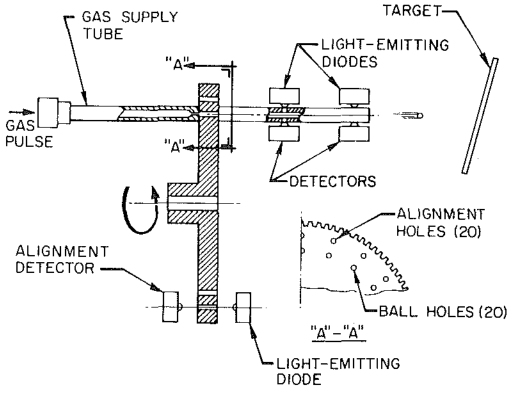

Fig. 5 Schematic drawing of the erosive particle gun

Studies of particle flow effects on erosion are being conducted at the University of Cincinnati, the University of California at Berkeley, and the University of Notre Dame. At the University of Cincinnati, studies of particle rebound characteristics (restitution ratios) and materials erosion at high temperatures (gas turbines) are being conducted (Tabakoff, 1985). The basic premise of this project is that erosion is a function of the exchange of energy between erodent particles and the material being impacted. Furthermore, an erosive impact is assumed to occur when the impacting particle is much harder than the target material.

Recently initiated work at the University of Notre Dame involves the development of models to describe the rebound of particles from a surface and experimental studies to verify the models and to relate particle rebound to material properties (Kosel and Sriram, 1987). Predictions of the models are being

Table 2 Average dimensions of craters formed during 30-m/s single-particle impact studies

	Average crater dimension		
	Strengthened (μm)	Annealed (μm)	Change (percent)
Hastelloy C-276			
30 deg Impacts			
Crater depth	5.4	7.3	+35
Lip height	2.2	2.3	+5
90 deg Impacts			
Crater depth	12.7	18.2	+43
Berylco 25			
30 deg Impacts			
Crater depth	4.9	9.4	+92
Lip height	2.5	7.9	+216
90 deg Impacts			
Crater depth	12.1	17.4	+44
4340 Steel			
30 deg Impacts			
Crater depth	4.5	8.9	+98
Lip height	3.4	5.1	+50
90 deg Impacts			
Crater depth	9.9	15.0	+52

compared with experimental measurements of rebound parameters. Multiple-impact experiments are being performed at the Universtiy of Cincinnati, and supplementary single- and multiple-impact experiments are being made at the University of Notre Dame. Experimental variables being considered in the projects include erodent particle shape, size, and velocity, and target material hardness and material treatments that affect hardness.

The University of California, Berkeley, project is developing an understanding of and a means of predicting two-phase (gaseous–solid) flow and erosion in tube banks typical of those used in fluidized-bed combustion (FBC) systems (Humphrey et al., 1987). The work consists of two activities including model development and experiments to determine erosion characteristics of the two-phase flow systems. A laminar flow model has been completed and tested, and a turbulence model will be developed and tested. In the experimental work, plastic cylinders are initially being used to examine erosion patterns and rates in several different configurations. Subsequent and detailed experiments will investigate alloys and tube-bank configurations typical of FBC units. Velocity and turbulence characteristics of the gaseous and solid streams will be determined in addition to erosion.

In addition to the erosion projects discussed above, the National Bureau of Standards is conducting a project to determine the basic mechanisms of galling and abrasive wear (Peterson et al., 1985). The purpose of the work is to develop an understanding of factors that affect the galling process and to determine the relationship between materials properties and the severity of galling. Pure metals and alloys are included in the testing. Surface topography data required by profilometry are being used to obtain a quantitative measure of galling damage. Parameters selected to measure galling damage include the maximum height of damage, displaced volume of damaged material, and shape of the damage based on the ratio (called the aspect ratio) of curve lengths summed parallel and perpendicular to the sliding direction. This work will soon focus on the study of abrasive wear like that which will occur in coal-fired diesel engines.

Assessments and Technology Transfer

One of the most important features of the AR&TD Fossil Energy Materials Program is the continuing effort to identify materials R&D needs in fossil energy systems. This identification of needs is accomplished in a variety of ways. Materials testing and failure analysis activities are conducted jointly with operators of pilot and demonstration plants. Frequently unanticipated problems or failures in these plants point out the need for additional materials research. Specific assessments of generic materials problems are also made to identify needed research. For example, an assessment of the causes of failure of ceramic filters is being conducted by Acurex Corporation. Proposals are being evaluated for a new project that will assess potential applications of ceramic composites in gas turbines. Based on these assessments and evaluations, needed materials research may be identified and initiated.

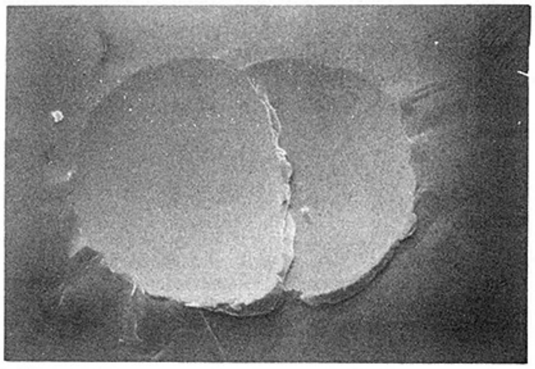

Fig. 6 Craters in 304L stainless steel produced by successive impacts (30 deg incidence, 45 m/s)

Technology transfer is vital to the health of the program and the entire scientific community. The transfer of information developed on the program is accomplished in many ways that may be classed as technology transfer. These include progress reports, topical reports, open literature publications, an annual conference and project review, and participation in other conferences and symposia. Other techniques are also employed to assure the transfer of technology.

For example, a consortium of industrial organizations has been established to cosponsor the development of user-friendly and intelligent software for a thermomechanical model of refractories in coal gasifiers. This thermomechanical model was developed by the Massachusetts Institute of Technology (MIT) on the AR&TD Fossil Energy Materials Program (Chen and Buyukozturk, 1985). Although it is quite complex, it provides an excellent technique to analyze the thermomechanical stresses that will exist in refractory-lined vessels, and it has been used (with assistance from the MIT researchers) by several different organizations. The user-friendly and intelligent software will permit the use of this complex model by engineers who are not expert in finite element analysis. Thirteen industrial organizations have joined ORNL in this consortium, and work is anticipated to begin in early calendar year 1988.

Summary

The AR&TD Fossil Energy Materials Program is a comprehensive program directed to understanding materials and materials behavior in fossil energy environments. To maximize the impact of the program on the materials community, three research thrust areas were identified and research was initiated in these three areas. These include structural ceramic composites, alloy development and mechanical properties, and corrosion and erosion of alloys. In addition to the research that is performed, a vigorous effort is made to transfer the developed technology to potential industrial users.

Acknowledgments

This research is sponsored by the U.S. Department of Energy AR&TD Fossil Energy Materials Program under contract DE-AC05-840R21400 with Martin Marietta Energy Systems, Inc.

References

Bates, J. L., Griffin, C. W., Weber, W. J., and Courtright, E. L., 1987, "Improved Ceramic Composites Through Fiber-Matrix Interaction," *Fossil Energy Materials Program Conference Proceedings*, ORNL/FMP-87/4, Oak Ridge National Laboratory, Oak Ridge, TN, pp. 74–88.

Carolan, R. A., Coulombe, B., and Li, Che-Yu, 1987, "Mechanical Properties and Microstructural Stability of Advanced Steam Cycle Materials," ORNL/Sub/85-27488/02, Cornell University, Ithaca, NY.

Chen, E. S., and Buyukozturk, O., 1985, "Modeling of Long-Term Corrosion Behavior of Refractory Linings in Slagging Gasifiers," *American Ceramic Society Bulletin*, American Ceramic Society, Columbus, OH, Vol. 64, No. 7, pp. 995–1000.

Clark, D. E., 1987, "Joining of Advanced Aluminides," *Fossil Energy Materials Program Conference Proceedings*, ORNL/FMP-87/4, Oak Ridge National Laboratory, Oak Ridge, TN, pp. 697–714.

Coon, D. N., Neilson, R. M., and Landini, D. J., 1987, "Characterization of $MgO-Li_2O-Al_2O_3-SiO_2$ Glasses for Use as Brazing Materials," EGG-MS-7523, Idaho Falls, ID.

Ellingston, W. A., Roberts, R. A., Vannier, M. W., Ackerman, J. L., Sawisa, B. D., Gronemeyer, S., and Kriz, R. J., 1987, "Development of Nondestructive Evaluation Methods for Structural Ceramics," *Fossil Energy Materials Program Conference Proceedings*, ORNL/FMP-87/4, Oak Ridge National Laboratory, Oak Ridge, TN, pp. 270–292.

Hsu, H. S., 1986, "A Review of the Development and Breakdown of Protective Oxide Scales on Alloys Exposed to Coal-Derived Atmospheres," ORNL-6323, Oak Ridge National Laboratory, Oak Ridge, TN.

Humphrey, J. A. C., Schuh, M. J., Schuler, C., and Schweitzer, M. O., 1987, "Particle Erosion in Turbulent Flow Past Tube Banks," *Fossil Energy Materials Program Conference Proceedings*, ORNL/FMP-87/4, Oak Ridge, TN, pp. 422–451.

Judkins, R. R., and Carlson, P. T., 1987, "Advanced Research and Technology Development Fossil Energy Materials Program Implementation Plan for Fiscal Years 1987 Through 1991," ORNL/TM-10242, Oak Ridge National Laboratory, Oak Ridge, TN.

Keiser, J. R., and Ficalora, P. J., 1986, "Effects of the Impact of Small Hard Spheres on Ductile Metals," *Microstructural Science*, American Society of Metals, Metals Park, OH, Vol. 13, pp. 237–246.

Kim, G. M., Gulbransen, E. A., and Meier, G. H., 1987, "Corrosion Mechanisms of Coal Combustion Products on Alloys and Coatings," *Fossil Energy Materials Program Conference Proceedings*, ORNL/FMP-87/4, Oak Ridge National Laboratory, Oak Ridge, TN, pp. 343–355.

Kosel, T. H., and Sriram, T. S., 1987, "A Study of Erosive Particle Rebound Parameters," *Fossil Energy Materials Program Conference Proceedings*, ORNL/FMP-87/4, Oak Ridge National Laboratory, Oak Ridge, TN, pp. 517–534.

Levy, A., and Man, Y. F., 1985, "Surface Degradation of Ductile Metals in Elevated Temperature Gas-Particle Streams," LBL-18686, Lawrence Berkeley Laboratory, Berkeley, CA.

Liu, C. T., Cathcart, J. V., Goodwin, G. M., Horton, J. A., Lee, E. H., and Campbell, J. J., 1987, "Development of Nickel-Iron Aluminides," ORNL-6412, Oak Ridge National Laboratory, Oak Ridge, TN.

Lowden, R. A., and Stinton, D. P., 1987, "The Influence of the Fiber-Matrix Bond on the Mechanical Behavior of Nicalon/SiC Composites," ORNL/TM-10667, Oak Ridge National Laboratory, Oak Ridge, TN.

McKamey, C. G., Liu, C. T., Cathcart, J. V., David, S. A., and Lee, E. H., 1986, "Evaluation of Mechanical and Metallurgical Properties of Fe_3Al-Based Aluminides," ORNL/TM-10125, Oak Ridge National Laboratory, Oak Ridge, TN.

Milewski, J. V., Gac, F. D., Petrovic, J. J., and Skaggs, S. R., 1985, "Growth of Beta-Silicon Carbide Whiskers by the VLS Process," *Journal of Materials Science*, Chapman and Hall, London, United Kingdom, Vol. 20, No. 4, pp. 1160–1161.

Natesan, K., and Bakker, W. T., 1985, "Corrosion in Coal Gasification Systems," *Proceedings, Conference on Materials for Future Energy Systems*, American Society for Metals, Metals Park, OH, pp. 185–193.

Natesan, K., 1986, "The Corrosion of Alloys in Mixed Gases," *Proceedings of the Electromechanical Society Symposium, High Temperature Materials Chemistry—III*, Z. A. Muir and D. Cubicciotti, eds., The Electrochemical Society, Inc., Pennington, NJ, Vol. 86-2, pp. 283–298.

Peterson, M. B., Bhansali, K. J., Whitenton, E. P., and Ives, L. K., 1985, "Galling Wear of Metals," *Wear of Materials—1985*, K. C. Ludema, ed., American Society of Mechanical Engineers, New York, pp. 293–301.

Singh, J. P., 1986, "A Review of the Effect of Flaws on the Fracture Behavior of Structural Ceramics," ANL/FE-86-3, Argonne National Laboratory, Argonne, IL.

Srinivasan, V., 1987, "The Effects of Microalloy Constituents, Surface Treatment, and Oxidation Conditions on the Development and Breakdown of Protective Oxide Scales," *Fossil Energy Materials Program Conference Proceedings*, ORNL/FMP-87/4, Oak Ridge National Laboratory, Oak Ridge, TN, pp. 384–396.

Starr, T. L., and Harris, J. N., 1987, "Development of Advanced Fiber Reinforced Ceramics, Final Report," ORNL/Sub-83-43369/01, Georgia Tech Research Institute, Atlanta, GA.

Starr, T. L., 1987, "Modeling of Fibrous Preforms for CVD Infiltration," *Fossil Energy Materials Program Conference Proceedings*, ORNL/FMP-87/4, Oak Ridge National Laboratory, Oak Ridge, TN, pp. 226–234.

Stinton, D. P., Caputo, A. J., and Lowden, R. A., 1986, "Synthesis of Fiber-Reinforced SiC Composites by Chemical Vapor Infiltration," *American Ceramic Society Bulletin*, American Ceramic Society, Columbus, OH, Vol. 65, No. 2, pp. 347–350.

Swindeman, R. W., Goodwin, G. M., Maziasz, P. J., Judkins, R. R., and DeVan, J. H., 1986, "Alloy Design Criteria and Evaluation Methods for Advanced Austenitic Alloys in Steam Service," ORNL-6274, Oak Ridge National Laboratory, Oak Ridge, TN.

Tabakoff, W., 1985, "Erosion Study of High Temperature Metals Used in Turbomachinery," *Proceedings of Symposium on High Temperature Corrosion in Energy Systems*, The Metallurgical Society of American Institute of Mining, Metallurgical, and Petroleum Engineers, Inc., Warrendale, PA, pp. 809–823.

Vedula, K., Michal, G. M., Mitchell, T. E., Welsch, G., Grobis, I., and Chang, S., 1987, "Investigation of the Effects of Microalloy Constituents, Surface Treatment and Oxidation Conditions on the Development and Breakdown of Protective Oxide Scales," *Fossil Energy Materials Program Conference Proceedings*, ORNL/FMP-87/4, Oak Ridge National Laboratory, Oak Ridge, TN, pp. 371–383.

Walter, J. B., and Lott, L. A., 1987, "Measurement of Ultrasonic Properties of Ceramic/Ceramic Composite Materials," EGG-SD-7621, Idaho National Engineering Laboratory, Idaho Falls, ID.

Wright, I. G., and Colwell, J. A., 1987, "The Effects of Microalloy Constituents on the Formation and Breakdown of Protective Oxide Scales on High-Temperature Alloys for Use in the Fossil Energy Industry," *Fossil Energy Materials Program Conference Proceedings*, ORNL/FMP-87/4, Oak Ridge National Laboratory, Oak Ridge, TN, pp. 356–370.

Wright, R. N., and Flinn, J. W., 1987, "Characterization of Rapidly Solidified Nickel Aluminide Powders," EGG-MS-7510, Idaho National Engineering Laboratory, Idaho Falls, ID.

Full-Engine Field Test: an Approach to Improve the Gas Turbine Combustion System

M. Gianola
Fiat TTG
Turin, Italy

For purposes of both final verification and optimization of TG 20 and TG 50 combustion systems, test programs have been carried out directly on full engines operating in the field, as well as in the test bench. These programs were carried out in two separate phases: the first one directed to determine the behavior at load by means of experimental data acquisition, including temperature distribution on the combustor exit plane for different burner arrangements, and the second one directed to optimize the ignition process and the acceleration sequence. This paper, after a brief description of the instrumentation used for each test, reports the most significant results burning both fuel oil and natural gas. Moreover, some peculiar operational problems are mentioned, along with their diagnosis and the corrections applied to the combustion system to solve them.

Introduction

All standard combustion systems of single-shaft engines built by the author's company consist of an annular air casing containing a certain number of flametubes.

A cannular-type combustion chamber has some advantages, in that performance tests for combustion efficiency, flame stability, ignition limits, basket temperatures, and exhaust smoke can be carried out in the laboratory using a segment of the full-engine combustion chamber containing only one basket. On the other side it is not possible to reproduce perfectly in such a test rig the real operating conditions and hence the outlet temperature profile that will be obtained in an actual engine.

In addition, problems due to unavoidable small fuel feed differences among the baskets of a full engine cannot be simulated.

A nonuniform temperature distribution at the combustor exit plane, i.e., at the turbine inlet section, may affect the life of turbine vanes and blades; therefore it is recommended to verify the behavior on the full operating engine at load. Also, the abovementioned fuel feed differences, which become more evident when fuel flows are very low and when all baskets interact with each other, require a verification of the cross ignition process.

Taking into account these considerations, the temperature distributions of the TG 50 gas turbine (18 baskets) and the TG 20 gas turbine (eight baskets) have been tested on a selected basket for each full engine, while temperatures and other significant parameters were measured at ignition and during the acceleration sequence on a certain number of the other baskets that are part of the two gas turbine combustion chambers.

Combustor Exit Temperature Measurement at Load

Combustion Basket Instrumentation. The instrumentation for the profile measurements consisted of five (for TG 50) and six (for TG 20) aspiration thermocouple rakes, which had been installed in a combustor exit section as close as possible to the turbine inlet section.

Figure 1 shows the test sections in the combustor or flametube transition duct, the thermocouple location details, and the selected position in the engine for the instrumented basket.

To ensure long rake durability, the characteristics of which are shown in Fig. 2, a high-pressure air system was used during all tests to back purge the instrumentation with cooling air during engine operation in the no data acquisition phases. The thermocouples are shielded within the rake body and have no parts exposed either to the flame or to the relatively cold metal wall and vane surfaces. This, plus a high aspiration flow velocity past the thermocouple junction, serves to minimize errors. Some tests made in the laboratory to compare thermocouple measurements with temperature deduced from exhaust gas-carbon balance yielded agreement within ±15°C.

It must be remarked that the back purge cooling air is extremely important during the ignition process, although temperatures are lower than at load, in order to prevent accidental unburned fuel from entering the aspiration holes.

A cooling flow lower than 40 kg/h per rake supplied at a pressure of about 15 bar and at a temperature of 310 K during all tests ensured that the rakes operated in very safe conditions; in fact, after more than 100 tests, only one thermocouple was lost.

For TG 50, the complete collection of 35 measuring grid

Contributed by the Gas Turbine Division of The American Society of Mechanical Engineers and presented at the 32nd International Gas Turbine Conference and Exhibit, Anaheim, California, May 31–June 4, 1987. Manuscript received at ASME Headquarters February 19, 1987. Paper No. 87-GT-205.

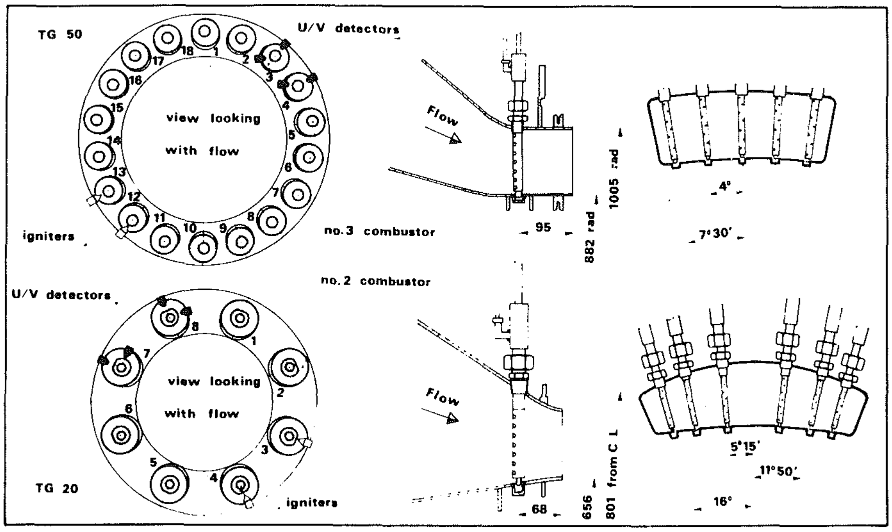

Fig. 1 Details of instrumentation for temperature profile measurements on TG 50 and TG 20

points required about 5 s, plus 20 s to display them on a paper printer, whereas for TG 20 the time from the initial reading of the first of the 42 thermocouples to the print of the last one was about 15 s. This was due to an improved data acquisition system that was not available when the TG 50 test was made.

During each test several temperature measurements were taken at the abovementioned time steps to ensure that a set of data could be recorded consistently with a steady-state operation condition of the gas turbine.

Test Configurations for TG 50 and TG 20. Figure 3 shows a typical TG 50/TG 20 combustor; Fig. 4 shows, with respect to TG 50 tests, the changes that have been made on rows of holes called No. 1, No. 2, No. 3, and No. 4 in Fig. 3.

Tests undertaken on TG 50 were run to try to separate effects due to various configurations of fuel nozzles from those of baskets. To accomplish this purpose, the temperature profile was measured with two different liquid fuel injectors in separate runs for three different basket configurations.

Therefore, after six sets of data were analyzed, the "best" basket-injector arrangement was chosen and one more test, with a screen provided around the basket to improve air distribution to the combustor, was run. For natural gas firing, the best basket from oil tests and the standard nozzle were used.

For TG 20 burning natural gas, changes have been made only on the nozzle and the best basket previously tested on TG 50 was utilized.

Altogether, a total of 13 different geometric arrangements, eight of them on TG 50 and five of them on TG 20, were tested.

Configurations No. 1, No. 2, No, 3, and No. 8 baskets have four elliptical secondary scoops in the dilution zone with none of them in line with the holes located in the primary zone of the combustor. These scoops in the dilution zone are positioned, referring to Fig. 3, on row No. 3.

Configurations No. 4 and No. 5 are called "rotated dilution basket" and have the four elliptical secondary scoops rotated one half pitch, so that their locations correspond to the 12-3-6-9 o'clock positions looking with flow.

The flow screen used in configuration No. 8 consists of a perforated cylinder and a neck section having eight rectangular openings aligned with the holes of the basket neck.

In configurations No. 6 and No. 7, the primary zone was rotated by maintaining the same number of holes with the same pitch, so that they were differently oriented with respect to the combustor chamber walls.

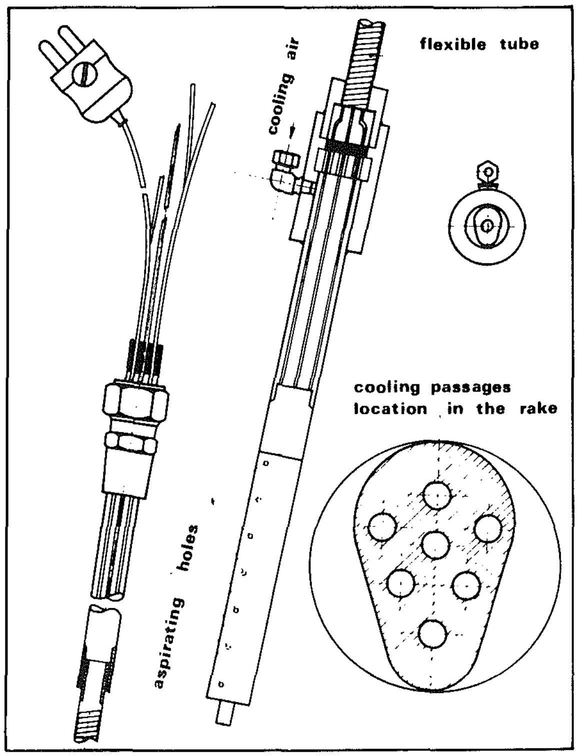

Fig. 2 Thermocouple rake

The dilution zone was completely changed, having two different rows with six circular holes each in line with the primary zone.

Figure 5 shows the gas nozzle geometries that were tested on TG 20 with a single basket configuration (items No. 1, No. 2, and No. 3 of Fig. 4).

TG 50 Results and Conclusions. For each of the eight configurations listed above, exit temperature profiles were taken over a range of operating conditions from 7 to 80 percent of base load.

Two typical temperature distributions are presented in Fig. 6, where all temperatures have been normalized at maximum temperature recorded during the test.

Figure 7 shows the normalized pattern factor for the eight tested configurations as a function of normalized combustor temperature rise, where PF is defined as

$$PF = \frac{T_{\max} - T_{\text{bot}}}{T_{\text{bot}} - T_{\text{inlet}}}$$

where

$T_{\max}$ = maximum temperature
T_{bot} = burner outlet temperature
T_{inlet} = basket inlet temperature

Both combustor temperature rise and pattern factor have been normalized by setting 1 as the highest recorded combustor temperature rise and 1 the corresponding pattern factor. Looking at Fig. 7, it can be easily concluded that the basket of configuration No. 3 shows an improvement over configuration No. 6, strictly speaking about pattern factors, from 35 percent at highest tested load to 100 percent at lowest tested load, but a substantial portion of these advantages could be lost, at high loads, in configuration No. 3, due to the 220/50 deg GPH injector.

If, for example, results from Fig. 7 are compared between configuration No. 3 and configuration No. 6 for the same NCTR = 0.76, it can be seen that

$$NPF3 = 0.55 \qquad NPF6 = 0.90$$

This means that configuration No. 3, from a pattern factor point of view, produces an improvement equal to 39 percent.

Configurations No. 5 and No. 4 are almost equivalent to configurations No. 2 and No. 3 at high load, but slightly worse at low loads.

The screen that was used in configuration No. 8 does not improve the basket operating conditions.

Comparing configurations No. 1 and No. 3, it can also be seen that burning both natural gas and distillate oil leads to the same results.

A normalized pattern factor ratio between two configurations I and J is defined as follows:

$$NPFR = \frac{NFP(I)}{NPF(J)}$$

From the pattern factor definition, for the same combustor temperature rise we can write

$$\frac{TMAX(I)}{TBOT} = NPFR * \frac{TMAX(J)}{TBOT} + (1 - NPFR)$$

This means that, for the same burner outlet temperature, the maximum temperatures, with NPFR as parameter, can be represented with the lines shown on Fig. 8.

There are some things to be specified about the measuring method and the relevant data reduction technique.

First of all, the under-airing situation in the test combustor due to the added flow resistance of the thermocouple rakes may cause less air flow through the test combustor, thus leading to a higher measured burner outlet temperature.

To investigate a possible blockage effect, the central and two side thermocouple rakes were removed from the transition duct exit, and repeated runs with configuration No. 3 were made. Data from this test and a comparison of turbine exhaust temperature readings confirmed that the blockage effect was negligible for burner outlet temperature value calculation, while the exit temperature surface shape was slightly affected.

Taking into account the results so far obtained, configuration No. 3 was chosen as the standard for the TG 50 engine.

TG 20 Results and Conclusions. As previously mentioned, five different gas nozzle configurations were run to verify the influence of the gas injection angle on the combustor exit temperature distribution over a power range from 0 to 80 percent of nominal base load power at ISO conditions.

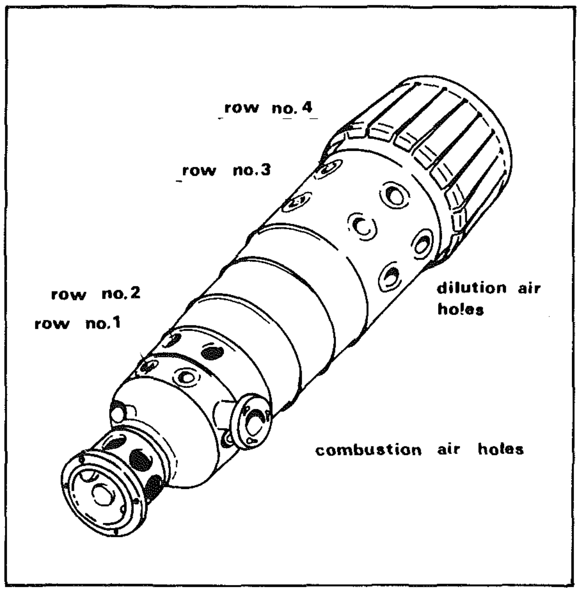

Fig. 3 TG 50 and TG 20 gas turbine combustor

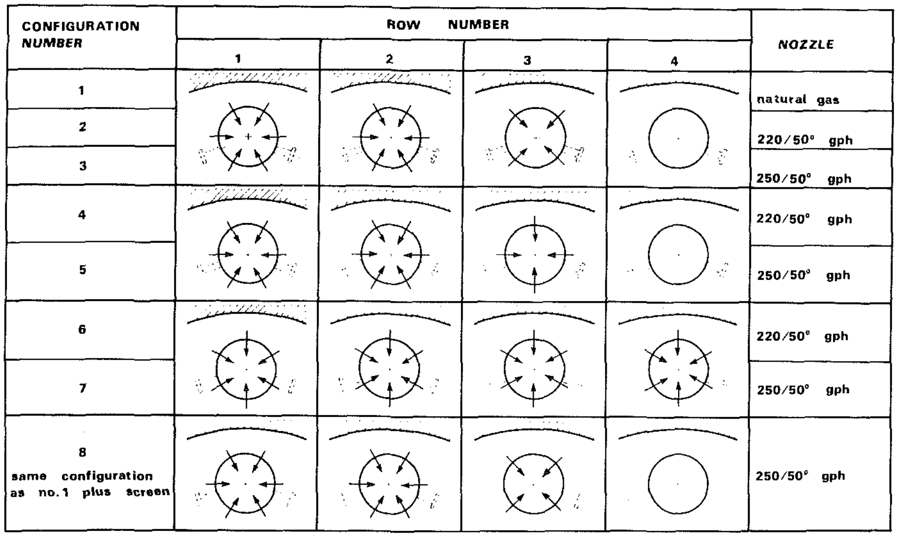

Fig. 4 Test configurations of air inlet holes through combustor

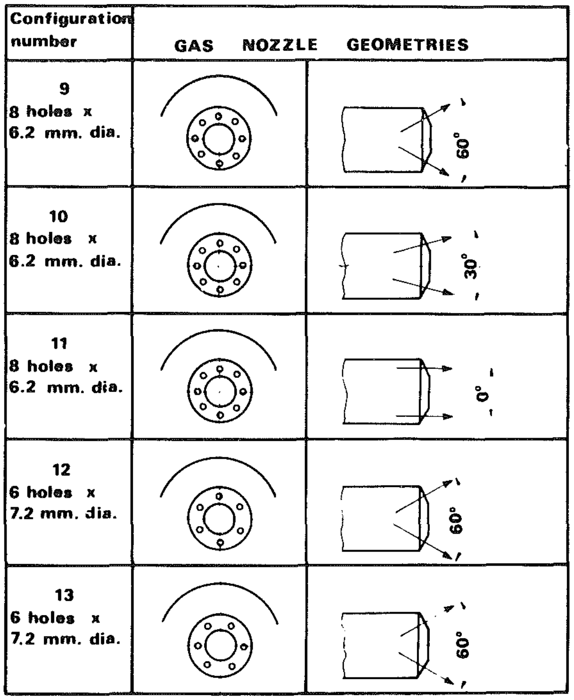

Fig. 5 Test gas nozzle configurations

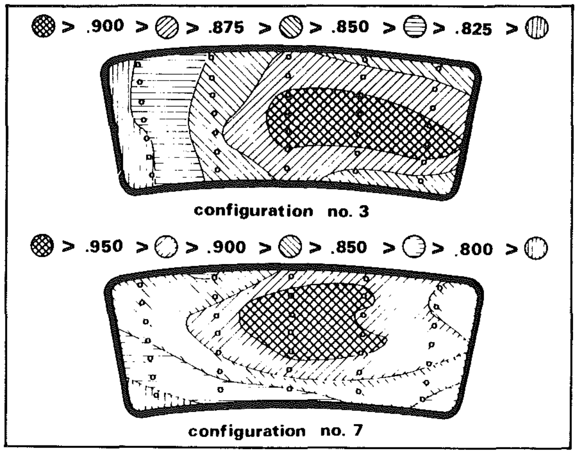

Fig. 6 Typical test results for TG 50

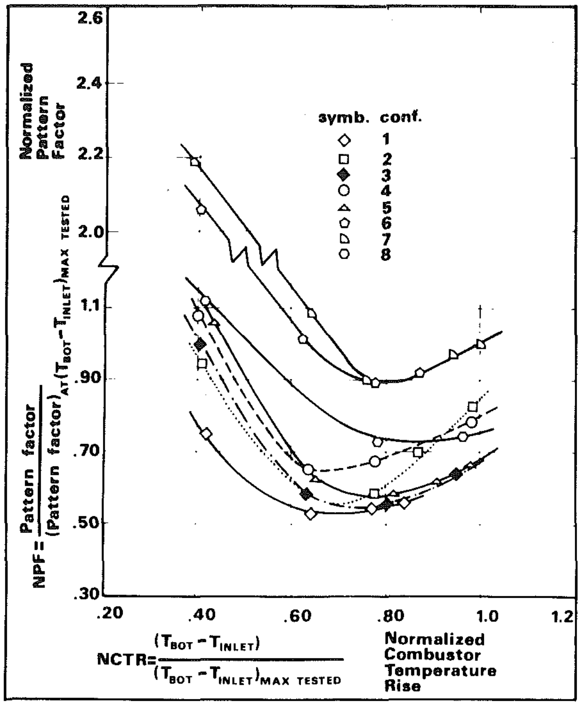

Fig. 7 TG 50 NPF versus NCTR

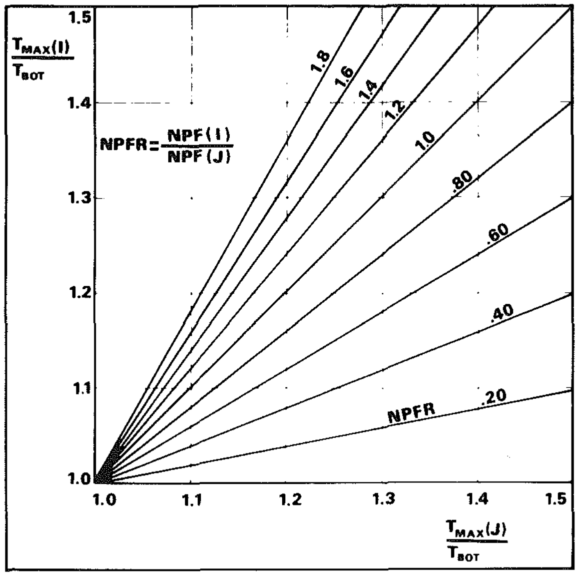

Fig. 8 T_{max}/T_{bot} relationship between configurations I and J

Figure 9 shows a typical profile measured during the tests with configuration No. 9 and the relevant central values obtained by circumferential interpolation at same radius, whereas Fig. 10 shows the pattern factor values obtained for all configurations.

In both Figs. 9 and 10 data are represented as normalized with the same technique used to normalize data for TG 50 described above. It must be specified that the represented pattern factors in Fig. 10 were calculated according to the previous definition, where T_{max} is the maximum measured temperature and T_{bot} is the recorded average value.

From Fig. 10 it can be seen that the pattern factor values relevant to the various nozzle configurations tend to cluster around a narrow band in the higher load operating range of the unit, so that no remarkable differences in performance can be depicted for the different nozzle configurations above a normalized combustor temperature rise of approximately 0.68.

Below this value, however, the measured pattern factors tend to be lower than expected, so that their trend is not consistent with the typical quasi-hyperbolic function of pattern factor versus combustor temperature rise.

For this reason, the measured temperatures of a selected number of tests were analyzed statistically. The outcome of the results obtained from circumferential plots shows that the average hottest temperatures are higher than recorded by the two central thermocouple rakes.

The results obtained by this analysis of the recorded temperature during test of configuration No. 9 show a typical trend of pattern factor versus combustor temperature rise as shown in Fig. 11.

As a conclusion, it can be said that the various modified nozzle configurations tested do not exhibit remarkable differences in their performance as regards the temperature profile when compared with the standard (No. 9) nozzle configuration.

Conclusions. In additon to tests carried out on the test rig, the full-engine tests at load added significant experience that induced us to introduce the improved tested configurations in engines already installed in plants, and to have them as standard configurations for new engines, besides giving a correlation between a test rig (one basket) and an engine in the field (all combustion system).

Ignition Process Tests

General Remarks. On both TG 50 and TG 20 the ignition sequence begins with the activation of two high-energy spark plugs fitted in two adjacent baskets. The remaining baskets are interconnected with cross-flame tubes to form two separate chains (usually called clockwise chain and counterclockwise chain).

The engine is completely ignited and then the acceleration sequence can start when the signals coming from two ultraviolet detectors fitted in the last basket of each chain are detected.

The time between the "fuel on" signal and the starting acceleration signal must be, obviously, as short as possible in order to prevent unburned fuel from entering the engine.

On both TG 50 and TG 20 tests, the basket represented in configurations No. 1 to No. 3 and the standard oil injector (250/50 deg GPH for TG 50 and 220/50 deg GPH for TG 20) shown in Fig. 12 were used.

As can be seen from Fig. 12, the "true" injector is surrounded by an "atomizing air cap," which is necessary to improve spray performance at low pressure drops across the nozzle.

Instrumentation and Tested Configuration for TG 50 and TG 20. On TG 50 three single point, grounded junction, chromel-alumel thermocouples were installed in the exit sec-

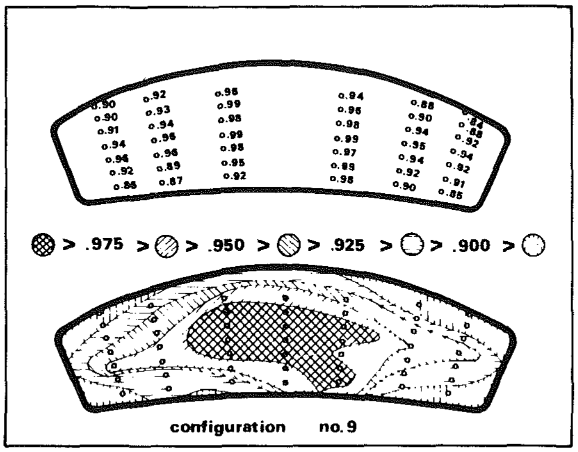

Fig. 9 Typical test results for TG 20

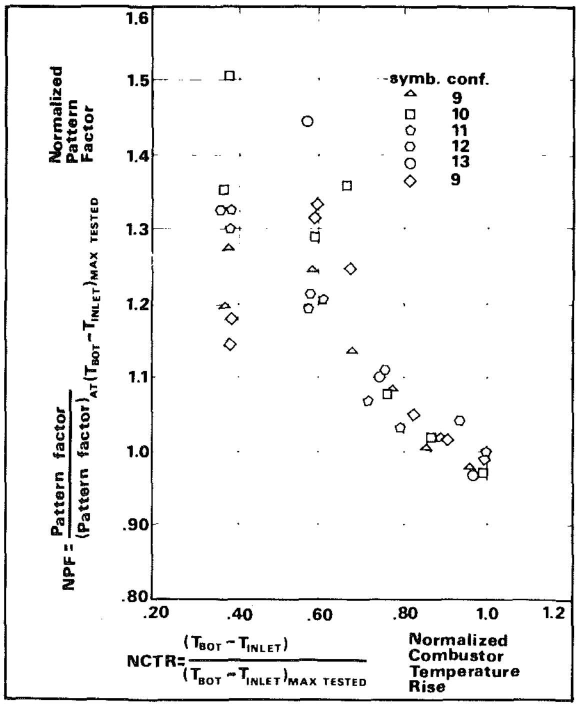

Fig. 10 TG 20 NPF versus NCTR

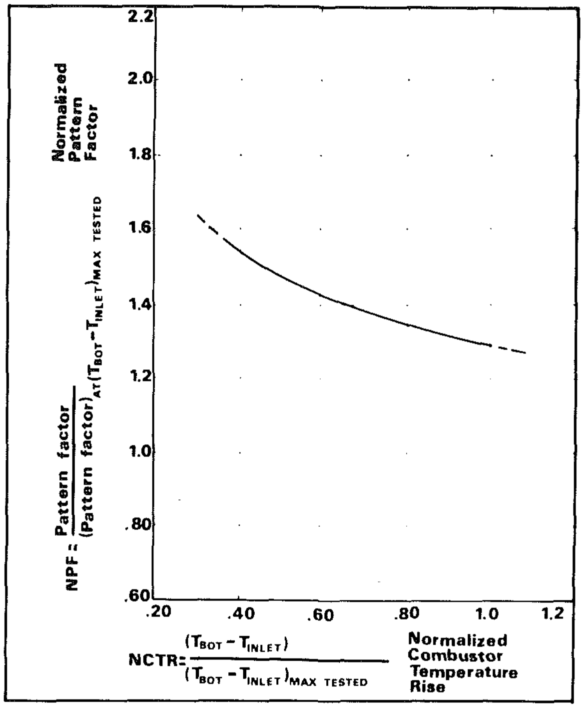

Fig. 11 TG 20 NPF versus NCTR

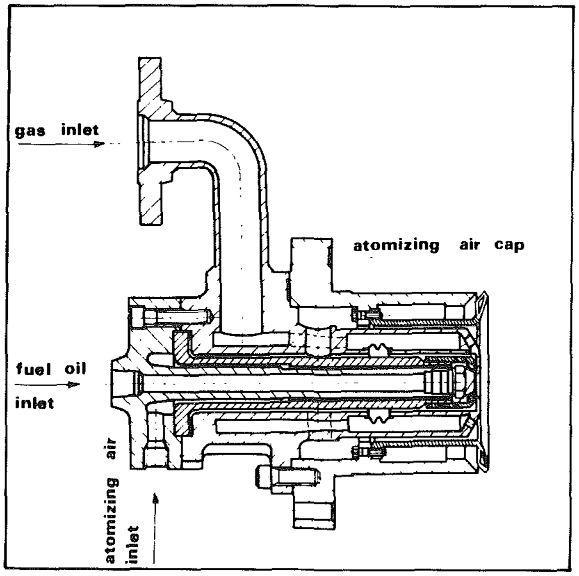

Fig. 12 Dual fuel nozzle sectional view

tion of the transition duct to measure ignition gas temperatures as shown, in detail, in Fig. 13.

The axial location of the thermocouples coincided with the rake plane used for the pattern factor evaluation. Initially only the No. 3 transition was instrumented with the ignition thermocouples, but this was later expanded to include the No. 12 transition piece.

In the standard configuration, the No. 3 engine position is located at the end of the clockwise ignition chain, while the No. 12 location corresponds to the igniter basket for the counterclockwise chain.

In addition to these temperatures (even if they do not represent the actual ignition temperature but were taken as significant for these tests), the most important engine parameters were recorded for each test such as speed, total fuel flow, fuel nozzle pressure, atomizing air pressure, ambient conditions, and fuel temperature. Engine exhaust thermocouples were replaced with a faster responding design type.

The tested configurations, from an engine point of view, included evaluations on atomizing air cap changes and different spark plugs, U/V detectors, and cross-flame tube arrangements.

All the configurations that had two distinct cross-ignition chains without an extra cross-flame tube for full circle ignition are listed below:

Configuration No.	Spark plug	U/V
1 Standard	12.13	3.4
2	17	3.4
3	16.17	3.4
4	12.13	18.1

For TG 20, the same instrumentation as per TG 50 was used, but the hardware changes were more severe than for TG 50.

In a set of tests, as will be seen in the TG 20 results section, all the baskets were equipped with spark plugs and more configurations of atomizing air caps were tested.

The outcoming results were recorded by a computer data system so as to have the most important parameters visualized in real time.

During the starting test program, an effort was made to minimize the length of each individual start in order to prevent significant warmup of the engine components, which could affect subsequent starting attempts. Since the maximum gas temperature occurred within the initial 15 s, the engine was usually manually tripped after 90–120 s into the start cycle.

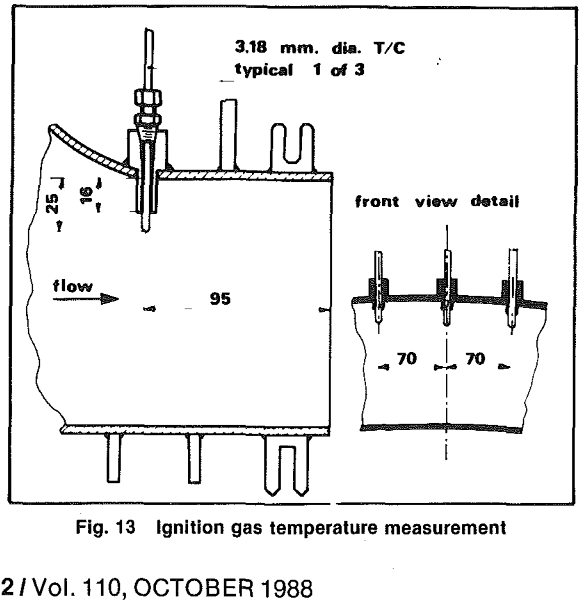

Fig. 13 Ignition gas temperature measurement

Most tests were run in the shop and then, when the "optimum" configuration was reached, one engine in the field was modified and instrumented according to the shop test to confirm the obtained results.

TG 50 Ignition Test Results and Conclusions. After the first set of tests with standard configuration No. 1, the existence of excessive gas temperature for the starting parameters originally set was realized.

Taking this remark into account, the test effort was directed and focused on reducing the ignition fuel/air ratio without sacrificing starting reliability.

The significant lowering of ignition temperature was accompanied by negative side effects; wide spreads in the thermocouples at the engine exhaust during the post ignition period were encountered with a chance of subsequent flameout further in the starting cycle.

This problem was eliminated by advancing the start of acceleration fuel ramp by 150 rpm.

In the attempt to improve ignition reliability at lower fuel flow and further reduce starting temperatures, modifications to the atomizing air caps were evaluated. In addition to the standard TG 50 four-hole atomizing air cap, a new six-hole atomizing air cap design was tested.

We were very confident to have a substantial improvement on starting reliability; in fact, experience has shown that minimum fuel/air ratio and the cross-ignition process are very sensitive to atomizing air cap geometry. Furthermore, visual observation showed that the six-hole cap had superior atomizing characteristics with smaller drops size, absence of fuel streaks, and a larger effective spray angle compared to those of the four-hole design. The results were encouraging, but not completely satisfactory: In many ignition attempts, the upper left basket of the engine was not able to light on and when flame was detected on basket No. 3 its temperature was always appreciably lower than in basket No. 12.

This why the No. 12 combustor is a spark plug position and lights on first in the sequence, while No. 3 lights last because it is a U/V basket at the end of the cross-ignition chain. The appreciable difference in measured gas temperature for the two positions is partially linked to the sequence of ignition.

To confirm that this behavior was caused by the side air changing, a test was performed in which the flow divider exit lines for No. 3 and No. 12 baskets were interchanged to determine whether possible fuel flow differences could be a contributing factor. This switch had no effect on the respective gas temperature measurements.

Then looking for a black area in the upper left of the engine, configurations No. 2, No. 3, and No. 4 were tested.

Three attempts with configuration No. 2 resulted in aborted starts with no indication of flame even in the No. 17 basket. Configuration No. 3 had a wide spread of ignition time: None

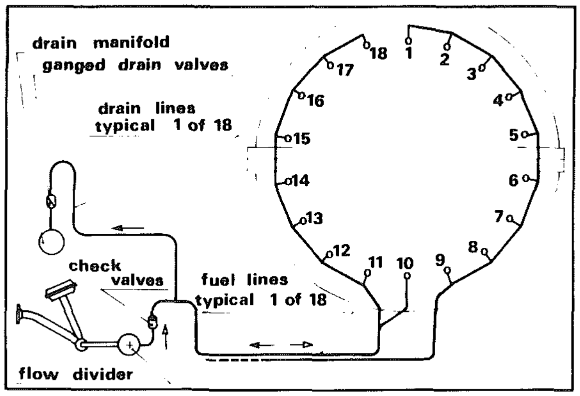

Fig. 14 TG 50 fuel oil schematic

of the baskets lit on for 15 to 20 s after ignition/fuel flow initiation, then within a second's time, the entire engine ignited with a loud noise.

Configuration No. 4 gave consistent and repeatable ignition times, with cross-ignition times for the clockwise and counterclockwise chains approximately equal.

Comparing results between configurations No. 3 and No. 4, it becomes evident that a potential problem was on the fuel flow feeding time.

Really, on TG 50, the ignition time is affected by the presence of an arrangement for draining fuel oil from the engine fuel nozzles following shutdown, as shown in Fig. 14.

Figure 15 shows the fuel filling times for the lines from flow divider to each basket.

In addition, it was found out, in two subsequent tests, that actually the lines were not completely drained of fuel following shutdown.

Although the partially filled lines would be expected to shorten the line filling time, it is evident from the above results that the drainage characteristics of the system are not readily predictable.

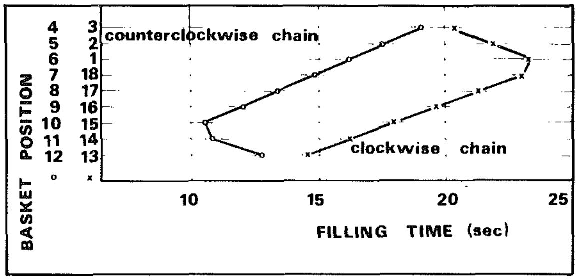

Fig. 15 TG 50 fuel line filling times

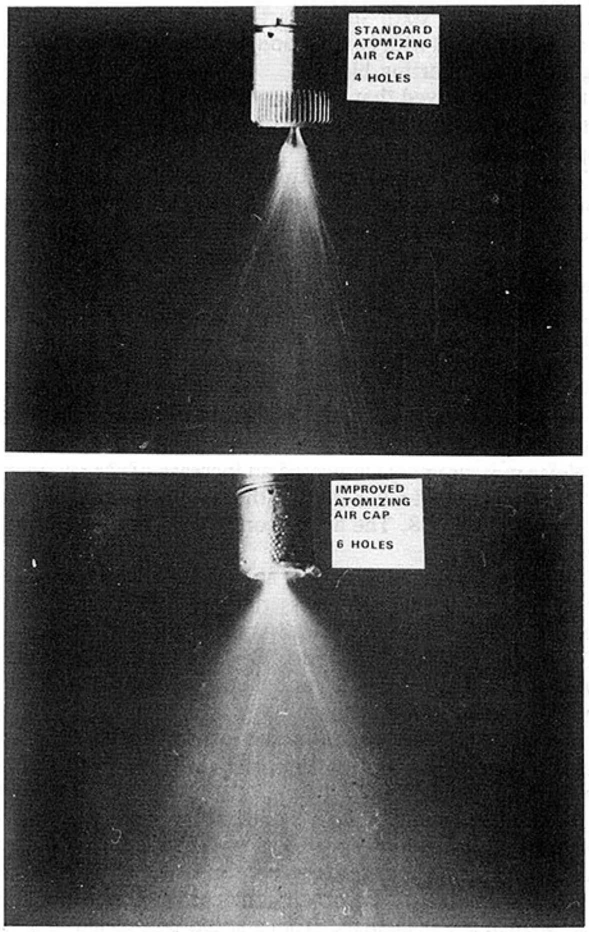

Fig. 16 Spray visualization

This trend is one reason to explain why the clockwise chain cross ignites more slowly than the counterclockwise chain. The second reason is that, when the fuel reaches baskets No. 1 and No. 18, these baskets are over-airing by the increased pressure in the combustor shell.

To avoid this problem, the fuel must feed all nozzles at the same time and to obtain this aim, on the shortest lines, volumes were added to equalize the filling times of all lines.

In such a way all the attempts were successful in shop tests,

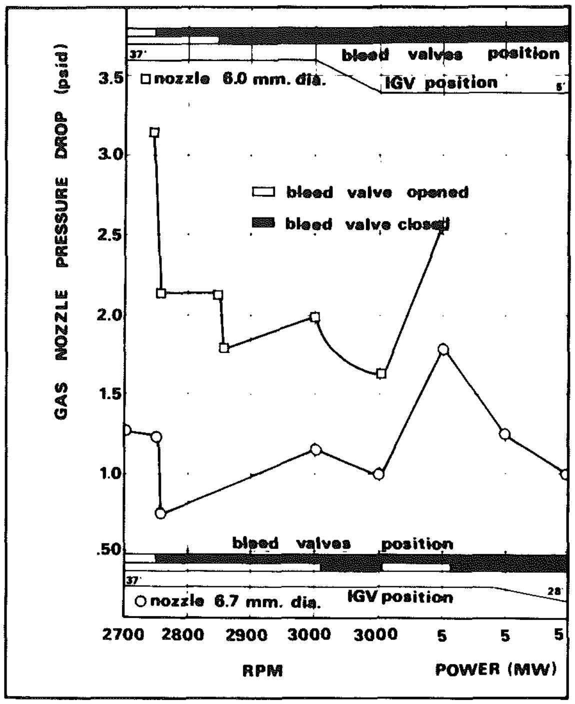

Fig. 17 Pressure drop across gas nozzle versus rpm power

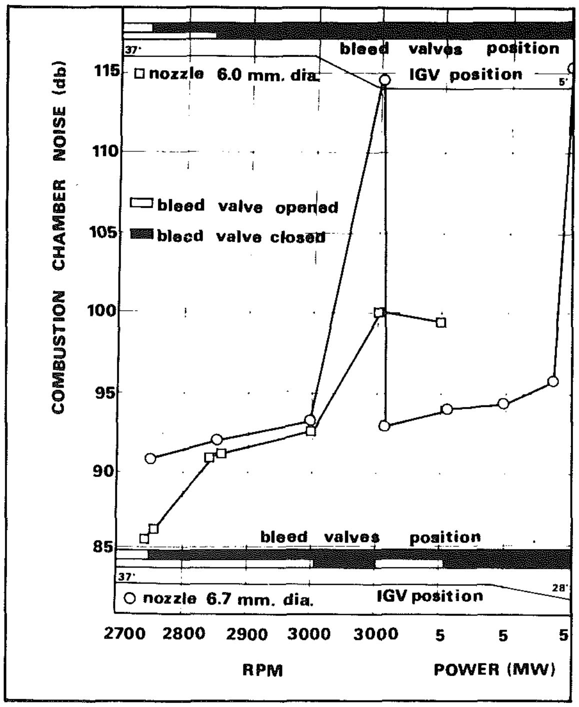

Fig. 18 Combustion chamber noise versus rpm power

and the engines in the field that use these features improved their ignition reliability considerably.

TG 20 Ignition Test Results and Conclusions. All the improvements previously tested on TG 50 were introduced to the TG 20 engine before running the first set of tests, but results were not good because all the ignition attempts were not as repeatable as in the TG 50.

It must be recalled that the original configuration for TG 20 has the spark plugs in baskets No. 3 and No. 4 and the ultraviolet detectors in baskets No. 7 and No. 8.

A second set of tests was focused to improve a new atomizing air cap; in fact on the TG 20 the liquid fuel nozzle is a 220/50 deg GPH instead of the 250/50 deg GPH of TG 50.

Five different configurations of the atomizing air cap were tested changing diameter and air injection hole direction. Results were visualized and for the standard and "the best" atomizing air cap they are shown in Fig. 16.

With the configuration using "the best" atomizing air cap, encouraging results were obtained, but some attempts failed because the last basket of each chain did not ignite. It was concluded that the over-airing problem encountered on TG 50 was more severe on TG 20.

To demonstrate this, one engine was equipped with all baskets having their own spark plug. It was found, running tests with only two adjacent igniters activated at the same time, that the spark plugs opposite baskets, which become the last one of each chain, were the most critical, from a cross-ignition point of view, independently of their position in the engine.

Moreover, these last baskets did not light on even if their own spark plugs were activated 5 s later than the spark plugs in the initial baskets, but the spark plugs would work excellent if they were pushed toward the basket axis of about 20 mm.

The interpretation of these results was that, probably, the fuel/air ratio in the last basket when only this one is not yet ignited is too low and the spray is not axial with respect to the basket.

The approach to solve the problem was, besides having a more accurate control of fuel at the same time on all the nozzles, to have a continuous cross-flame pipe connecting all baskets.

Test run in such an arrangement gave good results and the minimum fuel/air ratio for good ignition reliability, found with spark plugs fitted in baskets No. 1 and No. 2, was equal to the previous minimum fuel/air ratio found for TG 50.

It is evident that a continuous cross flame does not allow one to maintain the same control system in that the signals coming out from the U/V detectors located in baskets No. 5 and No. 6 are meaningless for the complete engine ignition.

As far as this problem is concerned a new control method was developed in that each basket temperature detected by the thermocouples at engine exhaust is instantaneously compared with the mean value; if this difference is lower than a prefixed value, the acceleration sequence can start; otherwise the engine must trip.

The results obtained in shop tests are confirmed by data coming back from all the plants where this configuration has been introduced.

Conclusions. The performed tests both at shop and their repetition in field allowed us to optimize the ignition and acceleration sequence so as to avoid overheating on these engines.

Moreover, the accumulated experience allowed us to solve quickly and without any further test campaign some ignition problems on some engines installed in field.

Operating Experience

Although the accumulated experience allows our engines to operate in quite good conditions, during the first complete startup in the field on the 12th TG 50 engine, noises from the combustor shell were heard at the moment of sixth-stage bypass closing (2800 rpm approximately). The same phenomenon, called "singing basket phenomenon" was noted, in the same plant, on the twin engine.

The phenomenon found on these two engines was never very severe and did not negatively influence flame stability (i.e., flameout has never been experienced) and its effects were only of an acoustical nature.

However, a test campaign was undertaken to investigate a phenomenon that was new in our TG 50 experience (11 turbogenerating sets operating for years without experiencing this phenomenon) and seemed to be related to differences, though small, that exist among fuel systems due to the different fuels utilized.

Therefore, measurements were taken to single out whether this phenomenon was due to factors not involving the unit, i.e., oscillations of fuel control valves or variations of the fluid-dynamic parameters controlling the combustion process, i.e., the sudden change of the axial compressor delivery pressure at the bypass closing.

Records proved that there was no remarkable fluctuation during this phenomenon even if the indications were not clear. This set of tests was performed with the original design configuration, i.e., gas fuel nozzle; eight holes, 6.7 mm diameter; IVG sequence: fully closed up to 2000 rpm; fully open at 2950 approximately rpm.

Different procedures in bleed closing were tested (i.e., increase sixth stage starting bleed closing time, engine speed change at which sixth stage starting bleed closes). All tests were unsuccessful with combustion noise appearing when closing sixth stage starting bleed.

It was also proved that the phenomenon was not connected with the axial compressor delivery pressure sudden rise, during bypass closing.

These tests were performed with the IGV locked at a prefixed angle during the complete starting sequence up to full speed in order to move away from the combustion instability by varying the fluid-dynamic conditions inside the combustor baskets.

A typical ΔP measurement across the fuel nozzle during the starting sequence is shown in Fig. 17.

The abovementioned tests showed a positive effect of the IGV change (two out of ten starts completed without combustion noise at sixth starting bleed closure) with the problem still present.

Noise measurements indicated an increase of the sound level in the 250 Hz band when closing the sixth stage starting bleed as shown in Fig. 18. The above confirmed the presence of an acoustic resonance.

Since test results, as described above, indicated the possibility of increasing the ΔP across the gas fuel nozzles, it was decided to test a new fuel nozzle with smaller gas orifices and IGV locked in a fixed position. The comparison between the two ΔP is shown in Fig. 17 and a comparison between noise levels is shown in Fig. 18.

Startups with this configuration proved to be completely noise free, confirming that the problem was solved with the new nozzle and IGV sequence.

Since a further case of combustion noise recurrence during a load rejection test was reported, it was decided to introduce a further change in the IGV sequence in order to give an extra margin for these extreme off-design operating conditions. The IGV sequence was changed from a speed-controlled to a load-controlled function.

This feature has been incorporated in the control system and with this final configuration, stability conditions are gained under any unit operating conditions encountered.

This phenomenon was classified as a "singing basket" phenomenon already known and discussed in technical literature [1, 2].

The problem is of an acoustic nature, where a small percentage of energy supports an acoustic resonance in the combustor basket and is self-sustaining since acoustic oscillations induce pulses in the combustion process, which in turn generates new and higher amplitude acoustic oscillations. It is given importance when its associated effects tend to cause flame blowout, mechanical vibrations, or other abnormal operating conditions.

Given the variety of factors that may influence this phenomenon, it is not possible to take them all into account during the design stage and therefore, the phenomenon may arise due to relatively modest deviations of the design parameters that, by contrast, gave positive results throughout the experience accumulated for the same type of engine. The possibility, however, to intervene on some of these parameters generally allows one to solve the problem in different ways.

Particularly, the phenomenon can be eliminated by increasing the fuel supply pressure and hence the ΔP across the fuel nozzle. When the mentioned ΔP is sufficiently high, the fuel flow rate will not change considerably with pressure fluctuations and therefore can be accepted from the operating standpoint. This leads to an interruption of the interactive loop between the fuel system and the combustion acoustic.

References

1 Tyndall, J., "Singing Flames," in: *Sound*, 4th ed., Lecture VI, 1883, p. 236.

2 Den Hartog, J. P., General Meeting of the Institution, London, Nov. 15, 1957.

T. T. Bowden

D. M. Carrier

L. W. Courtenay

Shell Research Limited,
Thornton Research Centre,
Chester, CH1 3SH, United Kingdom

Correlations of Fuel Performance in a Full-Scale Commercial Combustor and Two Model Combustors

A statistically designed correlation exercise has shown excellent agreement between the performance of Shell and Phillips model combustors and a full-scale Rolls-Royce Tyne combustor. These results are a strong vindication of the model combustor approach to predicting the response and performance of full-scale systems.

Introduction

Historically, the majority of work performed on aviation fuel combustion by Shell has involved the use of model combustors (Bowden and Pearson, 1983, 1984; Bowden et al., 1984). Inevitably, however, there is always some doubt whether the conclusions drawn from such studies are strictly applicable to full-scale applications in engines. For example, there is a great deal of evidence from small-scale studies that hydrogen content can provide a good prediction of fuel combustion performance (Blazowski, 1979; Bowden and Pearson, 1983, 1984; Bowden et al., 1984; Moses and Naegeli, 1979; Naegeli and Moses, 1980; Naegeli; et al., 1981). However, a recent computer study by Moses (1983) utilizing full-scale data of Gleason and Bahr (1979a, 1979b) concluded that hydrogen content was no better than the traditional combustion-related inspection properties.

To permit the effects of scale to be studied, a full-scale combustor facility, based on a Rolls-Royce Tyne combustor, was constructed. This report describes the correlation exercise carried out to determine the agreement between results obtained in two model combustors and the full-scale system.

Experimental

Two model combustors were used in the exercise; a Shell-developed model combustor and a Phillips 2″ combustor. This latter device developed by Phillips Petroleum Company has been used extensively in the USA for fuel combustion studies (Moses and Naegeli, 1979; Naegeli and Moses, 1979; Schirmer and Quigg, 1965). Its use in the present program therefore provides a useful cross reference with much North American data. Schematic diagrams of the Shell and Phillips combustors are given in Figs. 1 and 2. The Tyne combustor is illustrated in Fig. 3. Rig instrumentation and operational details have been fully described elsewhere (Bowden and Pearson, 1984; 1985; Bowden et al., 1984).

The three combustors were operated over a range of conditions in a statistically designed experiment incorporating two

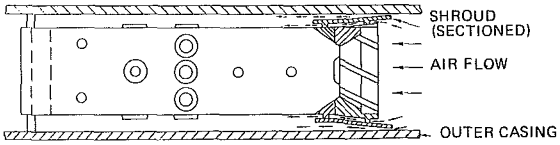

Fig. 1 Shell model combustor

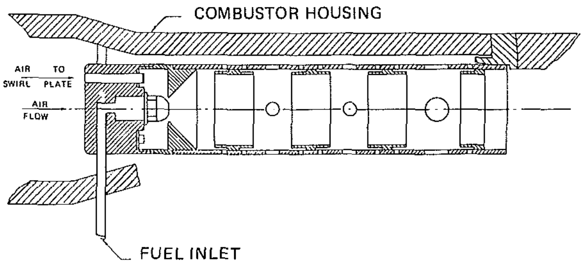

Fig. 2 Phillips 2″ model combustor

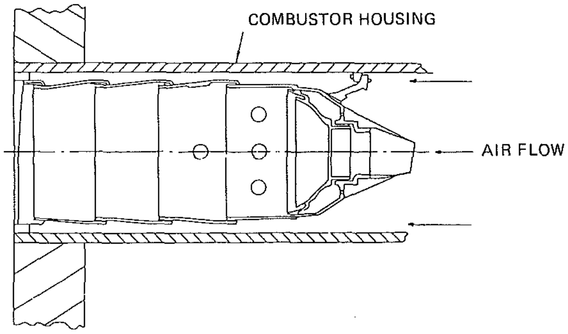

Fig. 3 Rolls-Royce Tyne combustor

Contributed by the Gas Turbine Division of THE AMERICAN SOCIETY OF MECHANICAL ENGINEERS and presented at the 32nd International Gas Turbine Conference and Exhibit, Anaheim, California, May 31–June 4, 1987. Manuscript received at ASME Headquarters February 6, 1987. Paper No. 87-GT-89.

Table 1 Matrix of test conditions used for combustor correlation exercise

Air/Fuel Ratio	Pressure, bar	Inlet Air Temperature, °C
60/1	10	350
60/1	12	350
60/1	10	500
80/1	10	350

Table 2 Combustion-related inspection properties of test fuels

Fuel	(H) Content, %w	Aromatic Content, %v	Smoke Point, mm	Naphthalene Content, %v	Description
Reference Jet A1	13.81	19.0	24	2.5	Reference fuel, well predicted by hydrogen content.
North Sea LGO	13.74	18.2	26	3.45	Light gas oil. Well predicted by hydrogen content
BS3	13.06	23	17	0.5	Kerosine blending stream. Well predicted by hydrogen content.
Jet A1	14.19	9.8	26	0.5	Low aromatic content Jet A1. Well predicted by hydrogen content.
High naphthalene kerosine	13.70	19.1	20	4.5	Specially blended high naphthalene content kerosine. Unpredicted by hydrogen content.
North Sea MGO	13.30	23.5	17	10.1	Medium gas oil. Unpredicted by hydrogen content.
BS6	13.75	6.7	23	<0.1	Kerosine blending stream. Overpredicted by hydrogen content.

Note : LGO and MGO are similar to No. 2 Fuel Oils (ASTM D396)

levels of pressure, temperature, and air/fuel ratio, as detailed in Table 1. These conditions were chosen to provide the most severe Tyne combustor operating conditions available within the limitations of the blowdown reservoir supplying the high-pressure air. The seven fuels selected for the program, whose combustion-related inspection properties are presented in Table 2, reflect the broadest spectrum of properties and performances, as observed in earlier work, to be found among practical kerosine fuels (Bowden and Pearson, 1985). This was considered a more valid approach, in the context of aviation gas turbine performance, than the use of esoteric research fuels such as the gas oil-like ERBS blends.

Measurements of combustion performance in terms of flame radiation and exhaust soot concentrations were made on the fuel set in each combustor at each operating condition. All test fuel runs were bracketed by runs with the reference Jet A1 and the results nondimensionalized in the following manner:

$$\text{Normalized Flame Radiation, NFR} = \text{Rt/Rr} \qquad (1)$$

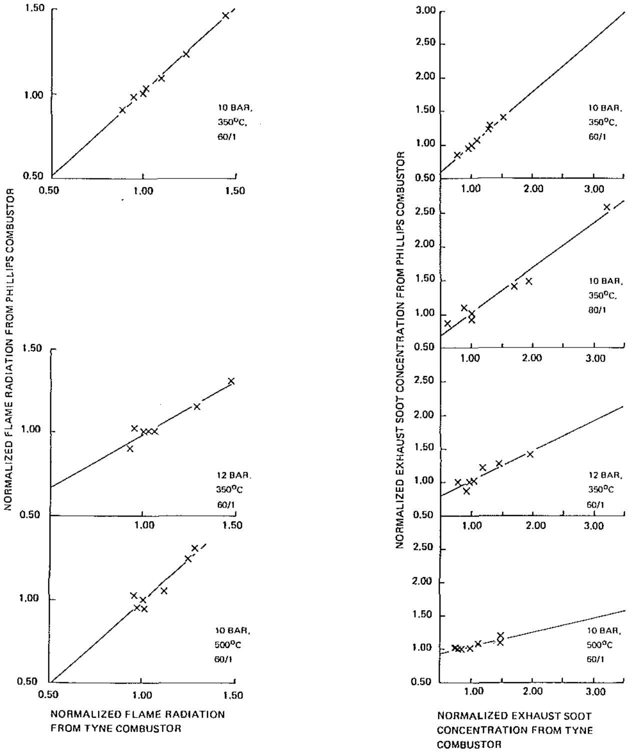

Fig. 4 Correlation between Tyne combustor and Phillips model combustor results

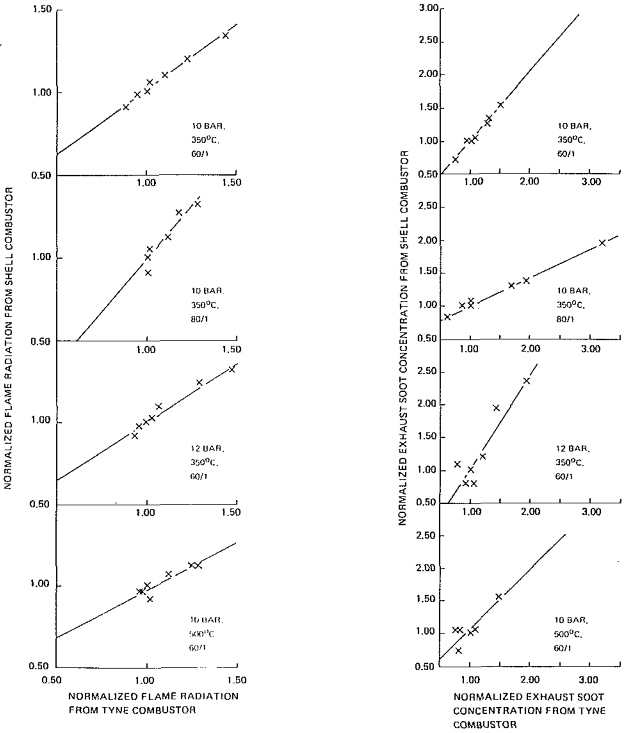

Fig. 5 Correlations between Tyne combustor and Shell model combustor results

where Rt = radiation from test fuel; Rr = radiation from reference fuel.

$$\text{Normalized Exhaust Soot Concentration} = \text{ESt/ESr} \qquad (2)$$

where ESt = exhaust soot from test fuel; ESr = exhaust soot from reference fuel; the reference fuel figure is the average of the two bracketing values.

Table 3 Results of combustor correlation exercise

Test condition	Fuel	Normalized radiation (Tyne)	Normalized soot (Tyne)	Normalized radiation (Phillips)	Normalized soot (Phillips)	Normalized radiation (Shell)	Normalized soot (Shell)
10 bar 350°C 60/1 AFR	Reference Jet A1	1	1	1	1	1	1
	North Sea LGO	1.02	1.09	1.03	1.06	1.06	1.06
	BS3	1.23	1.31	1.23	1.28	1.20	1.35
	Jet A1	0.89	0.76	0.91	0.85	0.91	0.72
	High naphthalene kerosine	1.10	1.28	1.09	1.23	1.10	1.26
	North Sea MGO	1.44	1.51	1.46	1.41	1.34	1.54
	BS6	0.95	0.95	0.98	0.96	0.98	1.00
10 bar 350°C 80/1 AFR	Reference Jet A1	1	1	1	1	1	1
	North Sea LGO	1.02	1.00	N.D.	0.93	1.05	1.06
	BS3	1.18	1.94	N.D.	1.49	1.27	1.39
	Jet A1	1.00	0.62	N.D.	0.85	0.91	0.82
	High naphthalene kerosine	1.12	1.68	N.D.	1.40	1.12	1.30
	North Sea MGO	1.29	3.21	N.D.	2.60	1.32	1.95
	BS6	1.0	0.87	N.D.	1.10	1.00	1.00
12 bar 350°C 60/1	Reference Jet A1	1	1	1	1	1	1
	North Sea LGO	1.03	0.80	1.01	1.00	1.03	1.09
	BS3	1.29	1.45	1.15	1.27	1.24	1.95
	Jet A1	0.93	0.92	0.90	0.88	0.92	0.81
	High naphthalene kerosine	1.06	1.20	1.01	1.20	1.10	1.20
	North Sea MGO	1.47	1.94	1.30	1.41	1.32	2.36
	BS6	0.96	1.06	1.02	1.01	0.98	0.80
10 bar 500°C 60/1	Reference Jet A1	1	1	1	1	1	1
	North Sea LGO	0.97	0.84	0.95	1.00	0.97	1.04
	BS3	1.24	1.48	1.24	1.09	1.13	1.56
	Jet A1	1.01	0.80	0.95	1.00	0.92	0.75
	High naphthalene kerosine	1.12	1.11	1.05	1.07	1.07	1.05
	North Sea MGO	1.28	1.49	1.30	1.20	1.13	1.56
	BS6	0.96	0.77	1.02	1.00	0.97	1.05

N.D. - Not determined

Table 4 Values of Pearson correlation coefficients *r* and Spearman correlation coefficients ρ: Shell and Phillips model combustors versus Rolls-Royce Tyne combustor

Operating condition	Shell combustor				Phillips combustor			
	Flame radiation		Exhaust soot		Flame radiation		Exhaust soot	
	r	ρ	r	ρ	r	ρ	r	ρ
10 bars, 350°C, 60/1 AFR	0.993	1.00	0.993	0.991	0.997	1.00	0.996	1.00
10 bars, 350°C, 80/1 AFR	0.954	0.972	0.997	0.973	-	-	0.981	0.883
12 bars, 350°C, 60/1 AFR	0.980	1.00	0.923	0.680	0.969	0.775	0.929	0.940
10 bars, 500°C, 60/1 AFR	0.930	0.764	0.913	0.673	0.947	0.721	0.885	0.906

Results

The results are presented in Table 3; individual linear best-fit correlations between the Phillips and Shell combustors and the Tyne combustor are shown in Figs. 4 and 5. Additionally the data were analyzed statistically in terms of Pearson correlation coefficients *r* and Spearman rank correlation coefficients ρ. The Pearson correlation coefficient is a measure of the scatter of the data about the best-fit correlation line. Thus when comparing sets of data from two combustors, the closer the value of the coefficient is to 1, the less is the scatter of the data about the best-fit straight line and the better the data are represented by that line. The Spearman rank correlation coefficient gives further insight into the relationship between two data sets; the closer this coefficient is to unity, the greater the similarity between the ranking of fuel combustion performance in the two combustors that are being compared. The results of this analysis are presented in Table 4. In the context of the present program, values of either correlation coefficient greater than 0.755 indicate better than 95 percent confidence. Clearly there is generally excellent correlation between the two model combustors and the Tyne.

The data were further analyzed in an attempt to identify the optimum form of the fit between the model combustors and the Tyne. The quantitative results of this exercise are lengthy but for the purposes of this paper can be summarized by stating that in all cases a linear correlation was found to be most appropriate. This finding yields a further dimension to the model combustor approach insofar as in principle only two determinations are required to define fully the relationship between model and full-scale combustor at a given operating condition.

Conclusions

1 Model combustors such as the Shell and Phillips designs can accurately predict fuel performance within full-scale combustors.

2 The linear correlations between the model and full-scale combustors examined mean that, for any given set of performance tests, the applicability of model combustor results to the full-scale case can be verified by a minimum of measurements.

3 Although combustor operating conditions and design influence the magnitudes of differences among fuels, their performance rankings are unaffected. Furthermore the results imply that a common mechanism of soot formation occurs within all three combustors.

4 Since work performed in model combustors can provide a valid alternative to full-scale testing, the capability of the Shell aviation combustion rig is greatly increased by the resultant ability to carry out those extended duration tests that would be otherwise precluded by air supply limitations.

Future Studies

All combustors examined so far have incorporated pressure-jet atomizers. However, it is possible that other forms of fuel preparation (e.g., air-assisted atomization, vaporization) may influence fuel performance in a different way and this area is currently being addressed.

Acknowledgments

The authors wish to thank the management of Shell Research for permission to publish this paper and the British Ministry of Defence for their support in this work. Acknowledgment is also due to Mr. A. F. McNab for undertaking the statistical analysis of the data and to Mr. R. M. Schirmer of Phillips Petroleum for provision of the Phillips combustor and related drawings.

References

Blazowski, W. S., 1979, "Dependence of Soot Production on Fuel Blend Characteristics and Combustion Conditions," ASME Paper No. 79-GT-155.

Bowden, T. T., and Pearson, J. H., 1983, "The Influence of Fuel Composition Upon Soot Emissions and Flame Radiation in a Model Gas-Turbine Combustor," *International Conference on Combustion in Engineering*, Vol. 2, I. Mech. E. Conference Publication 1983-3, Paper No. C70/83.

Bowden, T. T., and Pearson, J. H., 1984, "The Effect of Hydrocarbon Structure Upon Fuel Sooting Tendency in a Turbulent Spray Diffusion Flame," ASME *Journal of Engineering for Gas Turbines and Power*, Vol. 106, pp. 109–114.

Bowden, T. T., Pearson, J. H., and Wetton, R. J., 1984, "The Influence of Fuel Hydrogen Content Upon Soot Formation in a Model Gas Turbine Combustor," ASME *Journal of Engineering for Gas Turbines and Power*, Vol. 106, pp. 789–794.

Bowden, T. T., and Pearson, J. H., 1985, "The Effect of Fuel Composition Upon Combustion Performance in a Rolls Royce Tyne Combustor," ASME Paper No. 85-GT-39.

Gleason, C. C., and Bahr, D. W., 1979a, "Evaluation of Fuel Character Effects on the J79 Engine Combustion System," AFAPL-TR-79-2015.

Gleason, C. C., and Bahr, D. W., 1979b, "Evaluation of Fuel Character Effects on the F101 Engine Combustion System," AFAPL-TR-79-2018.

Moses, C. A., 1983, "Fuel Effects on Engine and Combustion Performance and Durability," presented at the CRC Symposium on Combustion Characteristics of Aviation Turbine Fuels, Dayton, Ohio, May 13, 1983.

Moses, C. A., and Naegeli, D. W., 1979, "Fuel Property Effects on Combustor Performance," ASME Paper No. 79-GT-178.

Naegeli, D. W., and Moses, C. A., 1980, "Effect of Fuel Molecular Structure on Soot Formation in Gas-Turbine Engines," ASME Paper No. 80-GT-62.

Naegeli, D. W., Dodge, L. G., and Moses, C. A., 1981, AFLRL-158.

Schirmer, R. M., and Quigg, H. T., 1965, "High Pressure Combustor Studies of Flame Radiation as Related to Hydrocarbon Structure," Phillips Petroleum Company Research Division Report 3952-65R.

Experimental Method for Combustion Efficiency Calculation in a Reheat Duct

A. Cadiou
Office National d'Etudes et de Recherches
Aérospatiales,
Châtillon Cedex, France

An efficient method for the experimental measurement of the combustion efficiency in a reheat duct has been developed at ONERA. Such a method is useful because numerous reheat tests are necessary to study the effect of geometry and flow characteristics on reheat performances. Static pressure measurements along the duct and gas sampling in its outlet cross section are the basis of this downstream-to-upstream method. Experimental results with a tri-annular V-gutter flame holder are presented. These results are also used for comparison with theoretical two-dimensional calculations applied to reheat ducts that ultimately may reduce the number of experiments necessary for the development of reheat combustion chambers.

Introduction

The perennial aerothermal performance goals for aircraft reheat systems are:

- to increase combustion efficiency and temperature in the outlet section;
- to increase combustion stability;
- to reduce the pressure loss of the stabilizer when there is no combustion.

The scope of this paper is limited to the study of combustion efficiency. For given upstream kerosine and air flow conditions (the turbine outlet conditions), the efficiency is a function of only two parameters, the geometry of the flame holder and the length of the reheat duct. The aim of manufacturers is to reduce the length of this duct without increasing the losses on the combustion efficiency and the stabilizer pressure loss by using better-suited stabilizers. In order to help the design of future reheat systems, it is useful to evaluate the effect of flame holder geometry on the reheat duct length necessary to have a determined value of the combustion efficiency. This information requires many experimental tests using different shapes of flame holder.

Therefore, an efficient experimental method for the combustion efficiency measurement is a useful tool for the manufacturer. This paper deals with a new method for this measurement.

The conventional experimental method to obtain combustion efficiency is gas analysis. This method leads to the use of probes that take samples of combustion products. The sample is analyzed and the combustion efficiency is calculated from the concentration of carbon monoxide, carbon dioxide, total unburned hydrocarbons, and nitric oxides. However, this experimental method would require a great number of probes that would perturb the aerodynamics of the flow. The use of a single probe requires the possibility of axial, radial, and angular displacements, but the technology of such a probe is not obvious. However, the main problem remains the long time necessary for data acquisition: For each axial position, several samples have to be picked into the very cross section of the flow in order to calculate a mean value of the efficiency and this operation has to be repeated all along the duct.

The method presented here only requires static pressure taps along the reheat duct and a gas sampling probe in the outlet cross section. The use of pressure taps for the combustion efficiency measurement is standard for a few manufacturers. However, their calculation is initiated with the upstream flow conditions. So, they have to evaluate the aerodynamic drag of the stabilizer in order to calculate efficiency downstream. This drag depends on combustion [1] and is difficult to quantify. With a probe in the outlet cross section of the reheat duct, the calculation is a downstream-to-upstream one and this drawback does not exist.

In the first part of this paper, the method will be presented; in the second one the test equipment will be described; in the third one results will be analyzed and finally compared, in the last part, with results of a two-dimensional calculation.

Method for Efficiency Calculation

Calculation of this efficiency is made by analyzing the effect of combustion on static pressure in a reheat duct of constant area cross section. Typical axial evolution of static pressure measured at the duct wall is presented in Fig. 1 [1].

The fast pressure drop through the flame holder characterizes the rate of blockage. Just downstream of the trailing edge of the baffle, the pressure slightly increases but the maximum remains below the upstream pressure level and the discrepancy is the pressure loss of the flame holder.

Contributed by the Gas Turbine Division of THE AMERICAN SOCIETY OF MECHANICAL ENGINEERS and presented at the 32nd International Gas Turbine Conference and Exhibit, Anaheim, California, May 31–June 4, 1987. Manuscript received at ASME Headquarters February 6, 1987. Paper No. 87-GT-90.

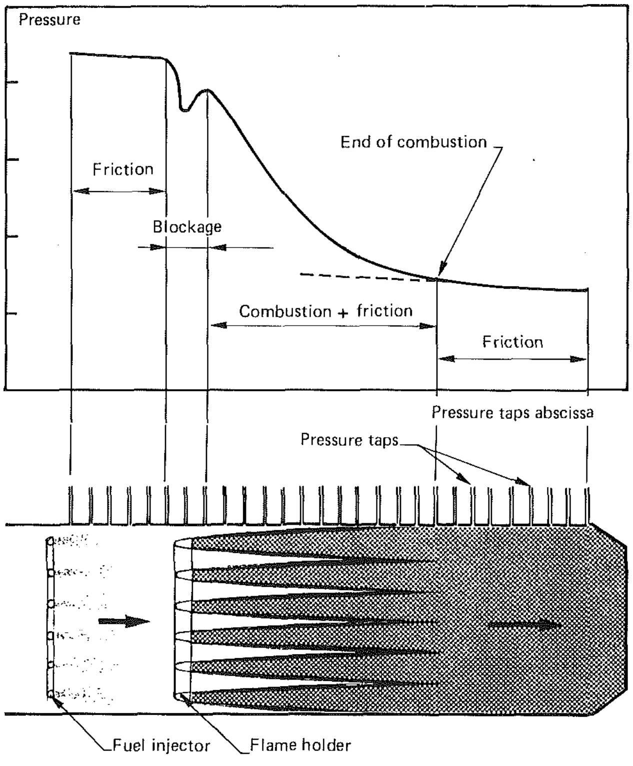

Fig. 1 Typical pressure drop in a reheat channel

Beyond the flame holder, the most important pressure drop corresponds chiefly to the combustion process into a subsonic constant-cross-section flow, and to a far lesser degree, to the friction along the pipe.

When the combustion is complete, the only process for pressure decrease is the friction; then, the longitudinal pressure gradient has a low and constant value. The upstream prolongation of the last linear pressure drop (dashed line) may be used to locate the "end" of the combustion as indicated in Fig. 1.

Therefore, pressure measurements are a good means for the evaluation of the maximum length necessary for combustion, the analysis of these results also allows calculation of mean combustion efficiency as a function of the distance from the flame holder as it is presented below.

In order to have a good reference at the outlet of the reheat duct, its length is chosen long enough so that combustion is completely terminated before the outlet section of the duct and uniform conditions prevail in this section. In this outlet section, the temperature value is too high for a thermocouple so a probe is used to measure temperature. This probe takes a sample of hot gases; it is cooled to avoid chemical reactions. The sample is transferred from the probe to analytical instruments through a heated line to avoid condensation. Nondispersive infrared analyzers are used for continuous monitoring of CO and CO_2; $C_x H_y$ and NO_x are respectively determined by means of a flame ionization detector and chemiluminescence. A calculation leads to the equivalence ratio ϕ_0, the combustion efficiency, and the temperature. The calculation is the following:

- the total carbon species measured lead to ϕ_0;
- the theoretical combustion temperature T_{th} is tabulated [2];
- the combustion efficiency is equal to:

$$\eta = 1 - A[I_e\mathrm{CO} - I_e\mathrm{CO}(T_{th})] - B\, I_e\mathrm{CH}_4 - C[I_e\mathrm{NO}_x - I_e\mathrm{NO}_x(T_{th})]$$

$$I_e\mathrm{CO} = \frac{28}{28.94}\ |[\mathrm{CO}]|\ \frac{1+\alpha}{\alpha}\ 10^3$$

$$I_e\mathrm{CH}_4 = \frac{16}{28.94}\ |[\mathrm{CH}_4]|\ \frac{1+\alpha}{\alpha}\ 10^3$$

$$I_e\mathrm{NO}_x = \frac{46}{28.94}\ |[\mathrm{NO}_x]|\ \frac{1+\alpha}{\alpha}\ 10^3$$

$$A = 2.34 \times 10^{-4} + 1.8 \times 10^{-8} T_1$$

$$B = 1.148 \times 10^{-3} + 3.75 \times 10^{-8} T_1 + 0.375 \times 10^{-10} T_1^2$$

$$C = 0.481 \times 10^{-4} + 0.25 \times 10^{-8} T_1 \quad (T_1: {}^\circ\mathrm{C});$$

- the temperature is calculated with the formula

$$H_i(T, \phi_0) - H_i(T_1, \phi_0) = \eta[H_i(T_{th}, \phi_0) - H_i(T_1, \phi_0)]$$

This method to calculate T has been compared to another one where T is obtained from the calculation of the enthalpy of all the different combustion products. The temperature obtained with this second method is equal to the previous one.

Now, using this reference value it is possible to obtain the mean value of combustion efficiency η in a cross section of abscissa x. This is presented below.

Consider the volume of fluid limited by the duct wall and by the two cross sections, x and 3 (3 is the outlet section). The following equations prevail:

mass conservation

$$\rho(x)A\ V(x) = \rho_3 A\ V_3 = \dot{m} \tag{1}$$

axial momentum balance

$$\dot{m}(V(x) - V_3) + (p(x) - p_3 A - F = 0 \tag{2}$$

where F is the action of the wall on the fluid caused by friction.

conventional equation of state

$$\frac{p}{\rho} = \frac{R}{m} T \qquad (R = 8.3136\ \mathrm{J/K}) \tag{3}$$

Nomenclature

A = duct area
H_i = stagnation enthalpy
k = turbulent kinetic energy
l = length of the reheat duct
$\dot{m}$ = mass flow rate
M = Mach number
m = molecular mass
p = static pressure
r = radial coordinate
T = temperature
V = velocity
x = axial coordinate
Y = fuel mass fraction
α = kerosine-air mass flow rate ratio
ϵ = turbulence dissipation rate
η = combustion efficiency
ρ = density
ϕ = equivalence ratio: ϕ_1 = equivalence ratio of the combustor; ϕ_2 = equivalence ratio of reheat; $\phi_0 = \phi_1 + \phi_2$
$|[X]|$ = molar concentration of X in humid combustion gases

Subscripts

1 = inlet section of the combustor
2 = inlet section of the reheat duct
3 = outlet section of the reheat duct

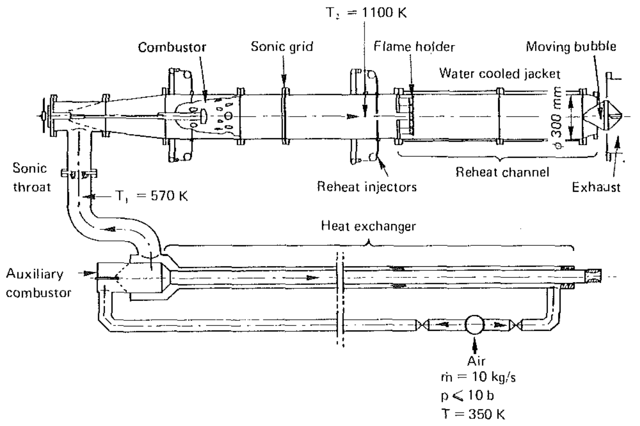

Fig. 2 Schematic view of the experimental setup

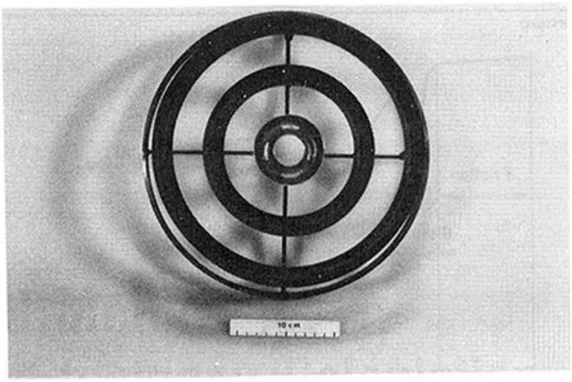

Fig. 3 Photograph of a flame holder tested

The slope of the pressure drop due only to friction is assumed to have a constant value K, which may be determined from momentum balance in the downstream part of the channel, when the combustion is over, and when the velocity of the flow has reached a constant value: $F=(p(x)-p_3)A$ or $F=K(x-l)A$ (K: Pascal/meter; l: meter). Equation (2) becomes then

$$\begin{aligned}&\dot{m}(V(x)-V_3)+(p'(x)-p_3)A=0\\ \text{with}\quad &p'(x)=p(x)-K(x-l).\end{aligned}\qquad (4)$$

The different steps for calculation are the following:

- equations (1) and (3) lead to V_3 (p_3 is measured and T_3 has been calculated);
- equation (4) leads to $V(x)$ ($p(x)$ and $\dot{m}$ are measured);
- equations (1) and (3) lead to $T(x)$.

The combustion efficiency is given by the following formula:

$$\eta(x)=\frac{H_i(T(x),\,\phi)-H_i(T_1,\,\phi)}{H_i(T_{th},\,\phi)-H_i(T_1,\,\phi)}$$

where $H_i(T,\,\phi)$ is the stagnation enthalpy of the combustion products at the temperature T, for an equivalence ratio equal to ϕ; T_{th} is the theoretical combustion temperature; T_1 is the air temperature at the inlet of the combustor. The values of these enthalpies are tabulated in [2]. The whole calculation is iterative because the molecular mass of the combustion products m depends on the combustion efficiency.

The following assumptions have been made to write equations (1) and (2): As quoted above, the static pressure is assumed to be constant in each cross section and a single wall pressure measurement is required in each section; this assumption has been verified several times and is perfectly correct as long as the curvature of the streamlines is small; however, wall pressure measurement is not sufficient near the recirculation zone, which is only a very small part of the reheat duct length.

The flow characteristics are assumed to be a function of x only since we study the one-dimensional flow equivalent to the actual one and the velocities and temperatures used in equations (1) and (2) are average values [3]. Calculation of the flow with combustion in such a reheat channel has been performed by Dupoirieux [4]. These calculations allow to estimate, in each particular case, the length from the flame holder for which this hypothesis is not valid. As stated above this length is small compared to the total length of the duct.

The present method for efficiency calculation is a downstream-to-upstream calculation which necessarily involves measurements in the outlet section. This might be considered as a drawback and does not exist in an upstream to downstream calculation. However, this last case involves knowledge of the drag of the flame stabilizer and this drag may be obtained only in tests without combustion.

Experimental Setup

The experiment was conducted in the rig shown schematically in Fig. 2. The reheat channel consists of a cylindrical chamber, 300 mm in diameter, equipped with a water-cooled jacket and containing reheat injectors and flame holder.

However, in order to model a turbojet engine afterburner, the incoming flow is successively preheated and vitiated by means of a heat exchanger and a combustor.

The air obtained at the outlet of the compressor [mass flow rate $\dot{m}=10$ kg/s; pressure $p\leq 10$ bars (10^6 Pa); temperature $T=350$ K] is first heated, without vitiation, up to 570 K, using a counterflow classical heat exchanger. Then, preheated air is fed to a burner that gives realistic vitiation and temperature of the flow (about 1100 K) at the inlet of the reheat channel. A sonic grid at the outlet of the combustor improves the uniformity of the velocity profile and improves the combustion efficiency of the combustor because of the higher pressure level, which is necessary in order to have sonic orifices. The distance between this grid and the kerosine injectors for reheat combustion has been experimentally determined in order to have a flat temperature profile. The reheat injectors of counterflow type are annular shaped; they have many holes (diameter 0.5 mm); kerosine is pneumatically sprayed and complete vaporization is obtained approximately 100 mm downstream. The distance from the injector to the flame holder is equal to 250 mm. One of the flame holders tested is shown in Fig. 3; it is made of three annular **V** gutters.

The air mass flow rate is measured with a sonic throat and the kerosine mass flow rates with turbine flow transducers. The temperature immediately upstream of the reheat injectors is measured with a chromel-alumel thermocouple. This thermocouple is not located between the injectors and the flame holder because the injection of kerosine and its vaporization may cause a decrease of the temperature, which is a function of the equivalence ratio. In the outlet section of the reheat channel a gas sampling probe is placed in the middle of the channel. The species gas concentrations are measured, and the equivalence ratio is calculated. Its value is compared with the ratio of kerosine and air mass flow rates. In some cases, when the flow is not quite homogeneous, the location chosen for the probe is the one where the best agreement between the two equivalence ratios exists. The species concentrations measured there must correspond to mean values. The gas species continuously analyzed are: CO_2 and CO with infrared analyzers; C_xH_y with a flame ionization detector; NO_x by means of chemiluminescence. These measurements give the reference values at the reheat duct outlet and static pressure measurements will give the axial evolution of efficiency.

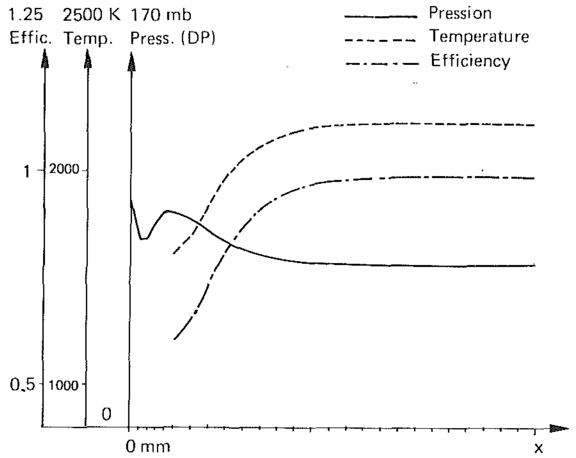

ig. 4 Graphic results of a test: variations of $p'(x)$, $T(x)$, and $\eta(x)$ versus he distance from the flame holder x

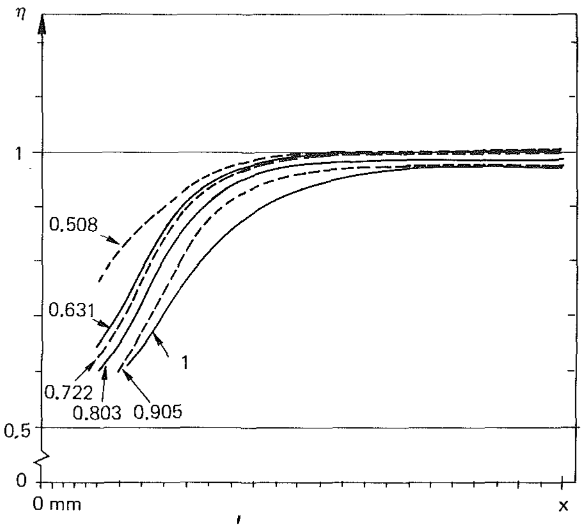

Fig. 5 Combustion efficiency as a function of distance from the flame holder x for different values of the overall equivalence ratio and for $T_2 = 1100$ K, $M_2 = 0.16$, $\dot{m}_{air} = 2.5$ kg/s, $\phi_2 = 0.22$

Twenty-seven pressure taps have been welded all along a generating line of the reheat channel. The pressure measurement must be very accurate to avoid a scattering in the values of the efficiencies calculated so we use the same pressure transducer with a SCANIVALVE commutator for all the pressures. The pressure transducer measures the difference between $p(x)$ and the atmospheric pressure. This transducer is convenient for pressure difference lower than 350 mb (5 Psi).

All the measurements are recorded with a computer, which calculates the values of the temperature and of the combustion efficiency all along the reheat channel. The duration for measurement and calculation is approximately 25 s. After each test, the graphs $\eta(x)$, $T(x)$, and $p(x)$ versus time appear on a screen. These experimental conditions allow the study of numerous flame holder configurations.

In the following section the results obtained with the three-V-gutter flame holder (Fig. 3) are summarized.

Experimental Results

The size of the experimental reheat duct is downscaled compared with actual engines. Its diameter is only 300 mm, but the temperature and Mach number of the flow during the tests are the same as in actual operating conditions.

The following results have been obtained with the three-V-gutter flame holder. These gutters are located in the same plane, and have the same height as shown in Fig. 3.

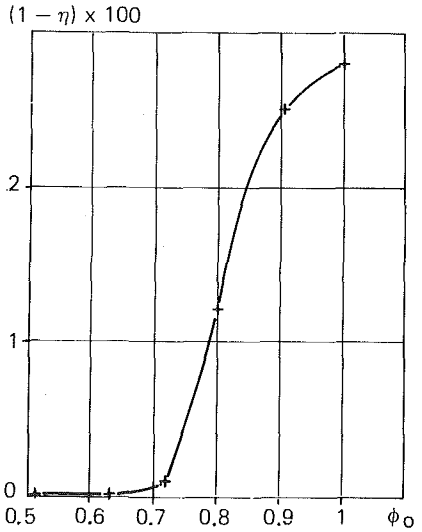

Fig. 6 Combustion inefficiency in the outlet section of the reheat duct as a function of the overall equivalence ratio for $T_2 = 1100$ K, $M_2 = 0.16$, $\dot{m}_{air} = 2.5$ kg/s, $\phi_2 = 0.22$

The experimental test conditions were as follows: temperature upstream of the baffle 1100 K; Mach number upstream of the baffle 0.16; air mass flow rate 2.5 kg/s; outlet pressure 1 atm.

Figure 4 represents the results given by the computer for an equivalence ratio equal to 0.22 for the main combustor and to 0.58 for the reheat. The different graphs represent the combustion efficiency, the temperature of the hot gases, and the pressure difference $p'(x) - p_a$ ($p'(x)$ is the static pressure without its friction term).

With the conditions given above, it is interesting to study the variation of the combustion efficiency as a function of the kerosine mass flow rate. Figure 5 shows the graphs $\eta(x)$ obtained for different values of the overall equivalence ratio ϕ_0, from 0.5 to 1. The kerosine mass flow rates of the main combustor and of the reheat are used for the calculation of ϕ_0. These graphs show the increase in length necessary to reach practically an asymptotic value of the combustion efficiency for values of ϕ_0 close to stoichiometric value. Combustion is shorter for low equivalence ratios.

In Fig. 6, the combustion inefficiency $(1-\eta) \times 100$ is represented as a function of ϕ_0 in the outlet section of the reheat duct (about 950 mm downstream of the flame holder). The increase of ϕ_0 from 0.5 to 1 leads to an increase of the inefficiency. Heterogeneous mixing of air and kerosine is probably the reason that the inefficiency increases. Because, for values of ϕ_0 below 1, in the flow there may be zones with an equivalence ratio over 1 and in these zones the combustion efficiency decreases.

This is an example of the studies conducted on the experimental setup. Another, more general type of test is the effect of the flame holder geometry on the combustion efficiency, and the aim of this research is to correlate the different curves $\eta(x)$ with a geometric parameter in order to reduce the number of tests necessary for the design of a new flame holder. Interesting results for the manufacturer have been obtained; some examples of the different shapes of flame holder tested are shown in Fig 7.

Comparison With Theoretical Calculations

The results of these experiments are also used for com-

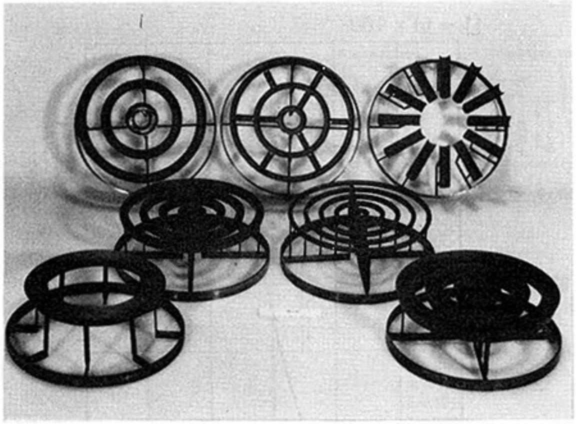

Fig. 7 Photograph of different flame holders tested

parison with the results of calculations in reheat ducts [4]. This allows the improvement of the theoretical models introduced in the numerical calculation.

The method used to solve the general equations is a finite volume semi-implicit two-dimensional (axisymmetric) method. The closing condition on turbulence is obtained by means of k-ϵ model. The model used for turbulent combustion is an "eddy break-up" model [5]. It is well suited to a premixed flame where the chemical characteristic time is very short compared to the turbulent mixture characteristic time; the turbulence actually controls the chemical reaction rate. It is valid only for equivalence ratios smaller than 1, which is the case of reheat ducts. With this model, the fuel reaction rate is written as

$$\dot{w} = -C_{\mathrm{comb}} Y(Y_e - Y)$$

where $C_{\mathrm{comb}} = C_{K0}\ \epsilon/k$; C_{k0} has a constant value; Y_e is the fuel mass fraction in the premixed flow upstream of the baffle. This calculation can be applied with conditions corresponding to an experimental test.

In the calculation the values of a few constants, such as C_{K0}, have to be evaluated. Experimental results are used in this way. Figure 8 represents experimental and calculated combustion efficiency variations for the same conditions as for Fig. 4. The value of C_{K0} chosen for the calculation is 3.4. It seems to be an accurate value.

When this value has been determined, direct comparison between tests and calculation is possible in order to know the validity of this constant and the limits of the turbulent combustion model.

However, it must be noticed that our experimental measurements only lead to average values. At O.N.E.R.A. there exist other test facilities less oriented toward industrial research and where local measurements of temperature and velocity are performed by means of laser velocimetry and C.A.R.S. (coherent antistoke Raman spectroscopy) and their results are also used for the validation of numerical calculations.

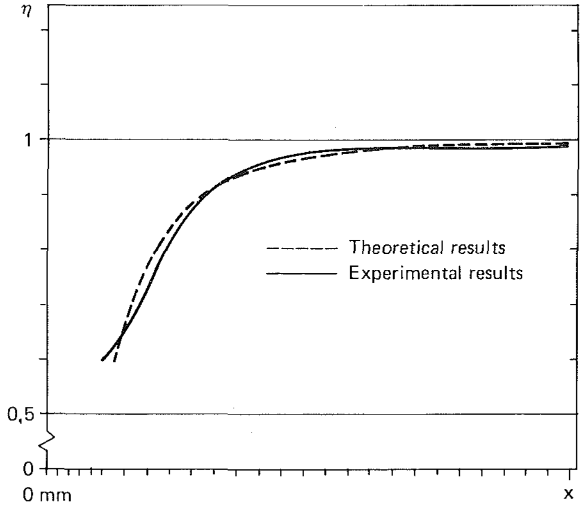

Fig. 8 Values of experimental and calculated combustion efficiency as a function of the distance from the flame holder for $T_2 = 1100$ K, $M_2 = 0.16$, $\dot{m}_{\mathrm{air}} = 2.5$ kg/s, $\phi_2 = 0.22$, $\phi_0 = 0.803$

Conclusion and Further Developments

The method presented here for the combustion efficiency measurement, oriented toward the needs of industry, is used for comparison of different reheat systems.

Because of the short time required for each test, many configurations can be tested, and the effect of parameters such as temperature upstream of the baffle, vitiation of the upstream flow, velocity of the flow, equivalence ratio of reheat, and geometry of the flame holder can be determined.

The aim of this work is to find the best combustion efficiency with a tradeoff between the length of the duct and the pressure drop induced by the flame holder. This optimization also results in experimental correlations particularly about the effect of geometric parameters in order to determine the size of a combustion reheat system for a preliminary design.

Acknowledgments

This work has been sponsored by the "Société Nationale d'Etudes et de Construction de Moteurs d'Aviation."

References

1 Barrère, M., and Mestre, A., "Stabilisation des flammes par des obstacles," presented at the Combustion Colloquium, Cambridge University, England, Dec. 1953.

2 Mc Intyre, R. W., and Metcalf, H., "Tables of the Thermodynamic Properties of Kerosine-Air Combustion Products up to 6000°K," Advanced Propulsion Research Group, Bristol Siddeley Engines Limited, Report No. 5060, July 1962.

3 Propulsion and Energetic Panel—Working group 14, "A Suitable Averaging Technic in Nonuniform Internal Flows," AGARD A. R. 182, 1982.

4 Dupoirieux, F., "Prédiction d'ecoulements turbulents réactifs," AGARD-CP No. 353.

5 Spalding, D. B., "Mixing and Chemical Reaction in Steady Confined Turbulent Flames," presented at the 13th Symposium (International) on Combustion, Salt Lake City, Aug. 1970.

Measurement of Temperature and Velocity Vectors in a Combusting Environment Using Low-Cost Probes

M. B. Khalil[1]
Assoc. Mem. ASME

E. G. Plett
Professor.

Department of Mechanical
and Aeronautical Engineering,
Carleton University,
Ottawa, Ontario, Canada K1S 5B6

Radial traverses were made to measure temperature distributions and velocity vectors in an atmospheric pressure test combustor burning gaseous fuels with heating values in the low-medium range. Temperature was measured using an aspirated pyrometer probe. Velocity vectors were determined from measurements of a five-hole probe (a two-hole probe was used prior to the five-hole probe to determine whether the flow was directed upstream or downstream). The measuring traverse was carried out across the entire diameter at ten sections along the combustor (which was specially designed to allow in insertion of probes at the ten axial sections, through three holes at 120 deg from each other around the circumference). These measurements were repeated for ten runs that incorporated a variety of operating conditions of the combustor. Temperature measurements were validated by application of the first law of thermodynamics. Velocities were validated using the principles of conservation of mass and angular momentum. The analysis showed that temperatures can be measured to within 10°C in a combusting environment of gaseous fuels for which the temperature is in the vicinity of 1500 K, by an aspirated pyrometer. The axial velocity component can be measured to an average accuracy of 7.6 percent using five-hole probes. The radial component of velocity can be obtained within ±5 percent in most of the combustion space. The accuracy of measuring the circumferential velocity component could not be validated, partly because it was extremely small. Also, in order to validate it, some independent means of establishing its origin is needed. In this case, due to the lack of precision in fabricating the combustor and the holes for air admission, as well as due to the extremely small value of this component in the present study, it was not possible to establish the reliability of the measured values. The study recommends the use of aspirated pyrometers and five-hole probes in a combusting environment, provided that the yaw angle does not exceed 60 deg and the three components of velocity have comparable magnitudes. The probes should be made as small as possible and frequent purging should be practiced in their operation to avoid errors due to blockage of probes' passages by water or dust particles. These probes were chosen for this application because of the ease with which they can be used, as well as for cost considerations.

Introduction

Evaluation of the performance of combustors and combustion equipment requires the determination of the values of some thermodynamic and flow properties, such as temperature and velocity. The accuracy of measuring these quantities determines the level of accuracy of evaluating the performance of the combustor under consideration.

Probes inserted into the flow to measure temperature and velocity have been used longer than any other means for determining such quantities. Such probes, however, by their very nature, produce errors in the flow properties due to the disturbances resulting from their insertion. The area through which the flow passes changes due to the presence of probes resulting in errors in measuring static pressure. Also, in recirculating flows, the disturbance resulting from probes' insertion may travel upstream and change the entire flow behavior from that of the undisturbed flow. In some combusting flows, probe materials might act as a catalyst (or as a chemical sink for some species) for the chemical reaction and thereby change the reaction kinetics of the flow. These disadvantages, however, do not outweigh the usefulness of appropriate probes as a

---

[1] Present address: Asecor Ltd., Manotick, Ontario, Canada.

Contributed by the Gas Turbine Division of the THE AMERICAN SOCIETY OF MECHANICAL ENGINEERS and presented at the 32nd International Gas Turbine Conference and Exhibit, Anaheim, California, May 31-June 4, 1987. Manuscript received at ASME Headquarters February 6, 1987. Paper No. 87-GT-91.

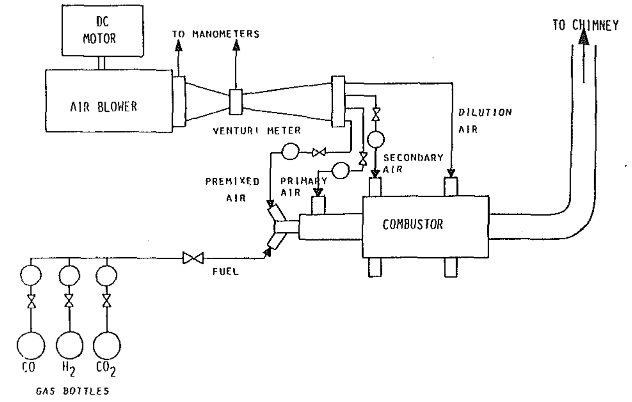

Fig. 1 Test rig layout

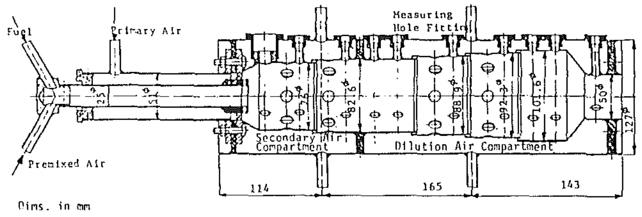

Fig. 2 Cross section of combustor assembly

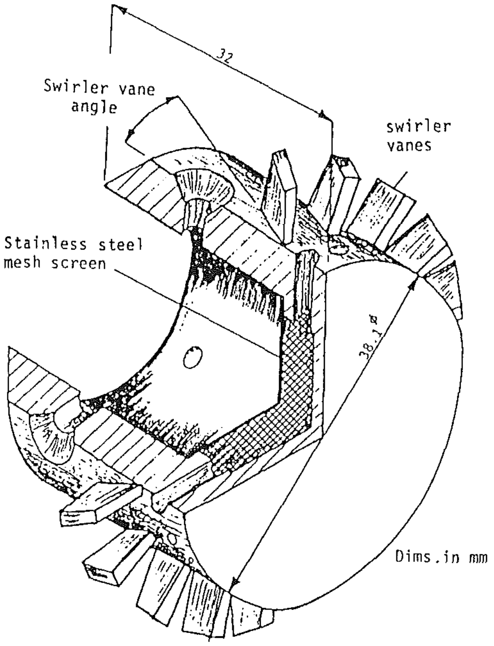

Fig. 3 Swirler-injector piece

reasonably accurate means of experimental measurements, since they are easy to use and of low cost compared to other more sophisticated means of measurements.

Experience in applying probes for flow measurements has resulted in improved probe designs, and therefore increased accuracy of their measurements. It is generally recommended that the smallest possible probe be used and the materials that might react with the flow be avoided [1].

The design and pertinent features of the probes used to measure temperatures and velocity vectors are described with sample results of the measurements given. The validity and accuracy of these measurements are evaluated in terms of their conformity to the conservation laws. The approach used in applying the conservation laws is outlined in the paper.

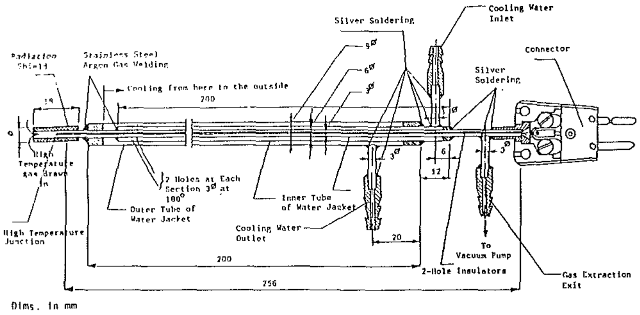

Fig. 4 Details of suction pyrometer

Experimental Setup and Instrumentation

Test Rig. The experimental setup consisted primarily of a test combustor, fuel supply, and air supply (Fig. 1). The combustor was designed to allow insertion of probes into the combustion space through three holes spaced 120 deg apart, located at ten axial sections along the combustor. Air was admitted separately at the four zones of the combustor (premixed, primary, secondary, and dilution), with a typical distribution of air among the zones of 10 percent premixed, 10 percent primary, 40 percent secondary, and 40 percent dilution. Several other features in the design of the combustor can be found in [2]. The exit section of the combustor was connected to the laboratory's exhaust system.

Figure 2 shows a cross-sectional drawing of the combustor assembly and Fig. 3 shows a schematic view of the swirler-injector piece mounted in the combustor. The fuel used for this investigation was supplied by blending its constituents (to resemble low-medium heating value gas) from commercial gas bottles. The three components of the fuel, CO, CO_2, and H_2, were metered separately before being mixed and admitted to the combustor. The air needed for combustion was supplied by a centrifugal blower of capacity of up to 1857 m^3/h at 3100 rpm. The blower was driven by a variable speed d-c motor, which provided a means of controlling the air flow rate. The total air flow rate was measured by a venturi meter mounted on the exit flange of the blower.

The air leaving the venturi was divided into two parts. The first part was directed to flow through six flowmeters en route to being admitted to provide the premixed, primary, and normally the secondary air. The second part was normally directed to provide the dilution air. The design of the combustor allowed for changing the proportion of air admitted at the various zones. The air flow rate to the dilution zone was determined by subtracting the summation of the flow through the six flow meters from the total air flow rate through the venturi meter.

Aspirated Pyrometer Probe. A radially traversing aspirated pyrometer probe was used to measure the temperature at the ten axial measurement sections. The probe was made of stainless steel with all welds in the flame region performed in argon (inert gas) atmosphere. The probe was water cooled to withstand the high temperature of the combustion gases. The probe surface temperature was maintained below 400°C (the safe operating temperature of stainless steel for this application). Figure 4 shows a cross-sectional drawing of the details of the probe. The thermocouple was made of platinum-platinum 13 percent rhodium (type R) wires, with a diameter of 0.2 mm. A suction pump was used to draw the high-temperature gases over the hot junction of the probe, through the ceramic shield. The thermocouple wires, insulators, and ceramic shield were supplied by Omega Engineering Inc.

It should be noted that the cooling of the suction pyrometer

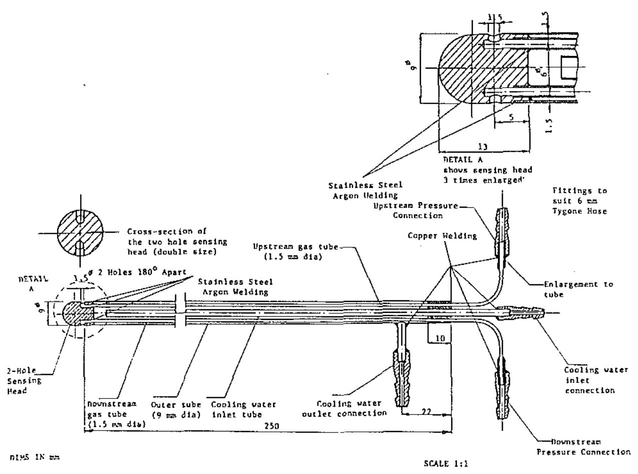

Fig. 5 Two-hole probe

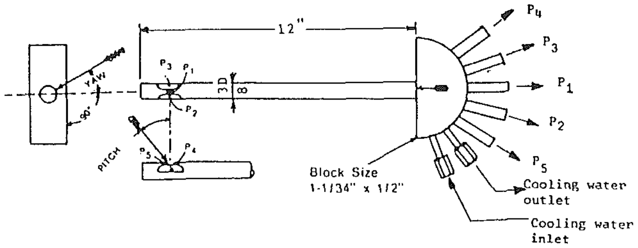

Fig. 6 Layout of the five-hole probe: main dimensions, pressures, and angles

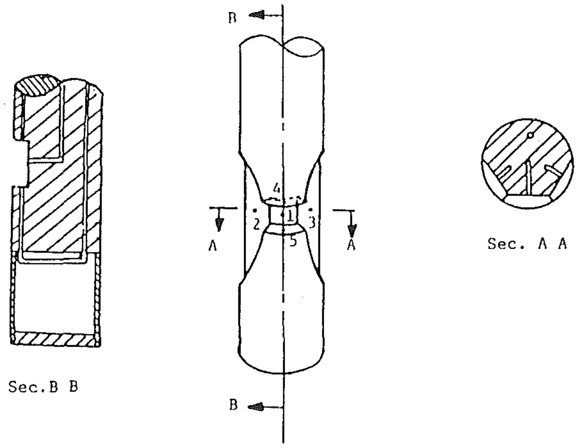

Fig. 7 Detail of five-hole probe tip

occurred in the portion of the probe that had the stainless steel jacket, and that the hot junction was in a region that was not cooled, but was surrounded by a ceramic radiation shield. Therefore, the probe should give the true reading of the local gas temperature without being affected by cooling of the probe surface or radiation to the cold liner walls. Appendix A contains a brief description of how the aspirated pyrometer probe was used to measure the gas temperature in the combustion region during this study.

It should also be mentioned here that the ceramic shield mounted on the aspirated pyrometer probe did not experience any noticeable deterioration in its mechanical properties over the period of this study (which extended over a period of two years, corresponding to service of about 500 h). This may be attributed to the precaution taken of allowing the cooling fluid to flow through the probe before it was inserted into the combustion space, which helped to reduce the thermal stresses resulting from rapid expansion of the metal parts near the joint where the ceramic shield is attached. It is advisable, in this context, to apply the "ceramic cement," to hold the ceramic shield attached to the metal portion of the probe, as close as possible to the end of the cooling jacket of the probe to avoid excessive thermal stresses that could cause crumbling of the ceramic radiation shield. Another factor that may have contributed to the life of the aspirated pyrometer probe was the clean gas combustion of this study. Purging with compressed air or nitrogen might be required in a slagging environment such as encountered with burning of liquid or solid fuels. Using steam as a coolant medium can also help in this case to prevent solidification of the fuel droplets or particles in the probe passages, because of the higher temperature allowed.

Two-Hole Probe. The two-hole probe was needed to determine the flow direction (i.e., up- or downstream) and to identify the recirculation zone in the combustion space. This is necessary because the five-hole probe cannot distinguish whether the flow is traveling upstream or downstream. Figure 5 shows a cross-sectional drawing of the two-hole probe that was designed and fabricated for this work. The probe simply has two holes located 180 deg apart around its circumference, with which it identifies the flow direction by allowing the pressure differential across the two holes to be measured, while the two holes are aligned parallel to the combustor axis. This probe was also made of stainless steel and was water cooled to withstand the high temperature inside the combustor.

Five-Hole Probe. A stainless steel, water-cooled, five-hole probe manufactured by United Sensors and Control Corporation (type DA-375) was used to obtain the velocity vector at the designated measurement sections along the combustor. Figure 6 shows a schematic drawing of the layout and dimensions of the probe, and Fig. 7 shows the details at the measuring tip of the probe. The five holes were located on a prism-shaped section in such a manner as to allow for measuring of the yaw angle, pitch angle, static pressure, and total pressure. The probe had its measuring tip along its stem, which simplified its insertion into the combustion space. The probe was rotated about its axis until the pressure difference ($P_2 - P_3$) was zero to allow measurement of the yaw angle by a protractor whose center was at the probe axis attached to the manual traverse unit. The location of the measuring tip along the probe stem allowed for a nulling operation of the probe without introducing error with respect to the top location, relative to the position where the measurement was required.

The procedure followed in measuring the velocity vector in the combustor region with the two-hole and five-hole probes is summarized in Appendix A. It should be mentioned that the five-hole probe was calibrated by the manufacturer and the calibration was checked before using it in this work. The check of the calibration was carried out using a setup consisting of an air supply, a plenum chamber with a nozzle attached, and the five-hole probe mounted on a device that allowed three degrees of freedom to the probe axis. Further detail can be found in [2], relating both to the calibration of the five-hole probe and to its use in conjunction with the two-hole probe.

Evaluation of Measurements

Temperature. Experiments were carried out on the test combustor with a range of operating conditions while making radial traverses of measurements of temperature and velocity vector, at each of the ten measuring sections located along the combustor [3]. A gas sample was taken from the gases flowing through the aspirated pyrometer for gas analysis. However, due to the limited sensitivity of our gas partitioner (Fisher 1200), the analysis was limited to CO_2, N_2, H_2, O_2, and CO.

Table 1 Summary of parameters considered for the various runs of the study

Run #	Swirler vane angle	$\dot{m}_f$	HV	HV	Fuel Composition			$\dot{m}_{air}$	Air Percentage at Various Zones %•				A/F
	°	kg/h	MJ/m^3	MJ/kg	CO%	CO$_2$%	H$_2$%	kg/h	Pmd	Pri	Sec	Dil	kg/kg
1	60	1.995	10.89	15.13	45.6	9.2	45.2	76.08	10	10	40	40	38.14
2	60	1.995	10.89	15.13	45.6	9.2	45.2	76.08	10	10	26.7	53.3	38.14
3	60	1.995	10.89	15.13	45.6	9.2	45.2	76.08	10	10	53.3	26.7	38.14
4	60	2.394	10.89	15.13	45.6	9.2	45.2	76.08	10	10	40	40	31.78
5	60	1.336	10.89	15.13	45.6	9.2	45.2	50.72	10	10	40	40	38.14
6	60	3.73	7.68	7.43	32.2	36.2	31.6	76.08	10	10	40	40	20.4
7	60	4.079	6.14	5.16	25.7	49.0	25.3	76.08	4	10	43	43*	18.6
			6.62	5.61	27.7	44.9	27.4						
8	0	1.995	10.89	15.13	45.6	9.2	45.2	76.08	4	10	43	43	38.14
		1.336											56.95
9	30	1.336	10.89	15.13	45.6	9.2	45.2	76.08	4	10	43	43	56.95
10	45	1.336	10.89	15.13	45.6	9.2	45.2	76.08	4	10	43	43	56.95

* *This is the final air distribution(2).*
• Pmd = Premixed, Pri = Primary, Sec = Secondary, Dil = Dilution

Table 2 Results of average temperature at first section of the combustor as calculated from energy balance and measurements of aspirated pyrometer

Method of obtaining av. temp.	Run #									
	1	2	3	4	5	6	7	8	9	10
Energy balance	1210	1210	1210	1206	1200	755	851	1117	1117	1076
Measurements of aspirated pyro.	1219	1218	1200	1198	1190	747	841	1107	1110	1170

The minimum concentration that could be measured with this gas chromatograph was 0.01 percent for CO and 0.05 percent for H_2 (by volume). Therefore, detailed gas analysis was not included as a part of this study.

Table 1 gives a summary of the operating conditions for the ten runs used in this investigation. Due to space limitations and for the sake of brevity, only samples of the results are given in this paper. Further details of the results may be found elsewhere [2, 3].

The temperature indicated by a thermocouple placed in a gas stream is its own temperature, which is the resultant of the various heat transfer modes bearing on the thermocouple junction [4, 5]. Errors in the measured temperature arise due to radiation and conduction heat exchange between the hot junction, the thermocouple wires, and the surroundings [4]. The aspirated pyrometer probe compensates for conductive heating by the gas as it passes over the hot junction, and also by shielding the hot junction to reduce the temperature difference between the junction and the surroundings, thereby reducing radiative losses. Conductive heat losses are minimized if fine wires are used for the thermocouple.

Chedaille and Braud [6] showed that the error due to the suction velocity in measuring the static temperature (rather than the total temperature) is less than 7°C at a suction velocity of 250 m/s. Since the suction velocity during this work was maintained at less than 50 m/s, it is implied that the error due to suction velocity was less than 7°C. It was found by Khalil et al. [4] that the effect of suction at the probe tip is limited to a sphere of 3 mm diameter at a suction velocity of 250 m/s. Therefore, the temperature measured by the suction pyrometer is considered to be representative of the value at the junction position. Aspirated thermocouples have a reasonably fast response (0.5 min), provided that a fine wire is used for the thermocouple. Some advantages of using aspirated pyrometer probes for measuring temperature in a combusting environment are enumerated elsewhere [2–6].

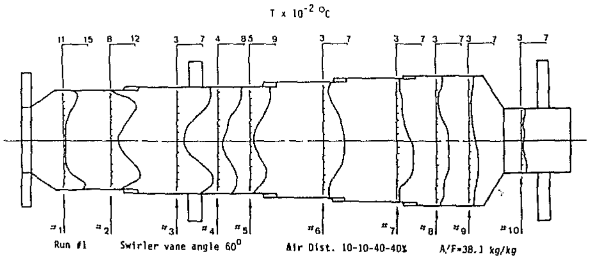

Fig. 8 Radial profiles of temperature along the combustor for run No. 1

Figure 8 shows a sample of temperatures measured at the various sections along the combustor during run 1. The shape of the temperature profiles along the combustor agrees with previously obtained profiles from experimental and theoretical studies. The temperature profiles illustrate the effect of the boundaries and are representative of the expected temperatures at the location of the measurements in the combustor [7].

Errors in measuring the temperature of a combusting flow are expected to be higher near a flame zone (or at regions of very high temperature) due to the increase of heat loss. Therefore, it was decided to perform a check on the validity of the temperature measurements at the first section of the combustor. The procedure followed to compute the average temperature at the first section from flow rates, radiative heat losses, and the energy content of the fuel, using an energy balance, is given in Appendix B.

Following the procedure of Appendix B, for the ten runs of this investigation (Table 1 gives the operating conditions during the runs), the computed average temperatures from energy balances and from temperature measurements are given in Table 2. The table shows that the maximum difference between the measured and computed temperature was 10°C, with the temperature in the range of 1500 K in the first section. This is considered as excellent accuracy in measuring the temperature by an aspirated pyrometer probe.

Velocity. Due to the lack of sensitivity of the conventional Pitot tube to flow direction in measuring the velocity vector, attention has switched to the use of multihole probes. The first detailed description of the application of the five-hole probe was given by Lee and Ash [8]. Multihole probes have since then been used in a wide variety of investigations (see [2] for a complete bibliography).

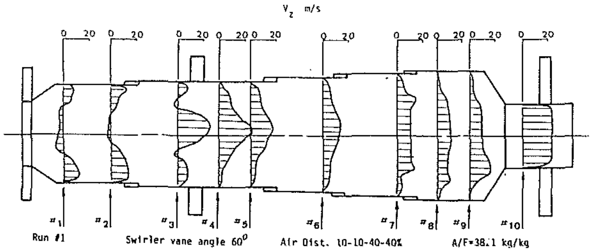

Fig. 9 Radial profiles of axial velocity along the combustor for run No. 1

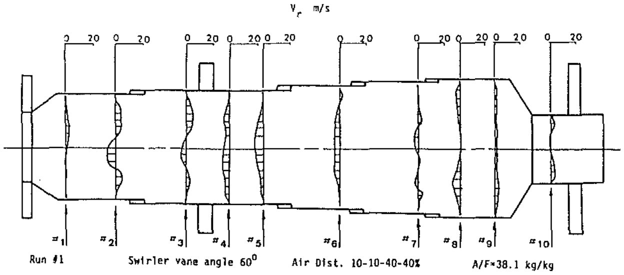

Fig. 10 Radial profiles of radial velocity along the combustor for run No. 1

The accuracy of determining the velocity vector depends on the accuracy of measuring the required pressure differences by the five-hole probe, namely $(P_1 - P_{\mathrm{atm}})$, $(P_2 - P_3)$, $(P_1 - P_2)$, and $(P_4 - P_5)$. The use of the five-hole probe in the nulling mode requires rotating the probe (about its axis) until $(P_2 - P_3)$ is zero, and the yaw angle is determined from the protractor reading in the manual traverse unit. The pressure differences were measured by a group of inclined manometers and a Hook gage manometer, which was equipped with a micrometer for more accurate reading of small pressure differences. The accuracy of reading the inclined manometers ranged from ±1.5 to ±4 percent. The Hook gage manometer is accurate to within 0.025 mm of water, hence its accuracy depends upon the value to be measured.

Operating the five-hole probe in the nulling mode improves the accuracy that can be achieved with the probe [9]. This is due to the simple manner of obtaining the yaw angle without the need for calibration. Frequent purging of the probe with compressed air or nitrogen [10] during measurements helps to remove any blockage in the passages leading to the manometers and thereby avoids a possible serious source of error.

An error analysis of measurements made with a five-hole probe by Gouldin [1] predicted errors to be less than 2 deg in yaw angle, 0.2 deg in pitch angle, and 3.5 percent in total pressure. Chue [11] and Dau et al. [12] found the accuracy in measuring static and dynamic pressure coefficients to be within 2–5 percent, and about 2 deg for pitch angle and 3–10 deg for yaw angle. Rhode et al. [13] estimated an accuracy of 5 percent for most measurements of five-hole probes, but it could reach 10 percent in regions of low velocity. The circumferential velocity component is expected to suffer the most in terms of accuracy due to its small value. Vu and Gouldin [14] found that five-hole probe measurements agree to within 2 percent with hot-wire anemometer results in regions of low turbulence levels and low velocity gradients. The difference, however, increased to 10 percent where turbulence and velocity gradients were higher.

The approach followed in this investigation to assess the accuracy of the velocity measurements by the five-hole probe was to apply the conservation principle pertinent to each component and to determine to what degree the measurements conform to the principle. The following sections describe the evaluation procedure for the three velocity components.

Table 3 Percentage difference in mass flow rate between values obtained from integration over section area and values obtained from inlet flow rates and open hole area, with the second value as the base value

$\Delta\dot{m}\% = \{(\dot{m}_f - \dot{m}_h)/\dot{m}_h\} \times 100$

Run # \ Sec. #	1	2	3	4	5	6	7	8	9	10	Abs. av.
1	-10.3	4.0	-4.6	18.2	-1.2	1.7	16.8	-0.5	8.1	2.5	6.8
2	-2.9	-8.9	-11.4	8.4	20.2	0.8	-5.5	-6.0	10.3	2.2	7.7
3	4.6	-12.9	-0.4	21.8	17.9	2.1	11.0	4.8	-2.5	-0.2	7.8
4	-8.6	-13.1	1.0	8.0	2.0	3.0	3.6	4.2	15.0	-2.5	6.1
5	-2.7	-5.2	-15.6	43.5	10.0	13.5	0.2	0.0	14.8	-2.0	10.8
6	2.9	-2.9	-6.1	1.3	2.0	1.4	4.6	-0.9	1.5	-0.7	2.4
7	3.7	-14.9	7.6	-7.1	3.1	8.4	3.7	3.0	-0.3	-1.5	5.3
8	24.5	-14.6	-15.9	4.8	2.0	6.3	3.9	18.7	16.8	-1.8	10.9
9	7.7	-13.7	-12.1	10.1	-8.1	4.8	4.5	14.4	10.8	-2.0	8.8
10	-4.1	-23.1	-6.7	1.2	7.4	4.5	10.2	19.5	11.8	0.8	8.9
Abs. av.	7.2	11.3	8.1	12.4	7.4	4.7	6.4	7.2	9.2	1.6	7.6

Axial Component of Velocity. Figure 9 shows a sample of the results of the axial velocity component plotted at the ten measuring sections along the combustor for run No. 1. In order to evaluate the accuracy of these results, the axial mass flow rate was computed, based on measured velocities, at all the measuring sections for the ten runs of this investigation. Appendix C gives a brief description of the procedure that was followed to interpret the results of this exercise in terms of the level of discrepancy in the axial velocity values at the various sections, upon application of the law of conservation of mass at these sections.

The results obtained upon application of the procedure of Appendix C for all sections for all runs given in Table 1 are summarized in Table 3. The last column and row of Table 3 contain the absolute mean value of the percentage difference in one run through all sections and in any section from all runs, respectively. The results in the table show a close agreement between the two approaches of calculating the mass flow rate at the combustor sections, especially near the exit section, where the difference was ±2.5 percent. It should be noted that while the difference seems to be higher at some sections, the absolute average for the ten runs is less than 7.6 percent. The maximum absolute average percentage difference for any run is about 10.9 percent. The maximum absolute average percentage difference at any section from all the runs is about 12.4 percent (at section 4). What might have contributed to the magnitude of error at this section is the fact that it is located between the secondary and dilution zones and if air leaked from one of these compartments into the other (Fig. 2), it would have produced an immediate error in the method of evaluating the accuracy of the measurements. The variation of these differences from one section to the other reveals that generally, for sections upstream of and including section 3, the mass flow rate calculated from velocity measurements is less than what is expected from the input air admitted up to that section. The opposite trend is found for sections 4–9. On the average, the mass flow, computed based on the axial velocity component obtained from measurements with the five-hole probe, agrees very well with the value deduced based on input mass flow rate.

Radial Component of Velocity. Figure 10 shows the radial profiles of the radial velocity component at the ten sections for run No. 1 as a sample of results. Examination of this figure and similar figures for other runs showed that there is a value for the radial velocity component that exists along the entire section even at the axis, with no change of sense for some profiles. At first glance, this could imply a discrepancy in the results due to the fact that such profiles require a source or sink flow at the combustor axis. However, the discrepancy might be alleviated if the gradients of the velocity vector com-

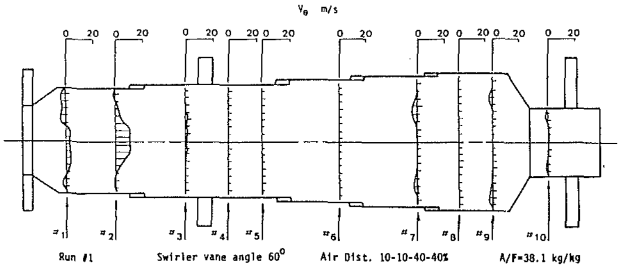

Fig. 11 Radial profiles for circumferential velocity along the combustor for run No. 1

Table 4 Difference in axial flux of angular momentum from calculations at the various sections and the inlet value to the combustor

$(G_{\phi s} - G_{\phi i}) \times 10^{4}$ Nm

Sec. # / Run #	1	2	3	4	5	6	7	8	9	10
1	-1.65	1.07	1.84	-0.06	-1.82	0.078	5.58	-2.86	-2.12	1.49
2	-1.25	-1.74	-1.85	-0.52	-1.19	-0.26	0.94	2.11	3.21	0.19
3	-1.06	-0.97	-0.50	-1.58	-1.81	3.12	-0.64	4.95	2.36	1.88
4	-6.08	-0.76	-7.10	0.43	1.03	0.11	2.97	2.51	1.75	6.12
5	-0.38	0.63	0.08	-1.00	-0.60	-0.32	0.68	0.12	-0.05	-0.58
6	0.64	0.47	0.53	-0.31	-0.99	-0.49	-0.87	-1.83	3.15	1.33
7	-0.91	-0.36	-0.58	-1.36	-1.07	-0.97	0.11	0.66	1.56	1.11
8	0.19	1.31	0.90	-0.82	-1.20	0.43	0.27	1.74	1.92	2.23
9	0.02	-0.04	-0.22	-3.73	-0.69	0.87	1.79	0.64	1.38	2.38
10	0.17	0.18	0.15	-0.44	-0.39	-0.11	3.76	3.30	0.80	1.91

ponents in the other two directions are large enough to compensate for the radial velocity component near the axis.

In order to assess the validity of the distributions obtained, the profiles that seemed suspect were examined in light of the continuity principle applied to a control volume in the vicinity of the combustor axis. This also indirectly checked the axial and circumferential velocity components. A semicylindrical control volume was adopted, for this purpose, at the combustor axis between adjacent measuring sections. The diameter of the control volume was taken to be equal to its axial length. This shape of the control volume allowed for consideration of the effect of the three velocity components as well as the effect of the lack of symmetry about the combustor axis. Appendix D outlines the procedure followed to do this.

Application of the procedure outlined in Appendix D to the radial velocity profiles at sections where they seemed unrealistic resulted in an average value of 3.5 percent discrepancy in the conformity of the results to the continuity equation. This means that the results of the radial velocity component are physically acceptable since, when used in mass flow computations, they provide close agreement with the other independently measured mass flows, for which the accuracy has been established as acceptable.

It should be pointed out that the accuracy of the calculations of the radial component of velocity is dependent on the accuracy of obtaining the pitch angle, which depends on the pressure difference $(P_4 - P_5)$ as obtained from the five-hole probe. At very low velocities (less than 1 m/s) the accuracy in measuring $(P_4 - P_5)$ is reduced due to the limitations of the manometer reading accuracy.

Circumferential Component of Velocity. The presence of a swirler in the flow passage of the primary combustion air produces a circumferential component for the velocity vector, for flow near the primary zone, in the same direction as that of the swirler vanes. This component should decay to zero near the combustor axis and more generally as the flow proceeds downstream toward the combustor exit. It should be near zero over the entire exit section.

Figure 11 shows, as an example, the radial profiles of the circumferential velocity component plotted at the various sections along the combustor for run 1. The circumferential velocity profiles presented in the figures, as well as those obtained for other runs, do not conform to the above-mentioned behavior and even, at most of the sections, show a negative value (opposite to the twist of the swirler vanes).

In order to check the validity of the circumferential velocity profiles, the axial flux of angular momentum was calculated at all sections for all runs, similar to calculating the mass flow rate, by integrating the required quantity over the section area. The effects of shear stresses and pressure differences on the axial flux of angular momentum were not taken into consideration, however. The axial flux of angular momentum supplied at the combustor head via the swirler was compared with the value obtained from integration over each section of the combustor. The procedure for doing this is summarized in Appendix E.

Table 4 presents the resulting difference in axial flux of angular momentum $(G_{\phi,s} - G_{\phi,i})$ in Nm, where $G_{\phi,s}$ = axial flux of angular momentum calculated by integration of experimental results at the sections; $G_{\phi,i}$ = inlet axial flux of angular momentum generated by the swirler. The results in Table 4 are given for all sections and all runs after following the procedure described in Appendix E. These results show that the two computations do not agree with each other at most of the sections. The results even suggest that the direction for the circumferential velocity may have been measured opposite to the direction offered by the swirler.

It should be noted, however, that the values of the axial flux of angular momentum at the combustor inlet are generally less than 8×10^{-5} Nm (compared to the value of 3.4×10^{-2} Nm for the product of axial momentum and combustor radius). If, during fabrication of the combustor, the holes that admit the secondary and dilution air were 5 percent off the radial direction (due to misalignment of the drill for example), that would result in an axial flux of angular momentum of 1.2×10^{-5} Nm at the third measuring section and higher values at downstream sections. The same can be said about the holes that admit the fuel-air mixture. If this misalignment was in the direction opposite to the twist of the swirler vanes, it would result in a negative circumferential component. Therefore, a 5 percent error in fabrication of the combustor could produce a value of the axial flux of angular momentum of the same order of magnitude as the value at the combustor inlet due to the swirler vanes. This can be one of the main reasons for the large discrepancy in the circumferential velocity measurements.

The fact that pressure difference and shear stress effects, particularly in the recirculation zone, were not accounted for in calculating the axial flux of angular momentum, could contribute to the difference obtained between the two values, especially with large temperature gradients in the combustion zone, which directly affect the density needed in the mass balance computation. Since the circumferential component was an order of magnitude (at least) less than the axial velocity component, when using the two values in a conservation equation to check the validity of the circumferential component, a small fractional uncertainty of the axial component could appear to produce a much larger fractional error in the circumferential component. Such small values of the circumferential velocity resulted in attempts to measure a pressure difference $(P_4 - P_5)$ of less than 0.025 mm water, where the manometer reading accuracy is very marginal.

Since no other approach was available to prove or justify the circumferential velocity profiles, they were shown [2] as dotted lines to convey this uncertainty.

Summary and Conclusions

Temperature measurements using an aspirated pyrometer probe showed very good accuracy in the combustion environment, which included regions with temperatures of up to 1500 K . The maximum difference between the measured value and the value that was expected based on energy conservation considerations was less than 10°C.

After evaluating the performance of the five-hole probe in measurements of the velocity vector in highly turbulent combusting flows (that contain a recirculating region), it was concluded that the measurement accuracy was quite satisfactory for the axial velocity and reasonable for the radial component, as verified by application of the continuity principle. The circumferential component could not be proven satisfactory (or otherwise). The variation in the reliability by which the five-hole probe responds to the three components is mainly due to the variation in their magnitudes, since the uncertainty in reading a manometer is approximately the same whether the reading is 1 cm or 0.0025 cm of water.

In order for the overall reliability of measurement of three velocity components with a five-hole probe as used in this study to be uniform, the three components would, in general, have to be of comparable magnitude to each other and none should be less than 10 m/s. Lower velocities will require high-precision manometers which, if the pressure difference is below 0.0025 cm of water, becomes impractical, which means that these low values cannot be accurately measured even with inclined (or Hook's) manometers.

The accuracy of the five-hole probe for pitch or yaw angles beyond 40 deg is highly degraded and the probe should not be used beyond this angle. A five-hole probe requires calibration, which is normally done in flows that are uniform in velocity and homogeneous in temperature and composition. This raises the possibility of another source of error when a probe thus calibrated is used in the present study with its highly sheared flow. The five holes in the probe occupy a circle of about 5 mm diameter. Therefore, placing this probe in a flow that has large thermal, dynamic, and chemical composition gradients may lead to another source of error as each of these holes measures in fact a flow that is different from the others. This is in contradiction to the basic assumptions in the calibration of the probe, which assume a uniform homogeneous flow in order to facilitate the application of Bernoulli's equation to the flow between the mainstream and any of the holes. Variation of the gradient of density, for example, from one region to another, is not accounted for in a usual calibration of this type of probe.

The above statements imply that for this research, the measured values of the axial velocity could be taken as generally acceptable; the values of the radial velocity component are acceptable but with less certainty than the axial velocities. The circumferential velocity values, on the other hand, should be treated with caution. This, however, does not negate the usefulness of the low-cost five-hole probe as a tool that is easy to use for obtaining at least the most significant components of the velocity vector in a recirculating, combusting environment.

Acknowledgments

This paper is based on the Ph.D. Thesis of M. B. Khalil. The research was supported in part by the Department of Energy, Mines, and Resources (EMR), Canada and by the Natural Sciences and Engineering Research Council of Canada (NSERC).

References

1 Gouldin, F. C., "Probe Measurements in Multi-dimensional Reacting Flows," *Testing and Measurement Techniques in Heat Transfer and Combustion*, AGARD C. P. 281, 1980.

2 Khalil, M. B., "Investigation of Combustion Characteristics of Low-Medium Heating Value Gases in an Atmospheric Pressure Combustor," Ph.D. Thesis, Carleton University, Ottawa, Canada, Sept., 1984.

3 Khalil, M. B., and Plett, E. G., "Experimental Investigation of Parameters Affecting the Performance of an Atmospheric Pressure Test Combustor Burning Low-Medium Heating Value Gas," presented at the ASME Winter Annual Meeting, Anaheim, CA, Dec. 1986.

4 Khalil, M. B., El-Mahallawy, F. M., and Farag, S. A., "Accuracy of Temperature Measurements in Furnaces," *Letters in Heat and Mass Transfer*, Vol. 3, No. 5, 1976, p. 421.

5 Beer, J. M., and Chigier, N. A., *Combustion Aerodynamics*, Applied Science Publishers Ltd., London, 1972.

6 Chedaille, J., and Braud, Y., "Industrial Flames," in: *Measurements in Flames*, Vol. 1, IFRF, 1972.

7 Swithenbank, J., Poll, I., Vincent, M. W., and Wright, D. D., "Combustion Design Fundamentals," *14th Symposium (Int.) on Combustion*, 1973, p. 627.

8 Lee, J. C., and Ash, J. E., "A Three-Dimensional Spherical Pitot Probe," *Trans. of the ASME*, Vol. 78, Apr. 1956, p. 603.

9 Chigier, N. A., "Velocity Measurements in Vortex Flows," in: *Flow, Its Measurement and Control in Science and Industry*, Vol. 1, R. B. Dowdell, ed., Instrument Society of America, 1974.

10 Chigier, N. A., "Pressure, Velocity and Turbulence Measurement in Flames," in: *Flow, Its Measurement and Control in Science and Industry*, Vol. 1, R. B. Dowdell, ed., Instrument Society of America, 1974.

11 Chue, S. H., "Pressure Probes for Fluid Measurement," *J. of Progress in Aerospace Science*, Vol. 16, No. 2, 1975, p. 147.

12 Dau, K., McLeod, M., and Surry, D., "Two Probes for the Measurements of the Complete Velocity Vector in Subsonic Flow," *J. of the Roy. Aero. Society*, Vol. 72, No. 696, 1968, p. 1066.

13 Rhode, D. L., Lilley, D. G., and McLaughlin, D. K., "Mean Flow Fields in Axisymmetric Combustor Geometries With Swirl," *AIAA J.*, Vol. 21, No. 4, 1983.

14 Vu, B. T., and Gouldin, F. C., "Flow Measurements in a Model Swirl Combustor," *AIAA J.*, Vol. 29, No. 5, 1982, p. 642.

15 Reynolds, W. C., *Thermodynamics*, McGraw-Hill, New York, 1965.

APPENDIX A

Procedure for Measuring Temperature and Velocity Vector

A 1 Temperature Measurement

1 The aspirated pyrometer (AP) was mounted into the manual traverse unit (obtained from United Sensor and Control Corp.).

2 The manual traverse unit (MTU) was fixed in place by a clamp at the section along the combustor, where the measurement was to be made, with the AP junction at the far end wall.

3 The suction pump was switched on and the temperature reading at steady state was recorded.

4 Using the linear vernier and the traverse scale, the AP was drawn radially out a distance of 5.0 mm and the new temperature reading was recorded.

5 The traverse was made across the diameter of the combustor for that measuring hole at that section; then the MTU (and AP) were moved to the second hole (at the same section) which is located 120 deg clockwise from the first hole, where the procedure was repeated.

6 The procedure was repeated again at the third hole of the section. The temperature at a given radial location was considered to be the average of the three readings on that side of the centerline, at that section.

7 The probe was then moved to another section, and the procedure repeated, until the entire combustor had been surveyed.

A2 Velocity Vector Measurement

1 A complete traverse of the combustion space was carried out using the two-hole probe (mounted on the MTU) to identify the recirculation zone or the boundaries of the reversed flow.

2 The five-hole probe was mounted in the MTU, which in turn was fixed by a clamp at the combustion section where the

velocity vector determination was desired, with the tip of the probe at the far wall of the liner.

3 The five-hole probe was placed in accordance with the flow direction indicated by the two-hole probe, rotated about its axis until the pressure difference indicating the yaw angle became zero, which allowed the yaw angle to be obtained from the protractor reading of the MTU.

4 The three pressure differences (Fig. 6), which indicate the dynamic pressure difference, total pressure, and pitch angle, were recorded at this position.

5 The probe was then moved radially a distance of 5 mm, using the MTU, and directed in accordance with the reversed flow boundaries, where the above procedure was repeated.

6 When the probe readings were taken over the entire diameter of one section, the MTU (with the probe) was moved to the next hole 120 deg clockwise at the same section.

7 The procedure was repeated at this hole and the third hole at each section.

8 The procedure was followed at all sections along the combustor.

9 The velocity vectors were computed at each of the three holes at each section, from the pressure differences measured, on the basis of the probe calibration, after correcting for reduction of flow area due to probe insertion.

10 The velocity components were obtained from resolving the velocity vector in the three directions, namely axial, radial, and circumferential.

11 The average value of each of the components was obtained from the three readings at the three holes, for each radial position for each section along the combustor.

APPENDIX B

Calculation of the Average Temperature at the First Section of the Combustor

This appendix illustrates briefly the procedure of calculating the average temperature at the first section of the combustor for the various runs of this investigation. A more detailed description can be found in [2].

1 From fuel and air flow rates at the combustor first section, the average values (over the section) of the concentrations of the reactants and products are calculated with the help of gas analysis.

2 From the above calculated values for concentrations of reactants, the total enthalpy at combustor inlet is calculated as described in many texts dealing with thermodynamics of combustion (e.g., [15]).

3 Knowing the concentrations of various components at the first section, the relative amounts of chemical and sensible enthalpy are found.

4 The heat loss by radiation from the combustor surface up to the first section is estimated from knowledge of combustor design and the average surface temperature at the first section.

5 The net sensible enthalpy of the products of combustion at the first section is calculated knowing the total sensible enthalpy and subtracting the estimated radiative losses.

6 A temperature is found (usually by a trial and error procedure) that is consistent with the concentrations and net sensible enthalpy. This is the average temperature at the first section.

APPENDIX C

Procedure for Evaluation of the Accuracy of Results of the Axial Velocity Component

This appendix outlines a procedure for evaluating the accuracy of the results of axial velocity measurements as obtained from the five-hole probe. The details of the procedure can be found in [2]. The steps are as follows:

1 Compute the mass flow rate at each section of the combustor, for the run under consideration, as follows:

$$\dot{m}_s = \int_A \rho v_z dA$$

where

$\dot{m}_s$ = mass flow rate at the sections being examined
$\int_A$ = integration over the area of the section
ρ = gas density
v_z = axial velocity

The above integration was performed numerically using the method of trapezoids. The area increment was calculated from the mean radius between the relevant two measuring points and the increment of distance between these two measuring points. The density of the gas was calculated from the equation of state at the mean temperature after calculating the gas constant based on the gas composition.

2 The mass flow rate at each of the measuring sections ($\dot{m}_a$) was calculated from the mass flow rate of fuel and the amount of air admitted up to the section under consideration. The amount of air admitted through the holes for secondary or dilution air as well as through holes for film cooling can be estimated to be proportional to the open area up to the section under consideration as a fraction of the total area available for flow to pass through. This is assuming a constant discharge coefficient for all holes of a particular type at a particular zone or ring of the combustor.

3 The percentage difference in the mass flow rate as computed from steps 1 and 2 is calculated as follows:

$$\Delta\dot{m}(\text{percent}) = \frac{\dot{m}_s - \dot{m}_a}{m_a} \times 100$$

where

$\Delta\dot{m}$(percent) = percentage difference in mass flow rate
$\dot{m}_s$ = mass flow rate calculated from integration of axial velocity measurements × density along the section area
$\dot{m}_a$ = actual mass flow rate that is expected to occur at the section based on measured flow rates to the combustor and on the combustor design

APPENDIX D

Procedure for Evaluation of the Accuracy of Results of the Radial Velocity Component

Figure D1 shows a schematic drawing of the control volume at the combustor axis, which was used to apply the continuity equation to determine the accuracy of radial velocity measurements. Axial flow resulting from the axial component of velocity will take place only through the two semicircular ends of the control volume. Radial flow is possible only through the curved surface of the cylindrical control volume (ABFDCEA). Circumferential flow is possible only through the flat surface of the control volume (ABCD). The approach followed here was simply to determine the net mass flow rate to the control volume from the results of velocity measurements to determine how close to zero it is.

1 The axial mass flow rates at both ends are calculated over the area following the same procedure described in Appendix B, with the exception that the cross section is a semicircle and extends only to the diameter of the control volume.

2 The radial mass flow rate is calculated by averaging the values of the radial velocity components at the four corners A, B, C, and D, assuming linear variation and considering the

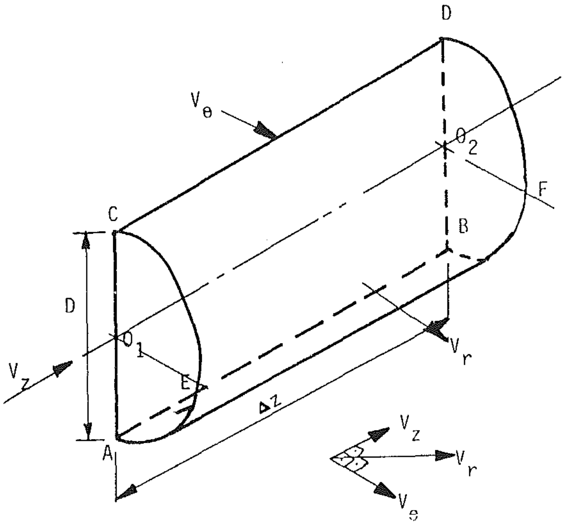

Fig. D1 Control volume at the combustor axis

resulting value to flow through the curved surface of the control volume.

3 The mass flow rate due to the circumferential component of velocity was estimated as follows: The circumferential velocity was averaged over AO1, O1C, BO2, and O2D. The average over CO1 and O2D was considered to flow through the area CDO2O1 and the average over AO1 and BO2 was considered to flow through the area ABO2O1.

APPENDIX E

Procedure for Evaluation of the Accuracy of Results of Circumferential Velocity Component Measurements

There are two bases for calculating the axial flux of angular momentum, which is conserved in swirling flows. Calculations are based on experimental measurements and on the swirler design and input flow rates. The procedure is carried out as follows:

1 The axial flux of angular momentum is calculated at any section of the combustor from the relationship

$$G_{\phi,s} = \int_A \rho v_z v_\theta r dA$$

where v_θ = circumferential velocity component. This step is to be carried out similarly to computing the mass flow rate at the combustor section, described in Appendix B.

2 The axial flux of angular momentum at the inlet to the combustor due the presence of a swirler is calculated from the following expression, given by Beer and Chigier [5]:

$$G_{\phi,s} = \int_{r_i}^{r_o} \rho v_z v_\theta 2\pi r^2 dr$$

where r_i = inner radius of swirler: r_o = outer radius of swirler.

If the axial velocity v_z is assumed to be uniform over the range r_i-r_o, the circumferential velocity v_θ will be uniform because $v_\theta = v_z \tan\theta$ for straight vanes of angle θ to the combustor axis.

$$\begin{aligned} G_{\phi,i} &= \int_{r_i}^{r_o} \rho v_z^2 2\pi r^2 dr \tan\theta \\ &= 2\pi\rho v_z^2 \tan\theta \int_{r_i}^{r_o} r^2 dr \\ &= 2/3\pi\rho v_z^2 \tan\theta (r_o^3 - r_i^3) \end{aligned}$$

Substituting for v_z from the mass flow rate through the swirler and the swirler open flow area (neglecting the thickness of the vanes),

$$G_{\theta,i} = \frac{1}{5\pi\rho} (\dot{m}_{pri})^2 \frac{r_o^3 - r_i^3}{(r_o^2 - r_i^2)^2} \tan\theta$$

where $\dot{m}_{pri}$ = mas flow rate through the swirler (primary air).

The values $G_{\phi,i}$ were calculated from the operating flow rate for the ten runs with the value of θ substituted corresponding to the swirler mounted during the run. The density was calculated assuming that the flow achieved a temperature of 300°C at the swirler exit section.

It should be mentioned here that $G_{\phi,i}$ can be computed from measurements of pressure drop and torque at the combustor inlet with fewer assumptions required. The operation of the combustor at atmospheric pressure and the separate admission of air to the combustor zones prevented us from following this route.

Methods for Achieving a Combustion-Driven Pressure Gain in Gas Turbines

J. A. C. Kentfield

M. O'Blenes

Department of Mechanical Engineering,
University of Calgary,
Calgary, Alberta, Canada

The objective of the work was to compare on both an ideal and, where possible, an actual basis the approximate performances of four types of pressure-gain combustor. Such combustors are potentially suitable for use in gas turbines in place of conventional steady-flow combustors. The ideal theoretical performance comparison was based on a specially conceived, universal, analytical model capable of representing, in a fundamental manner, the dominant features of each of the systems studied. The comparisons of nonideal performance were based on actual test results and, where these were not available, on ideal performance characteristics suitably modified to take irreversibilities, etc., into account. It was found that in general the pressure-gain potential of the concepts studied increased with increasing system complexity. It was also found that with most concepts the combustor pressure ratio achievable increases with combustor temperature ratio.

Introduction

The general advantage derived from the use of a gas turbine combustor capable of generating a stagnation-pressure increase, instead of the customary loss of stagnation pressure that occurs with conventional steady flow combustors, is shown diagrammatically in Fig. 1. Figure 1 depicts an elementary gas turbine cycle on the temperature-entropy (T, S) plane. It is clear from Fig. 1 that a combustion-driven pressure gain results, for a prescribed maximum cycle temperature, in a potential for an increased net work output with a resultant reduction in specific fuel consumption. Figure 2 presents the results of a quantitative evaluation, for prescribed component efficiencies, of the response of simple gas turbines to a 1 percent reduction of combustor pressure loss. The resultant increase in output presented on the ordinate of Fig. 2 also represents the corresponding percentage increase in thermal efficiency or, equally, the percentage reduction in specific fuel consumption due to a 1 percent reduction in pressure loss or increase in pressure gain.

A pressure-gain combustor is here defined as having substantially steady inflow and outflow, although nonsteady processes occur within the combustor system in order to generate a higher stagnation pressure at the pressure-gain combustor outlet than prevails at the inlet. It is always possible to substitute a steady-flow combustor, albeit with some performance loss, for a pressure-gain combustor. Pressure-gain combustor-equipped gas turbines should not be confused with what have, in the past, been termed constant volume gas turbines such as those built according to a concept due to Holtzworth [1] or more recent proposals [2, 3], in which the flow through the turbine is substantially nonsteady.

The purpose of the present paper is to identify, at least approximately, the inherent performance potential of each of the four classes of device that have been proposed, and in some cases at least partially developed, as pressure-gain combustors. Past proposals include reciprocating internal combustion engines, detonation wave devices, dynamic pressure exchangers, and valveless pulse combustors. By categorizing these devices in terms of their approximate performance potential, and relative complexity, it is possible to identify operational regimes where each excels relative to the others.

Analytical Model

In order to compare the relative merits, on the basis of their approximate performances, of the four pressure-gain com-

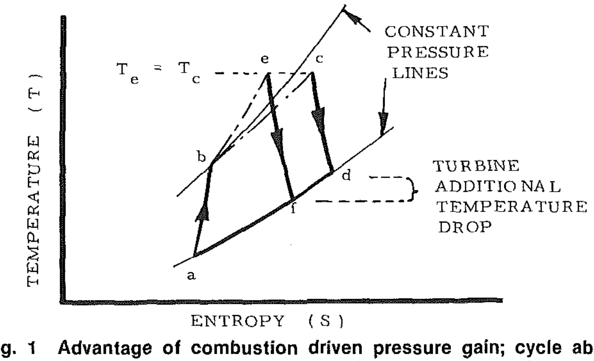

Fig. 1 Advantage of combustion driven pressure gain; cycle abcd: pressure loss during heat addition; cycle abef: pressure gain during heat addition

---

Contributed by the Gas Turbine Division of THE AMERICAN SOCIETY OF MECHANICAL ENGINEERS and presented at the 32nd International Gas Turbine Conference and Exhibit, Anaheim, California, May 31-June 4, 1987. Manuscript received at ASME Headquarters February 10, 1987. Paper No. 87-GT-126.

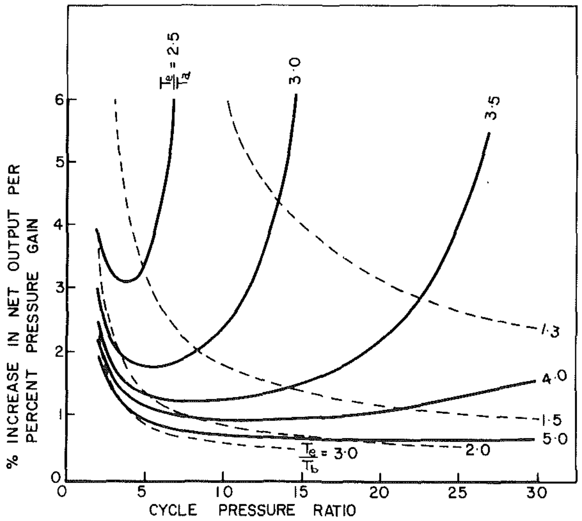

Fig. 2 Influence of combustion driven pressure gain on performance of simple cycle, shaft power, gas turbines; see Fig. 1 for definition of subscripts *a*, *b*, and *e*; $\eta_C = \eta_T = 0.85$, $\gamma_C = 1.40$, $\gamma_T = 1.34$, $C_{pT}/C_{pC} = 1.125$, $\dot{m}_C = \dot{m}_T$

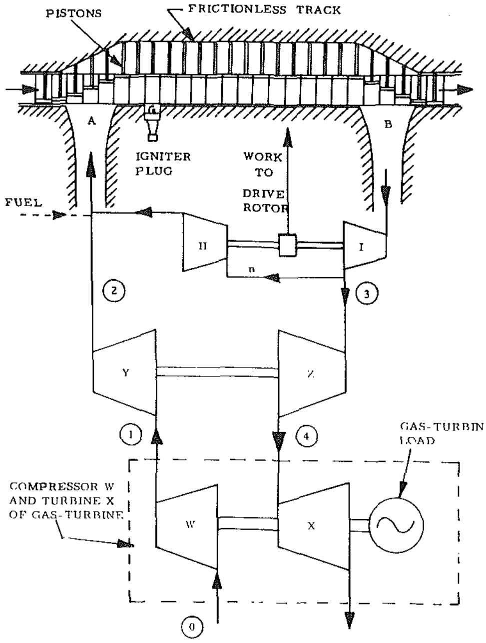

Fig. 3 Analytical model for analysis of ideal performances of pressure-gain combustors

bustor concepts considered here, it is desirable to use a common model capable, by the omission or inclusion of various components, of modeling, in a broadly representative sense, the ideal performances of combustors based on reciprocating internal combustion engines, detonation wave concepts, dynamic pressure exchangers, and pulse combustors. The model selected for the task is illustrated diagrammatically in Fig. 3. The model does not purport to represent, even diagrammatically, any known real machine but rather an ensemble of compressors and expanders (represented diagrammatically as turbocompressors and expanders) in conjunction with a cellular device, shown at the top of Fig. 3 and within any cell of which the flow is nonsteady, that serves as a purely constant volume combustor. The only work terms associated with the rotary, cellular combustor for ideal cases in which friction is ignored are those due to the (net) difference between the inflow and outflow flow-work terms. It is this net term that constitutes the power input, for an ideal frictionless case, required to drive the cellular rotor of the constant volume combustor; this work is extracted from expander I or, if a recirculation of products of combustion is provided to inlet duct A from outlet B, jointly by expanders I and II. Expander Z, which drives compressor Y, allows the cellular constant volume combustor devices to be, in effect, supercharged. The components, *W* and *X*, within the dotted boundary represent the remainder of the gas turbine, with load, to which the pressure-gain combustor is connected.

If the combustor model is considered with expander II omitted the resultant system can be regarded as representing a reciprocating internal combustion engine type combustor. Here no differentiation is made between the nominal cycle differences of spark ignition and diesel engines. In the case of a spark-ignition engine combustion is nominally at constant volume, a situation identical with the model. For the case of a diesel engine the combustion process is, nominally, at constant pressure as distinct from the constant volume combustion situation of the model; however for most modern diesel engines combustion occurs with a resultant significant pressure rise. Hence, since approximate results are adequate for the present purposes no account was taken of the nominal cycle differences between spark ignition and diesel engines. The elimination of expander II also implied, implicitly, that no products of combustion were recirculated. The compression process of a reciprocating internal combustion engine was modeled by compressor Y and the expansion process by expanders I and Z connected in series and indicated in Fig. 3.

For a true, ideal, constant volume pressure-gain combustor without charge precompression in the combustor and without recirculation of combustion products, expanders II and Z, and compressor Y were eliminated, stations 1 and 2, and 3 and 4, respectively, therefore becoming coincident. For a device that

Nomenclature

a = acoustic velocity
C_p = specific heat at constant pressure
$\dot{m}$ = mass flow rate
n = fraction of combustor exhaust mass flow recirculated
P = stagnation pressure
S = entropy
T = stagnation temperature

u = gas velocity
α = $\phi\ (T_0/T_2)$
γ = isentropic index
η = isentropic efficiency
η_{MECH} = mechanical efficiency of combustor model (Fig. 3) inflow and outflow processes
ϕ = equivalence ratio

Subscripts

C = compressor
S = supercharger outlet
T = turbine or expander
0, 1, 2, ... / a, b, c, ... = cycle or other stations (see diagrams)

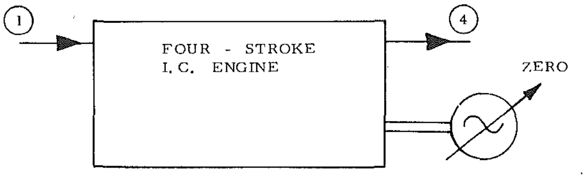

Four-stroke reciprocating i. c. engine as a pressure-gain combustor, $P_4 > P_1$, no net shaft power.

Fig. 4 Four-stroke engine as a pressure-gain combustor

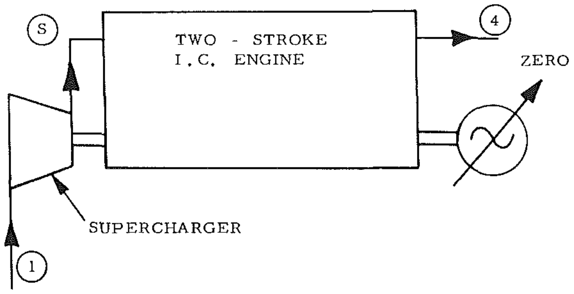

$P_4 > P_1$, ~s a pressure-gain combustor, shaft power.

Fig. 5 Two-stroke engine as a pressure-gain combustor

can best be described as approximating a constant volume combustor with products recirculation but without charge precompression expander Z and compressor Y were eliminated. Care was taken throughout the analysis to account appropriately for all flow-work terms. The entire analytical procedure used for all cases was based on the application of simple, elementary, thermodynamic concepts and hence will not be discussed here in further detail.

Reciprocating Engine-Based Combustors

There appear to be at least two ways in which a reciprocating internal combustion engine could be employed as a pressure-gain combustor. If a four-stroke engine is used, and following from the previous outline of the theoretical treatment no fundamental differentiation is made between the combustion processes in spark ignition and diesel engines, a combustion-driven pressure gain is fundamentally achievable by back-pressuring the engine exhaust. This case is illustrated diagrammatically in Fig. 4. For such an engine application to qualify as a pressure-gain combustor the entire engine output would be used in pumping the exhaust gases against the imposed back pressure and hence there would be no net shaft power available from the engine, a situation indicated in Fig. 4. The resultant pressure gain is represented by the stagnation pressure difference (P_4-P_1). Presumably, for reasons associated with the need to control the combustor temperature ratio, T_4/T_1, any pressure-gain combustor based on a four-stroke engine is most likely to be based on a diesel cycle. The writers are not aware of any actual attempt to build a four-stroke-engine-based pressure-gain combustor.

If a two-stroke engine is substituted for one of the four-stroke type it is not possible, because scavenging could not take place, to employ an exhaust back pressure greater than the pressure applied to the engine inlet ports. In fact the inlet pressure must exceed the exhaust back pressure to achieve a scavenger flow through the system, at least to a first approximation ignoring any benefits obtainable from nonsteady flows in the engine inlet and exhaust tracts. To overcome this difficulty it is essential to use the engine power to drive a supercharger as indicated in Fig. 5. Again, to comply with the previously given definition of a pressure-gain combustor, there will be no remaining net shaft power as is implied in Fig. 5. In the past a diesel combustor of the type indicated in Fig. 5 has been tried by Rolls-Royce; this machine constituted a portion of an experimental gas turbine, the T.100; so far as is known to the writers there are no test results available for this unit in the open literature.

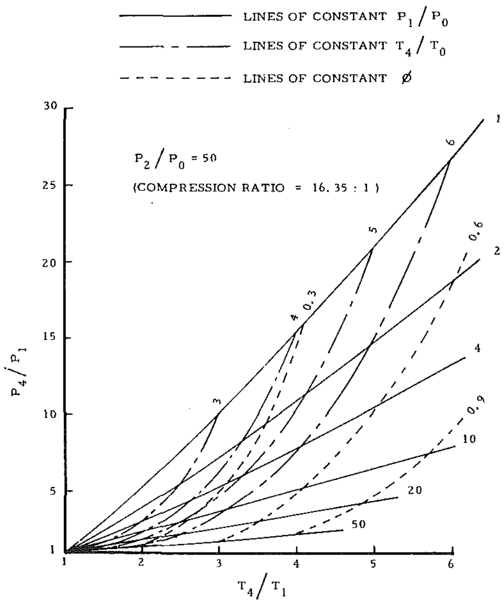

Fig. 6 Ideal air-cycle performance of internal combustion engine type pressure-gain combustors

Thermodynamically, at the level of the simple analytical model proposed here, there are no performance differences between the four-stroke and two-stroke based combustors. An idealized performance map for an internal combustion engine-based pressure-gain combustor, operating with an overall system pressure ratio $P_2/P_0 = 50{:}1$ (see Fig. 3), is presented in Fig. 6. The performance was established from use of the previously described analytical model. In practice difficulties with diesel type pressure-gain combustors relate to startup; it should be noted that an overall system pressure ratio $P_2/P_0 = 50{:}1$ corresponds to a (volumetric) compression ratio of 16.35:1, a value typical of medium-sized diesel engines but a compression ratio obtainable due to the contribution of the gas turbine compressor W, assistance not available at startup. Furthermore diesel type pressure-gain combustors are, in gas turbine terms, both relatively heavy and complex. It may be possible to ameliorate the startup problem by using yet more complex diesel engines incorporating variable compression ratios. Such engines have been tried in the past. Among the arrangements tested have been hydraulically adjustable pistons (British Internal Combustion Engine Research Association), junk heads (used on at least one version of the Rolls Royce T100 unit referred to previously), and variable geometry drive-train systems of one form or another.

Elementary Constant Volume Combustor

The pressure gain potential of an idealized constant volume type pressure-gain combustor that does not feature precompression of the air charge, over and above that obtainable from the gas turbine compressor W, can be established from the system shown in Fig. 3 when expanders II and Z, and compressor Y, are eliminated. The pressure ratio, P_3/P_2, achievable versus the corresponding combustor temperature ratio, T_3/T_2, is shown in the upper curves of Fig. 7, for two values of γ, when there are no losses of any kind. In Fig. 7 the zero loss cases are signified by assigning a mechanical efficiency value (η_{MECH}) of unity and the isentropic efficiency (η_T)

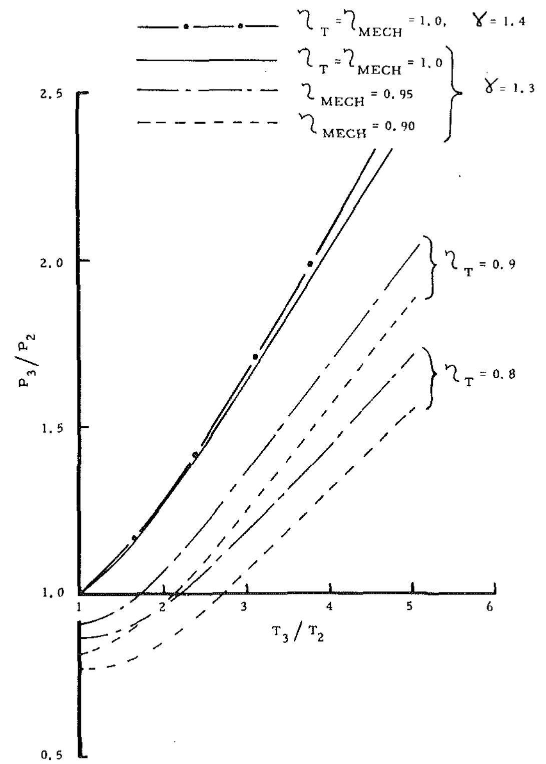

Fig. 7 Ideal performances of constant volume pressure-gain combustors without charge precompression; performances with losses also included

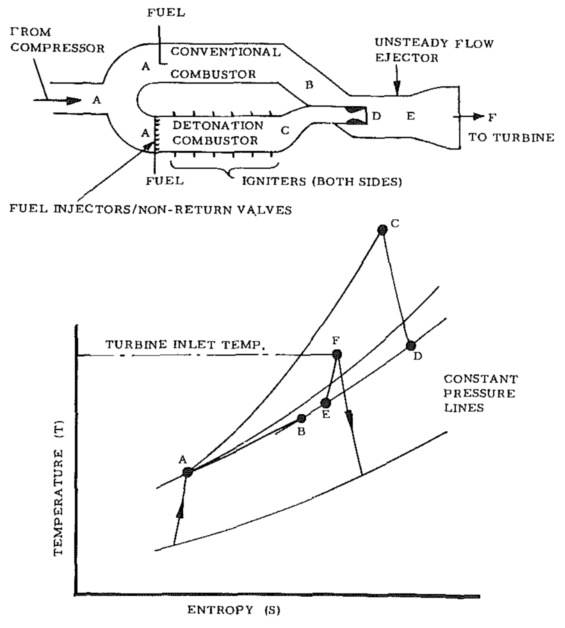

Fig. 8 Wortman-type detonation-wave pressure-gain combustor

also of unity for the expander, or driving turbine (component I of Fig. 3). While any pressure-gain combustor consisting of a multitude of cylinders, or cells, each containing a piston, is clearly impractical because of complexity a question that can be asked is how sensitive is a constant volume combustor to losses of magnitudes likely to be representative of practice? An indication of the penalties associated with losses was obtained by re-evaluation of the combustor performance, for $\gamma = 1.3$, with mechanical efficiencies, η_{MECH}, of 0.9 and 0.95 and also with expander isentropic efficiencies of 0.8 and 0.9. The results are presented in the lower part of Fig. 7. It can be seen that for combustor temperature ratios in the region of 2 to 3, a zone typical of many gas turbines, losses can eliminate the potential advantages of pressure-gain combustion.

While the foregoing analysis, summarized in Fig. 7, is clearly an oversimplification, three classes of pressure-gain combustor can be described, to a first-order approximation, as essentially constant volume combustion devices without major charge precompression, in the pressure-gain combustor, prior to combustion. Such systems include: (*i*) some combustors employing detonation waves, (*ii*) some dynamic pressure-exchanger type combustors, and (*iii*) most valveless pulse combustors.

Detonation Wave Combustors

Several suggestions have been made to employ detonation waves as a means of obtaining a combustion-driven pressure gain. An indication that detonation-wave combustion can be approximated as a constant volume combustion headed by a superimposed translating, strong, pressure spike has been given by Helman et al. [4]. One proposal for a detonation wave combustor for gas turbines is due to Wortman [5]; the upper part of Fig. 8 shows a Wortman-like device diagrammatically. The detonation wave is initiated by a number of igniters and travels transversely in the detonation chamber. The pressurized products of combustion pump, by means of a nonsteady flow ejector, products of combustion emerging from a conventional, steady flow, combustor. The flow leaving the gas turbine compressor is bifurcated; a portion enters the detonation wave combustor; the remainder enters a conventional combustor. It would appear that this arrangement makes the total system more controllable and better able to meet turbine inlet temperature restrictions than would be the case if all the combustion took place in the detonation chamber. It would also seem that a nonreturn valve is required at the upstream end of the detonation wave combustor to inhibit blow back. An attempt is made to illustrate the functioning of the Wortman system on the temperature ~ entropy ($T \sim S$) plane in the lower part of Fig. 8. Over and above the irreversibilities associated with the detonation wave another major source of irreversibilities is likely to be the nonsteady flow ejector system, although it is well recognized that nonsteady flow ejectors are generally less irreversible than the steady flow type [6].

Rostafinski [7] performed an analysis of the Wortman detonation wave combustor and came to the conclusion that a performance could be expected that is somewhat similar to that of dynamic pressure-exchanger type pressure-gain combustors. So far as is known to the writers detonation wave pressure-gain combustors have not yet been developed to the point where an attempt has actually been made to demonstrate a detonation wave type pressure-gain combustor suitable for gas turbine applications. Numerous laboratory experiments have, however, been made based on detonation wave phenomena [8]. Potential problems with detonation wave combustors appear to be related to structural fatigue, due to the relatively high, and intermittent, firing pressures; the prevention of inlet back flow; inherent system irreversibilities and, possibly, high rates of heat transfer to the wall of the detonation chamber.

Dynamic Pressure Exchangers

Pressure-gain combustors based on the concept of the dynamic ressure exchanger, while not yet ready for commercial application, have been developed relatively extensively. A dynamic pressure-exchanger, a device featuring a continuously rotating cellular rotor running between closely fitting end plates, is illustrated diagrammatically in Fig. 9. The arrangement, and sequence, of the porting in the end plates governs the cyclic functioning of a pressure exchanger. When a cell

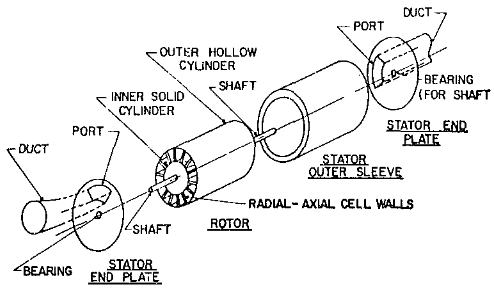

Basic arrangement of a simple pressure exchanger

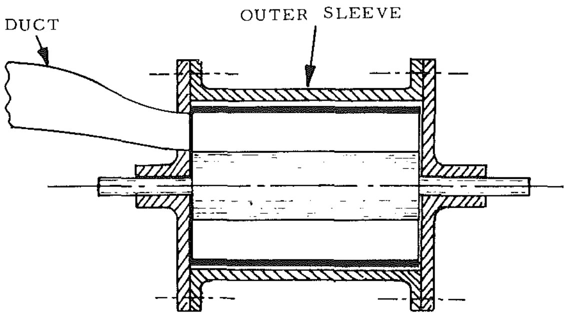

Cross-section of a simple pressure exchanger

Fig. 9 Basic configuration of a dynamic pressure exchanger

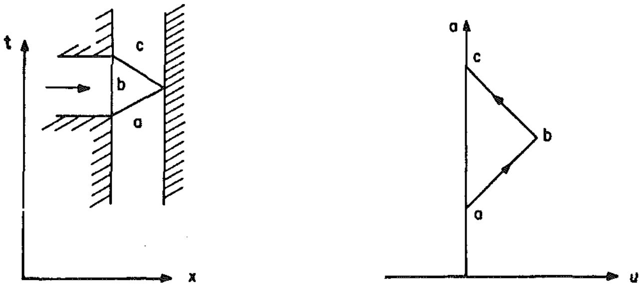

Filling process on x∼t and a∼u planes

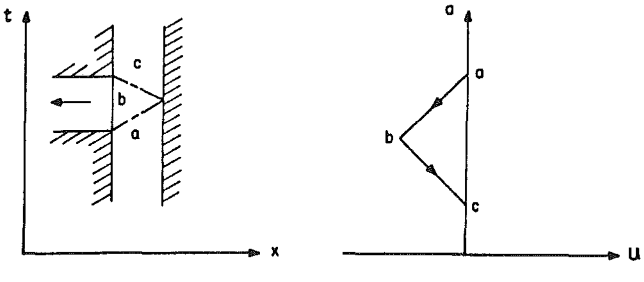

Emptying process on x∼t and a∼u planes

Fig. 10 Fundamentals of cell filling and emptying processes

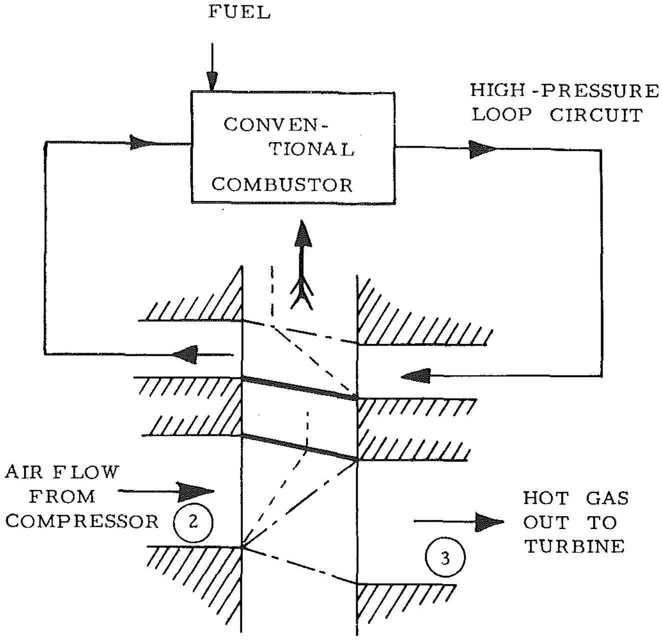

Fig. 11 Arrangement of a dynamic pressure-exchanger pressure-gain combustor with separate combustion external to the pressure-exchanger rotor

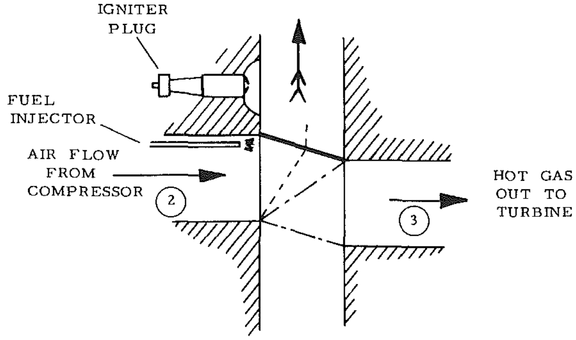

Fig. 12 Dynamic pressure-exchanger pressure-gain combustor with combustion in cells

runs past a port containing gas at a higher pressure than that in the cell a filling process is initiated. When the pressure in the cell exceeds that in the port a cell emptying occurs. Simple cell filling and cell emptying processes are shown on the time ∼ distance *x* plane at the top and bottom of the left-hand side of Fig. 10, respectively. Detailed descriptions of basic pressure-exchanger wave processes have been given elsewhere [9, 10]. The diagrams of acoustic velocity *a* versus gas velocity *u*, appearing on the right-hand side of Fig. 10, allow the ideal pressure ratios of the wave processes to be established for prescribed *u* values [10]. The $a \sim u$ diagrams are known as state diagrams and the notation *a*, *b*, *c*, on the $a \sim u$ plane corresponds to the similarly identified zones on the $t \sim x$ plane.

By combining, in various ways, cell filling and emptying processes, a cyclic arrangement of the type shown in Fig. 11 can be hypothesized. The thick solid lines represent shock waves; expansion waves are shown chain-dotted, and demarcation lines, between the original cell contents and fluid entering the cells, are shown dotted. The cycle depicted in Fig. 11 constitutes, in a very basic manner, the arrangement of pressure-gain combustors operated experimentally, in the past, by both Rolls-Royce in Britain [11] and General Electric in the United States [12]. The arrangement shown in Fig. 11 results, despite the use of a conventional steady-flow type combustor, in a higher stagnation pressure in port 3 than that of the air entering port 2. Fairly recently Sladky et al. [13] have demonstrated a more compact form of pressure-exchanger pressure-gain combustor, Fig. 12, in which combustion occurs, at constant volume, within the cells of the pressure exchanger. It is easy to show that, on a fundamental basis, the cycles of Fig. 11 and 12 are thermodynamically comparable. This can be appreciated by realizing that the heat ad-

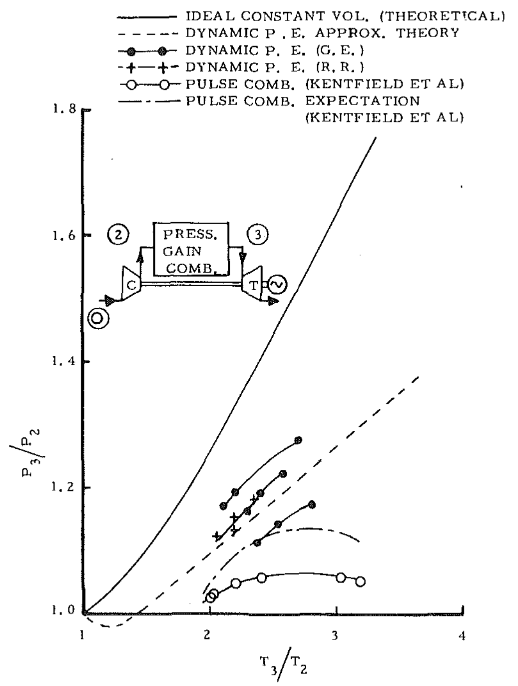

Fig. 13 Pressure-gain performances of pressure exchangers and valveless pulse combustors

dition process, as perceived by an observer in a cell, is in effect at constant volume for the arrangement shown in Fig. 11 although the chemical reaction actually takes place externally to the cells at a constant pressure; this proposition is discussed in somewhat more detail elsewhere [10].

Test rig performances obtained by Rolls-Royce and by General Electric with their experimental pressure-exchanger pressure-gain combustors are presented in Fig. 13. The solid line in Fig. 13 is the theoretical ideal performance of an elementary constant volume combustor for $\gamma = 1.3$ and corresponds, therefore, to the solid line of Fig. 7. The dotted curve is the result of a relatively detailed prediction of the performance of a dynamic pressure-exchanger type pressure-gain combustor using a method of analysis based upon the results of pressure-exchanger filling and emptying tests [14].

A dynamic pressure-exchanger pressure-gain combustor has, inherently, only one major moving part, namely the rotor. If the configuration is of the type shown in Fig. 11 some relatively difficult duct work is needed to connect the combustor to the pressure exchanger. While the system of Fig. 12 is much more compact presumably the combustion arrangements are somewhat more unusual and are, in general, not so well developed practically. The pocket adjacent to the igniter is intended to allow cells in which combustion is already occurring to initiate combustion in those approaching the igniter zone. Such an arrangement was proposed by Spalding [15].

Valveless Pulse Combustors

Valveless pulse combustors, also sometimes referred to as aero-valved pulse combustors [16], were proposed by Reynst as a form of pressure-gain combustor for gas turbines [17]. Valveless pulse combustors have been considered preferable, because of the absence of any moving parts, to more conventional valved pulse combustors. The automatic inlet valve of most conventional pulse combustors appears, also, to be relatively vulnerable to thermal damage due to the passage of heated air from the compressor delivery and also due to the fairly intensive combustion within a pressure-gain pulse combustor.

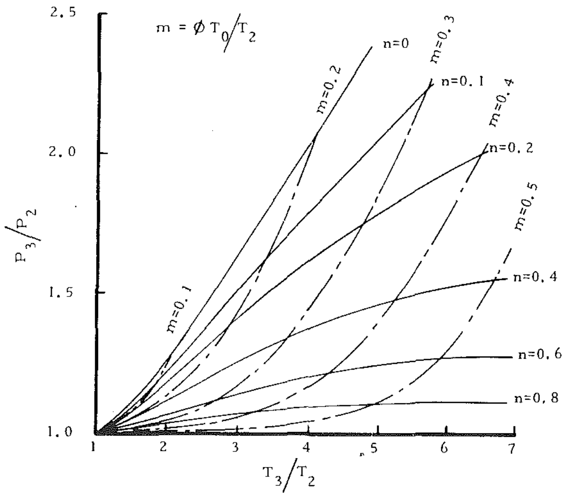

Fig. 14 Influence of exhaust product recirculation on the ideal performance of a constant volume combustor ($\gamma = 1.3$)

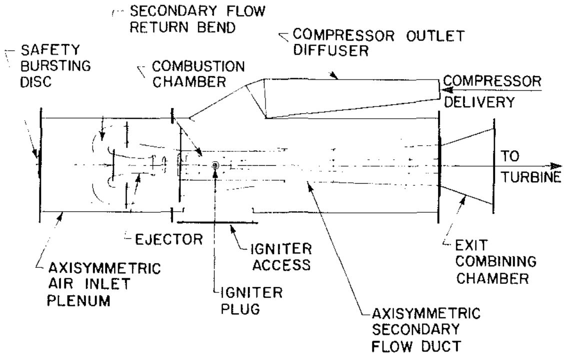

Fig. 15 Valveless pulse combustor tested on a small gas turbine

Fairly recent laboratory work using a small pulse combustor has resulted in the demonstration, external to a gas turbine, of a stagnation pressure-gain of approximately 6 percent [18]. It is these tests that contribute the lower "pulse-combustor" characteristic presented in Fig. 13. Projections indicate [18] that a stagnation pressure gain in excess of 10 percent may be obtainable with larger pulse combustors (chain-dotted curve of Fig. 13). A question that can be asked in why, when both a dynamic pressure exchanger and a valveless pulse-combustor pressure-gain combustor are nominally constant volume combustors, is the performance of pulse-combustors so much poorer as implied in Fig. 13? The answer relates, in part, to the fact that generally a dynamic pressure exchanger has a greater inherent charge precompression than a pulse combustor but a factor of, it would appear, greater importance is the presence of a relatively large portion of residual products, which remain in the pulse combustor combustion zone after each cycle. The influence of residuals is demonstrated, in terms of the simple model of Fig. 3, by recirculation of mass fraction n to inlet A of the products discharged from outlet B. The influence of increasing n, for a prescribed value of T_3/T_2, on the ideal combustor pressure ratio P_3/P_2 can be seen from Fig. 14. The residuals remaining in the combustion zone of a pulse combustor are of vital importance in initiating combustion for the subsequent cycle [16]. A value of n of approximately 0.5 appears to be representative of a highly loaded pulse combustor suitable for a gas turbine application.

Figure 15 shows, diagrammatically, a form of pulse combustor that has recently been used on a very small, low-pressure-ratio gas turbine unit. The results obtained, which typically resulted in a pressure gain of about 1 1/2 percent,

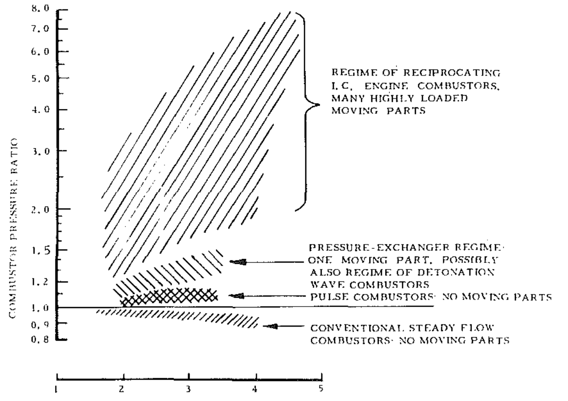

Fig. 16 Summary of the performance potential of several types of pressure-gain combustor

will shortly be reported fully [19]. The results of earlier work using a more primitive version of the apparatus shown in Fig. 15 have been reported previously [20].

Overview

In the most general sense it can be seen, from a comparison of Fig. 6 with the upper curves of Fig. 7, that the ideal pressure ratio of a pressure-gain combustor increases with increasing charge precombustion compression. Nevertheless, it is apparent from Fig. 7 that a significant combustor pressure ratio is achievable without any charge precompression provided the system irreversibilities can be minimized. It would appear that the price to pay for a substantial charge precompression is in terms of system complexity. If, for example, a diesel-type reciprocating internal combustion engine is employed as a pressure-gain combustor, along the lines illustrated in Fig. 5 for example, then a comparatively large number of relatively highly loaded moving parts are employed in the pressure-gain combustor whereas a pressure-gain combustor based on, say, a dynamic pressure exchanger involves only a single major moving component. Furthermore the latter is not expected to impose significant startup problems whereas, as stated earlier, a diesel type pressure-gain combustor may present a startup problem due to a low overall compression ratio. Startup problems increase as the design pressure ratio of the gas turbine compressor W (Fig. 3) increases. For very low-pressure-ratio gas turbine compressors the situation tends to approach that at startup of a conventional turbocharged diesel.

The ultimate in simplicity, insofar as the absence of moving parts is concerned, is the valveless pulse combustor. However the price here appears to be related to the achievement of only a modest pressure gain. It would appear that, at best, detonation wave gas turbine combustors are not likely to have performances better than those of simple pressure-exchanger concepts considered here and, if the control of irreversibilities is not good, they may be but little more effective than valveless pulse combustors.

For some gas turbines, for example those used for aircraft applications, weight and bulk are both important considerations. It would appear that the bulk of a valveless pulse combustor is greater than that of a steady-flow combustor of equal output. The prime reasons for this are apparent from Fig. 15 and relate to the presence of long tuned ducts in the case of the pulse combustor. A dynamic pressure-exchanger system, at least of the type tested by Rolls-Royce and General Electric, is likely to be heavier and more bulky than a conventional steady-flow combustor due to the prescence of the pressure-exchanger rotor and casing. A diesel-based pressure-gain combustor is also likely to be relatively heavy and bulky. It is not, of course, the weight and bulk of the combustor in isolation that are important but rather the specific weight and specific bulk of the entire engine equipped with a pressure-gain combustor.

Figure 16 is an attempt to present a summary of the pressure-gain performance aspect of the work reported here. The internal combustion engine regime was established by modifying the idealized results of Fig. 6 to allow for engine mechanical efficiency, etc. The pressure-exchanger and pulse-combustor regimes are based on available test data as indicated in Fig. 13. It can be seen that the various pressure-gain combustor schemes appear to "stack" indicating that an increase of pressure-gain potential is associated with an increase in complexity with the valveless pulse combustor and conventional steady-flow combustor being of roughly equal complexity in that neither contains moving parts.

Conclusions

The main conclusions drawn from the work reported here are as follows:

1 The pressure-gain potential of the combustors studied increases with increasing system complexity.

2 With the possible exception of pressure-gain combustors based on the dynamic pressure-exchanger concept and those employing detonation waves, the systems investigated have performance characteristics that imply that each particular type of system is best suited to a particular pressure-gain regime. This conclusion is well illustrated when the combustor performances are presented on a combustor pressure ratio versus temperature ratio plane.

3 It was found that for most of the concepts investigated the combustor pressure ratio attainable increases with combustor outlet-to-inlet temperature ratio.

Acknowledgments

The writers wish to thank the Natural Sciences and Engineering Research Council of Canada for financial assistance, which made this work possible.The aid was in the form of Operating Grant No. A7928 extended to the first author.

References

1 Thring, M. W., ed., *Pulsating Combustion, The Collected Works of F. H. Reynst*, Pergamon Press Ltd., London, 1961, Chap. 2.

2 Catchpole, B. G., and Runacres, A., "Constant Volume Gas Turbine Experiments With Gaseous Fuel in a Rotating Pocket Combustor," Mechanical Engineering Note ARL/ME 353, Aeronautical Research Laboratories, Dept. of Defense, Melbourne, Australia, Oct. 1974.

3 Williams, J. E., "The Constant Volume Gas Turbine – Revision of the Simplified Theoretical Analysis," Mechanical Engineering Note ARL/ME 356, Aeronautical Research Laboratories, Dept. of Defence, Melbourne, Australia, Feb. 1975.

4 Helman, D., Shreeve, R. P., and Eidelman, S. "Detonation Pulse Engine," presented at 22nd Joint Propulsion Conference, Huntsville, AL, June 1986, AIAA Paper No. 86-1683.

5 Wortman, A., "Detonation Wave Augmentation of Gas Turbines," Twentieth Joint Propulsion Conference, AIAA, Santa Monica, CA, June 1984.

6 Lockwood, R. M., "Interim Summary Report on Investigation of the Process of Energy Transfer From an Intermittent Jet to Secondary Fluid in an Ejector Type Thrust Augmenter," Report No. ARD-286, Hiller Aircraft Corp., Palo Alto, CA, Mar. 1961.

7 Rostafinski, W., "Comparison of the Wave-Rotor-Augmented to the Detonation-Wave-Augmented Gas Turbine," *Proceedings Wave Rotor Research and Technology Workshop*, Naval Postgraduate School, Monterey, CA, Mar. 1985, pp. 271-283.

8 Shchelkin, K. I., and Troshin, Ya. K., *Gasdynamics of Combustion*, Mono Book Corporation, Baltimore, MD 1965, Chap. 1.

9 Azoury, P. H., "An Introduction to the Dynamic Pressure Exchanger," *Proceedings, IMechE*, Vol. 180, Part 1, No. 18, 1965.

10 Kentfield, J. A. C., "The Pressure-Exchanger: An Introduction Including a Review of the Work of Power Jets (R&D) Ltd.," *Proceedings Wave Rotor Research and Technology Workshop*, Naval Postgraduate School, Monterey, CA, Mar. 1985, pp. 9-49.

11 Moritz, R., "Rolls-Royce Studies of Wave Rotors (1965-1970)," *Proceedings Wave Rotor Research and Technology Workshop*, Naval Postgraduate School, Monterey, CA, Mar. 1985, pp. 116-124.

12 Mathur, A., "A Brief Review of the G. E. Wave Engine Program, 1958-63," *Proceedings Wave Rotor Research and Technology Workshop*, Naval Postgraduate School, Monterey, CA, Mar. 1985, pp. 171-193.

13 Sladky, J. F., Jr., Thomas, B., and Sandhur, A., "Internal Combustion on Wave Rotors," presented at 21st Joint Propulsion Conference, Monterey, CA, July 1985, AIAA Paper No. 85-1412.

14 Kentfield, J. A. C., "An Approximate Method for Predicting the Performance of Pressure Exchangers," ASME Paper No. 68-WA/FE-37, 1968.

15 Spalding, D. B., Private Communication, 1968.

16 Putnam, A. A., Belles, F. E., and Kentfield, J. A. C., "Pulse Combustion," *Progress in Energy Combustion Science*, Vol. 12, 1986, pp. 43-79.

17 Thring, M. W., ed., *Pulsating Combustion, The Collected Works of F. H. Reynst*, Pergamon Press Ltd., London, 1961, Chap. V.

18 Kentfield, J. A. C., Rehman, A., and Cronje, J., "The Performance of Pressure-Gain Combustors Without Moving Parts," *AIAA Journal of Energy*, Vol. 4, No. 2, 1980, pp. 56-63.

19 O'Blenes, M., "The Application of a Pulse Combustor to a Small Gas Turbine," M. Sc. Dissertation, University of Calgary (to be published).

20 Kentfield, J. A. C., and Yerneni, P., "Pulsating Combustion Applied to a Small Gas Turbine," presented at the ASME Gas Turbine Conference, Houston, TX, Mar. 1985, Paper No. 85-GT-52.

Journal of Engineering for Gas Turbines and Power

Technical Briefs

Numerical Prediction of the Internal Two-Phase Flow in a Variable Air Atomizer

J. Militzer,[1] D. T. Shiu,[2] and K. C. Watts[3]

Introduction

Coal-water mixtures (CWM) have become a viable alternative to fuel oil, because of the similarity in the modes of burning, storage, and transportation. However, the abrasive characteristic of the suspended coal particles in the CWM has led to the requirement of nozzles of unique design. One such nozzle, the conical variable gas atomizer (VGA) nozzle (Walsh, 1982) shown in Fig. 1, uses high-velocity air to atomize the CWM and to protect the nozzle walls from excessive wear. Physical investigation of the flow inside the nozzle is virtually impossible due to the multiphase nature of the flow and to its minute dimensions. However, studies using numerical simulation models give useful insight into the hydrodynamics of the flow inside the nozzle. Using a computer program called PHOENICS developed by Spalding (1981), the present authors have sought to determine the distribution of velocity, pressure, and volume fraction within this nozzle in order to explain some observed coal deposition on the internal walls and also to define those regions of the nozzle more susceptible to erosion. No other work has been reported on the flow inside this nozzle.

Computational Model

The flow is modeled by assuming two continuous fluids interacting through an interphase friction term. The axisymmetric flow is described by eight conservation equations, namely, two continuity equations (one for each phase), four momentum equations (two for each phase), and two turbulence equations for the air phase, plus a relation ensuring that the sum of the volume fractions of the two phases must equal unity. The dependent variables are the two volume fractions, four velocity components, two turbulence parameters, and the static pressure. The general form of the conservation equations is given by Spalding and Markatos (1984). The interphase friction coefficient used in the momentum equations was assumed constant and equal to 10^4 Ns/m^4. The air turbulence effective viscosity was calculated using the k-ϵ turbulence model as given by Rodi (1980). Due to its complex geometry the flow domain was divided into four regions, as shown in Fig. 1. Initially, the single-phase air flow was calculated in regions 1 and 3, thus producing the necessary boundary conditions for the two-phase flow in region 4. In regions 1 and 3 the inlet turbulence velocity fluctuations were assumed to be of the order of 1 percent of the mean air velocity. The water flowing from region 2 into region 4 was assumed to have uniform inlet velocity. The range of simulated total air mass flow rates was 0.009 to 0.042 kg/s and the liquid flow rate varied from 0.042 to 0.25 kg/s. The air liquid mass flows were varied from 0.1 to 1.0, values that simulate those used in practice.

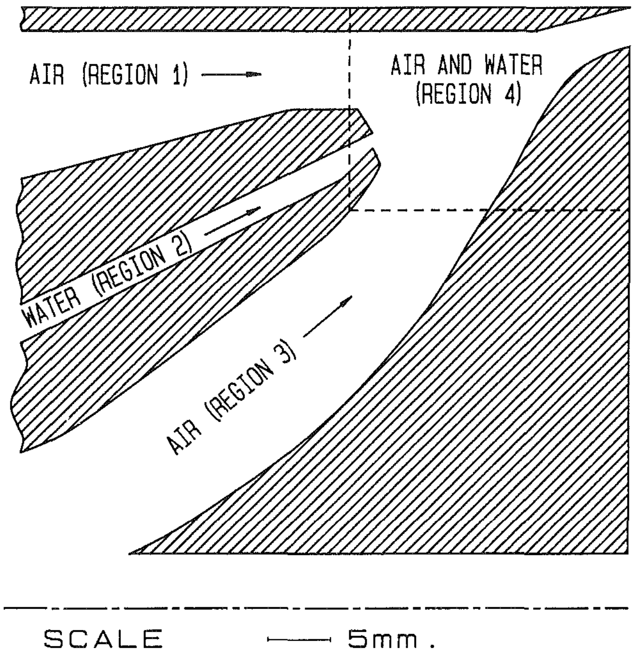

Fig. 1 Cross section of one side of the conical variable gas atomizer

Results and Discussion

The predicted distribution of air and liquid velocities and static pressure cannot be checked by experiment, but their appearance agreed with the results intuitively expected in all flow conditions.

Fine droplet size is produced by the shearing action of the high-speed air jets on either side of the slow-moving liquid stream. Figure 2 shows the slip velocities between the phases. Large slip velocities are observed throughout the flow. Both the liquid phase and the gas phase are greatly accelerated as they move toward the exit, thus ensuring the production of very fine droplets. This confirms the good atomization characteristics of the VGA nozzle.

---

[1] Associate Professor, Department of Mechanical Engineering, Technical University of Nova Scotia, Halifax, Nova Scotia, B3J 2X4 Canada.

[2] Graduate Student, Department of Mechanical Engineering, Technical University of Nova Scotia, Halifax, Nova Scotia, B3J 2X4 Canada.

[3] Professor, Department of Mechanical Engineering, Technical University of Nova Scotia, Halifax, Nova Scotia, B3J 2X4 Canada.

Contributed by the Power Division for publication in the JOURNAL OF ENGINEERING FOR GAS TURBINES AND POWER. Manuscript received by the Power Division December 2, 1986.

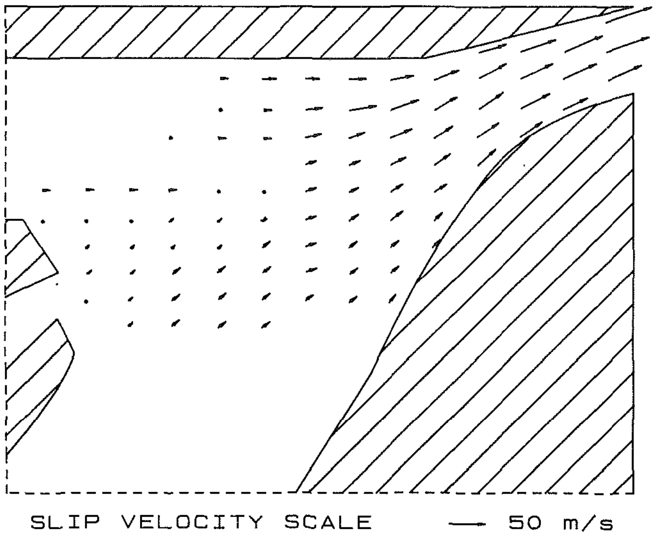

Fig. 2 Slip velocity between air and water phases in the two-phase mixing region (region 4, Fig. 1)

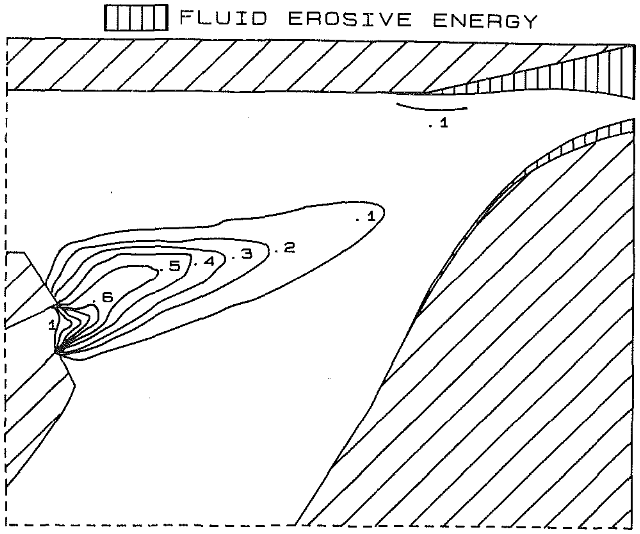

Fig. 3 Contours of constant volume fraction and area of high fluid erosive energy in the two-phase mixing region (region 4, Fig. 1)

The calculation of the kinetic energy of turbulence of the air phase in region 4 showed the existence of high levels of turbulence, particularly behind the blunt noses, where a separation or recirculation zone occurs (the static pressure computations confirm the presence of the separation region). The high levels of kinetic energy of turbulence throughout the flow field is also thought to aid in the fine droplet formation through shearing on a microscopic level.

One example of constant volume fraction distribution (volume of liquid to total volume) is noted in Fig. 3. In general for all flow conditions investigated, volume fraction values larger than 0.1 are contained within the two air jets. However, as the liquid flow rate is increased, the 0.1 contour becomes open ended through the exit of the VGA nozzle. One interesting exception to the containment of the volume fraction is shown for one set of flow conditions in Fig. 3. A portion of the 0.1 volume fraction line is shown to exist near the upper surface leading to the exit of the nozzle. This concentration may occur due to the deflection of the water by the differential air stream velocities. This phenomenon was experimentally confirmed by the accumulation of coal on the nozzle outer wall in the series of experiments carried out by Batra et al. (1984).

The erosive energy in a liquid (Rehbinder, 1977) is proportional to the product of the liquid mass flow rate times its velocity squared, or by the product of the volume fraction of the liquid and the cube of its velocity. Based on this relationship, the rapid increase in potential wear along the nozzle walls is noted in Fig. 3 for one representative flow condition. It is evident that the air stream does not completely prevent the liquid from reaching the nozzle walls and considerable wear potential is experienced at the nozzle tip. The amount of wear potential on top and bottom walls is a function of the deflection of the liquid by the air jets.

In conclusion, this study has described the internal hydrodynamics of the variable gas atomizer using the PHOENICS program. Fine atomization is predicted as a consequence of the shear rates between the phases and due to the high turbulence levels observed. A tapering of the exit of the liquid jet from region 2 would give less recirculation behind the blunt noses with less liquid phases reaching the upper surface of the nozzle. The conflicting constraints of good atomization (which requires a high differential velocity between the phases) and protection of the wall from wear (which requires a low liquid velocity with respect to the wall) must be balanced in practice.

Acknowledgments

The assistance provided by A. Singhal and F. Owens from CHAM of NA in the use of PHOENICS is gratefully acknowledged. The financial assistance provided by the National Science and Engineering Council of Canada is also gratefully acknowledged.

References

Batra, S. K., Walsh, W. A., Jr., Pegg, M. J., and Todd, A. E., 1984, "Combustion Test Results of Second Generation Coal Liquid Mixture Burners," *Proceedings of the 6th Symposium on Coal Slurry Combustion and Technology*. Orlando, FL.

Rehbinder, G., 1977, "Slot Cutting in Rock With a High Speed Water Jet," *Int. J. Rock Mech. Min. Sci. and Geomech. Abst.*, Vol. 14, pp. 229–234.

Rodi, W., 1980, "Turbulence Models and Their Application in Hydraulics, a State of the Art Review," International Association for Hydraulic Research.

Spalding, D. B., 1981, "A General Purpose Computer Program for Multi-dimensional One and Two-Phase Flow," *Mathematics and Computers in Simulation*, Vol. 23, pp. 267–276.

Spalding, D. B., and Markatos, N. C., 1984, "Introduction to PHOENICS," Lecture notes at CHAM of NA, Huntsville, AL.

Walsh, W. A., Jr., 1982, United States Patent No. 4314670*.